# Self-Assembly and Real-Space Modeling in Binary Hard-Particle and Quasicrystalline Systems

by

Andrew T. Cadotte

A dissertation submitted in partial fulfillment
of the requirements for the degree of
Doctor of Philosophy
(Applied Physics)
in The University of Michigan
2022

Doctoral Committee:

Professor Sharon C. Glotzer, Chair
Professor Michael Engel
Professor Cagliyan Kurdak
Associate Professor Xiaoming Mao

Andrew T. Cadotte
cadottea@umich.edu
ORCID iD: 0000-0002-6299-7315

## DEDICATION

This work is dedicated to my wonderful partner Leo; and to my family, Rozanne, Vance, Vicky, and Alyx, who have all supported me throughout the many years.

## ACKNOWLEDGEMENTS

I would like to thank my advisor, Professor Sharon Glotzer, for all of her support throughout the years. Her thoughtful questions and constructive feedback have never failed to inspire my creativity.

I thank Professor Cagliyan Kurdak and Cynthia McNabb for being my family in the Applied Physics department. Their kindness has always helped in innumerable ways.

Finally, I would like to thank all of the Glotzer lab members for their friendship and collaborations. In particular, I would like to thank Dom Fijan for all of his work with the quasicrystal project. I would also like to thank past Glotzer group members; Pablo Damasceno, who first introduced me to the Glotzer group, Richmond Newman for his ever-helpful coding advice, Julia Dshemuchadse for her constant encouragement, and current group member Kwanghwi Je for his help with *Chapter Six.* I would also like to thank Karen Coulter for her work and dedication to the Glotzer Group. I would also like to thank Rob Pettigrew at Scholarspace for his invaluable work in finalizing this manuscript.

## Table of Contents

## LIST OF FIGURES

## List of Appendices

## Glossary

**phason:** In the higher-dimensional projection, a phason error is a lattice point that exists outside of the cut window, but is still included in the projection. The phason flip is the tile movement that erroneously includes or omits a lattice point from this cut window.

**tiling:** A tiling consists of one or more different geometric shapes that fill space without any overlaps or gaps. Tilings can be ordered or disordered, periodic or aperiodic.

**covering:** Coverings consist of repeating motifs that overlap portions of their tiles. Tiles that overlap must match both position and orientation. Like a tiling, a covering also fills space without gaps.

**covering motif:** A special motif in a quasitiling where it has been proven that every tile belongs to the covering motif, and no tile exists in the quasitiling which does not belong to the covering motif.

**layering:** A layering is a special concept introduced in this thesis to simplify the tiling description of a quasilattice. Like a covering, portions of a motif are allowed to overlap, but the tiles are no longer required to match position or orientation. Layering rotations are equivalent to phason flips.

**quasilattice:** A quasilattice comprises the lattice points that make up the ordered tiling of a quasicrystal. A quasicrystal is a quasilattice that is decorated with particles.

**random/ideal tiling:** An ideal tiling is a quasilattice that displays perfect hierarchical order. But as errors are introduced via phason flips, the tiling becomes less ordered and will exist somewhere on the random-ideal tiling continuum.

**construction:** The cycling process described within this thesis is capable of "tiling out" the quasitiling in a way that yields a perfect tiling. Matching or covering rules are explicitly not capable of this, so I refer to the former as *construction*.

**fundamental polygon:** A basic polygon that sits at the bottom of the tiling hierarchy

**characteristic polygon:** The fundamental polygons (e.g., square and triangle) are assembled into a polygon that has sides equal to the symmetry of the tiling. These characteristic motifs always have broken rotational symmetry/

**petal motif:** The characteristic polygons are made from the characteristic polygons, and will always have a polygonal motif with a rotational symmetry matching the tiling in the *layering* picture. E.g., the Penrose tiling has a pentagonal motif comprising five characteristic decagons.
**second-order polygons:** The petal motifs are assembled into second-order polygons either as a set of covering motifs, or as a single type of layering motif, up to chiral symmetry.
**second-order characteristic polygon:** The second-order polygons are assembled into the second-order characteristic polygon, and the cycle can repeat. E.g., the second-order decagons can be assembled into a second-order petal motif, and so on.
**polygonal cycle:** A concept introduced in this thesis whereby we take fundamental polygons, construct them into a characteristic polygon, that is then constructed into a petal motif, and then constructed into a second-order polygon. The process then repeats by constructing a second-order characteristic polygon, a second-order petal motif, and so on.
**ring:** characteristic polygons can be used to expand the size of the petal motif to ensure the petal motifs will fill space.
**ring conflict:** if too many rings are placed around a petal motif, two petal motifs on the first layer will begin to overlap, causing ambiguity in the tiling. This mismatch means the petal motif has been expanded too far.
**quasi-unit cell**: Like a unit cell from classic Crystallography, a quasi-unit cell could be used to build a new quasitiling. But the *covering motif* from earlier quasitiling work has not been used to *construct* a quasitiling, rather it has just been shown that a quasitiling contains **only** the *covering motif.* In the *polygonal cycling* method, we can construct the quasitiling from *characteristic polygons*. This ability to *construct* brings this concept of a quasi-unit cell more in line with the classical concepts of a unit cell.
**einstein:** a hypothetical tile that forces aperiodicity. This can be done via matching rules, or the shape itself. The tile may or may not be simply connected, as in the Socolar-Taylor Einstein solution.

## ABSTRACT

In this thesis, I will show a fundamentally new way to understand and construct quasicrystal tilings based on a new formulation of the quasi-unit cell called layering. There are many methods for generating quasitilings including Ammann/pentagrid methods, cut-and-project higher-dimensional projections, deflation/inflation substitutions, and various approaches using matching rules and non-local forced moves. The only other method which has a real-space quasi-unit cell comes from covering theory. However, covering approaches, much like matching-rule approaches, do not provide a recipe for error-free construction of the quasitiling and lack a description of the phason flips—a new type of local particle movement only observed in quasicrystals. In this thesis, I will showcase that layering does provide a way to construct perfect quasitiling from a quasi-unit cell and naturally gives rise to a real-space description of the phason mode of particle movement. This new method was applied to the three Penrose pentagonal tilings, the Ammann-Beenker octagonal tiling, the Tübingen triangle decagonal tiling, the Niizeki-Gähler dodecagonal tiling, and finally the Ammann-Kramer-Neri icosahedral tiling. In addition, simulations were performed using a patchy hard-particle set of Penrose rhombuses as a demonstration of the power of the analysis method. The last chapter of this thesis reports the formation of a binary crystal of hard polyhedra due solely to entropic forces. Although the alternating arrangement of octahedra and tetrahedra is a known space-tessellation from Maurolyctus in 1529 (Lagarias, 2015), it had not previously been observed in self-assembly simulations. Both known one-component phases—the dodecagonal quasicrystal of tetrahedra and the densest-packing of octahedra in the Minkowski lattice—are found to coexist with the binary phase. Apart from an alternative, monoclinic packing of octahedra, no additional crystalline phases were observed.

## Chapter One
## Introduction

Contrary to numerous popular science articles, ideal quasicrystals are assuredly not intermediate between ordered and amorphous states (Grimm & Joseph, 1999), as changing the orientation of even a single pair of tiles will disrupt the quasiperiodic order. The perfect tiling may look disordered when viewed with the unprepared eye, but this thesis will present a method to easily see the order that is hidden in a quasicrystalline tiling without resort to the traditional methods, and in a manner that does not require drawings or calculations—in effect, a way that does not require the generation of a perfect tiling and then later comparison of the tilings. This method is also different from the generalized lifting protocol that can be used to view the mathematical window that represents a given tiling's cut-and-project, or shadow, had it been generated from a cubic-lattice of hypercubes. Similar to deflation, this method—which I call *layering*—makes use of the fact that quasicrystals are based on self-similar hierarchical lattices. Deflation, however, can only generate more tiling and does not provide a sense of structure that is otherwise found throughout crystallography—contingent on a *unit cell*. Quasicrystals are universally viewed as incredibly complex materials. Here, their tilings are presented with a formalism that is simple enough to allow anyone to not only visualize their arrangement, but also, with practice, to use this mnemonic to memorize the construction of any level of quasicrystal hierarchy. This work further expands on the covering concept from tiling theory of a *quasi-unit cell*. This work also effectively describes a new kind of order parameter—one based on clustering—for quasicrystalline systems.

This idea—that a quasicrystal tiling actually consists of a single motif that *layers* over itself to produce the bulk array of different possible clusters in the tiling through a series of phason flips/rotations—actually appears to be a general property of these tilings that has never been demonstrated in the literature. It works similarly to the polygonal cycling model that is also introduced and detailed in these chapters, which create a set of coverings. But unlike coverings, the underlying tiles do not need to match. Curiously, it turns out that the top and bottom motifs

are related through what is called a phason flip. This is intriguing because, prior to this research, the only theoretical explanation for the origin of the phason flip is the cut-and-project model. The covering model, which this work has built on, and that was originally proposed by Burkov (Burkov, 1991), is the recognition of a quasi-unit cell (E. A. Lord & Ranganathan, 2001). The layering model proposed herein is not only an extension of the quasi-unit cell, but is also a real-space assembly protocol—what I am here calling a *construction*. Not only can this allow a real-space visualization of the quasicrystalline tiling in its entirety, but it also greatly simplifies the concept of what it means to be a quasicrystal tiling. Although *Chapter Two* deals specifically with just the Penrose rhombus tiling, the same method has been applied to all three Penrose tilings, the Ammann-Beenker, the Tübingen tiling, the Socolar shield/butterfly tiling and related dodecagonal tilings, and even the icosahedral Ammann-Kramer-Neri tiling. It is my hope that this simplification will inspire an interest in quasicrystal tilings that extends well beyond the fields of crystallography and self-assembly. Artists, engineers, architects, and many others may benefit from this non-mathematical approach to the construction of quasicrystal tilings.

*Chapter Seven* was my first introduction to quasicrystals, and it dealt with the question of whether regular hard tetrahedra and octahedra, with matching edge lengths and no attractive potentials, will self-assemble into a binary crystal. This question had been explored before (Khadilkar & Escobedo, 2012), but without success. We know that tetrahedra, if mixed in a phase with enough tetrahedra, will self-assemble into a dodecagonal quasicrystal (Haji-Akbari et al., 2009), and these are all apparent through the figures in this chapter. But what is a dodecagonal quasicrystal, exactly, beyond the fact that it has a 12-fold diffraction pattern? This set the stage for my curiosity.

The Penrose tiling is the simplest tiling to apply the method to, and so it is the first quasilattice tiling that I describe. This will make understanding the following chapters easier. This order parameter characterizes the quasilattice defect—a phason—in real-space for any arbitrary level of hierarchy, and so not only frames the entirety of the quasilattice in a straightforward way, but also makes error detection easy to do. This method is then applied to a two-dimensional patchy hard-particle simulation in *Appendix A*.

Quasicrystals, at least historically, were defined by possession of what was called non-crystallographic symmetry. Before the discovery of quasicrystals, every crystal then discovered—at least the ones we knew about—contained only the “allowed” classical

symmetries of 1, 2, 3, 4, and 6-fold axes. A crystal has a specific symmetry if we can rotate it by a certain angle and get back the same image that we started with. If we can do this for 180°, for instance, then the crystal has 2-fold symmetry. If we rotate it by 90° to get back to the same image, then the crystal has 4-fold symmetry, and so on. The proof of the impossibility of crystals having symmetries outside of these allowed symmetries rests on the fact that crystals are periodic, and it seems no one prior to 1982 stopped to consider the possibility that an ordered, but aperiodic, material could have other symmetries. It was even later realized that quasicrystalline tilings can be generated with any arbitrary symmetry, including those previously only represented by classical symmetries (Lifshitz, 2000) —thus "non-crystallographic symmetry" is no longer a hallmark feature of quasicrystal.

The first quasicrystal was discovered in 1982 by Daniel Shechtman in a rapidly cooled Al-Mn alloy, but not published until 1984 (Shechtman et al., 1984) to further refine the results. Even today, although there is a lot more that we can say about quasicrystal properties, there is no universally accepted definition of what a quasicrystal *is* (Lifshitz, 2000; Senechal, M., 2007; Wolny et al., 2018).

It was a 10-fold symmetric pattern, corroborated by excellent theoretical work (Levine & Steinhardt, 1984) that led to the discovery of quasicrystals—one strictly not allowed to exist in periodic materials. There is a catch here, however. Somehow, random quasicrystal tilings had also not been discovered in materials. It was not until the growth of quasicrystals with pin-point diffraction spectra that there was serious consideration of the possibility of self-assembled materials with ideal, or at least less random, quasicrystalline tilings, but even these "ideal" tilings have significant amounts of disorder when viewed with the *layering* process described herein. This is because *random* (vs. *ideal*) tilings, which don't necessarily have any hierarchical order, can still have sharp Bragg peaks.

Lacking this translational symmetry, it was a puzzling question to experimentalists in the 1980s as to what exactly, then, is a quasicrystal? Shechtman's discovery of quasicrystalline matter ushered in a revolution in crystallography, forcing a redefinition of "crystal" as "a material exhibiting essentially a discrete diffraction pattern" (IUCr, 1992). The work presented in *Chapter Two* was pursued to explore and elaborate on the nature of Penrose tilings, and also to develop new analysis software. Although a phason strain analysis provides a metric for

determining where along the random-ideal continuum a given tiling is located, it does not provide a means of visualizing what exactly this means.

This quote (A. E. Madison, 2015) regarding the (not yet presented) icosahedral quasicrystal (*Chapter Six*) also captures some of what I want to address in *Chapter Two*. The author offers a similar critique of the higher-dimensional cut-and-project method—insofar as it is both amazingly useful, and also simultaneously awkward to use in some circumstances,

> The detailed method, by which the positions of the planes in the zonohedra were obtained, as well as the correct deflation of each cell, was difficult to understand without access to some 3D models. The complicated matching rules, the constant need to recall higher-dimensional representation in order to verify the local environment of a given cell, and the need to cross-check the specification reference table in order to perform decoration correctly – all of these complications hinder the accurate analysis and practical use of the algorithm. Moreover, we have a firm conviction that a three-dimensional description of a three-dimensional object is always preferable.
>
> On the other hand, the higher-dimensional approach represents today the only successful way in solving the quasicrystals puzzle, so it would be silly to criticize it. We don't mean to look for disadvantages, but rather to highlight the inherent difficulties due to the lack of any alternative.

In presenting a solution to this real-space analysis question, which I am calling the layering method, we need to be proficient in understanding the concepts of *tiling*, *covering*, *matching rules*, and *phasons,* and how they've been used in the history of quasicrystals. Finally, I will review the currently known ways of generating quasicrystals, that take the form of *deflation/inflation*, *Ammann bars*, and *cut-and-project*, so that we can better understand how to compare and contrast the new *covering* and *layering* construction methods proposed herein.

## Symmetry

Before we start examining the quasilattice, let's review a few fundamental concepts in crystallography. Nominally, quasicrystals are described as ordered—they contain long-range order but lack periodicity. Translational symmetry exists when, e.g., a unit cell can be copied and translated along some vector to a new location (***Figure 1.1***). The repetition of this process yields additional perfect crystalline tiling, and so an infinite periodic structure can be generated.

**Figure 1.1** An array of rhombuses can be tiled periodically by moving copies along the horizontal and vertical directions. This unit cell is a fundamental concept in crystallography.

## Tilings

When a shape or multiple shapes can be placed into a certain pattern to fill all of two-dimensional space with no gaps, spaces, or overlaps, it is said to have tiled the plane. Tilings are also known as a tessellation or parquetry. A real tiling has a space between adjacent tiles, perhaps filled with cement, glue, or dirt; mathematically, this space is treated as a heavy outline of tiles.

Polygons or polyhedra are said to tile space if they have this space-filling property—they leave no gaps or spaces that are not represented by that set of tiles. Quasilattices are also tilings of space. Within the group of tilings that are called quasilattices (or quasicrystals, if they are also decorated with particles), there exists a spectrum from random to ideal tilings. For the purposes of this thesis, random tilings are just what they sound like—they contain the same tiles as the ideal tilings, but are not arranged into any particular hierarchical order[1]. Random tilings fill space. Ideal tilings also fill space, but have the added property of perfect hierarchical order (like a fractal—where scaled down versions of the shape are placed inside of itself, e.g., the Sierpiński triangle). These tilings can be generated by any of the classic methods of cut-and-project, deflation, Ammann bars or pentagrid bars, and so on.

[1] What made random tilings hard to distinguish from ideal tilings, at least in materials, is that they can still have sharp Bragg peaks in their diffraction spectra. These sharp spectra had long been associated with perfect order in periodic materials—hence the confusion. **Sharp diffraction spectra are not a measurement of the long-range correlations of a quasitiling—only the orientational order of a space-filling random tiling.**

An ordered tiling that lacks translational symmetry is called a non-periodic tiling. The set of points at the vertices of this non-periodic tiling creates a quasilattice. If we decorate the quasilattice with particles—perhaps just at the vertices, or something more complex—then we call it a quasicrystal.

## Coverings

Tilings are generated from a tile or set of tiles, whereas coverings are generated from a motif or set of motifs. Coverings are allowed to overlap, **provided that the region of overlap matches exactly**. Covering also means that there are no gaps—all of the motifs fit on top of each other along the respective edges of their composite tiles with no gaps or spaces. Conway was one of the first to observe that the cartwheel in the Penrose kite-and-dart tiling (***Figure 1.2)*** appears to cover the plane (Grünbaum & Shepherd, 1986). This is to say, it fills space and it is allowed to overlap itself. Gummelt later proved that these decorated decagonal motifs (***Figure 1.3***) do indeed cover space in 2D (Gummelt, 1996), and so they now bear her name. **Gummelt's prescription for overlaps, however, is actually quite complex—and it is not a recipe for constructing the decagonal motifs into a space-filling tiling. In this respect, I talk about *coverings* here as an old concept, but I will introduce a *covering construction* in *Chapter Two* which is new. This *covering construction* will form the basis for understanding the *layering construction*.** In the same way as a *matching rule*[2], Gummelt proved that an ideal tiling will contain only this covering motif, and obey these covering rules. In that respect, what is to follow in this thesis is a novel way to use these decagonal motifs to do something that matching rules cannot—construct the infinite ideal tiling. This method works by first building a polygon, and then another polygon from those parts, and then eventually repeating the cycle. **The second polygon—a pentagon in the case of the Penrose rhombus tiling—is important because it defines the symmetry of the tiling**. Not only can we construct the tiling, but we can do so in a way that is simple enough to memorize after some effort.

[2] Discussed later in *Chapter One*

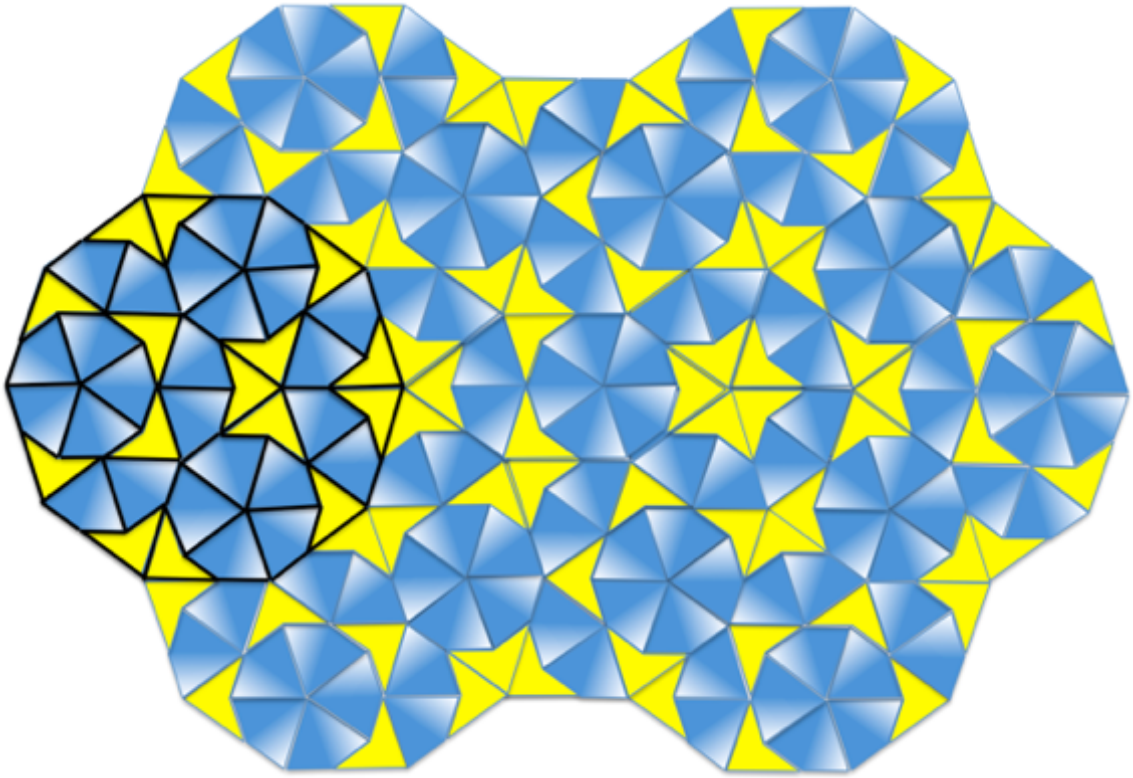

**Figure 1.2:** This is an example of the Penrose P2 kite-and-dart tiling, with Conway's cartwheel pattern (left, bolded) highlighting some of the quasilattice (Grünbaum & Shepherd, 1986). This cartwheel pattern can **cover** the plane of the P2 tiling[3].

[3] To repeat the process outlined in *Chapter Two*, take the kite-and-dart cartwheel (bolded) and place an arrow on it that points to the right. Assemble five of the cartwheels such that the arrows all point radially outward, but overlap to the same extent as shown in this figure (a skinny hexagon is the overlap region). This will form the core of the new petal motif. Next, take another set of five cartwheels and keep their arrows all pointing outward radially. Assemble them around the core such that they meet edge-to-edge with no overlaps, and are aligned and overlapping with five of the symmetric kite wheels. This is the first ring. It works very similarly to the core and first ring of the Ammann-Beenker tiling, except those have a 180° difference between the arrows of the core and first ring.

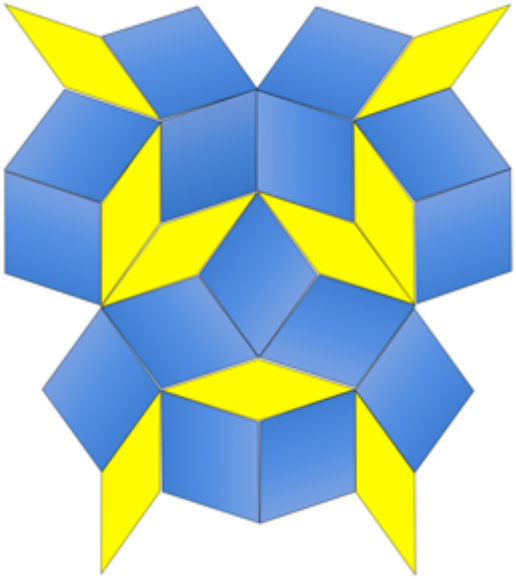

**Figure 1.3:** This figure shows the Gummelt motif, which is a single motif that can **cover** the entirety of the Penrose tiling. This is equivalent in function to the cartwheel patch shown in bolded outline in ***Figure 1.2***.

## Layerings

Like the polygonal cycling covering method, layerings are another new concept that I am introducing in this thesis. Unlike a covering, the motifs stacked onto each other do **not** need to match during an overlap. I introduced this concept because I saw an opportunity to greatly simplify the description of the quasitiling. The Penrose tiling, as we shall soon see, requires at least three types of pentagonal motif for the simple construction method described here. But with the layering concept, we only need one type of pentagonal motif. The number of polygonal covering motifs increases for each tiling that I examine beyond the Penrose tiling, culminating in twenty-six for the Ammann-Kramer-Neri tiling. There we will see that the layering concept works equally well and offers a dramatic reduction in the number of motifs required to describe its construction.

## Phasons

Interestingly, as we transform from the covering model to the layering model, the phason unit of the quasitiling naturally falls out of this description. To better understand what this means, and how it comes about, let's first explore the concept of phason in some depth.

It was not known to Penrose at the time, but phasons, a type of tile flip, enter into the tiling picture with his addition of jigsaw edges—now called *matching rules* (Henley, 1988; Strandburg, 1991). Tiles that violate matching rules can be regarded as phason defects, and it is expected that phason flips can energetically restore the defective portion of tiling to an ideal tiling. Phason flips can, in fact, transform a random tiling to an ideal tiling and actually take any finite patch of ideal tiling and transform it into any other finite patch of ideal tiling (Henley, 1988; Strandburg, 1991). In this ideal picture of a quasicrystalline tiling, the ideal tiling represents the lowest energy configuration of the tiling, whereas deviations from ideal are then in a higher-energy configuration, and contain the class of random tilings.

In quasicrystalline materials, phason flips are a form of atomic displacement unique to quasicrystals, and are held to be responsible for many of their unique properties, like heat or electrical distribution (Janot, 1997)[4]. This specific heat and thermal conductivity, combined with their high hardness, has led to their development as novel thermal barrier coatings (Abe et al., 2003; Pope & Tritt, 2006). In the cut-and-project model, phasons are understood as lattice positions that are outside of the cut window for a given projection (Bak, 1985; Jarić, 1988; Levine & Steinhardt, 1986b). The lifting protocol can be used to generate this effective cut window and show how close a given tiling is to the ideal tiling. Random tilings can be ergodically accessed from the ideal tiling via phason flips. In this study of quasilattice tilings, however, phasons will just be represented by their simple tile flips.

**Random Tilings and Phason Flips**

A random Penrose tiling has orientational order—every rhombus is edge-aligned with one of the five-fold axes of the pentagonal quasilattice, but has no long-range quasiperiodic order. It is also space-filling. Because of this long-range orientational order, the random tiling can produce 5-fold diffraction patterns. Since quasicrystals were originally defined to describe

[4] These phason modes are like "loose rocks" that soak up energy into other modes as the phason propagates (Abe et al., 2004). This provides some intuition for their unusually low room temperature thermal conductivities of 1-3 $Wm^{-1}K^{-1}$. At 1000K, AlCuFe quasicrystals still have a thermal conductivity less than 10 $Wm^{-1}K^{-1}$. Contrast this with stainless steel at ~20 $Wm^{-1}K^{-1}$, or copper at ~400 $Wm^{-1}K^{-1}$.al., 2004). This provides some intuition for their unusually low room temperature thermal conductivities of 1-3 $Wm^{-1}K^{-1}$. At 1000K, AlCuFe quasicrystals still have a thermal conductivity less than 10 $Wm^{-1}K^{-1}$. Contrast this with stainless steel at ~20 $Wm^{-1}K^{-1}$, or copper at ~400 $Wm^{-1}K^{-1}$.

these non-crystallographic diffraction spectra, it seems suitable to include random tilings as a type of quasilattice. In terms of the Fibonacci growth riddle, however, random tilings would not present much of a mystery—they can assemble because of pressure and appropriate potential settings (Damasceno et al., 2017). This is to say, **there is no growth riddle for random tilings—and quasicrystals that are grown contain a great deal of random tiling.** Phason flips can be understood in this context as alterations to a perfect Penrose tiling that preserve the space-filling characteristic—they preserve the overall 5-fold orientational order, but do not preserve the long-range quasiperiodic order, if there was any. Phasons are thus capable of taking a tiling from a completely random tiling to an ideal one, i.e. they are ergodic (Henley, 1988). Because of this, it would seem to me that a random tiling is something altogether different from a quasicrystal—they share orientational but not necessarily any hierarchical order. Other literature sources take no issue because of the original use of the word in experimental studies (Steurer, 2018). In any case, it's clear that **unbiased** phason flips introduce errors in the perfect quasicrystal tiling, and that these errors will eventually remove the long-range quasiperiodic order but preserve the orientational order—which relates phason flips to some aspects of Henley and Elser's definition of a random "quasiperiodic" tiling. **Were these phason flips biased toward reducing the energy of the system, we would expect them to drive the system toward a more ideal tiling.** One other thing to note is that Henley differentiates between "perfect quasicrystal" and "ideal quasicrystal," where a random tiling is "perfect" because it has Bragg peaks, but is not ideal because of structural disorder (DiVincenzo & Steinhardt, 1999).

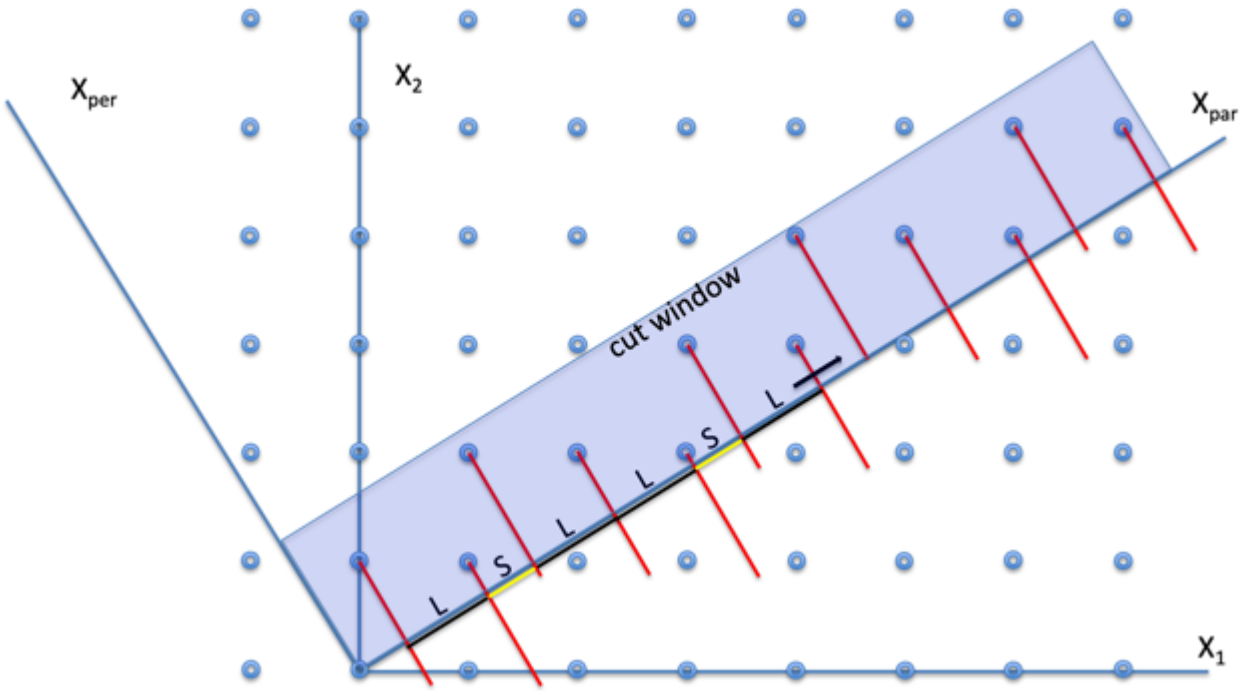


**Figure 1.4:** This diagram shows the creation of a one-dimensional quasilattice—the Fibonacci Sequence represented with short S and long L segments. A cut is made through a two-dimensional periodic (square) lattice at an irrational angle, $1/\emptyset \approx \mathbf{35.4}°$. The blue rectangle shows the cut window that represents every lattice position that will be included when projecting the quasilattice. The size of the cut window is arbitrary but, if it were infinite, the points on the quasilattice would be mathematically *dense*—there would be a point at, well, every point. Now, we take our projection axis to be through the origin, and the sequence reads LSLLSL, which is indeed the first six letters of the Fibonacci Sequence. Instead of a cut window, we could also place lines on the lattice points and include them as points if they intersect the parallel axis (red lines) —this is just an alternate representation of the projection method.

Note that the Penrose tiling, constructed from two types of rhombus, is usually constructed from the five-dimensional primitive hypercubic lattice, which is much more complicated than ***Figure 1.4*** (Baake et al., 1990). However, as was apparent from de Bruijn's work (de Bruijn, 1981), one dimension is unnecessary—the pattern can be projected from a 4D lattice plane within the hypercubic lattice. This lattice plane is the intersection of the 5D lattice with the 4D hyperplane.

The regular Penrose pattern can be generated by a "Voronoi complex," but a "dual complex" can be used instead to generate a different decagonal quasiperiodic tiling—one with the same acute and obtuse golden triangle in the Robinson decompositions. This will be the Tübingen tiling discussed in *Chapter Four*.

### Matching Rules, Growth, and Phasons in the Penrose Rhombus Tiling

One of the strengths of either the covering or layering models is that they do not rely on matching rules for construction. Still, as a means of verifying that a tiling is assembled correctly,

it is useful to understand matching rules and how they work. Likewise, it is important to understand matching rules for the value they can play as energetic assembly rules (however imperfect) when understanding how real quasicrystals grow. To that end, let's review the concept of matching rules and how they connect with the work presented in this chapter.

It was recognized early on (Dworkin & Shieh, 1995) that matching rules cannot grow (without reconfiguration) an ideal quasicrystal because **they favor the connection of tiles that will later force matching-rule violations.** One could place a hundred defect-free tiles, for instance, and later find that, after placing another thousand defect-free tiles, a region appeared where a new rhombus cannot be placed without creating a phason defect. This is only avoided if the tiles are assembled in exactly a manner allowed by some region of the infinite Penrose tiling (tilings within the same local isomorphism class). Even Penrose (Penrose, 1989) pointed out that, "...the spontaneous growth of large regions of such quasicrystalline five-fold symmetric substances seemed to me virtually insurmountable." This even led him to speculate on the possibility of non-local quantum entanglement as the source of quasiperiodic order.

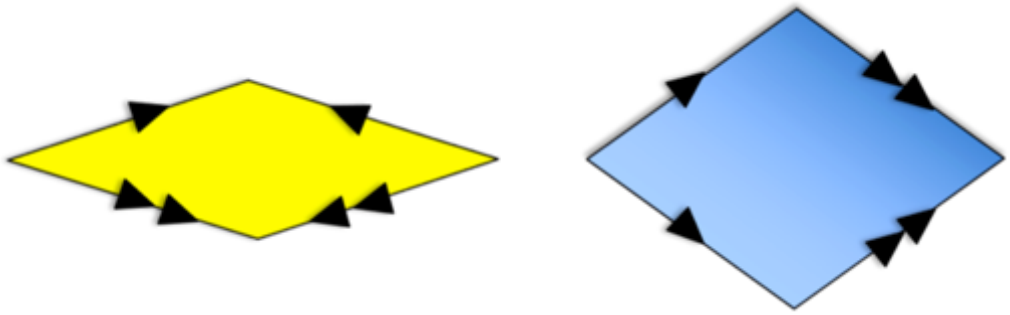

**Figure 1.5:** Matching rules, in the form of single and double arrows along the edges of the Penrose rhombuses, can restrict their tiling to only aperiodic forms. We cannot use them to assemble an ideal Penrose tiling, but an ideal tiling will not violate them. Effectively, we can use them to error check a quasilattice, but not to create the quasilattice**—at least not without the ability to reconfigure the tiling later on.**

The matching rules in the P2 rhombus tiling can be demonstrated by the addition of single and double arrows to the sides of the rhombuses (***Figure 1.5***). Arrows from two edge-to-edge polygons must match both count and direction. In this way, Penrose proved that the tiles can only tile space aperiodically by showing that the tile ratio approaches an irrational number—the golden ratio. An ideal Penrose tiling has no matching-rule violations—but do not let this deceive you because the Penrose matching rules are not rules for assembly. That is to say, if you were to take a collection of Penrose rhombuses on a large table, each which had been precisely marked with the correct matching rules, and set about to assemble a large ideal Penrose tiling,

you would find that, initially, the job was relatively easy. Knowing just a bit about what the rhombus tiling looks like, you could build the short and long hexagons, and either assemble them into worm lines along the 5-fold axes of the Ammann bars, or some other motif, but you would eventually find that you created a dead end where the matching rules forbade the addition of more tiles. As the tiling grows, you may find yourself undoing larger and larger layers of tiling in order to fix old errors. In this way, building a correct Penrose tiling using only matching rules becomes an exponentially difficult problem. I've always thought about the maximum possible size of perfect Penrose tiling that a human could build in a lifetime using matching rules alone—it's probably not very large! Grimm summarizes it well (Grimm & Joseph, 1999),

> At first, the tile-by-tile growth of a quasicrystal may even seem to be an impossible task. However, for certain tilings, there exist collections of local conditions, so-called matching rules, that enforce quasiperiodicity. **Nevertheless, these matching-rules do not really solve the problem: they only state that if you managed to tile the space without violating the matching rules, you will indeed have constructed a quasiperiodic tiling.** But they do not guarantee that a given finite "legal" patch (i.e. one that does not violate the rules) can in fact be extended to an infinite tiling of space. So, in this sense, **matching rules are not sufficient to provide a simple algorithm for the construction of ideal quasiperiodic tilings** [emphasis added].

## Ammann Bars, Fibonnaci Sequences, and Palindromes

Ammann bars are not only a way of constructing quasilattices, they also make it easy to see a phason flip in a given quasitiling. To better understand what this means, I am going to cover some of the history and use of Ammann bars.

Robert Ammann, a self-described amateur mathematician, independently discovered the Penrose rhombus tiling in 1976 (Gardner, 1997). He played an impressively large role in the tiling description of many quasilattices, and so his work is worth reviewing here. Ammann bars, as they are now called, are drawn onto each rhombus in ***Figure 2.15*** and ***Figure 2.16*** and are one way of generating a perfect quasicrystal lattice. To create the perfect Penrose tilings when starting with just these bars, we first draw five sets of parallel lines at the appropriate degrees of separation (360/5 =72 for decagonal). The bars should have Fibonacci spacing (some bars are spaced widely, some are short, and both should follow a correct Fibonacci Sequence e.g.,

LSLLSL, to be explained shortly[5]. Then, each intersection of bar uniquely defines the type and orientation of a given rhombus. Fat rhombuses in the Penrose tiling are one type of line intersection and skinny rhombuses are a different kind of line intersection. This wide and short spacing of the Ammann bars corresponds to what is known as the Fibonacci Sequence[6]. Fibonacci (1170 – 1250), known then as Leonardo of Pisa, a businessman and mathematician, was interested in bringing the Middle East's powerful decimal and algebraic systems to European business minds. He wrote many books—the most popular of which was Liber Abaci written in 1202—filled with examples that he had personally solved (Livio, 2003). Included as an example was the Rabbit Number[7]. Take two numbers, 1 and 2, add them together to get 3. Then add 2 and 3 to get 5, and so on. Then we have the Fibonacci Sequence (1, 2, 3, 5, 8, 13, 21, 34, 55, 89…). Then taking any two sequential numbers in the sequence, it can be shown that they converge to the golden ratio, $\phi \approx \frac{1}{2}(1 + \sqrt{5})$. In fact, applying the Fibonacci protocol to any two numbers, whereby they are added, and the larger one is added to the sum, will also produce an incommensurate ratio between the larger and sum that approaches the golden ratio. This is somewhat disturbing—for what does adding two sequential numbers have to do with pentagonal symmetry rather than, say, octagonal or dodecagonal?? It may be related to the fact that the golden ratio is the most irrational of all irrational numbers, which can be seen in the fractional expansion. These are known as Lucas Numbers after French mathematician Édouard Lucas (1842-1891) (and who also named the Fibonacci Sequence). For example, two numbers I have chosen at random, 45, 89 can generate the sequence (45, 89, 134, 223, 357, 580, 937, 1517…). The ratio 1517/937 is equal to ~1.6189968—which is already quite close to the decimal value approximation of the golden ratio 1.6180339, differing by about 0.0009!

In the context of quasicrystals, the Large and Small sequences represent one of the simplest contexts in which to study a quasilattice. To begin, we first take a baby rabbit, S. The baby rabbit grows into an adult rabbit, L. The adult rabbit then has a baby rabbit, S. The adult rabbit, which is still alive, then has yet another baby rabbit, S. The previous baby rabbit, S, has now grown into an adult rabbit, L. This leads to the sequence,

[5] This differs from the pentagrid method, where the bars are equidistant.

[6] Purportedly occurring as early as ~400 BC in work done by Pingala (Singh, 1985)

[7] The Rabbit Number was not intended to be a realistic model of rabbit growth—but it was intended to be a realistic demonstration of the power of the numeric and algebraic systems that Fibonacci was introducing.

| **S** | **1** |
|---|---|
| **L** | 1 |
| **LS** | 2 |
| **LSL** | 3 |
| **LSLLS** | 5 |
| **LSLLSLSL** | 8 |
| **LSLLSLSLLSLLS** | 13 |

Fibonacci deflation protocol (left) and number of elements (right). If we divide sequential numbers of elements with the larger over the previous, e.g. 13 and 8, we will get a ratio that is closer and closer in value to the golden ratio.

In the mathematics of quasicrystals, this is known as a deflation protocol (Socolar & Steinhardt, 1986)[8]. In the Fibonacci deflation protocol, we transform S to L, and L to LS. This deflation protocol yields the golden ratio in exactly the same way as the Fibonacci numbers. By taking the ratio of the last and second-to-last total numbers of L's and S's, we converge on the value of the golden ratio. The worm lines in the perfect Penrose tiling (***Figure 2.5, Figure 2.8***) will also express perfect Fibonacci Sequences in the form of fat and skinny hexagons made from fat and skinny Penrose rhombuses (consider ***Figure 2.10 (c)).*** The worm line is defined as a row of these fat and skinny hexagons. The only caveat is that completed Fibonacci Sequences (which are worm lines with no interruptions), when they exist in perfect (infinite) Penrose tilings, must always be palindromes. This can be understood either from the deflation protocol (Socolar, personal communication), (Levine & Steinhardt, 1986b) or, if we assume that each worm line (***Figure 2.8***) must always start with the beginning of the Fibonacci Sequence (LSLLSL…) rather than somewhere else down the chain, then **there is no distinguishing between the start and end of the sequence and this necessitates that they are palindromes**. This is in contrast to Gardner's original suggestion that Fibonacci chains in the infinite Penrose tiling are of arbitrary length (Gardner, 1997).

[8] This can also be seen in the well-known Thue-Morse Sequence, which is the sum of bit-wise negated binary numbers (Allouche & Shallit, 1999)


**Figure 1.6:** I created this method to visualize Fibonacci palindromes. If we take a correct Fibonacci Sequence (red) and overlap it with a left-to-right version of itself (blue), the overlap region corresponds to the set of all Fibonacci palindromes. The overlap regions shown above are L, LSL, LSLLSL, and so on. The number of L and S components in each sequential Fibonacci palindrome obeys golden-ratio scaling, as mentioned in the table above.

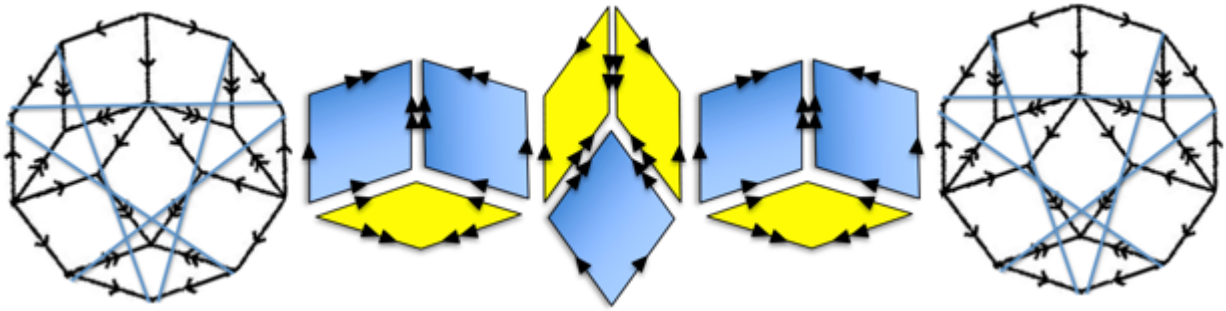

**Figure 1.7:** Any complete worm line in the perfect Penrose tiling is bounded by two decagons. Each decagon acts as a gate which will allow two worm lines to progagate through, and other worm lines will terminate at the decagon. Above is shown a worm line containing three hexagon units, which is bounded on either side by two decagons. This worm line, like all other bounded worm lines in the perfect Penrose tiling, is palindromic.

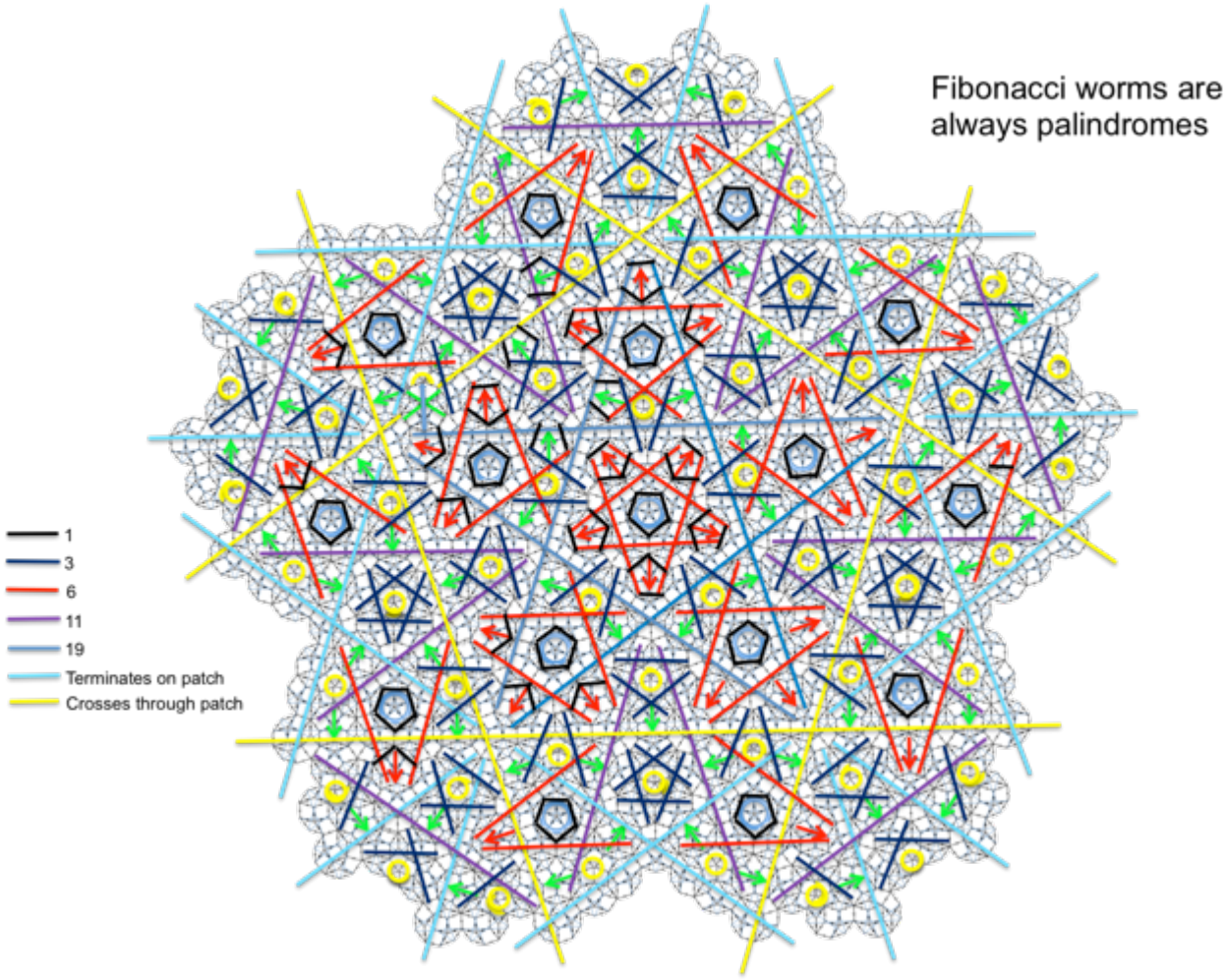


**Figure 1.8:** Blue, red, and green arrows reflect the pentagonal motifs in ***Figure 2.4***. Each Fibonacci worm has been colored to indicate its respective length. Each (complete) worm line begins at a decagon acting as a gate, and these gates only allow the crossing of two worm lines. Worm lines coming in from any other angle will begin/terminate at these gates. Yellow worm lines cross the patch and have no beginning or end, and so are not palindromic, but only in finite/incomplete patches. The accompanying legend shows how many hexagon segments are in each palindromic worm line. Worm lines can also be thought of as layered, in the sense described in this thesis. Though since there are worm lines of infinite length (as long as they are palindromes), the layer hierarchy[9] would also be infinite.

[9] This will be covered in *Chapter Two*.

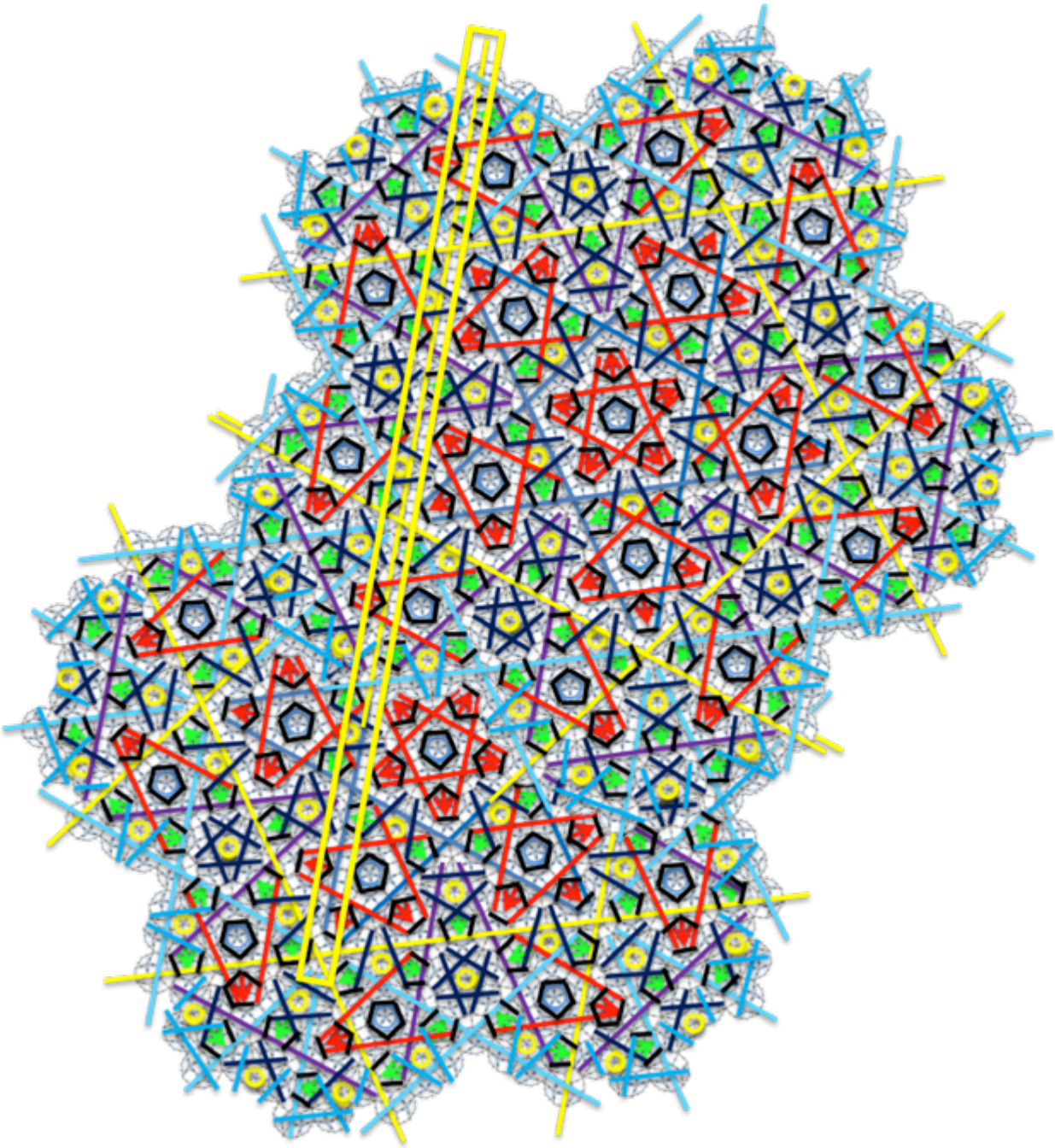

**Figure 1.9:** If we layer two larger pentagons (***Figure 1.8***) that have the palindrome markings, we can see how worm lines open and close to produce larger, correct motifs. In ***Figure 1.8***, there are some yellow worm lines that cross the patch entirely. In this figure, we see how these yellow lines now join other worm lines on the bottom motif and find a termination point. One has been outlined with a long yellow rectangle.

For Ammann bars, disjointed bars reflect worm lines (rows of fat and skinny hexagons) that have been phason flipped in such a way that they create a single localized phason defect.

The energy required to flip an entire worm line is equal to the energy associated with that small defect, so it's very easy to create these kinds of single-arrow matching-rule violations, as opposed to the double-arrow matching-rule violations which have a much higher energy cost (***Figure 2.9***) (Strandburg & Dressel, 1990). The single and double arrow matching rules are interesting in this respect, as they were not originally intended to reflect energetic differences, but were instead used to force aperiodicity. As briefly mentioned earlier, there's a related technique called the pentagrid method that de Bruijn showed is mathematically equivalent to the higher-dimensional projection (de Bruijn, 1981), and that one uses lines with equal spacing instead of Fibonacci spacing.

For the most part, we can think of Ammann bars as just relating to the planes of the quasicrystal—and they do indeed appear this way when we are looking at a three-dimensional model. The entire Penrose rhombus tiling is made from ribbons of worm lines (***Figure 2.8***), for instance, that crisscross in each of the five directions and are woven together in this complex way with the Ammann bar construction method. You can even treat the worm lines as being layered, in the sense defined earlier in this chapter. Like a basket woven from strips of bark, the worm lines move over and under each other, and hide what is below them. So far as I am aware, no research has yet to carry this idea into the realm of coverings or quasi-unit cells. Although we can use Ammann bars to create the Penrose tiling, I posit that just like deflation (covered in the next section), this method still fails to provide us with a conceptual picture of what a quasicrystal is—insofar as providing us a way to visualize it in our heads.

## Deflation/Inflation, or Simply Substitution

Deflation relies on the fact that quasilattices contain hierarchical organization, just like my polygonal cycling method that is discussed earlier. But deflation is a much simpler process, and ultimately quite different from what I have shown so far in this chapter. To better highlight these differences, I describe the process of deflation with much more depth than is needed to understand *Chapter Two*—**this review of deflation is presented to contrast it with my work**.

Deflation protocols are a general property for most quasilattice tilings. ***Figure 1.10*** and ***Figure 1.11*** show the deflation protocol for the Penrose rhombus tiling. Rhombuses are scaled down (and made smaller) by a factor of the golden ratio and are used to recreate the new rhombuses in a specific way. The ability to deflate a tiling and produce more of it reflects the

general hierarchical nature of a quasilattice tiling, much like a fractal. The bottom set of images is the Robinson triangle decomposition, which just means the Penrose rhombuses are cut in half into the Robinson triangles, and the corresponding top figures show what happens if we take the entire rhombus and place it as required by the Robinson decomposition. E.g., scaled-down skinny rhombuses will fit onto the green-colored golden triangles and would actually stick out from the perimeter of the new rhombus shape. In this way, Penrose rhombus deflations can be regarded as imperfect, or not bounding volume hierarchical (Henle, F., 2012—not to be confused with Henley, C.) (***Figure 1.10***), whereas Robinson triangles do have bounding volume hierarchy since they can be subdivided into larger scaled-up versions of the same triangles. Ultimately, this just means that the deflation protocol looks different as we execute it for different tilings, but each still works to deflate any given tiling into more tiling.

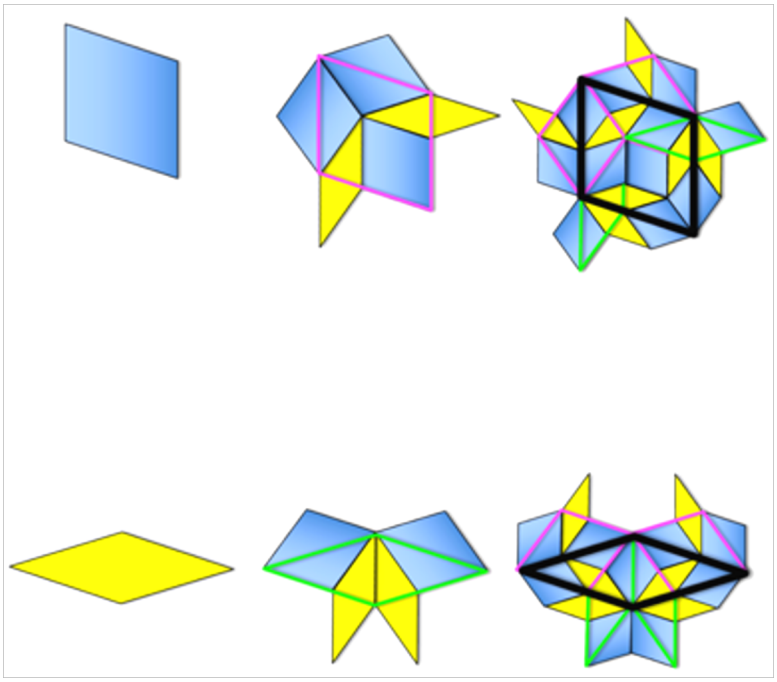

**Figure 1.10:** To perform a deflation, smaller copies of the polygon are placed within the old shape in a specific way. This process is iterated many times, and produces larger motifs of ideal tiling at each step. The Penrose deflation protocol is not bounding volume hierarchical, and so the new scaled-down shapes will extend beyond the perimeter of the original shape.

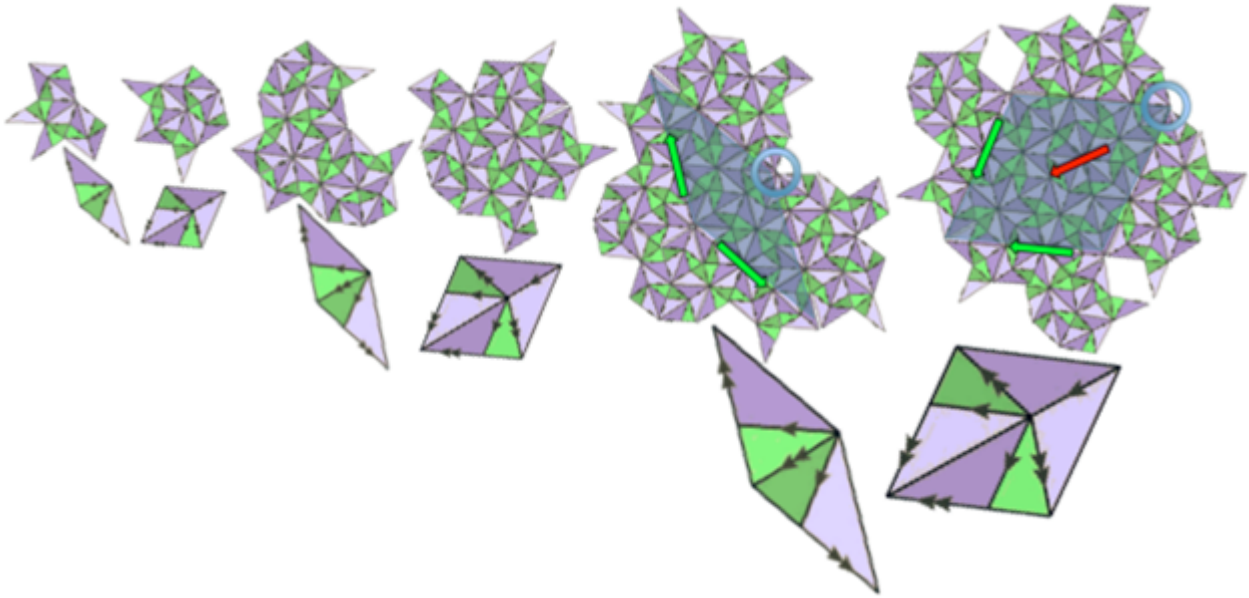

**Figure 1.11:** A fat and skinny rhombus from the Penrose P2 tiling have been deflated/inflated into a larger tiling. Note that at each stage moving from the left to the right, a fat or skinny rhombus can be inset into the image, as has been done explicitly for the final two rightmost images (blue shaded rhombus outlines). Deflation/inflation is often used interchangeably (Steurer & Deloudi, 2009). Deflation is usually taken to mean the above process, moving to the right, and inflation is taken to mean reducing the number of subdivisions. But I think subdivision, or un-subdividing, are less ambiguous terms.

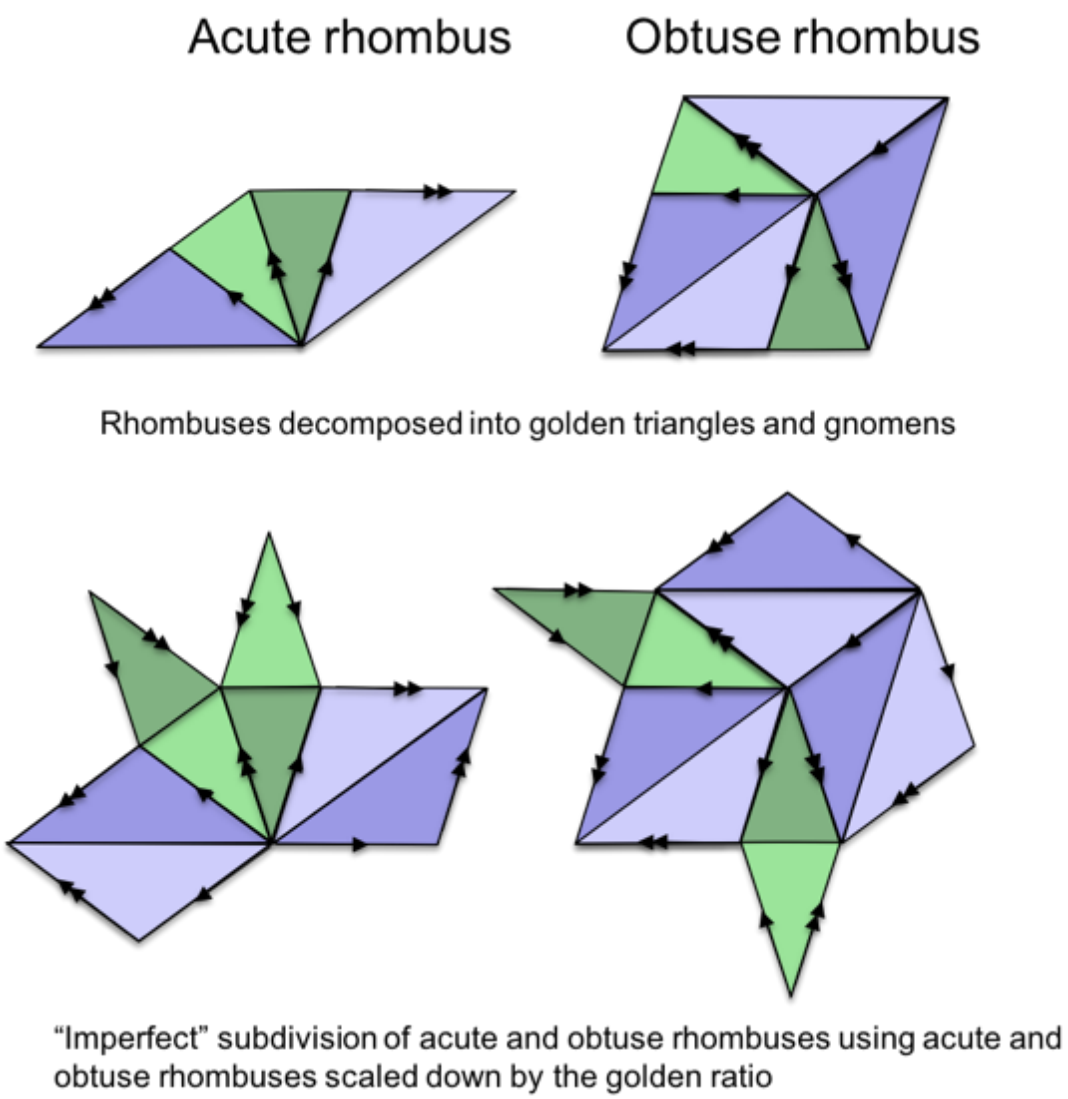


**Figure 1.12:** The deflation rules of the Penrose tiling are "imperfect" if we consider the deflation using only the original rhombuses. If, however, we deflate using the Robinson decomposition, we find that we can deflate each rhombus without the polygons leaving the boundary of the original deflated rhombus[10]. This is interesting, but does not make much practical difference in the generation of the tiling using either method since the region of tiling that extends beyond the polygon will match the neighboring polygon in the sense that it still obeys covering rules.

### Penrose's Discovery and Fractals

For any reader interested in better understanding the commonality between fractals and quasicrystals, it will be instructive to review some of the history surrounding Penrose's work.

[10] *Chapter Two* mentions this as the bounding volume hierarchical property.

His interest in tiles stemmed from an older question called the Domino Problem. This asks whether there exists an algorithm for deciding whether a given finite set of tiles will tile the plane. In 1961, logician Hao Wang found algorithms to list the sets of tiles that cannot tile the plane, and tiles that can do so periodically (Wang, 1961). His student, Robert Berger, then showed that Wang's conjecture—that a finite set of tiles is solvable if and only if it has at least one periodic solution—was false, by finding a set of 20,426 tiles that can only tile the plane aperiodically. This launched the study of aperiodic tilings. This set was later reduced by Berger to 104 tiles, and Hans Läuchli even further reduced it to 40 (Grünbaum & Shepherd, 1986). Finally, Raphael M. Robinson (whose Robinson triangles will be introduced later) reduced it to 6 (Robinson, 1971).

Roger Penrose then enters the scene seeking to further reduce the set of these tiles. He first discovered the P1 pentagonal tiling, which has 6 types of tile and is based around pentagons instead of squares like the Wang tiles. He later reduced this to 2 tiles with the addition of the P2 kite-and-dart and P3 rhombus tilings (Penrose, 1974). Penrose wanted to study aperiodicity, and knew that he might attain an aperiodic pattern by forcing 5-fold symmetry in a tiling—a clever move since he knew that pentagons cannot tile the plane periodically. He started with what's known as a pentaflake—based on the work done by Dürer (Dixon, 1991) —because it partially tiles the plane and has five-fold symmetry. The pentaflake (***Figure 1.13***) is a kind of fractal where we take a regular pentagon, and place 5 more regular pentagons—with the same orientation—into the corners of the larger pentagon. A sixth and final pentagon is rotated by 36° and placed in the center. Continuing this process will generate the pentaflake. Note, however, that there are gaps created where no new pentagons can be placed. **Of greater importance, there are gaps (at higher iterations than Figure 1.13) where new pentagons can fit, but there is more than one way to place them!**

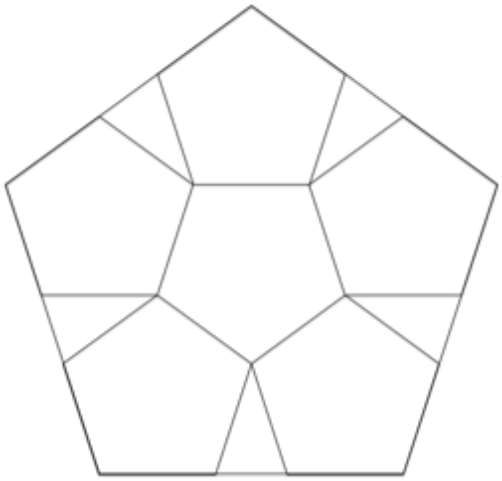

**Figure 1.13:** A pentaflake with one degree of iteration. Note that the pentaflake is a fractal**—it is not yet a quasitiling.** Six pentagons, with side lengths scaled down by $\mathbf{1} + \boldsymbol{\varphi}$, where $\boldsymbol{\varphi}$ is the golden ratio, are placed inside a larger pentagon.

Penrose discovered that by creating jigsaw edges on the pentagons and other five shapes that filled in the other non-pentagon portions of the pentaflake that he could force the entire tiling to obey the aperiodic criterion[11]. He then proved that the tiling was indeed aperiodic by showing that, in the limit of infinite tiles, the ratio of one tile type to another type will then converge to an irrational fraction—the golden mean (or integer multiples thereof), which has been associated with pentagonal symmetry since ancient times (Livio, 2003). In contrast, tile ratios of periodic tilings must converge to rational fractions.

[11] This is also to say he forced the pentagons to choose a position in the ambiguous locations, which is effectively the phason flip in the P1 tiling.

## Fractals and Quasilattices

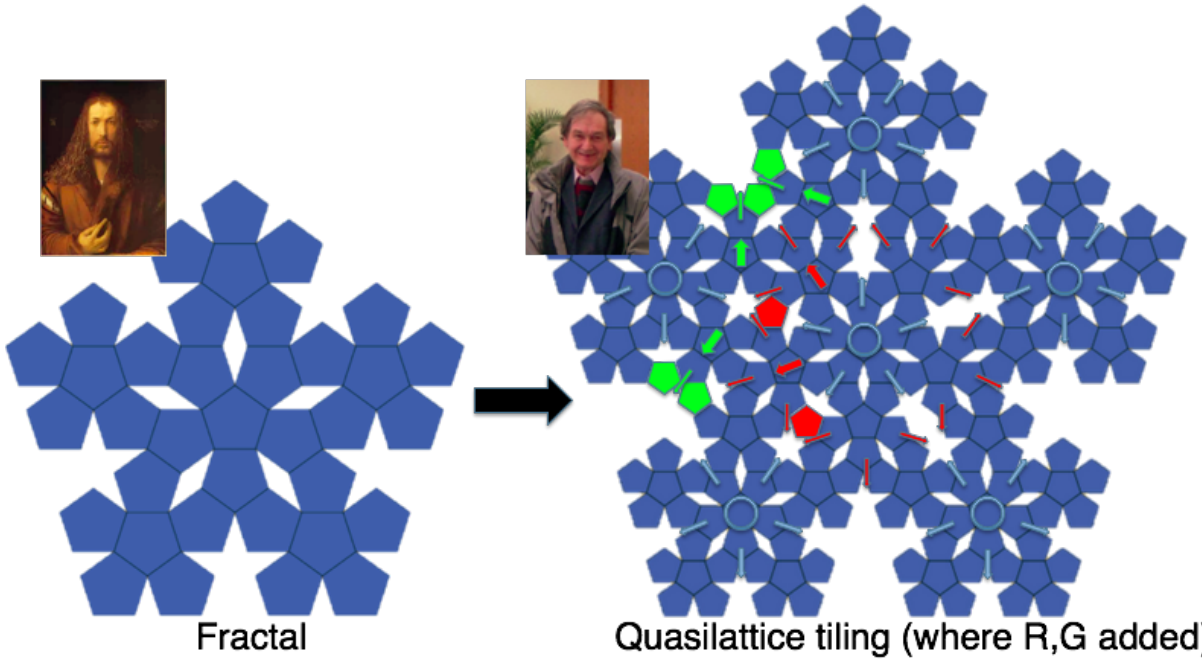


**Figure 1.14:** Fractals and quasicrystals both have self-similar scaling, but what are the differences between them? With an understanding of the layering method, we will no longer need matching rules to complete the pentaflake fractal on the left into a Penrose P1 tiling on the right. Instead, we can arrange our pentagons so that they obey the BRG motifs that correspond to the appropriate rhombus. An image of each author has been included with Albrecht Dürer on the left, and Roger Penrose on the right. Note how the red pentagons on the left image can sit in two different positions. The matching rules introduced by Penrose address this for fixing phason errors, but the layering protocol will address the ambiguity for actual *construction* of the ideal tiling.

## The Pentagonal P1 Penrose Tiling

The pentagonal P1 tiling developed by Penrose started with a fractal—the same one that Dürer created long ago (Dürer, 1525). It's also known as a Sierpiński pentaflake. Penrose derived the P1 tiling by taking this fractal and filling in the void spaces using pentagons marked with matching rules, as we have just reviewed. A new approach demonstrated in ***Figure 1.14*** is to tile outward using the layering scheme—complete the pentagons, rhombuses, and decagons (which will be covered in *Chapter Two*). It could also be approached energetically. The conversion of a pentaflake into P1 could be accomplished by mapping the system to P3 and adding decagons with random positions and orientations. As the decagons underwent phason flips to complete effective rotations, the system could reach equilibrium by satisfying the outward tiling hierarchy. This model of growth has, to my knowledge, never been demonstrated by simulation or experiment. Although we have seen improvements to quasicrystal tilings

through apparent phason flips (Nagao et al., 2015), we do not have an energetic tiling that demonstrably always moves toward a more ideal tiling.

This step-by-step assembly can be understood with either energetics, or entropy. Penrose created his first tiling by finding a set of matching rules that forced the pentagons into positions that maintained the long-range order. Later, it was realized that these matching rules could be used to represent energies (Steinhardt & Jeong, 1996). It has also been realized that self-assembly by shape alone represents a type of entropic force (Harper et al., 2015; Van Anders, Ahmed, et al., 2014; Van Anders, Klotsa, et al., 2014). Quasicrystals can be assembled through this entropic force alone (Haji-Akbari et al., 2009), or by a combination of entropic and energetic interactions (Engel et al., 2015). Regardless of the origin of the quasicrystalline order, the entropic or energetic interactions must create a suitable geometric force field to favor creation of effective matching rules (or at least self-assemble via incommensurate-length prototiles[12] that fill space, like random Penrose tilings) if this picture of quasicrystal growth is correct.

[12] Prototiles are simply the base level of tile—they are not made from a more basic fundamental tile.

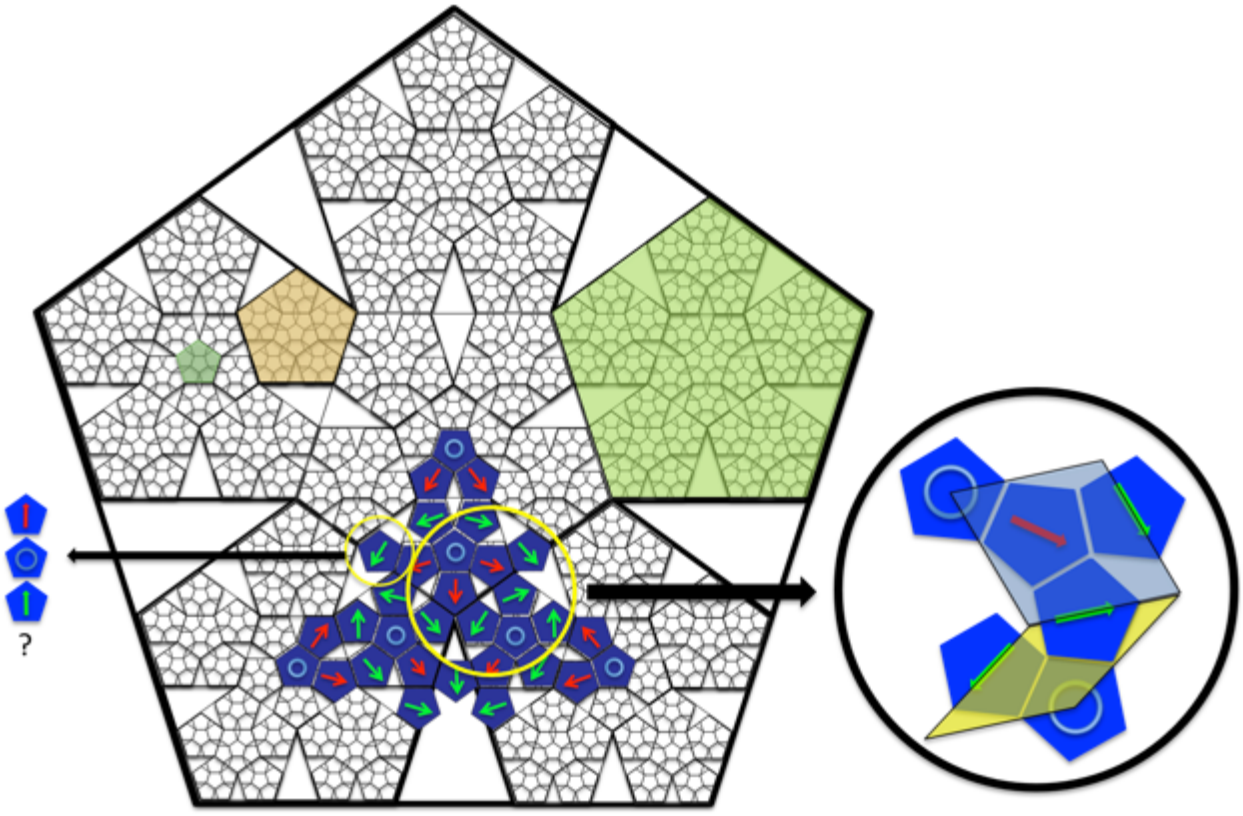

**Figure 1.15:** Pentaflake fractal with P1 Gummelt motif. The overlap between the two shows the origin of the rhombus Gummelt motif, as well as the shape of the equivalent Gummelt motif in the P1 tiling. The circle inset on the right shows the mapping between pentagons and P3 obtuse and acute rhombuses.

The pentaflake fractal is generated by placing smaller pentagons, scaled down by the golden ratio, into the interior of the original pentagon. Five have the same orientation, and the sixth is flipped upside down, or rotated 36°, depending on how you want to look at it. This process is then repeated to generate finer iterations of the pentaflake (***Figure 1.15***). In the mapping between the pentagonal P1 and rhombus P3 tilings, we can extract the pentagonal version of Gummelt's original tiling motif and overlay it with the pentaflake. In doing so, we see the origin of the Gummelt motif—it is formed from the vertex of three joined pentaflake pentagons. Quasicrystal tilings share the same skeleton as a fractal, but have the void spaces filled in with the Gummelt motif. This can be seen in ***Figure 1.15***, where a P1 Gummelt motif, seen in ***Figure 1.16***, has been placed onto the pentaflake fractal. **While the P1 tiling is not covered in *Chapter Two*, this simply serves to illustrate that it can just as easily be used to construct P1 once the *layering* fundamentals are understood.**

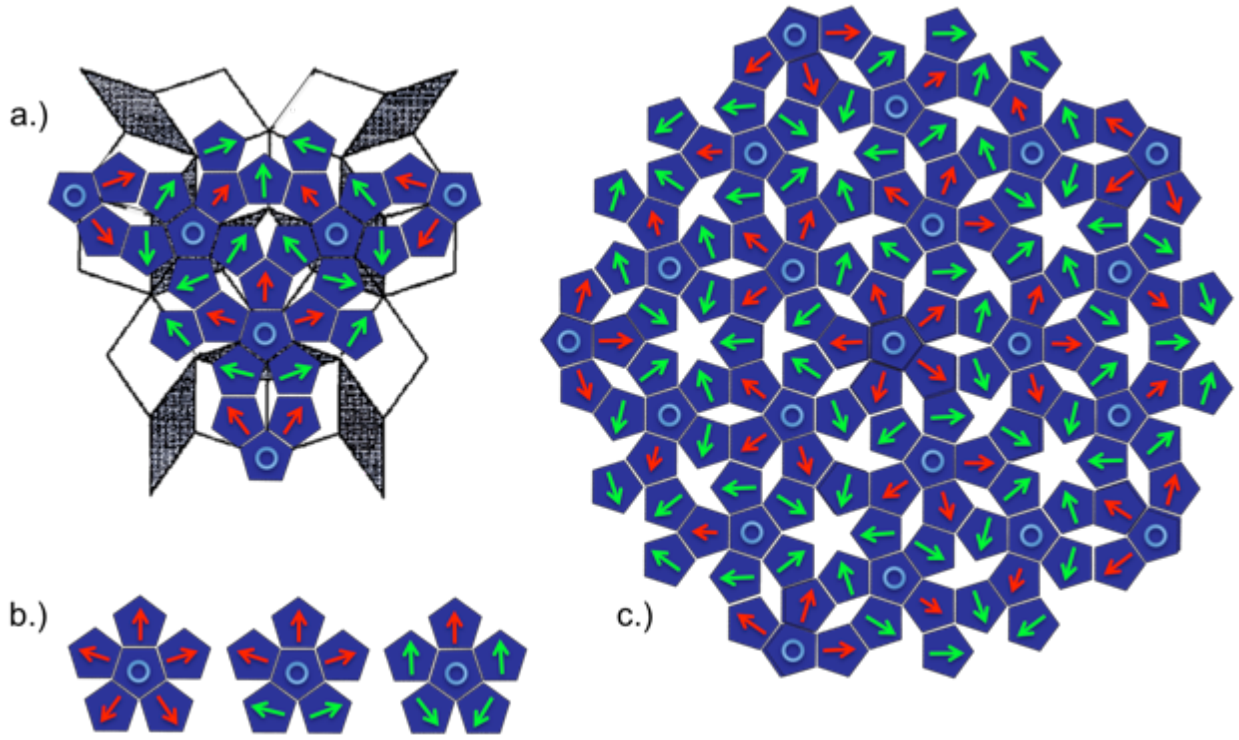


**Figure 1.16:** The Gummelt motif equivalent in the P1 pentagonal Penrose tiling is made from the same three pentagons from ***Figure 2.4 (d)***. Five copies of the P1 Gummelt motif can then be formed into a new pentagonal ring (c). The black-and-white portion of (a) is the P3 rhombus Gummelt motif (Gummelt, 1996), overlaid with the equivalent motif in the P1 pentagonal Penrose tiling.

## Experimental Reconfiguration

The next observation that researchers made was that, perhaps, the experimental quasicrystals were not actually ideal at all, and were better explained by something called the random-tiling hypothesis (Henley, C., 1988). However, it was later realized that matching rules might indeed play a role in growth, culminating in the work of Nagao (Nagao et al., 2015), who show the *in situ* growth of a quasicrystalline front and the subsequent phason re-arrangements that follow to lower the phason strain of the system. Phason flips, by nature, are only allowed in the context of a local space-filling tiling. They lose context and meaning when the local tiling has gaps in the form of missing atoms. So, it does not make sense to talk about phason flips or phason strain when there is not at least a random tiling—which is present in this experimental growth front. The growth scenario is then stipulated to be the formation of atoms into a space-filling tiling, which then, if it is an energetically stabilized quasicrystal, undergoes successive

phason flips into a more ideal tiling. One goal of this thesis is to provide this process with a tiling perspective. **How is the tiling changing in real space, and how can we improve particle-interaction potentials to better encourage these phason flips or trends?** Without a real-space tiling model, phasons exist only in the higher-dimensional projections. Indeed, in most real simulation or experimental results, phason lifting may be the only practical way to measure phason strain. If, however, there are only a few defects, then it will be possible to use this real-space model to concisely state what is defective in the tiling, and how it needs to change in order to mend it. **In that respect, this model could be very useful in designing custom shapes or potentials to create better energetically stabilized quasicrystals.**

Presented in this thesis is a method to understand a quasicrystalline tiling in real space, and ultimately a real-space method for writing software to characterize the hierarchy of a given quasicrystalline tiling that does not depend on higher-dimensional projections. This is important to have for conceptual clarity, in addition for avoiding abstract higher-dimensional mathematics.

Although quasicrystals have been studied extensively over the last 40 years, they are in many ways still mysterious—both in their tiling structure and how they are able to grow. We know they have a self-similar hierarchy, but what does it look like? We know they can be projected from cuts through higher-dimensional lattices, but why and/or how does this work? Moreover, we know that they exhibit long-range quasiperiodic order when they are ideal or close to ideal structures, but how do they solve the Fibonacci locality riddle of long-range correlation with only local interactions?[13] These are all questions that I investigated and sought to answer in my research. I hope that the reader comes away with a vision, perhaps for the first time, for what a quasicrystal actually *is*, and perhaps with some sense of how they might arise.

[13] The fundamental idea behind this riddle is: during growth, how can we establish non-local correlations with only local interactions? The answer appears to be that we can't —not without error correction whereby there is communication across the quasicrystal (via phasons) that can anneal out the defective regions (Nagao, 2015). There is no currently known way to grow an ideal quasicrystal with local matching rules and no error repair process.

## Chapter Two

## A Layering Construction of the Penrose Rhombus Tiling

### Introduction

Penrose tilings provide a model for studying decagonal quasicrystal structure and growth. There are many ways to generate perfect Penrose tilings, but none provide a method for generating new tilings through a simple visual understanding of the tiling structure. In this chapter, I will present a method to construct Penrose tilings that is simple enough that a user can take a collection of rhombuses and assemble the infinite tiling from memory—without recourse to computations, line drawings, subdivisions, or complex lists of allowed vertices. This assembly protocol may also provide insights for understanding quasicrystal growth in 2D and 3D quasicrystal simulations (Damasceno et al., 2017). There are two primary results of this chapter. The first is the development of a *covering* model of *construction*—a hierarchical cycle of polygons which are assembled into yet-larger polygons. This uses three covering motifs and obeys normal covering rules (tiles below must match position and orientation) during construction. The second is the development of a *layering* model of construction. This introduces a fundamentally new way to understand quasilattice tilings. Whereas the polygons in a covering must match position and orientation, this condition is removed for layerings. Layerings instead follow the requirement that the polygons undergo a specific kind of phason flip. The covering model of construction will provide the basic idea of the hierarchical polygonal cycle, and the layering model will show how it can be simplified. The Penrose tiling is the simplest to describe with this approach and it will be the template on which the other quasicrystal chapters are based.

Every chapter follows a fundamental algorithm: we assemble a characteristic polygon from fundamental (or primitive) polygons. The characteristic polygon is assembled into a petal motif. The petal motif is assembled into what I am calling second-order polygons. These second-order polygons are then assembled into a second-order characteristic polygon. Although

each tiling introduces a new concept involved in the algorithm, or new levels of complexity, the underlying idea is the same for each chapter. This chapter will introduce the concept of a hierarchical polygonal cycle, which is capable of *constructing* the Penrose rhombus tiling. The polygonal cycle can be completed with either a set of covering petal motifs—requiring many different kinds of petal motif—or it can be done with a single petal motif in a process developed in this thesis called layering. These two approaches are contrasted with an eye for determining which is the conceptually simpler of the two. A detailed algorithm for the Penrose rhombus tiling is presented at the end of this chapter.

Presumably, this method went undiscovered because overlapping motifs were required to adhere to the rules of a *covering*. But in dropping this rule for the new *layering* method, a new set of phenomena are found. The first of these is the creation of a more robust quasi-unit cell concept. The old quasi-unit covering motif was not a recipe for *construction*, whereas this one is. I believe this is more in spirit with the classical unit cell concept. This means that the quasi-unit cell can be used as a map to build additional quasitiling, whereas the older concept of a *covering* quasi-unit cell (Gummelt, 1996) only contains a set of rules which a perfect quasitiling must obey. In this respect, the old quasi-unit cell covering rules behave exactly like a set of matching rules—and we know that attempting *construction* via matching rules will eventually lead to dead ends which force matching-rule violations.

The second discovery is that when these petal motifs are overlapped during their placement in the quasi-unit cell, their overlaps automatically produce the phason flip for that tiling. It is unknown why this appears to be the case for all of the tilings with simple phason flips (the hexagonal bronze mean tiling being an interesting and singular exception). The bronze mean tiling (Dotera et al., 2017) is a slightly modified version of the dodecagonal square-triangle tiling, which does not have a phason flip (or at least not of the simple kind—nothing is reported in the literature), and both it and the bronze mean tiling have a simple enough architecture as to not really need layering at all to understand their construction. While their phason picture via layering is unclear, their motif picture may be too simple to benefit significantly from the layering method.

Also of note is that this process is not a fluke for the Penrose tilings—it works for every tiling in this thesis, and several others that were not included. It appears to be a general property of quasitilings. The work on *covering* motifs in this thesis also extends it beyond mere matching

rules and into an algorithm capable of *construction*. In that respect, this is a novel extension of general *covering* theory.

At the most basic level, *layering* provides a simple real-space method for visualizing quasitiling motifs. The unit cell of ***Figure 2.1*** is a straightforward summary of this approach, but it will be explored in great depth later in the chapter.

## A Covering Construction of the Penrose Tiling

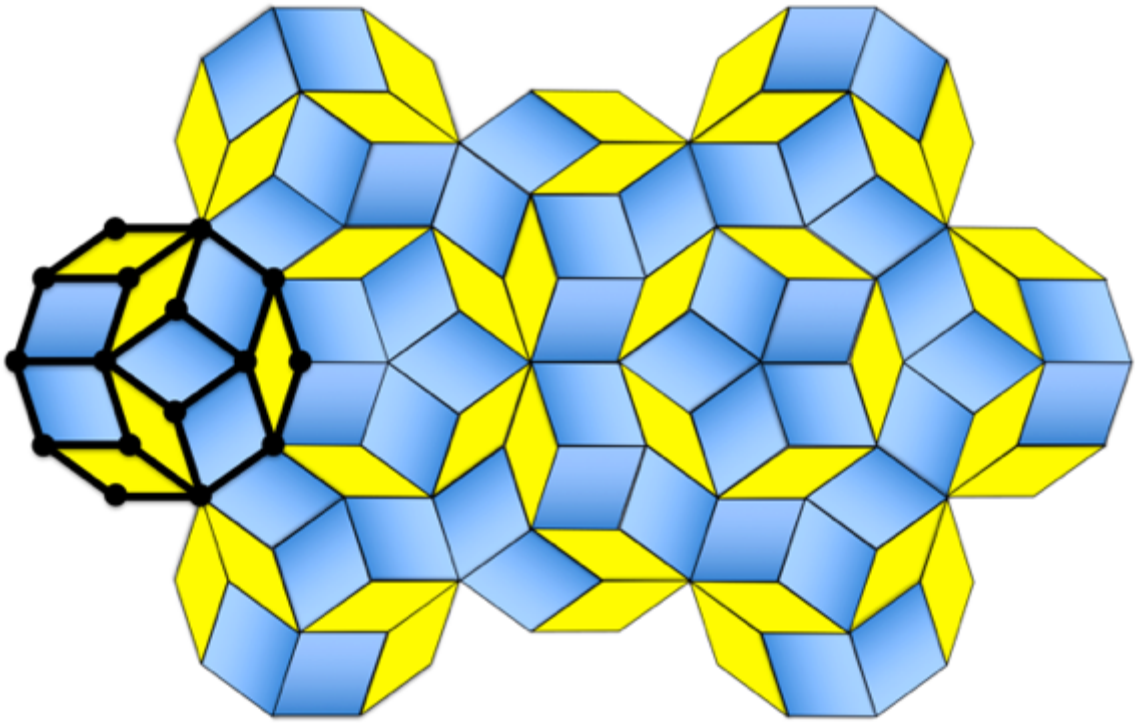

**Figure 2.1:** An example of a finite section of the rhombus Penrose P3 tiling is shown. Vertices and edges, marked by the black circles and lines on the left side of the drawing, outline a decagonal motif within the quasilattice.

The Penrose rhombus tiling (Penrose, 1979) is one of the earliest known non-periodic tilings (***Figure 2.1***). The tiling begins with a specific type of acute and oblate rhombus. Normally, Penrose tiles are shown with matching rules. But since we are not going to use matching rules for the new method outlined below, they have been omitted from the figures for most of this chapter.

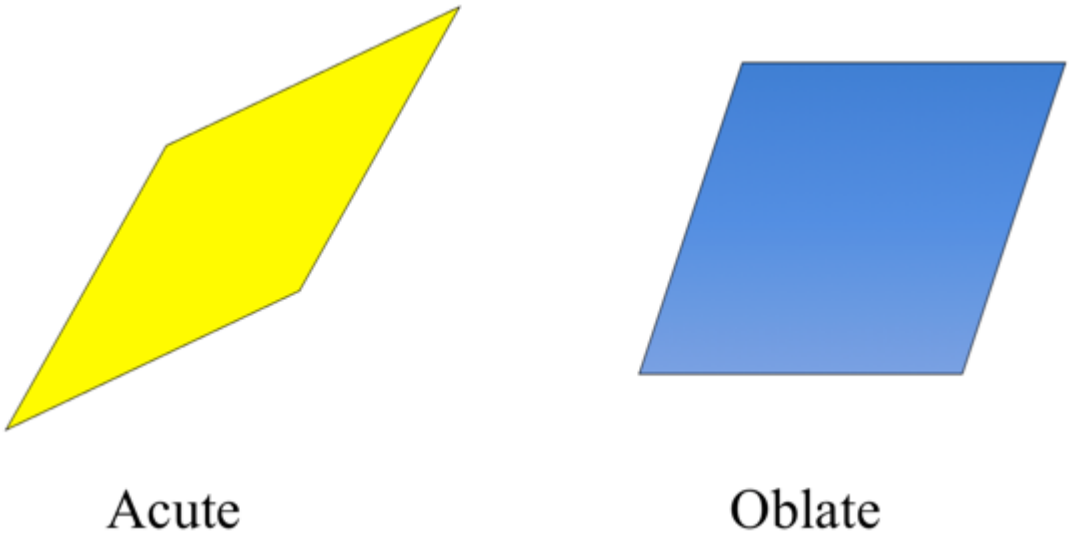


**Figure 2.2:** The rhombus Penrose tiling (P3) (***Figure 2.1***) comprises two rhombuses with angles in multiples of 36° (left: 36°, 144°; right: 72°, 108°).

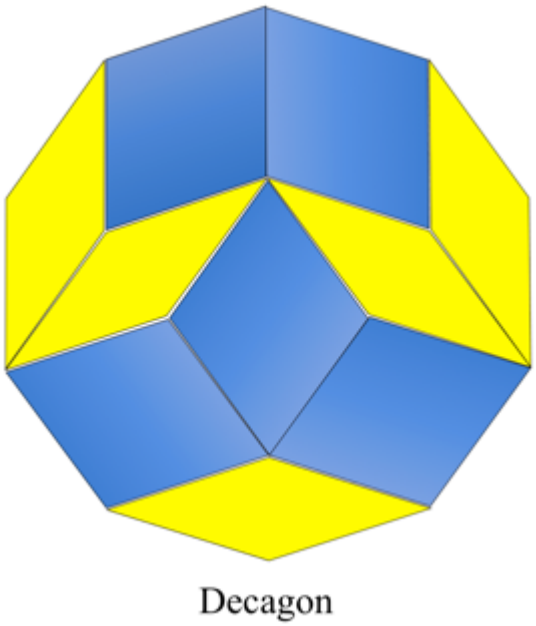


**Figure 2.3:** The rhombuses are then assembled into this decagonal motif. These decagonal motifs are similar to the Gummelt motif shown in ***Figure 1.3***, but they are missing the outer tiles. It's entirely possible to use the Gummelt motif instead, but we will begin with the decagonal motif for the sake of simplicity.

Many motifs can be observed in the Penrose tilings, but the Gummelt motif (***Figure 2.4 (a)***) is unique in that it is the smallest motif that can *cover* the tiling.

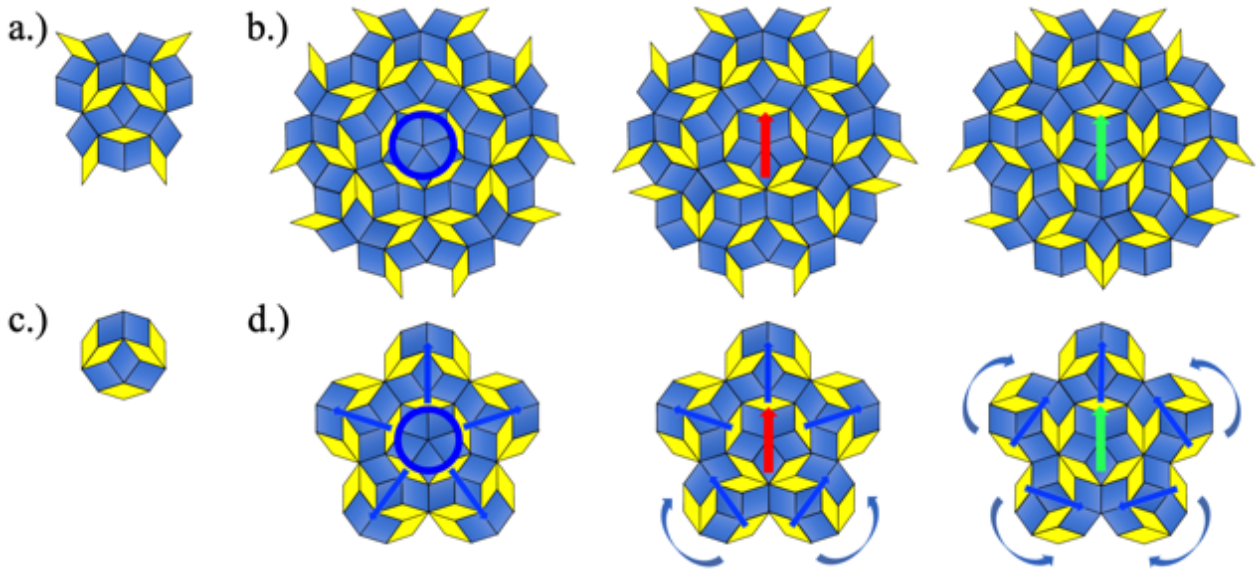


**Figure 2.4:** The Gummelt motif shown in (a) contains the decagon from ***Figure 2.3***. The Gummelt motif can be used to create pentagonal motifs seen in (b). This decagonal motif (c) is also used to create the other figures of (d), except for the star region in the center made from five obtuse rhombuses. **The additional polygons of the Gummelt motif effectively act to tile in the space left over by the decagon when making the tiling, and so create the five-fold oblate rhombus star with their extended pieces**. All decagons in the P3 rhombus tiling are part of one of the pentagons **(as drawn from the center of each of the five decagons in the pentagonal motif)** in (d)—this is my mapping between P3 and the pentagonal Penrose tiling (P1). The blue pentagonal motif (with blue circle) is rotationally symmetric. The pentagonal motif with the red arrow has two decagons rotated by 108°, and the pentagonal motif with the green arrow has four decagons also rotated by 108°, with CW or CCW indicated by the curved blue arrows. Although the Gummelt motif (Gummelt, 1996) is not the decagon of ***Figure 2.3,*** it still works in a similar way (b)[14]. For simplicity, we will not be using the pentagonal motifs in (b) and will instead use those in (d), since they are still covering structures, minus the oblate rhombus star at the center of the pentagonal motifs—it has been added in any way for the sake of simplicity, and it will make it easier to understand the construction method. Note that this petal motif is slightly larger than the minimal set from ***Figure 2.1***. The method works for a large range of petal motif sizes.

The motifs of ***Figure 2.4*** can then be used to construct larger versions of the original two rhombuses (it will look the same as ***Figure 2.5,*** since the differences between layering and covering motifs will disappear—also consider ***Figure 2.12***). When these pentagonal motifs are used, they form a covering, whereby the covering comprises two complete overlaps of the decagonal motif from ***Figure 2.3***.

[14] Note that ***Figure 2.4(b)*** extends beyond the bounds of the ring-conflict limit, which is discussed in ***Figure 3.19***. This means that the Gummelt motif will *cover* if we use all three of the covering motifs, but it will not *layer* if we use only the rotationally symmetric motif.

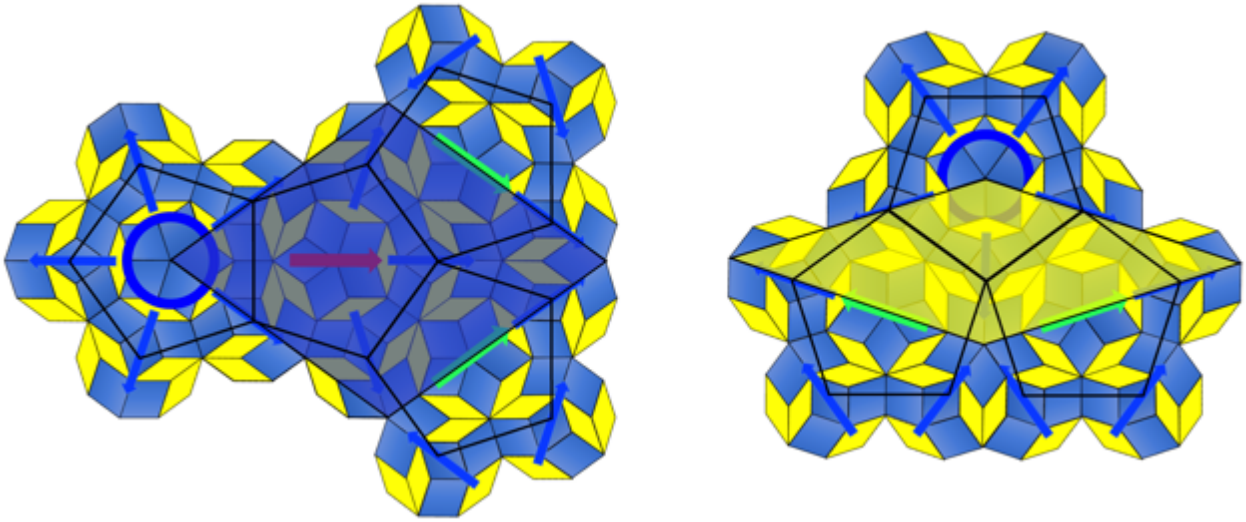

**Figure 2.5:** Each of the three types of pentagons can then be used to assemble two different motifs that define the larger rhombuses. Note that each of the pentagonal motifs (as seen with the black pentagons) meets edge-to-edge with neighboring pentagons, and that each pair of decagons that decorate the vertices of the edge-to-edge neighboring pentagons will overlap completely. Note also that blue pentagonal motifs sit on vertices of the new rhombohedral network, red pentagonal motifs sit inside obtuse rhombuses, and green pentagonal motifs have their arrows aligned with the edges of the larger rhombohedral network (the yellow rhombus). If a vertex does not contain a pentagonal motif with a blue circle, it instead has the matching-rule inverted version of the five-fold oblate rhombus star, wherein all of the oblate rhombuses are rotated 180°. A complete version of this motif can be seen on the bottom vertex of the second-order acute rhombus (yellow) in the right-most image.

In ***Figure 2.5***, two second-order rhombuses are shown. On the left, we see the second-order oblate rhombus made from four petal motifs—left-to-right ordering as a blue pentagonal motif, a red pentagonal motif, and two green pentagonal motifs. Since these are the covering petal motifs from ***Figure 2.4***, we do not need to specify the order in which they are placed. All tiles will match the orientation and position of the tiles beneath. Likewise, the oblate second-order rhombus is shown on the right, with top-down ordering as a blue pentagonal motif followed by two green pentagonal motifs. Once we have these second-order rhombuses, they can be assembled into the decagon shown in ***Figure 2.3***, to produce ***Figure 2.6***. That second-order decagon can then be used to create the pentagonal motifs of ***Figure 2.4***, and so on, which shows how the method is a cycle of alternating polygonal hierarchies.

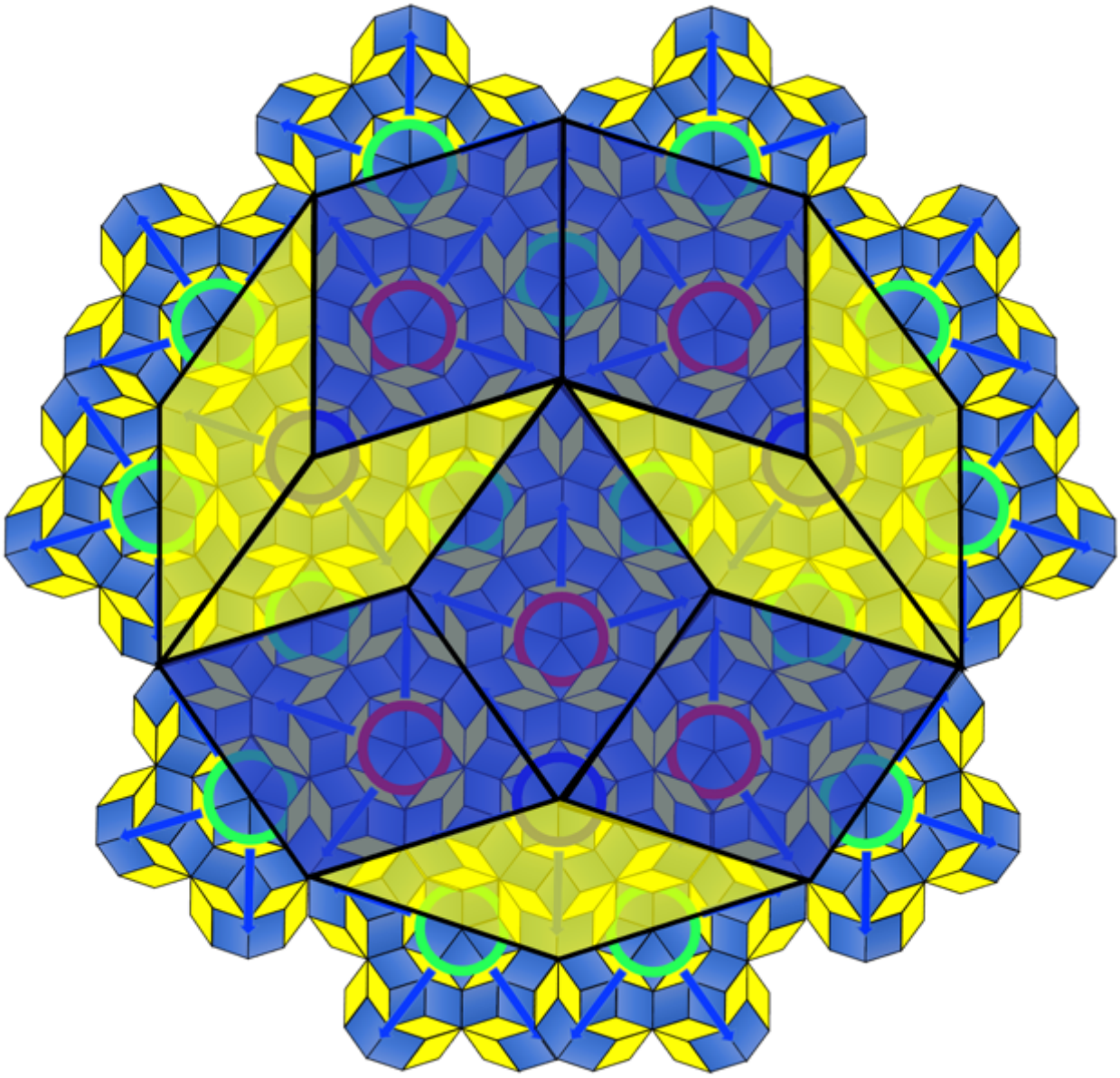

**Figure 2.6:** ***Figure 2.4*** and ***Figure 2.5*** show four hierarchical steps to make "fluffy" rhombuses (fat & skinny). A larger decagon can then be constructed from the new larger rhombuses and this completes the self-similar hierarchy. The new decagons can then be used to construct yet larger pentagons, rhombuses, and decagons. This is the final step of the polygonal cycle.[15]

[15] An astute observer may note that I have used the layering (and not covering) method to construct this image, which is discussed in the next section. All this means is that the patch of ***Figure 2.6*** that exists outside of the bolded octagon would need further pentagonal motifs to correct it. E.g., as described in ***Figure 2.5***, the bottom vertex of the second-order decagon should be a five-fold symmetric star of oblate rhombuses. The layering model (up next!) easily corrects these defects as the tiling is expanded outward.

The P1 (pentagonal) to P3 (rhombus) mapping of the Penrose tiling is perhaps one of the most interesting and insightful for understanding the nature of quasilattice tilings. It is well

## Layering

Layering utilizes the basic pentagonal motif, shown in ***Figure 2.4 (d) (left).*** By layering a blue motif with itself to **complete two whole decagon overlaps**, the other pentagonal motifs can be generated, shown in ***Figure 2.4 (d) (center and right).*** If a pentagon is drawn within a blue pentagonal motif using the centers of the decagons as the vertices (as in ***Figure 2.5***), then these layerings correspond to edge-to-edge pentagons. Intriguingly, the construction of a new motif is simply a rotation of a decagon by 108°, which will be discussed shortly. Additionally, this process points out an important property of quasicrystals, whereby the quasi-unit cell is allowed to overlap with itself. The origin of these various kinds of overlap is no longer a

---

known, for instance, that pentagons cannot tile the plane in two dimensions[15]. Looking carefully at a Penrose tiling with the pentagonal motifs of ***Figure 2.4*** in mind, we can get the strong sense that we have solved some of the problem of pentagon tiling in two dimensions. These are pentagons that have been fluffed (extended beyond the original pentagon) out with rhombuses to cover the two-dimensional plane! Without the extra tiles provided by the decagonal motifs—which extend beyond the boundary of the pentagon—the pentagons will leave spaces that create the five non-pentagon tiles of the P1 tiling.

In the literature, the pentagonal motif of ***Figure 2.4(d)*** has only been mentioned (Boström & Hovmöller, 2001) for its presence in what are called approximants—best described by the researcher who coined the phrase, Christopher Henley (1955-2015), as "periodic structures…whose unit cell is indistinguishable from a fragment commonly occurring in the icosahedral phase" (Henley, 1989). The writings of Boström state that, "This tile cannot tile the plane itself, but it may well play a role as a tile in a decagonal quasicrystal." This motif of decagons, however, is mentioned only with the outline of the individual decagons and not any of the rhombus construction—this means that we lose useful information about decagon orientation since they are **hollow**.[15] In contrast, the method of construction outlined in this chapter maintains the orientation of every polygon—aka, there are no hollow polygons. ***Figure 2.6*** concludes the polygonal cycle, described here for the first time, for understanding the *construction* of an ideal Penrose tiling with a covering method.

mystery, as they are a direct consequence of arranging the blue motif in this edge-to-edge pentagonal way, which ultimately reproduces the ideal Penrose rhombus tiling. **In essence, a pentagonal Penrose tiling is a pentaflake fractal, which has had the holes filled in a manner to consistently produce blue pentagonal motifs (rotationally symmetric pentagonal motifs); these pentagons are then used to create the second-order rhombuses.** Likewise, a Penrose rhombus tiling is this same fractal of P1 pentagons, but whose vertices have been "fluffed" out with decagonal motifs such that they fill the gaps in the pentaflake fractal. All of these shapes together will produce a space-filling tiling. It is well known, for instance, that pentagons cannot tile the plane without gaps. Penrose showed us how to do it with pentagons plus other shapes. This mapping shows how we can do it with an effectively pentagonally-shaped motif. Consequently, a Penrose tiling is a space-filling tiling of these pentagonal shapes, and these layerings (or pentagonal coverings) are how it avoids the otherwise impossible aspect of this space-filling pentagon proposal. Although other research has highlighted the importance of hierarchical clusters of clusters in, for instance, icosahedral quasicrystals (Janot & De Boissieu, 1994), these models use motifs that do not fill space and rely on "glue" components to fill in the gaps. These glue components will exist separately from the quasi-unit cell. In contrast, the layering method outlined here shows how to perform the hierarchical assembly of clusters of clusters with a single motif type, **an extension of the original concept of a quasi-unit cell**, whose transitions into other covering motifs is mediated by a phason flip, in the form of decagon rotations.

It has been suggested that the covering decagon is an energetically stable unit in assembling a quasicrystal (Jeong & Steinhardt, 1994). Five of these covering decagons can be used to create the rotationally symmetric "blue" motif. By rotating pairs of decagons in accordance with the layering protocol described in ***Figure 2.11***, we can create the other two *covering* pentagonal motifs. With the understanding that matching rules reflect energetics, it can be seen that the different covering pentagons created in ***Figure 2.4*** reflect the idea that these clusters have comparably low energy states as the original blue motif, since there are no internal matching-rule violations and provided that the local environment does not create any either[16]. The phason flip can then be treated as just a way to rotate the decagon to produce other covering

[16] Although each of the covering pentagons contains zero matching-rule violations, it is possible to create versions that do (which are not shown in ***Figure 2.4***) and so these other versions do not exist in the ideal Penrose tiling.

pentagonal motifs with the same configurational energy as the blue motif. The simple connection between phason flips and decagon rotations is discussed here now.

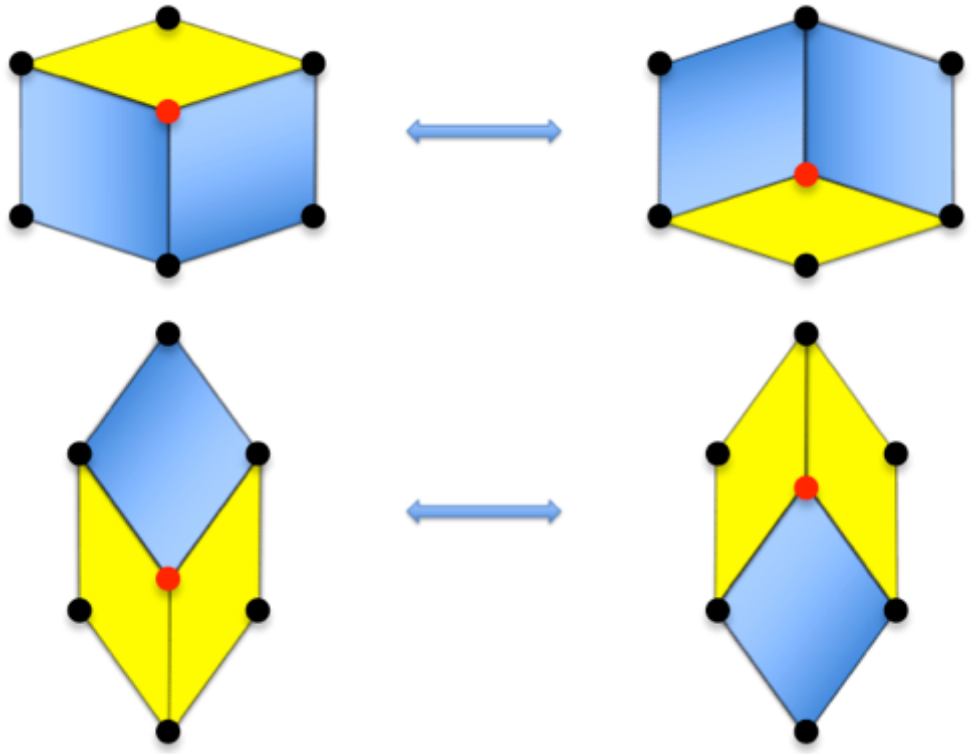

**Figure 2.7:** Simple phason flips in the Penrose rhombus tiling. 180° rotations of hexagons made from the two types of rhombuses in the Penrose tiling perform the phason flip. Black circles indicate one possible decoration of the quasilattice with particles. The phason flip can be seen as the movement of a single particle (shown in red). If this flip happens and it restores agreement among the matching rules (***Figure 2.8***), then the system will drop to a lower energy state. If the system flips and moves to a higher energy state, then it is considered a phason defect. But phasons are always relative to a specific motif and location—we could have a system where we flip one hexagon to create a phason defect, and then make all of the phason flips necessary to the rest of the tiling in order to restore it to one of the allowed ideal patches. This makes the concept of a phason error somewhat arbitrary.

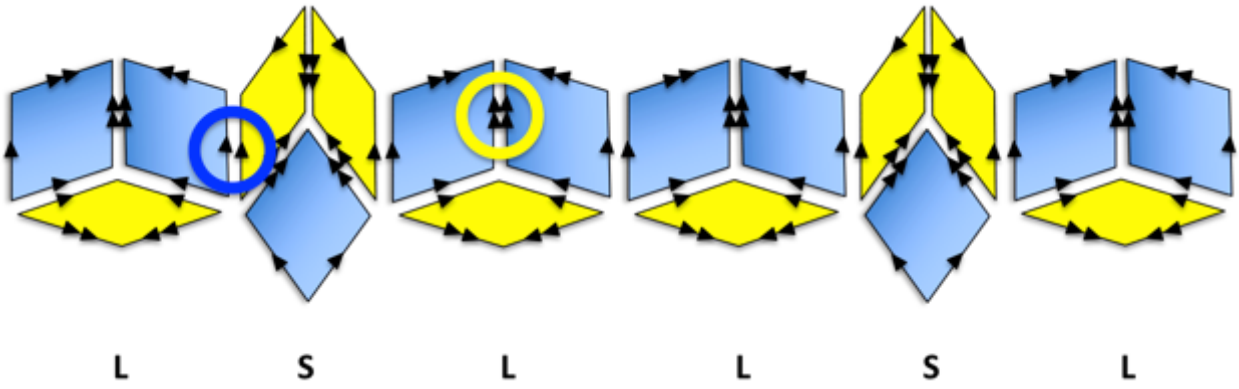


**Figure 2.8:** The Penrose tiling contains ribbons of fat and skinny hexagons—of varying lengths—that make up the entire tiling. Here is an example of an LSLLSL sequence, which is the third palindrome (discussed soon) in the Fibonacci Sequence. Note the

matching-rule arrows—both single and double arrows match for the entire length. An example of a single-arrow matching rule is shown in the blue circle, and an example of a double-arrow matching rule is seen in the yellow circle.

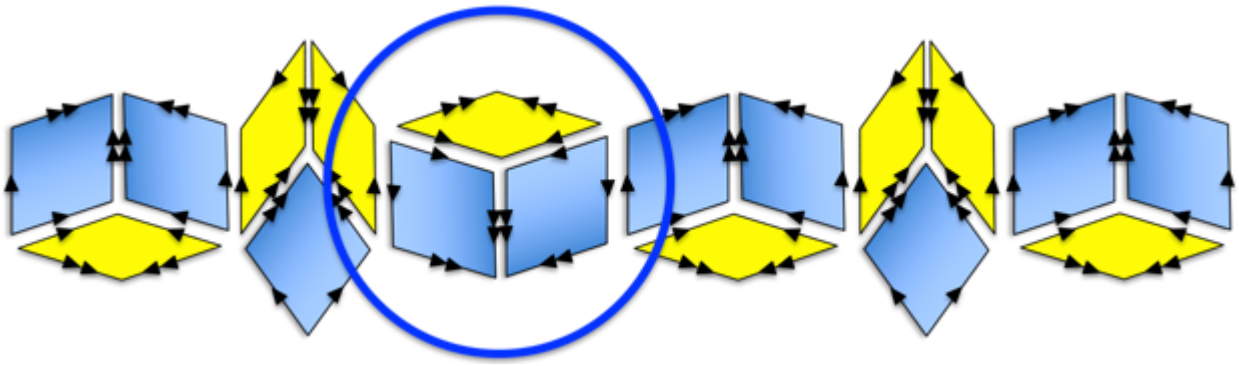

**Figure 2.9:** A simple conception of the phason flip consists of rotating one of the hexagons by 180°, shown above in the blue circle. This phason flip produces two single-arrow matching-rule violations. It could also be produced by rotating one of the skinny hexagons in the same fashion.

### Phason Flips as Decagon Rotations

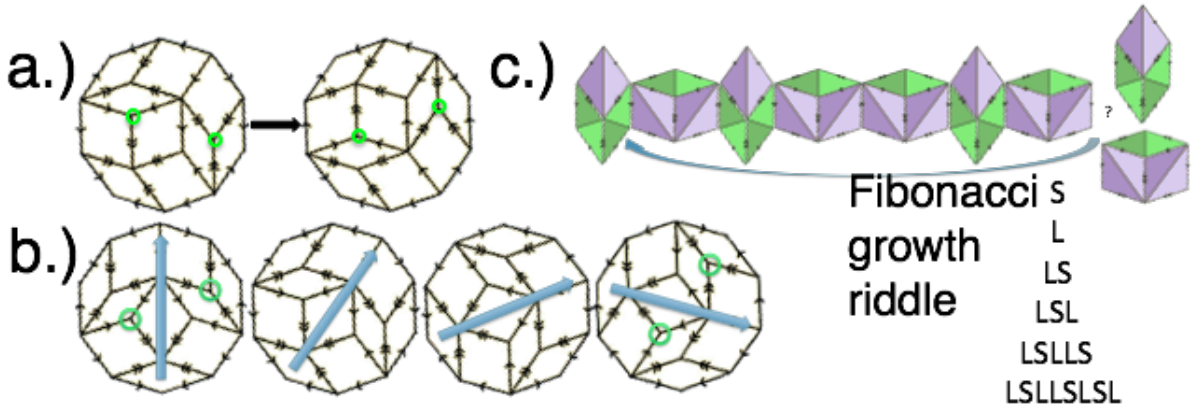


**Figure 2.10:** A phason flip can be understood as a re-arrangement of a non-periodic tiling that causes only local matching-rule violations (a). This leads to a localized increase in the potential energy of the system. **The Fibonacci growth riddle concerns the creation of perfect Fibonacci Sequences (L, LS, LSL, etc.) in the ribbons or worm lines of the tiling.** As seen on the right side of (c), we can place either a fat or skinny hexagon—both can satisfy the local matching rules. How do we know what the correct choice is? **We do not, and this is the major challenge posed by the growth riddle.**

Phasons are normally understood as flips that re-define the tiling—they are thought of as single changes along the Fibonacci Sequence of a Conway worm line (***Figure 2.10 (c)***) (Grünbaum & Shepherd, 1986). Fibonacci Sequences can also be seen as worm lines in ***Figure 2.15*** and ***Figure 2.16***, and phasons could propagate along them in what is called a zipper move

(Oxborrow & Henley, 1993). A new way to think about phasons in the Penrose tiling is instead to consider them as 108° rotations of a decagon (36° for each step in the figure above—108° is the interior angle of a regular pentagon). Layering blue pentagons on blue pentagons then produces two decagon rotations that cause a redefinition of their respective Fibonacci Sequences. Decagons could then "rotate" to minimize their local energy as many times as needed. Note that in an atomic (or any kind of particle) system with atoms on the vertices of the lattice, no actual rotation is needed—only two particles need to move since there are two hexagon flips in a 108° decagon rotation and one particle flips each respective hexagon. If the atomic decoration is more complex, then the atomic cluster at the phason position has a short distance to travel, relative to the lattice spacing, as well as a low potential barrier because of the quasilattice spacing—which is an important characteristic of a phason flip. **Essentially, particles at phason locations experience a low-barrier double potential well, which can be seen from the geometry of the lattice.** It is curious that phasons, normally associated with quasicrystal stability and growth, naturally emerge from this description of the quasilattice. While it is unknown whether this decagonal motif rotation plays a role in the growth-and-error repair process, we do know that it can happen in real quasicrystals (He et al., 2021). It may be that the matching rules are not strong enough to bias the decagons along a particular orientation.

The conceptualization of phason flips as tile flips was already understood (Socolar & Steinhardt, 1986), **but will be understood in a more complete real-space manner with the layering perspective presented in this thesis**. With this new understanding, we will see that phasons flips are what happens when we layer motifs on top of each other, and these specific phason flips are then used to construct the entire set of possible covering clusters seen in a given quasilattice tiling. This real-space approach to understanding phason flips is one way of simplifying the overall picture and reducing what might sometimes be unnecessary conceptual baggage. To quote Madison (A. E. Madison, 2015),

> We are strongly convinced that a three-dimensional description is always preferable for a three-dimensional object. This may be exemplified by the quotation from the monograph by Hyde et al. [29]: "The problem is to relate observed diffraction patterns with non-standard, supposedly disallowed, crystallographic symmetries, to the atomic distributions that cause them. That problem remains. **Because while a physicist living in [a] world made up of equations and group theory has no difficulty in constructing the universe, its scaling laws, and singularities like black holes, as a realization of a**

**sixteen dimensional group say, the chemist is more narrowly constrained. A three-dimensional atom has a certain pedestrian reality that does not so easily lend itself to a mapping onto six dimensions** [emphasis added].

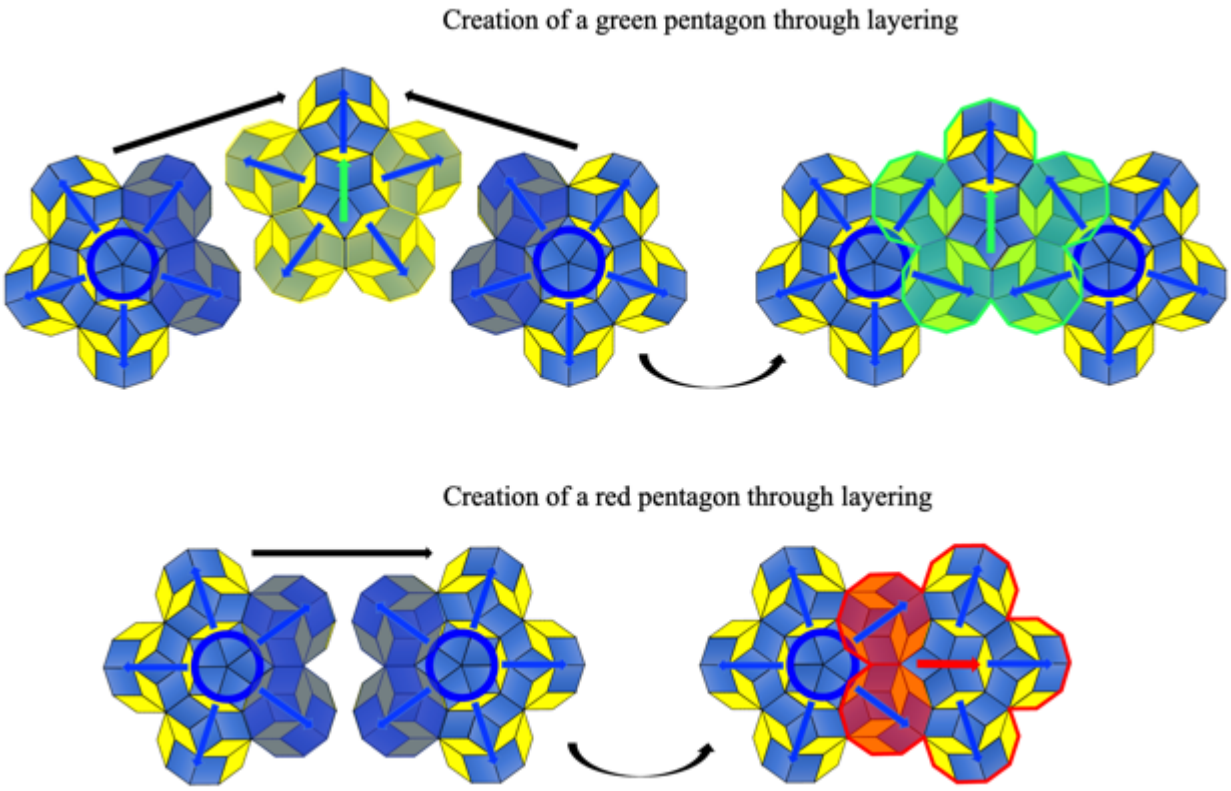


**Figure 2.11:** A blue motif has complete five-fold rotational symmetry. By layering it with itself, the other clusters in the Penrose tiling— shown above in green and red outlines—can be generated from this single blue motif. An important point to note is that all of these pentagonal motifs are a simplified version of the pentagonal motifs made with Gummelt motifs that was shown earlier. Since this is **not** a covering, the bottom and top decagonal motifs do not need to match. Instead, they are related to each other via phason flips, as discussed in this chapter and then again in the *Chapter Three* section on phasons.

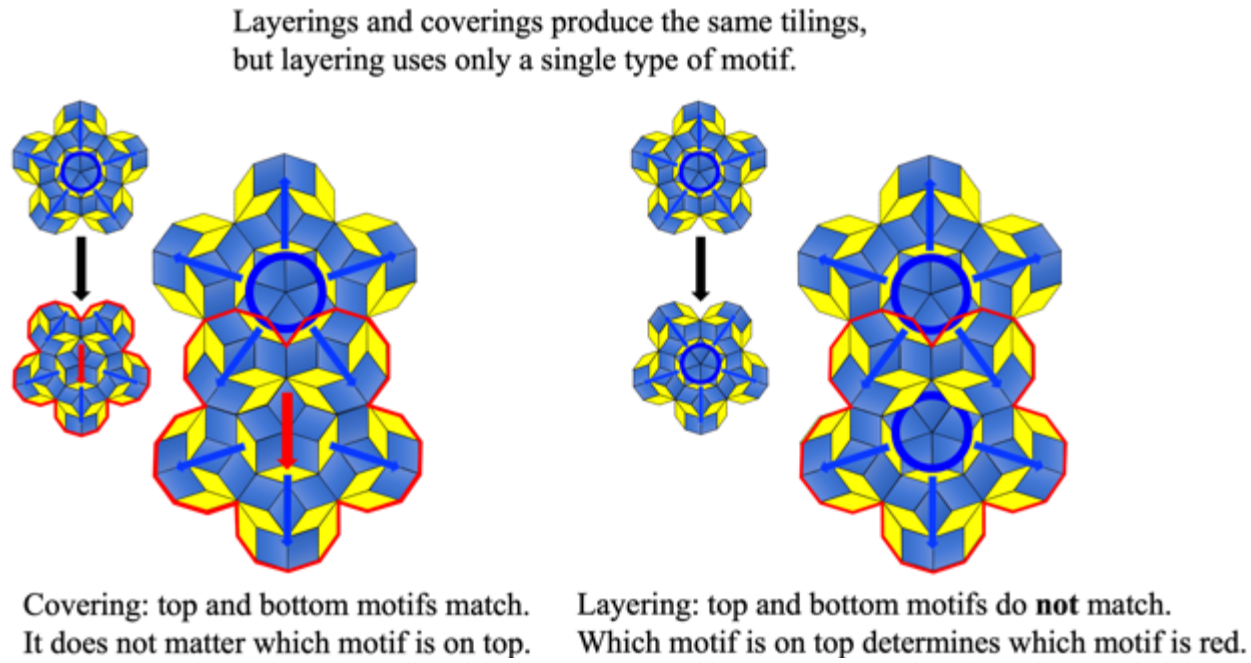


**Figure 2.12:** Layerings and coverings will result in the exact same resulting motifs. But note how the small pair on the left uses a blue pentagonal motif and a red pentagonal motif (red pentagonal outline), whereas the small pair on the right uses only blue pentagonal motifs. The pair of motifs on the right could produce an asymmetric red pentagonal motif on the top or the bottom, depending on which blue pentagonal motif is on the top layer. Much like the Gummelt motif, the layering method only requires a single motif.

As shown in ***Figure 2.12***, layerings and coverings will result in the same motif. **But the covering method will require more than one type of pentagonal motif (*Figure 2.4 (d)*), whereas the layering only requires one.** The Penrose tilings only have three covering pentagonal motifs, but the Tübingen or Ammann-Kramer-Neri tilings have many more. While the Gummelt motif is a single motif that covers the tiling, the original Gummelt *covering* rules are not a protocol for *construction*. **The new polygonal cycling method shown here is a method for construction. We can use *layering* with the single rotationally symmetric pentagonal motif, or we can use the three *covering* pentagonal motifs, to *construct* the Gummelt motif into an ideal Penrose tiling without using matching rules or grids.** When comparing the three covering pentagonal motifs, or the single layering pentagonal motif method, the latter is noticeably simpler since we only need to describe a single type of motif.

***Figure 2.13*** shows the yet-larger decagon of ***Figure 2.6*** separated into its respective blue, red, and green layers. Although there are fifteen green pentagonal motifs, it is important to note that most of the green pentagonal motifs, on a per tile basis, are actually *layered* (and thus hidden) by the tiles of the other pentagonal motifs. In the layering picture, these green

pentagonal motifs are actually just a pentagonal motif with a blue circle on the green layer, but the overlying blue pentagonal motifs will share complete decagon overlaps with these underlying pentagons and effectively rotate the decagons into the green pentagonal motif configuration—as seen from above the layering. The Penrose tiling is a seemingly miraculous iteration of this same quasi-unit cell—the blue pentagonal motif—in a pattern that hierarchically repeats as each polygon is constructed into the next larger version, starting with rhombuses, then decagons, pentagons, and then back into yet-larger rhombuses.

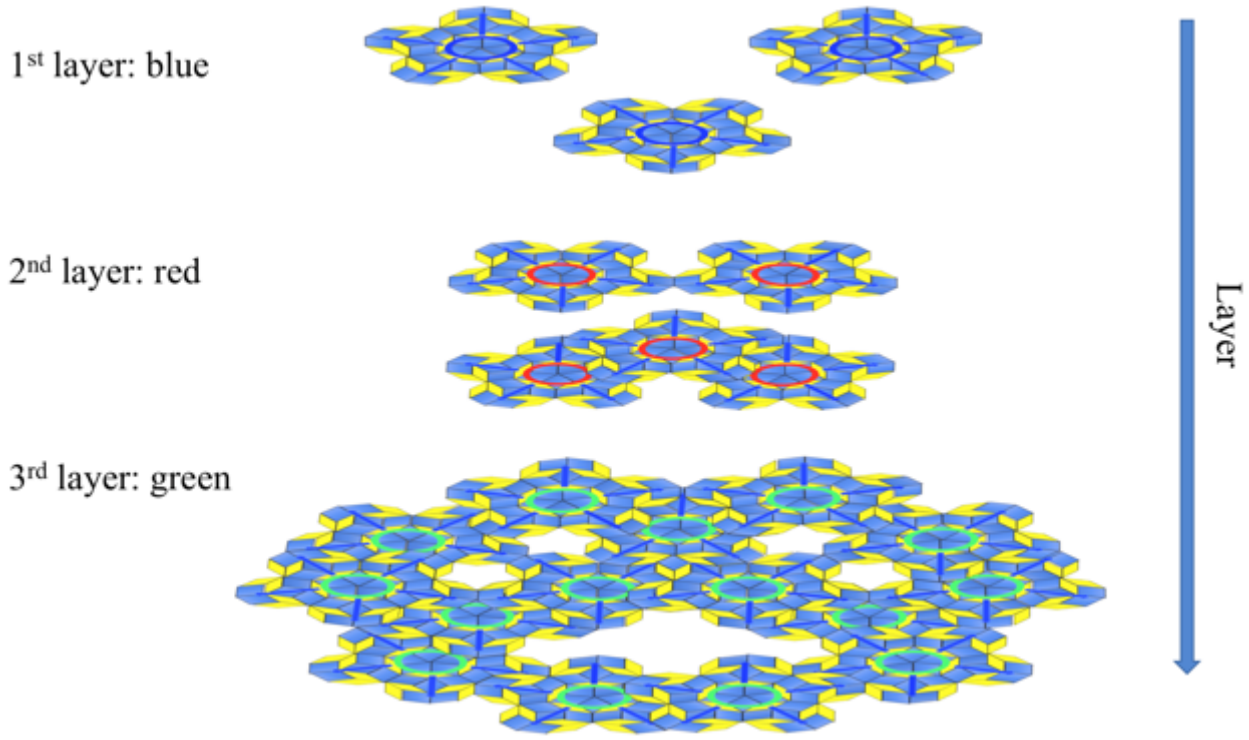


**Figure 2.13:** Remarkably, only the blue pentagon is required if we no longer require a covering—**all of the pentagonal motifs here are blue, or rotationally symmetric pentagonal motifs. They only have different colors to highlight that they are on different layers.** I call this a layering to emphasize that, unlike in a covering, the underlying tiles no longer match as coverings. P3 can then be regarded as blue pentagonal motifs sitting in one of three layers, ordered from top to bottom as blue, red, and green (BRG), respectively. We no longer need to recognize the different covering pentagons of ***Figure 2.4 (d)***, as it is now all automatically taken care of by the layering method.

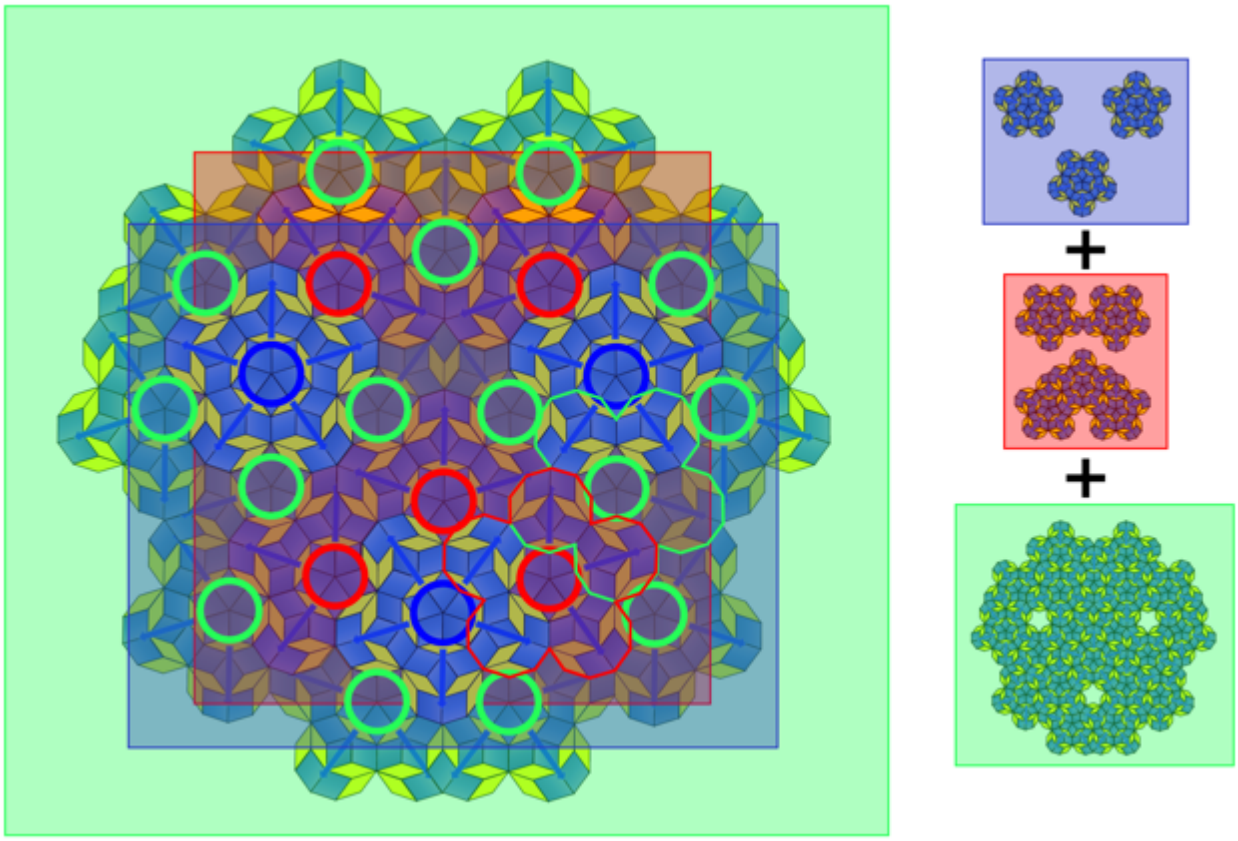

**Figure 2.14:** If we were to look straight down onto the image of ***Figure 2.13***, we would see the motif as presented above. The second-order rhombuses from ***Figure 2.5*** are used to create a second-order decagon. The blue pentagonal motifs are on top, followed by red pentagonal motifs in the middle, and lastly green pentagonal motifs on the bottom of the layering. The three covering pentagonal motifs from **Figure *2.4 (d)*** are still here—created by this process—the decagon rotations required to make the three covering pentagonal motifs are produced automatically from the layering process. Within the bolded black decagon, there are three blue pentagonal motifs, five red pentagonal motifs, and five green pentagonal motifs. One red and one green pentagonal motif have been highlighted with bolded outlines. These are all correctly defined because the layering is complete. **Note how the five green pentagons contained within large decagon have their composite decagons correctly re-oriented by the surrounding blue and red pentagonal motifs.** The same is true for the five red pentagons contained within the second-order decagon, which are defined by the three blue pentagonal motifs. **This image captures the heart of what is meant by layering—each of the respective covering motifs are automatically generated when layerings are created with a single type of motif.** And although I chose to do it with the blue pentagonal motif, having decided it was the simplest approach, I could also have used all red or all green pentagonal motifs—the method is symmetric.

The three layers from ***Figure 2.13*** are viewed as though they were stacked with blue on top, then red, and then green, to create the image shown in ***Figure 2.14***. Note how each red or green pentagonal motif—complete within the large black decagonal outline of the second-order decagon—is transformed from a rotationally symmetric pentagonal motif to a green pentagonal motif by the red or blue pentagonal motifs above it. A sample outline has been drawn for a red and green pentagonal motif in the lower righthand corner. Each layer, despite the coloring, now has only blue pentagonal motifs. The motifs on the red and green layers no longer need arrows

because that information, along with the rotation of each decagon, **is automatically generated when the layers are stacked**. The only information we need to construct the tiling is the location and orientation (there are only two orientations of pentagonal motif in the ideal Penrose tiling) of each blue motif in each respective layer.

The hierarchy for the Penrose tiling is now complete. To summarize, we start with the rhombuses in ***Figure 2.2***. These are assembled into the decagon in ***Figure 2.3***. That decagon is used to create the three different covering pentagons in ***Figure 2.4 (d)***, which can then be assembled into new larger second-order rhombuses in ***Figure 2.5***, and then a new second-order decagon like ***Figure 2.6*** or ***Figure 2.14***. Likewise, **we can skip the covering pentagonal motifs altogether and use layering information to construct the ideal Penrose tiling. Both methods are new, and so both are reported here.** Of some interest, however, is how the pentagons create the new second-order rhombuses in ***Figure 2.5***. In most quasilattice tilings that I have taken apart with this layering method, each vertex comprises the center of a rotationally symmetric motif (of pentagonal, octagonal, icosahedral, etc., symmetry) of the new hierarchy layer. In the Penrose tiling, however, they do not—they contain either the five-fold oblate rhombus star seen in the center of the pentagonal motif, or its matching-rule inverse, whereby the oblate rhombuses are rotated 180° (an example can be seen in ***Figure 1.3***). This complexity is an interesting characteristic of the Penrose layering hierarchy, and it is something that appears to set it apart from the other quasitilings. In the hyperspace projection, the Penrose tiling can be projected down from a 5D cubic hyperlattice through a series of multiple pentagonal-cut windows. In this respect, it is more complex than the Tübingen tiling, which is projected through a simple decagon. It is some wonder then that in the layering picture, the Penrose tiling is quite simple, whereas the Tübingen tiling is substantially more complex. It may be that the additional complexity of the Penrose tiling in the higher-order projection is expressed via this means of second-order lattice decoration.

**The size of the petal motif is not determined by the method**, but rather there is a maximum and minimum limit to the size of the motif. If a petal motif is increased beyond its maximum size, then neighboring petals on the same topmost layer will have conflicting tilings at their boundaries—called a *ring conflict* in this thesis. As the petal motif increases in size, fewer layers are needed to generate the tiling. Likewise, as the petal motif is decreased in size, more layers are needed to generate the tiling. If the petal motif is too small, it will not create a space-

filling tiling. **To prove the petal motif is space-filling, we only need to show that it is space-filling within all second-order polygons. This ensures that any second-order shapes created with those second-order polygons will also be space-filling.** The minimum petal motif, provided it is space-filling in the second-order motif, is therefore the smallest petal motif that will create a space-filling tiling when used to construct a second-order polygon.

## Symmetry in the Layering Method

The same operations that are performed by layering a blue pentagonal motif over another blue pentagonal motif can also be accomplished by layering a red pentagon over another red pentagon, as shown in ***Figure 2.15***. Note: the motifs are all decorated with red arrows because they are all the same red pentagonal motif shown in ***Figure 2.15 (b),*** layered with itself to create the blue and green pentagonal motifs as seen in the Penrose tiling. In this case, the red pentagons can undo the operations represented by blue-on-blue, and they can reproduce the same three covering pentagonal motifs as in ***Figure 2.4***. ***Figure 2.16*** shows the same process repeated using the green pentagonal motif.

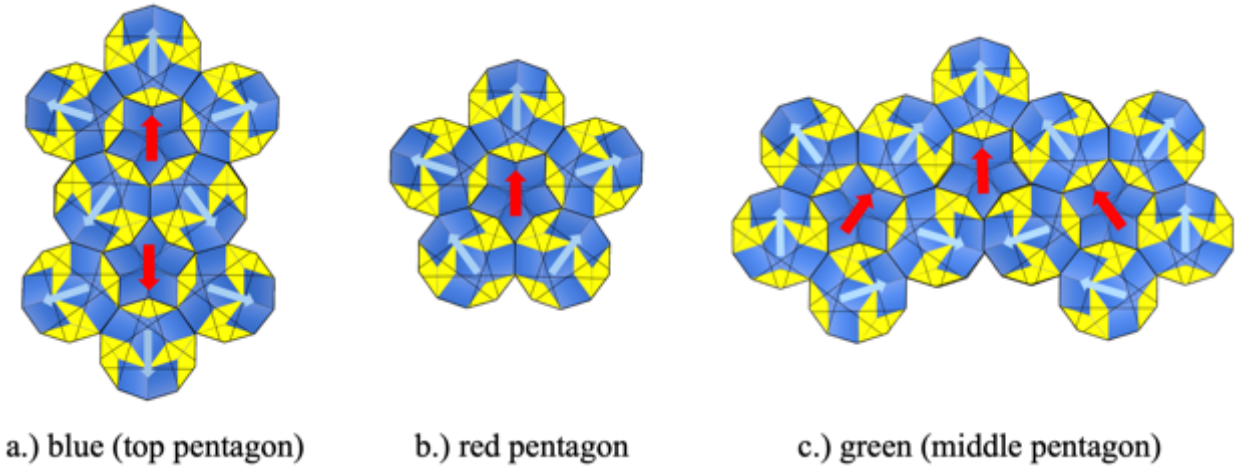


**Figure 2.15:** Although the blue pentagonal motif appears to play a central role in this description of the Penrose tiling, the other pentagonal motifs can just as easily be used as a quasi-unit cell. In (a), we see the construction of a blue pentagonal motif (top) made from the layering of two red pentagonal motifs, in (b) the original red pentagonal motif, and in (c) a green pentagonal motif (middle) made from the layering of three red pentagonal motifs. This reflects a natural mathematical symmetry, whereby any

pentagonal motif can be used to invert the decagon rotations of the others. These figures also contain Ammann bar markings, which are explained in *Chapter One*.

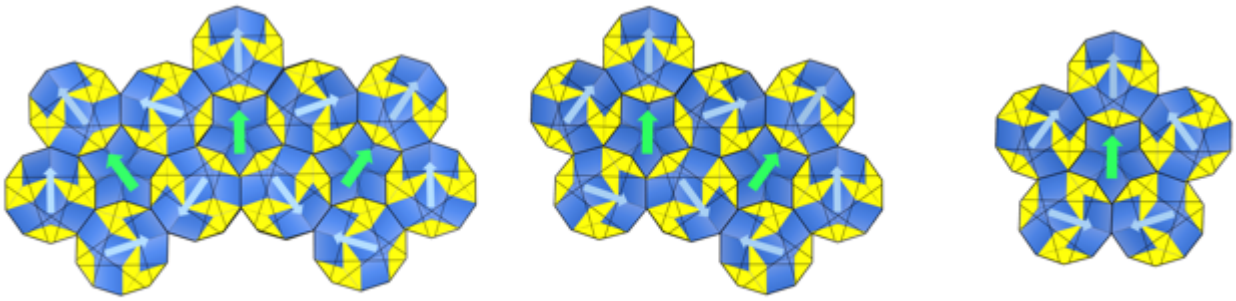

a.) blue (middle pentagon)

b.) red (left pentagon)
(arrow direction changes)

c.) green

**Figure 2.16:** In (a), we see a reconstructed blue pentagonal motif (middle), (b) shows a reconstructed red pentagonal motif (left), and (c) is the original green pentagonal motif. When using a different color pentagonal motif, the layer stack order is changed. Hence, if we are using red, then the layer order is red, blue, green. If we are using green, then the layer order is green, red, blue. The rule is simple: the top layer exists with a *single* pentagonal motif, the second layer is created by *two* pentagonal motifs, and the third layer is created by *three* pentagonal motifs.

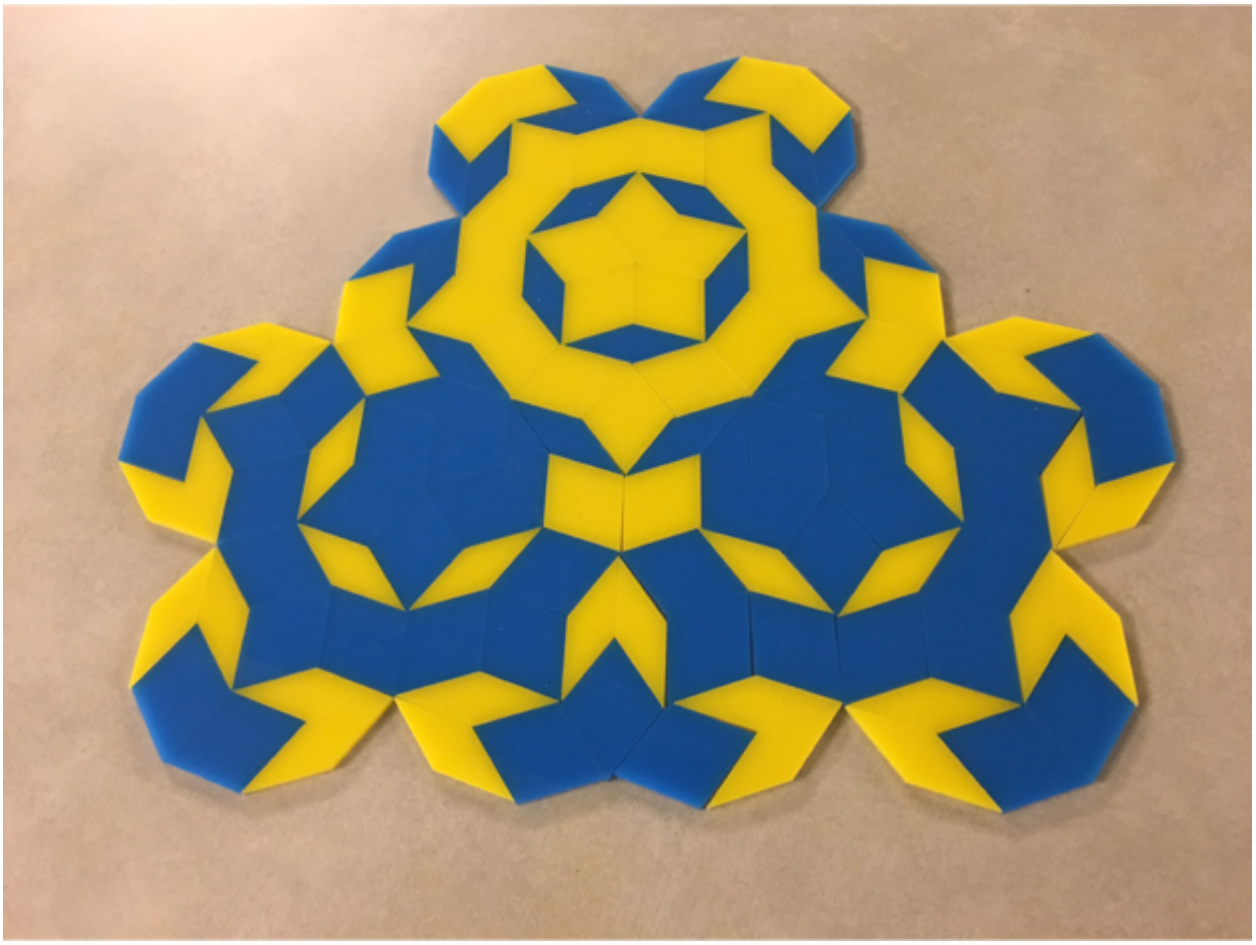

**Figure 2.17:** With the layering method, the generation of new Penrose tilings is relatively straightforward. No matching rules are required—and would not help since they don't prevent eventual errors. In the above picture, tiles have been arranged by hand and represent a blue pentagonal motif (top), followed by two red pentagonal motifs on the bottom. (Note that the red pentagonal motifs could be changed to green with additional pentagonal motifs). By continuing to assemble tiles in the manner laid out in ***Figure 2.5***, we can guarantee the assembly of an ideal Penrose tiling of any arbitrary size.

***Figure 2.17*** shows the creation of a second-order oblate rhombus (***Figure 2.5, right***). With some effort, it's possible to memorize the construction of the *infinite* Penrose tiling—a feat not otherwise possible via other methods, in my opinion. By understanding quasitilings as cycles of polygonal hierarchies, we can form—for the first time presented in literature—a real-space mental image of what the quasitiling looks like, which is provided by no other means of their generation.

## An Algorithm for Constructing the Penrose Tiling by Layering

For any reader interested in understanding or programming the Penrose rhombus tiling using a mathematical algorithm via layering, such has been provided here. Positions, orientations, and translations are given for the assembly and placement of each motif.

### Generating the Pentagonal Motif from the Characteristic Decagon

The rotationally symmetric pentagonal motif can be generated by starting with the characteristic decagon from ***Figure 2.4(c)***[17]. Copy this motif and choose the bottom vertex of the acute rhombus as the axis of rotation. This vertex will be a distance of one edge length from the center of the new pentagonal motif. Rotate the characteristic decagon CW (or CCW) 36°. Repeat this process three more times (for a total of five characteristic decagons). Each characteristic decagon should fit edge-to-edge with its neighbors, with the bottom vertex of each acute rhombus pointing radially inwards. Finally, place a five-fold star of oblate rhombuses in the center[18]. The rotationally symmetric pentagonal motif (to which you can add a blue circle) is now complete.

### Creating the Second-Order Oblate Rhombus

Start with the 1st pentagonal motif we created from the characteristic decagon and rotate it CCW 18° with respect to its rotational center. Copy this 1st motif and translate it to the right (assuming a rhombus edge-length of 1) by $2\tau + 1$, where $\tau$ is the golden ratio, while also rotating it CW 36° with respect to its rotational center. This will create a complete overlap between two of the characteristic decagons—but note that this 2nd pentagonal motif must be placed beneath the 1st. The 1st pentagonal motif will be placed at the blue layer (first or topmost), and the second at the red layer (second).

The 1st pentagonal motif should be copied again, but not rotated. It should then be translated $2\tau + 1$ to the right, and then translated $2\tau + 1$ at an angle of 36° above the horizonal.

---

[17] The creation of the characteristic decagon is entirely identical to the creation of the second-order decagon which is detailed later in this algorithm—the translation and rotation of each second-order polygon is simply performed on a fundamental polygon instead

[18] Curiously, the P2 kite-and-dart petal motif has a core comprising five overlapped decagonal cartwheel motifs with five additional copies of those same motifs forming a ring around it. I don't know why the P3 rhombus tiling does not follow this pattern—but neither does the AKN.

The same process should be repeated, but with a translation of $2\tau + 1$ to the right plus a distance of $2\tau + 1$ at an angle of 36° **below** the horizontal. These 3rd and 4th pentagonal motifs will share two complete characteristic decagons each with respect to the 2nd pentagonal motif. These last two pentagonal motifs are on the green (third) layer, so should sit below both the blue and red layers. Since the layer positioning of the two pentagonal motifs on the green layer are concealed by the blue and/or red layers, their layer position with respect to each other does not matter.

**Creating the Second-Order Acute Rhombus**

Start with the 1st pentagonal motif and orientation that was created earlier and rotate it CW 36°. This pentagonal motif sits on the blue layer. Copy this pentagonal motif again and rotate it CCW 36°, and then translate it a distance of $2\tau + 1$ at an angle of 36° to the left of the vertical (or 54° below the horizontal). This 2nd pentagonal motif sits on the green layer, so will be below the 1st pentagonal motif. Likewise, copy the 1st pentagonal motif again and rotate it CCW 36°, but now translate it a distance of $2\tau + 1$ at an angle of 36° to the right of the vertical (or 54° below the horizonal). Like the 2nd pentagonal motif, this 3rd pentagonal motif also sits on the green layer. The 2nd and 3rd pentagonal motifs—which both sit on the green layer—will create different overlap patterns depending on which one is on top, but this part of their motif is entirely concealed by the blue and/or red layers, so it does not affect the tiling.

**Creating the Second-Order Decagon**

We can begin with a second-order acute rhombus. Align it so that its long axis is horizontal—the same orientation from the paragraph above. The center of the single pentagonal motif with the blue circle in this second-order acute rhombus can be taken as the (0,0) origin, if desired. It is also the axis of rotation for each type of second-order rhombus in this section. Next, copy this second-order acute rhombus and then translate it $5 + 3\tau + \frac{2}{\tau}$ at an angle of 36° left of the vertical, while also rotating it CCW 36° with respect to the pentagonal motif with the blue circle (its top vertex). Copy this translated second-order acute rhombus, and rotate it CW 144° again with respect to its pentagonal motif with the blue circle.

We will then repeat this procedure for the mirror symmetric side. Copy the original second-order acute rhombus, translate it $5 + 3\tau + \frac{2}{\tau}$ at an angle of 36° right of the vertical, while also rotating it CW 36° with respect to the pentagonal motif with the blue circle. Copy this

translated second-order acute rhombus, and rotate it CCW 144° with respect to the pentagonal motif with the blue circle. This completes the placement of the five second-order acute rhombuses.

Turning now to the second-order oblate rhombuses, we can take the original second-order oblate rhombus from our earlier construction and rotate it CCW 90° (so that its long axis is vertical and the pentagonal motif with the blue circle sits on the bottom). Place this second-order oblate rhombus such that the pentagonal motif with the blue circle (its bottom vertex) *covers* the pentagonal motif with the blue circle (its top vertex) of the 1st second-order acute rhombus that we placed. This will be the correct placement of the 1st second-order oblate rhombus.

Next, copy this 1st second-order oblate rhombus and rotate it CW 72° with respect to the pentagonal motif with the blue circle. Copy it again and rotate this 3rd copy CCW 72° with respect to the same pentagonal motif with the blue circle. Next, copy the 1st second-order oblate rhombus and translate it $5 + 3\tau + \frac{2}{\tau}$ at an angle of 36° right of the vertical, while also rotating it CCW 36° with respect to the pentagonal motif with the blue circle. This is the position of the 4th second-order oblate rhombus. The 5th second-order oblate rhombus can be placed by copying the 1st and translating it $5 + 3\tau + \frac{2}{\tau}$ at an angle of 36° left of the vertical, while also rotating it CW 36° with respect to the pentagonal motif with the blue circle.

Note that these orientations, rotations, and translations will work for this hierarchical polygonal cycling using either *covering* or *layering* methods. If the second-order polygons are created from the three *covering* motifs, then each edge-to-edge mating of the second-order polygons will create additional coverings—and eventually an ideal Penrose rhombus tiling. **If, alternately, the second-order polygons are created entirely from rotationally symmetric pentagonal motifs, then *layering* order needs to be enforced as the final step in order to create the ideal Penrose rhombus tiling**—which is the whole idea of the layering, after all. **Essentially, the complexity of the many covering motifs is instead stored as the layering order of a single type of motif.**

**Conclusion of the Penrose Algorithm**

This completes the placement of 5 second-order acute rhombuses, and 5 second-order acute rhombuses, to complete the construction of the new second-order decagon. This second-order decagon can then be assembled into a new rotationally-symmetric pentagonal motif (with a

blue ring) by copying and rotating the second-order decagon (CW or CCW) 72°, with respect to the same (now second-order) vertex described earlier for the assembly of the pentagonal motif, for four iterations (to produce five second-order decagonal motifs in total). Once this new pentagonal motif is assembled, the process can be repeated indefinitely. This method can be identically performed using either ***Figure 2.4(a)*** or ***Figure 2.4(c)***. The iterations produced by the characteristic decagon of ***Figure 2.4(c)*** will have pentagonal motifs that are missing the internal star of oblate rhombuses, but that is the only difference.

## Conclusion, Future Work, and Current Applications

Penrose tilings have many interesting properties, which is why I covered this model first. As Senechal says, "Just as Penrose tilings are the Drosophilae of tiling theory, icosahedral clusters may be crystallography's stem cells" (Senechal, 2008). The perfect Penrose tiling has, for instance, the highest hyperuniformity—the suppression of long-wavelength density fluctuations—among pentagonal tilings (Lin et al., 2017)[19]. Icosahedral quasicrystals, a type of three-dimensional quasicrystal projected from six-dimensional hypercubic lattices, can produce Penrose tilings if cut along one of the five-fold axes (Indelicato et al., 2012). An icosahedral quasicrystal has six planes with five-fold symmetry, and these axes can be rotated by 72° to return to the same tiling configuration. It was suggested by de Bruijn that the fat and skinny rhombuses of the Penrose tiling are actually the same 3D shape, but seen from different angles. By assuming these flat 2D shapes are actually 3D, de Bruijn created what is known as the *Wieringa roof* (Grünbaum & Shepherd, 1986). This construction was one of the first indications of the existence of the three-dimensional Penrose tiling later discovered by Ammann, Kramer, and Neri. This chapter made it possible to apply the same concept to this 3D quasilattice, which will be covered in *Chapter Six*. There have been other attempts to simplify or otherwise offer different models of Penrose tilings (Ajlouni, A., 2011; Polyakov, 2008), but none accomplish the goal of this chapter to present a real-space model of the tiling.

**As a result of this work, we are able to visualize the tiling structure of a quasilattice in a way that is not available with current methods.** Analyzing the hierarchical clusters

[19] I conjecture that this is a result of the golden ratio having the highest degree of irrationality, as can be seen in its fractional expansion.

described here can provide an alternative descriptor for phason errors and dynamics, and may lead to a better understanding of rapid quasicrystal growth in 2D and 3D simulations. The model also provides a clear visual aid for understanding the difference, but deeply shared commonality, between fractals and quasilattices. This protocol has been applied here to the Penrose rhombus tiling, and in later chapters to the octagonal Ammann-Beenker tiling, Tübingen tiling, dodecagonal Socolar shield tiling, and even the Ammann-Kramer-Neri (AKN) tiling of the icosahedral quasicrystal. The AKN tiling is a particularly interesting example, since the AKN does not have a known deflation protocol.

In the next chapter, I will apply the same technique to the octagonal Ammann-Beenker tiling. This chapter will introduce two additional levels of complexity. The first is the concept of rings—this shows how we can expand the petal motif to ensure that it fills space. The second is chirality, where a second-order polygon has a mirror twin. Each chapter will build on the complexity of the previous.

## Chapter Three

### A Layering Construction of the Ammann-Beenker Octagonal Tiling

## Introduction

In this chapter, I apply the new layering method to the Ammann-Beenker tiling. It is a more complex tiling than the Penrose tilings, and introduces a new concept which I call an expansion ring. A ring is added when the petal motif (which is here an octagonal motif—it plays the same role as the pentagonal motifs from *Chapter Two*) is not large enough to produce a space-filling tiling. Increasing the size of a petal motif will reduce the number of covering petal motifs needed, but will also increase the complexity of the motif, and so presents an interesting trade-off. The layering method works to efficiently detail the construction of the Ammann-Beenker tiling and demonstrates how the layering method can be generalized beyond the Penrose tilings.

The Ammann-Beenker tiling is a binary quasilattice tiling like the Penrose rhombus or kite-and-dart tiling. It is put together in much the same way as the Penrose tilings, but with some important differences. We start with two fundamental polygons, assemble them into a characteristic polygon—an octagon instead of a pentagon this time—that can be assembled into an octagonal petal motif. Just like the characteristic decagon[20], the characteristic octagon has bilateral or mirror symmetry. Likewise, the octagonal petal motif has full eight-fold rotational symmetry corresponding to the symmetry of the tiling. Just like the pentagonal petal motifs from the Penrose tiling, these octagonal motifs are found to overlap in a specific way to construct yet-larger second-order polygons. In this way, we will see that the Ammann-Beenker tilings can be quite simple to visualize. Additionally, a detailed algorithm for the Ammann-Beenker tiling is presented at the end of this chapter.

[20] The characteristic decagon has bilateral or mirror symmetry and is the core of the motif that Gummelt proved will cover the Penrose tiling (Gummelt, 1996).

The Ammann-Beenker tiling begins with two fundamental shapes—a 45-135 rhombus and a square with matching edge lengths.

## Fundamental Polygons

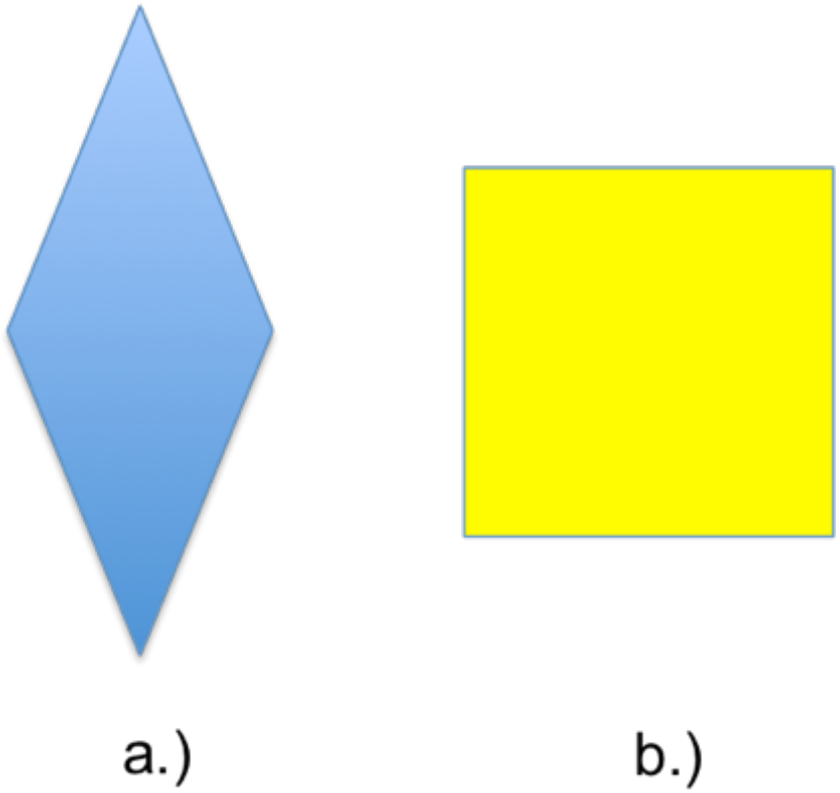


**Figure 3.1:** The Ammann-Beenker tiling is constructed from a 45-135° rhombus and a square. Each has matching edge lengths.

These fundamental polygons can then be put together into a characteristic octagonal motif.

## Characteristic Octagon Motif

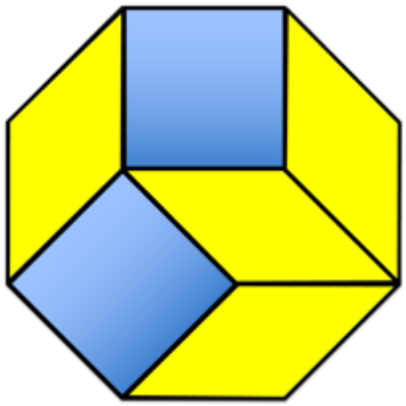

**Figure 3.2:** The Ammann-Beenker tiling contains a primary motif in the form of a characteristic octagon, which is made from two squares and four rhombuses.

This characteristic octagon (***Figure 3.2***) behaves similarly to the characteristic decagon, which is the interior of the Gummelt motif seen in *Chapter Two*.

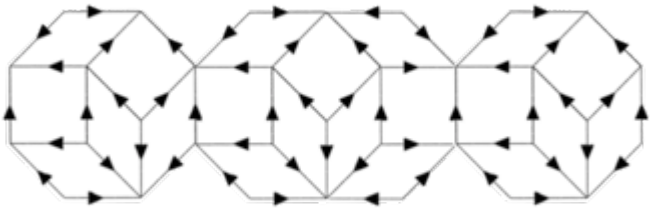

**Figure 3.3:** The octagons can be strung together, with the shapes matching in each layer—these overlaps obey the rules of a covering.

Just as the Penrose tiling is based on the golden ratio, the Ammann-Beenker tiling uses a related number called the silver mean[21] or Pell number[22]. Each Pell number is equal to the sum of twice the previous Pell number and the Pell number before that[23].

[21] The Pell numbers have been known to mathematicians since ancient times and could be used to calculate rational approximates to the square root of two, which is useful for calculating rational approximations to the coordinates of a regular octagon (Posamentier, 2007).

[22] There is also a bronze mean/ratio that can be used to construct a hexagonal quasilattice, which is not discussed in this thesis (Dotera et al., 2017).

Like many quasilattice patterns, we can think of the eight-fold symmetry as arising from two orientations of squares, with the void spacing comprising other geometric figures. The Penrose P1 tiling has two pentagons at different orientations, for instance, with other geometric shapes filling the gaps[24]. In the Ammann-Beenker case, we have two orientations of square, and a void space filled in by the 45-135° rhombuses. The Penrose tiling, likewise, can be envisioned as two different orientations of pentagon, with the void space filled in with stars, boats, and rhombuses.

Also similar to the Penrose tilings, which have worm lines that obey the Fibonacci Sequence, the Ammann-Beenker tiling has worm lines that obey what is called the Octonacci sequence. Here, the substitution protocol for generating this sequence is L -> LLS, and S -> L. Another expression of the substitution protocol is *r* -> *R*, and *R* - > *RrR*. This subtle difference is important, because now *r* is the short diagonal of a rhombus, and *R* is the long diagonal of a rhombus. There are also worm lines that are made from squares and hexagons, as can be seen in ***Figure 3.4***.

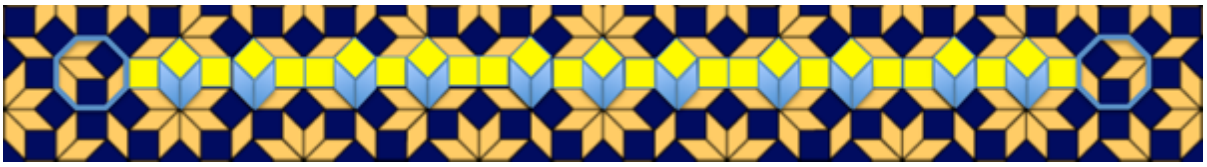

**Figure 3.4:** A worm line in the Ammann-Beenker tiling. This one is made from squares and hexagons (two rhombuses and a square). Note the ends which are the octagons from ***Figure 3.2***. (Image comprises a handmade worm line with a background tiling from the Tilings Encyclopedia which can be found at https://tilings.math.uni-bielefeld.de/substitution/ammann-beenker/)

Just like the Penrose tiling, the worm lines in the Ammann-Beenker tiling are closed off by octagons (instead of decagons). Likewise, these octagons only let through two worm lines and block the others. Similarly, the worm line that is caged in by these two decagons is a palindrome.

---

[23] As a quick example, let's start with the numbers 0, 1. 2 times 1 plus 0 is equal to 2. 2 times 2 plus 1 is equal to 5. 2 times 5 plus 2 is equal to 12, 2 times 12 plus 5 is equal to 29, and so forth, giving the sequence 0, 1, 2, 5, 12, 29, 70, and so on.

[24] The origin for these two orientations is easy to understand from the fractal construction of the pentaflake. Two orientations of small pentagon are needed within each large pentagon, and each small pentagon therefore has two orientations that flip back and forth in the two orientations of the large pentagon (***Figure 1.13***, ***Figure 1.14***, ***Figure 1.15***). These two orientations are then the only kind of orientation we can get.

This chapter will demonstrate how the Ammann-Beenker tiling is very similar to the Penrose tiling. We can take the characteristic octagon from ***Figure 3.2*** and make a ring from it, for instance, without violating the known matching rules. Note how the shaded blue rhombus inside each octagon is on the radially outward side. We will also later draw arrows on the characteristic octagons that point outwards.

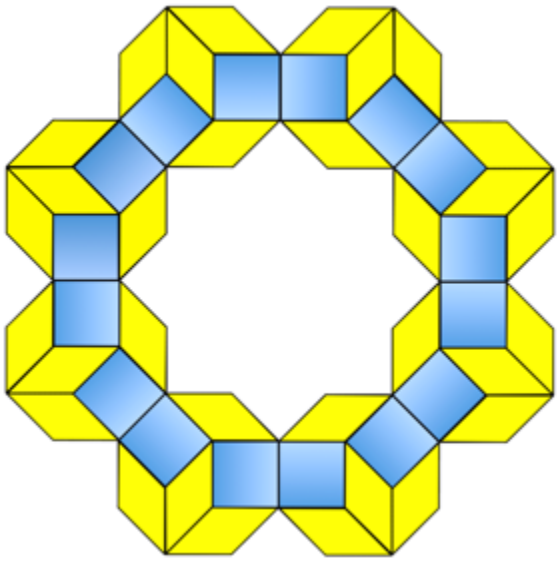

**Figure 3.5:** Octagonal ring motif made from eight of the fundamental octagons from ***Figure 3.2***. Note that the corner of the octagon with three rhombus vertices is oriented to point outward from the center.

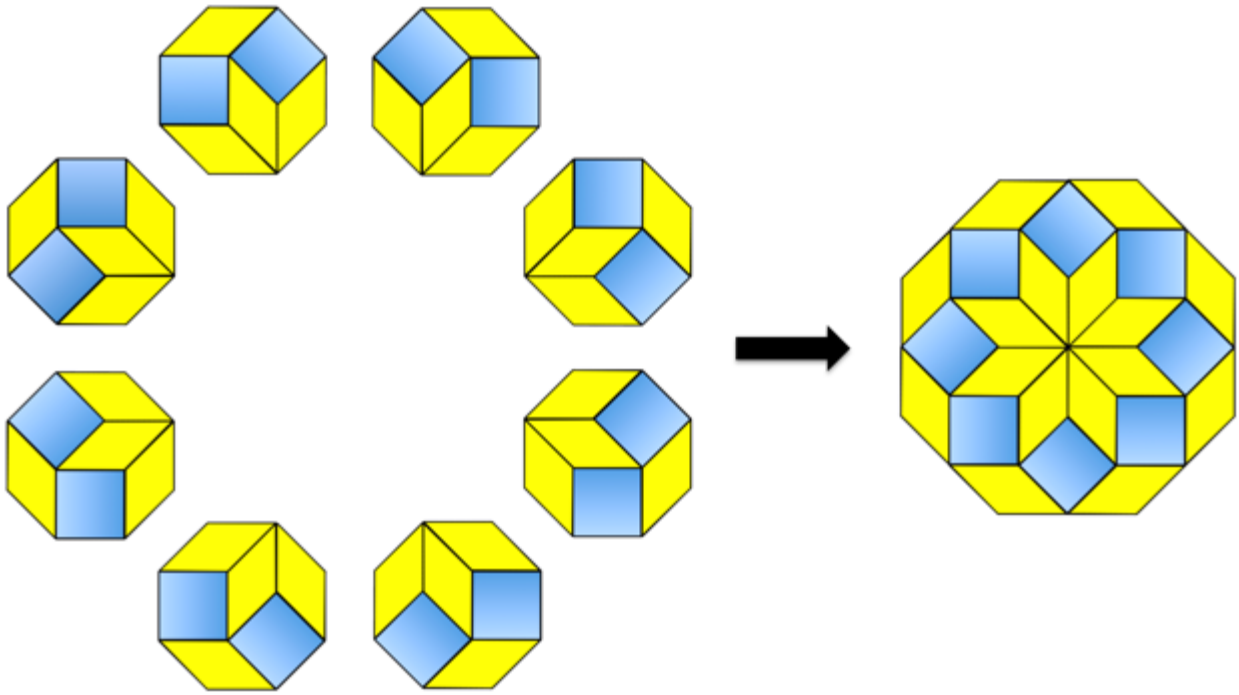

**Figure 3.6:** The core of the octagonal motif can be made by starting off with the ring from ***Figure 3.5***, **rotating all of the octagons by 180°**, and then creating a covering by moving all of the octagons inward radially until they all meet at a central vertex.

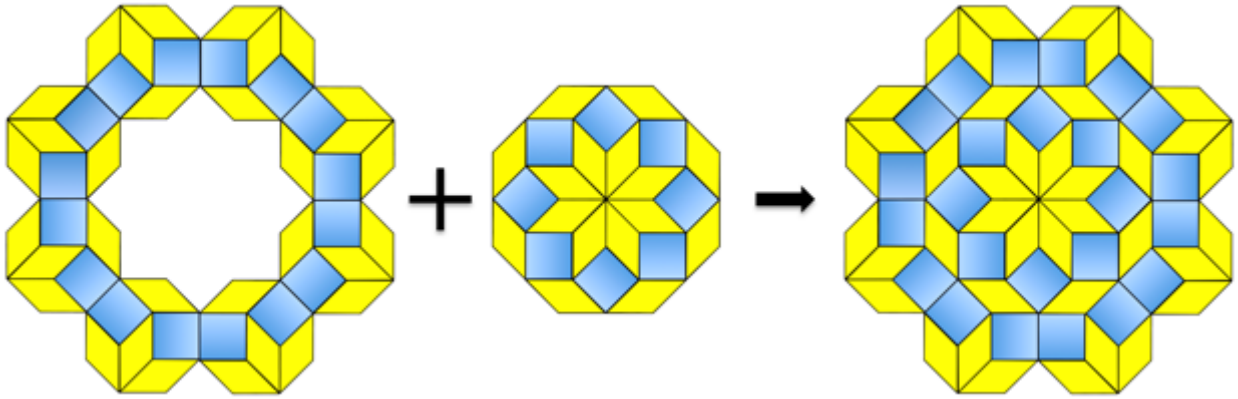

**Figure 3.7:** This shows an octagonal motif made by combining ***Figure 3.5*** and ***Figure 3.6***. The final image on the right is a covering made entirely from the octagon in ***Figure 3.2***.

Although the motif shown in ***Figure 3.7*** has no matching-rule violations (if we had drawn them), this would not guarantee that it is a motif in the Ammann-Beenker tiling. Rather, the infinite Ammann-Beenker tiling is guaranteed to not have any matching-rule violations. It is

important to remember that a quasilattice tiling cannot be constructed with matching rules alone—we may always have a patch of tiles that has no violations, but which later forces a violation down the road. This may even occur thousands of tiles later. Since we cannot use the matching rules for construction, I have only drawn them for ***Figure 3.3***.

Here is an image from Penrose (Penrose, 1989) illustrating this backtracking problem with the Penrose P2 tiling,

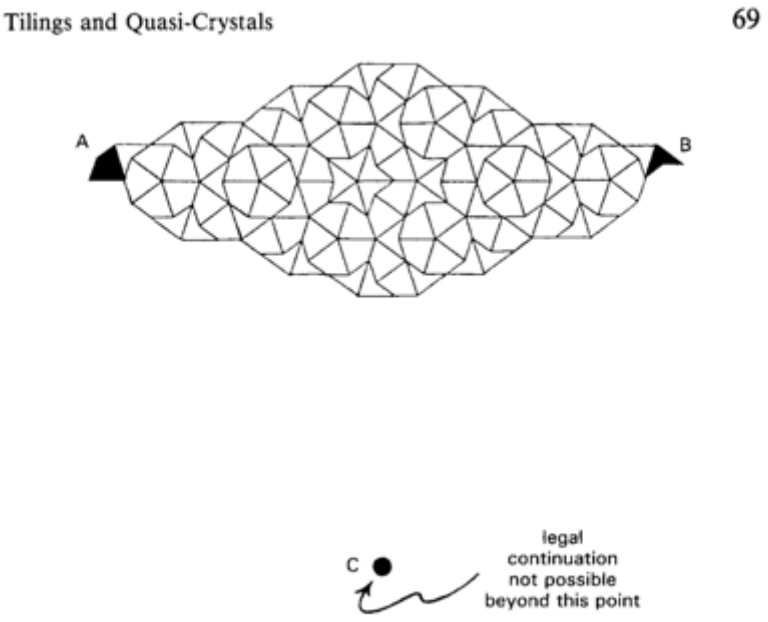


Figure 16. The placing of a kite at A is incompatible with a dart at B, whereas each would be correct without the other. The incompatibility only becomes evident when C is reached

**Figure 3.8:** R. Penrose, "Tilings and Quasi-Crystals; a Non-Local Growth Problem?", 1989. A black kite has been placed at site A which is incompatible with the dart at site B. Despite the matching rules allowing violation-free tiling for a wide swath of tiling (which has not yet been placed), this incongruity between A and B introduces an inevitable conflict at site C, the black dot, where further tiles cannot be placed without a matching-rule violation.

To better understand what I mean by *construction*, we can compare it with the Onoda method. In the same 1989 work mentioned above, Penrose shows the impossibility of what is called a local-local growth algorithm. As an alternative, Onoda (Onoda et al., 1988) shows the existence of a global-local algorithm capable of producing tilings that only produce defects linearly. Onoda's method asks whether a tile placement has more than one option. If there is

only one option, then the tile is forced—and a tile can be placed in this location. If there is more than one location, then a tile cannot be placed there. So this sense of artificiality is what is meant as global. It would be strange to expect a real material to grow this way, but the model has always been more interesting for lack of competition than for any established experimental reality. It is interesting theoretically because it works as well as it does! **Similar to Onoda's model, the *construction* method proposed in this thesis would also be a global-local algorithm.** I know what the characteristic octagon is supposed to look like, so I can assemble the square and rhombus into that shape (***Figure 3.2***). But there is nothing intrinsic to the square or rhombus that tells me I must place it into the octagon shape—not even the matching rules. Knowing how to cycle the polygons through different hierarchies is global information.

The octagonal motif is made from an outer ring of "outward" pointing octagons, and an internal ring of "inward" pointing octagons (***Figure 3.7, right***)[25]. This will be our default "blue" octagonal motif that has the highest degree of rotational symmetry, and this is where we'll start building the layering protocol that was described in *Chapter Two*. Previous research (Aboufadil et al., 2014) mentions this motif in passing, but does not give it a central importance[26].

[25] Similar to the kite-and-dart P2 Penrose tiling (not shown for brevity)

[26] This is not surprising since that research focuses instead on using the multigrid approach (similar to the Ammann bar method in *Chaper One*) to understand 14th century Moroccan tilings.

## Layering

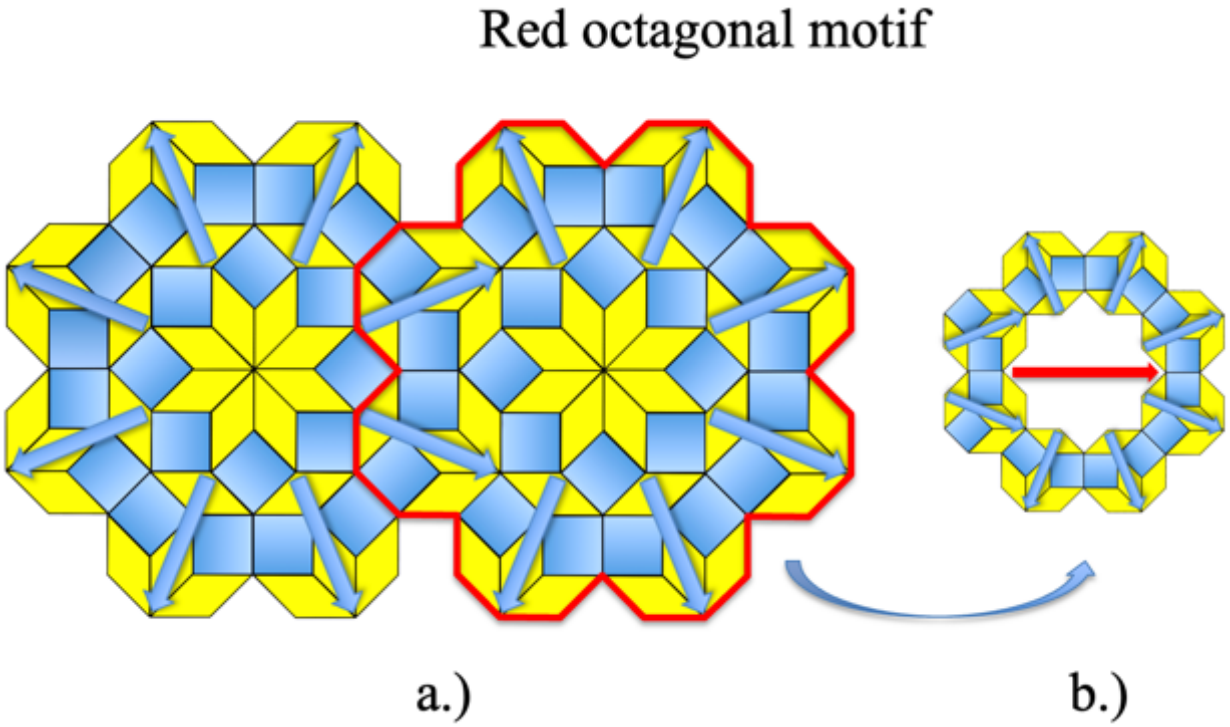


**Figure 3.9:** In (a), we see the layering of two default or "blue" octagonal motifs. In (b), we see the outer portion of the new "red" octagonal motif that is created by this layering.

## Octagonal Covering Clusters

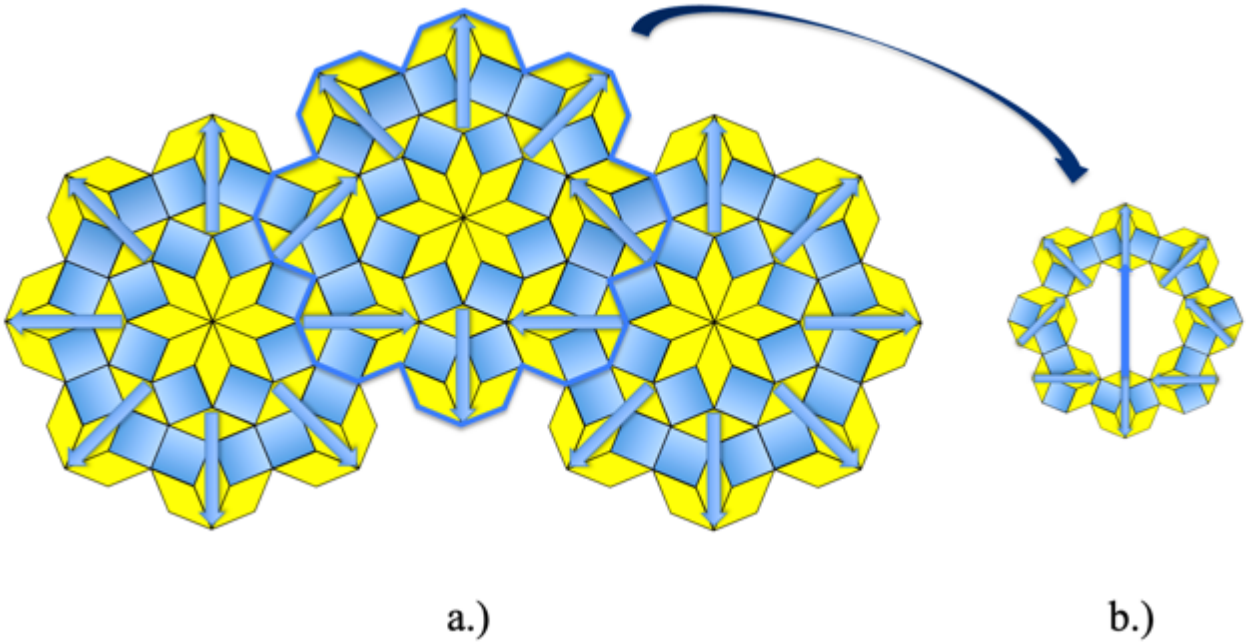


**Figure 3.10:** A light blue octagonal motif made from three layered blue octagonal motifs (a). In (b), we see that a total of four characteristic octagons have undergone 135° rotations—the other four remain pointing outward in their original orientation.

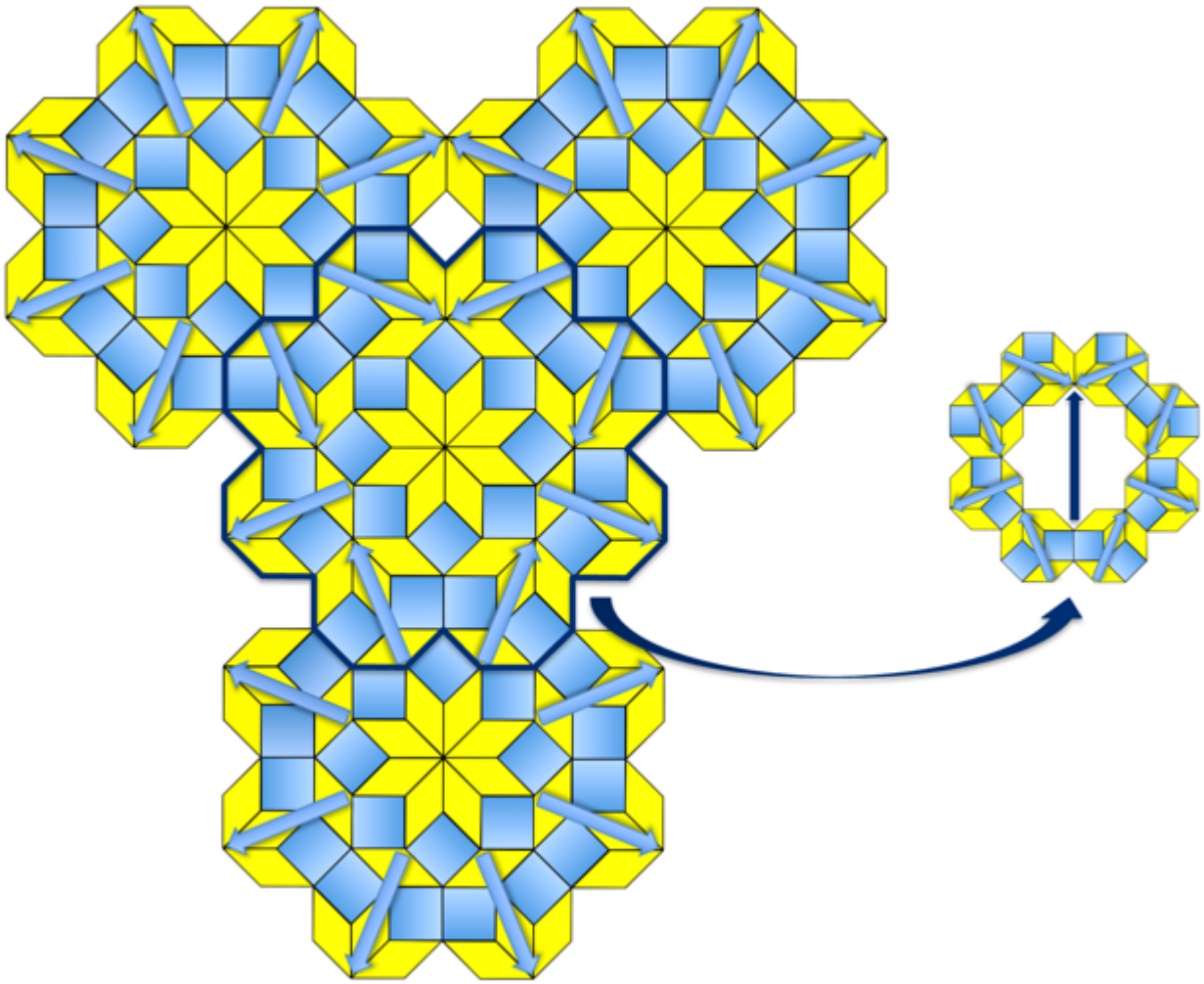

**Figure 3.11:** A dark blue octagonal motif made from four layered blue octagonal motifs (a). In (b), we see that a total of six characteristic octagons have undergone 135° rotations—only two remain pointing outward in their original orientation.

So far, we have generated a total of three new octagonal motifs beyond the rotationally-symmetric blue octagonal motif. These are effectively octagons (as drawn through the centers of the characteristic octagons that comprise the octagonal petal motifs) that have been placed edge-to-edge. After placing three octagonal motifs around a central octagonal motif, there is no longer any room to place a fourth (***Figure 3.12***). **This appears to set a natural geometric limit on the number of total octagonal motifs, both in the Ammann-Beenker tiling and others.**

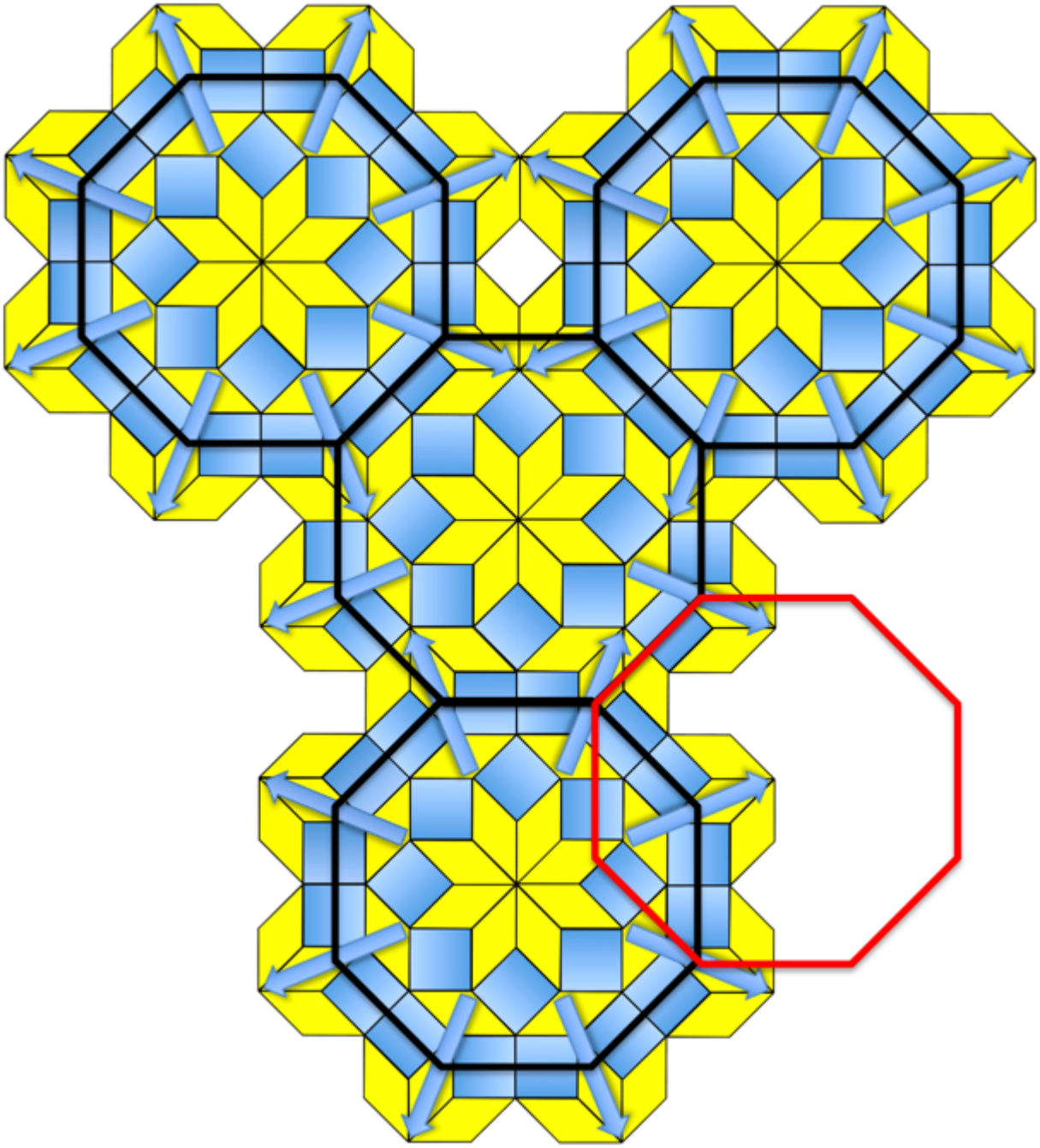

**Figure 3.12:** There is no more room for an additional edge-to-edge octagonal motif around the central octagonal motif (the new red octagon does not fit without overlapping pre-existing octagons). Curiously, this geometrical limit appears to set the number of covering petal motifs that are used in a quasilattice tiling.

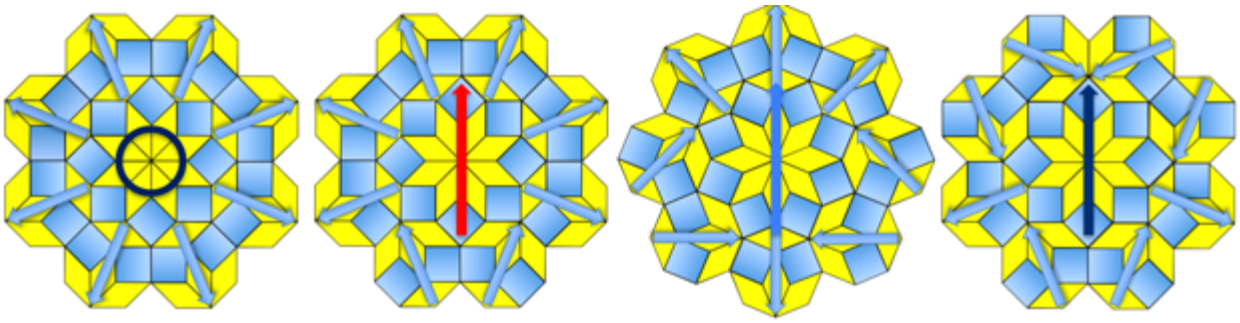

**Figure 3.13:** Octagonal covering motifs, from left to right in order of number of required characteristic octagon rotations.

Now that we have our octagonal covering motifs, we can begin assembling them into new yet-larger second-order squares and second-order rhombuses. Recall from *Chapter Two* that the order of the layering is governed by the number of rotated characteristic decagons (or octagons, here) in the petal motif. This just means that the rotationally symmetric blue octagonal motif will layer over the "red" here because the red has two rotated characteristic octagons. Likewise, the red motif will layer over the "light blue," which in turn will layer over the "dark blue." Because these specifically are **covering** motifs, it means there is no actual layering yet—they can fit together without any conflict because the characteristic octagons have **already** been rotated. But if we were to replace them all with rotationally symmetric octagonal motifs motifs, like the leftmost motif in ***Figure 3.13***, then their coloring would tell us which layer to put them on. To reiterate, the color of a layering motif does not determine what the motif looks like in isolation, only where it goes in the stack of layers. Likewise, the color of a covering reflects how many of its characteristic polygons have been rotated.

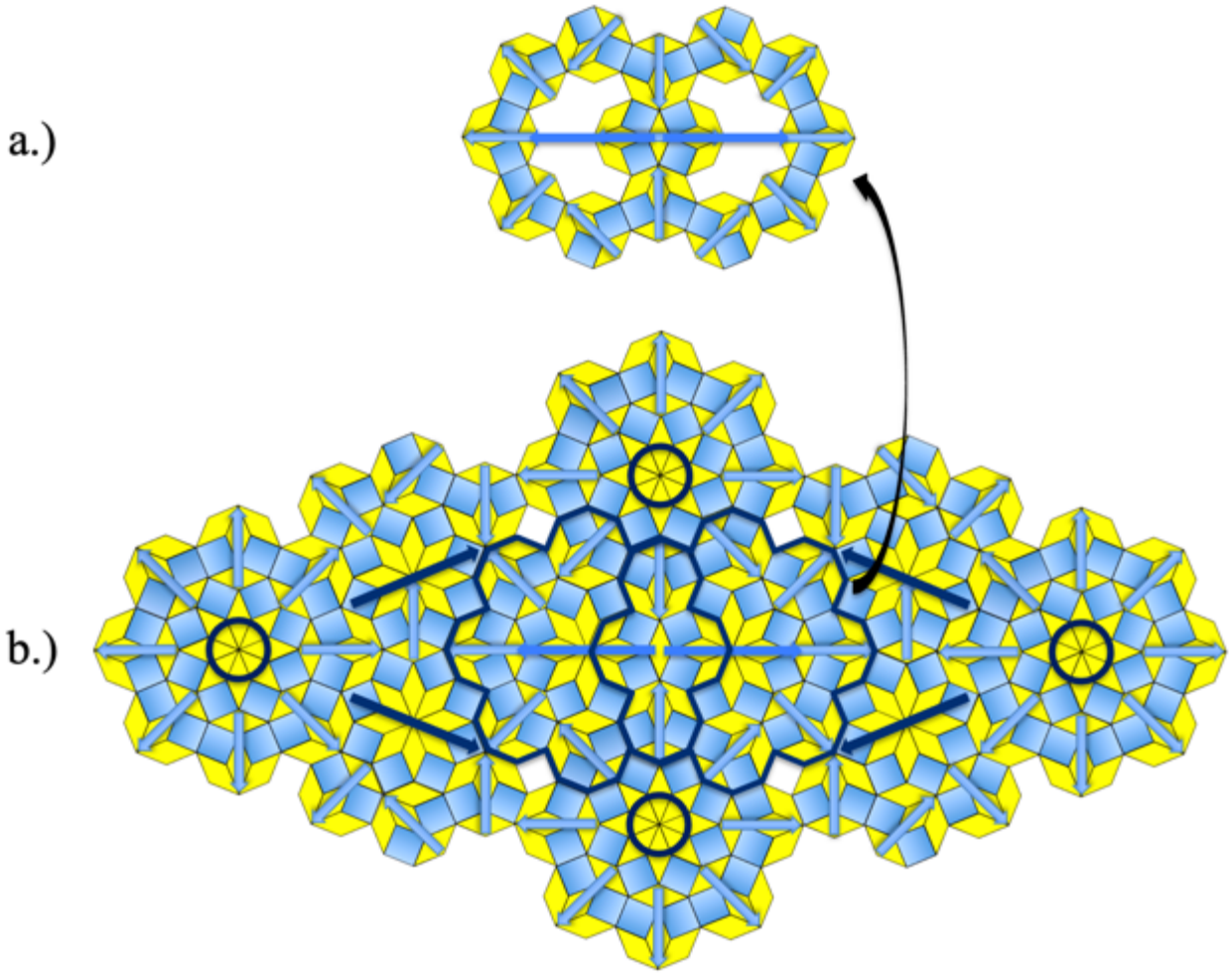


**Figure 3.14:** Four blue (circles), four dark blue, and two light blue (with light blue arrows) octagonal motifs have been used to construct a new second-order rhombus (b). In (a), a detailed view of the two light blue octagonal motifs is provided. The light blue octagonal motif has a different axis of symmetry (the arrow points to the center of a characteristic octagon rather than between two of them), and this image highlights how they connect because of this. If not for this orientation, they would not be able to overlap their outer ring in this manner.

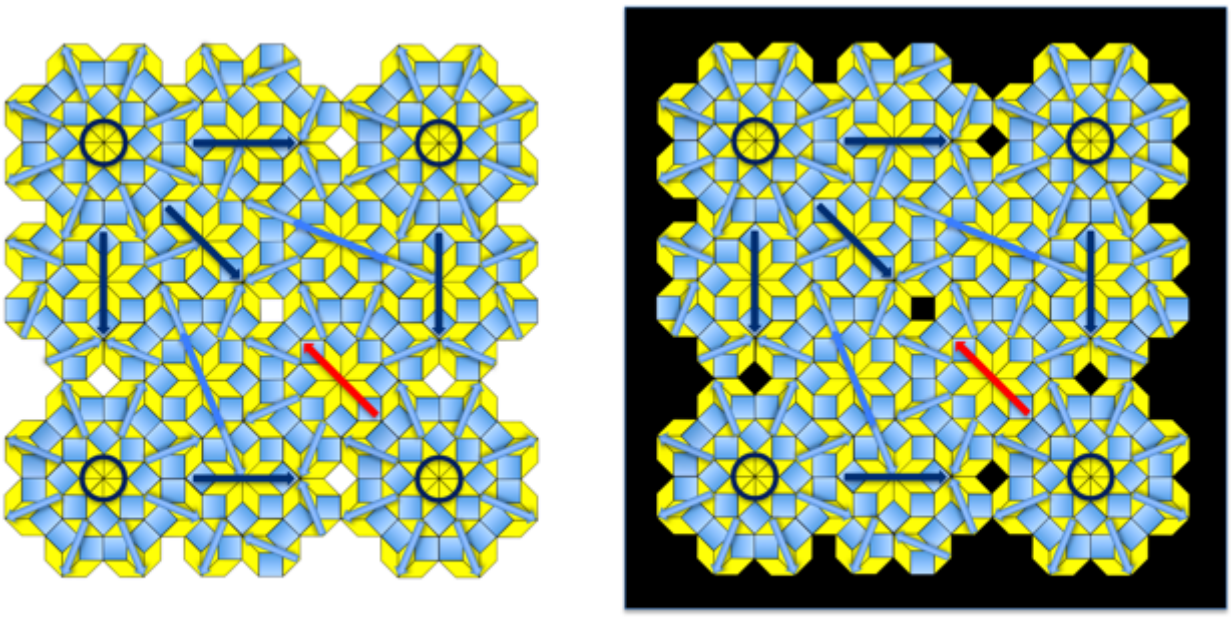

a.) b.)

**Figure 3.15:** The second-order square is made from four blue (with a ring instead of an arrow), five dark blue, two light blue, and one red octagonal motif (a). The layering order is, from top to bottom, blue, red, light blue, and then dark blue. If this order is followed, the tiling motif will be correct. In (b) however, there is obviously a problem as it is not actually a space-filling tiling. There are five square holes in (b)! How do we fix this?

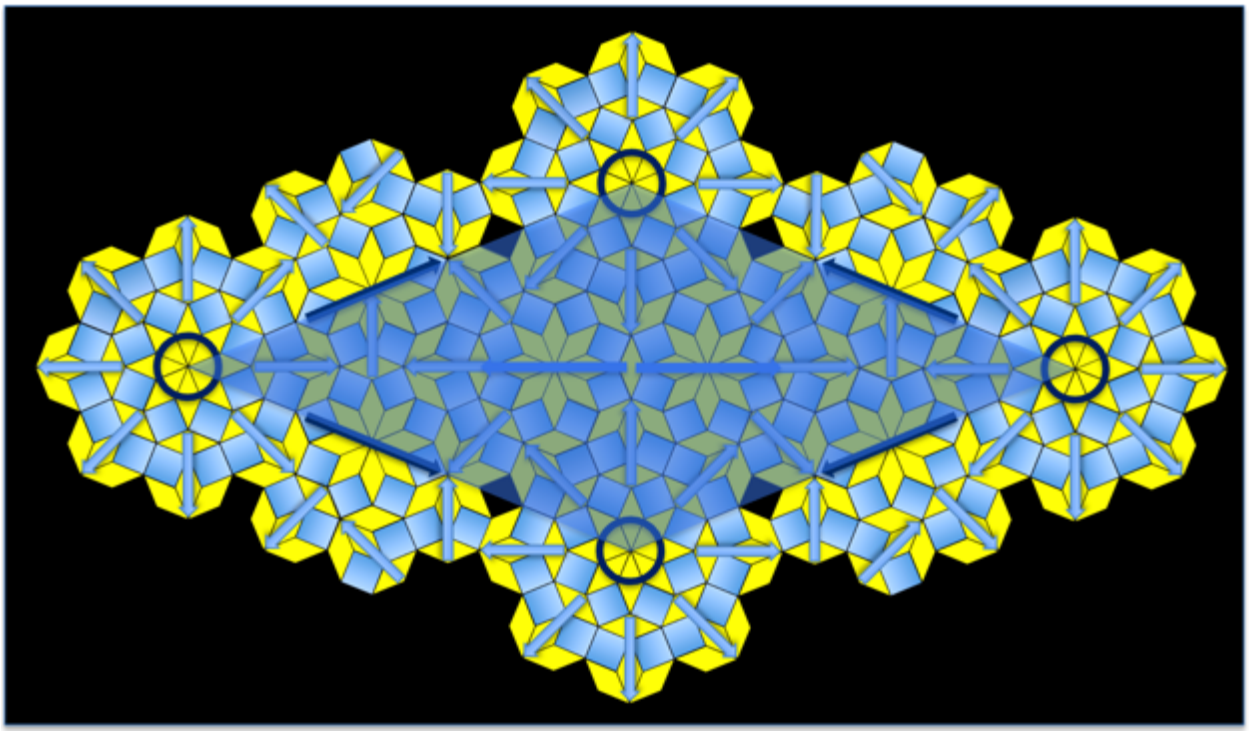

**Figure 3.16:** The new second-order rhombus contains the same square holes as the square in ***Figure 3.15***. There is a larger distance of interaction (which is just the distance between the center of one octagonal motif to the other) that would produce a rhombus-shaped hole, except for the fact that the dark blue octagonal motifs are close by and can fill in this space. This will change later as we consider a different approach.

## Expanding the Octagonal Motif

The layering hierarchy uses these four octagonal motifs to recreate a correct Ammann-Beenker tiling of a second-order square. As noted before, the order of the layering is determined entirely by whichever octagonal motif has the largest number of phason flips in the form of characteristic octagon rotations—this being the bottommost tile. But as we see in ***Figure 3.15*** and ***Figure 3.16***, there is a problem with this octagonal motif set because it is not actually space-filling.

### First-Ring Expansion

There is a simple solution, however, which occurs in several of the quasilattice tilings. We can expand the octagonal motif to include more of the surrounding characteristic octagons. The expansion is shown in ***Figure 3.17***. ***Figure 3.18*** and ***Figure 3.20*** show how to use it.

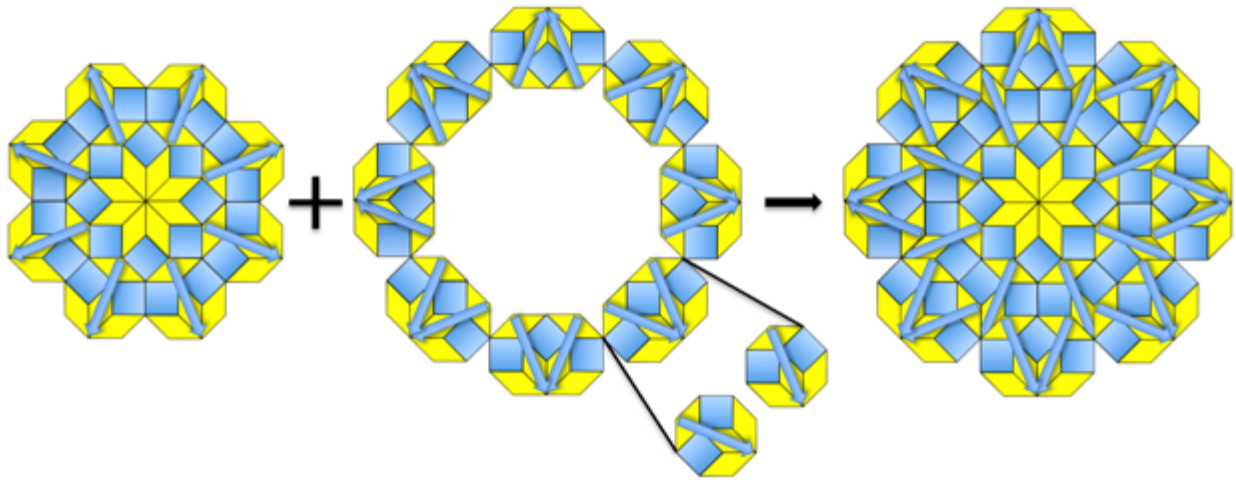

**Figure 3.17:** We can start expanding our octagonal motif by adding a ring of sixteen characteristic octagons around the original octagonal motif—this will obey covering rules. The second ring has eight pairs of characteristic octagons, each of which is a partial covering overlap of two characteristic octagons, shown in the middle figure.

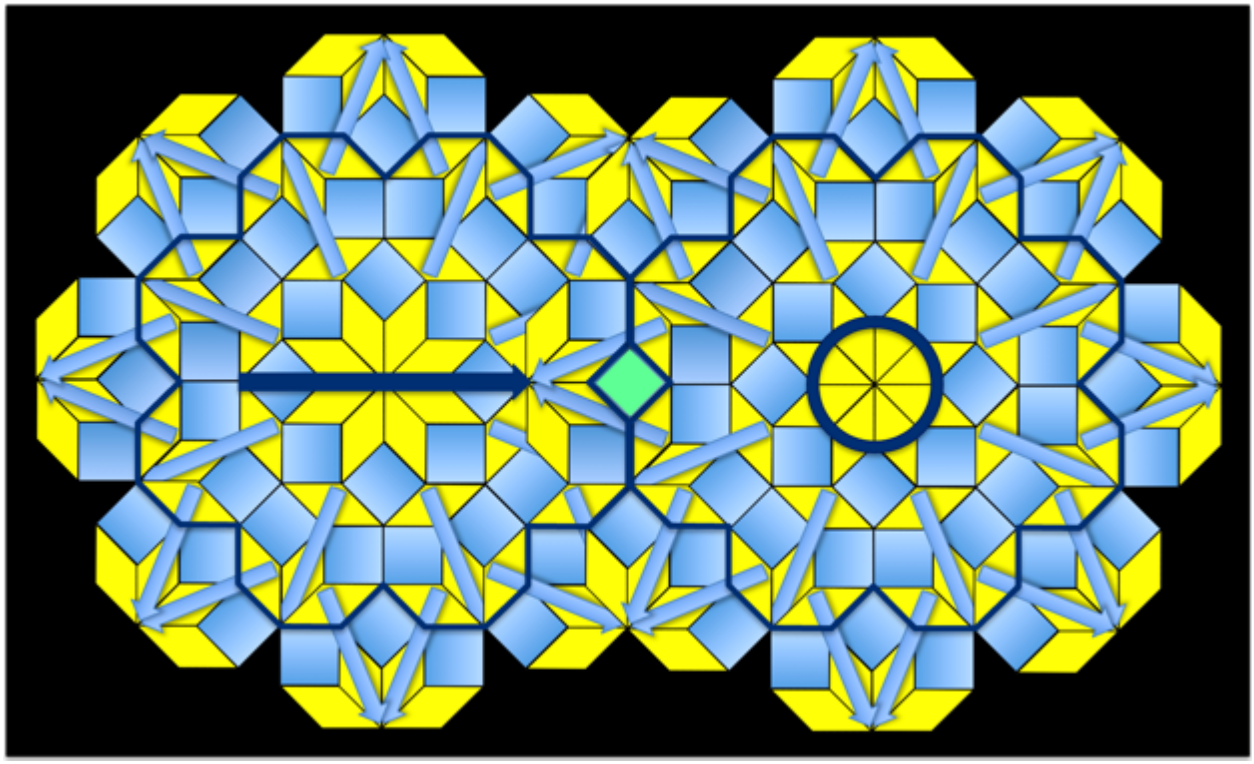

**Figure 3.18:** The holes from ***Figure 3.15*** and ***Figure 3.16*** can be filled in with this expanded ring of characteristic octagons. The square hole is now highlighted with a green square.

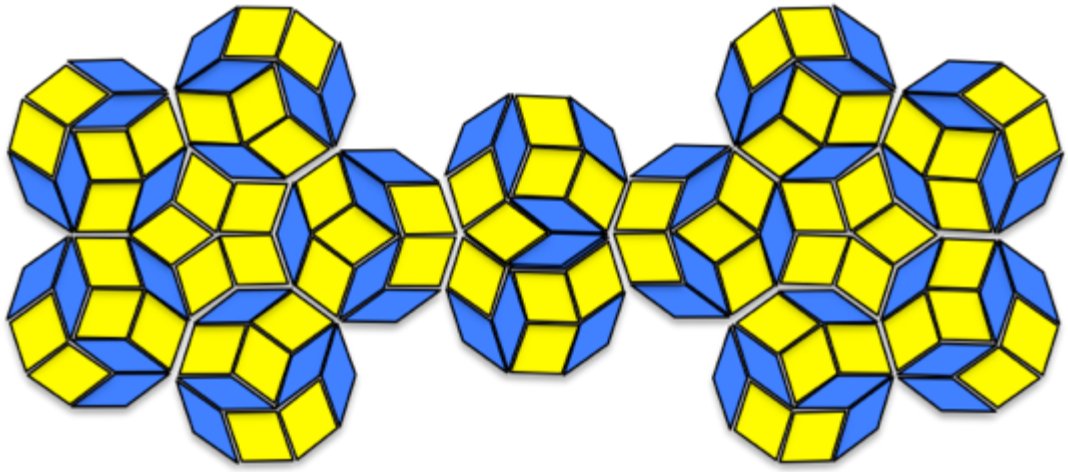

**Figure 3.19:** Interestingly, we cannot perform the same maneuver in the P3 rhombus Penrose tiling. Once additional characteristic decagons are added to the pentagonal motif, an immediate conflict can be generated at the meeting point of two rotationally symmetric "blue" pentagonal motifs. The two overlapping characteristic decagons in the center of the image must belong to either the left or right pentagonal motifs, but they cannot belong to both. So this cannot be a consistent expansion for the pentagonal motifs of the Penrose rhombus tiling—this means that the pentagonal motif is as large as we can make it. This turns out to be true for any of the second or third-ring expansions seen in this thesis—we reach a point where the ring cannot expand anymore without creating conflicts. Fortunately, each tiling becomes space-filling before we reach this ring-conflict limit.

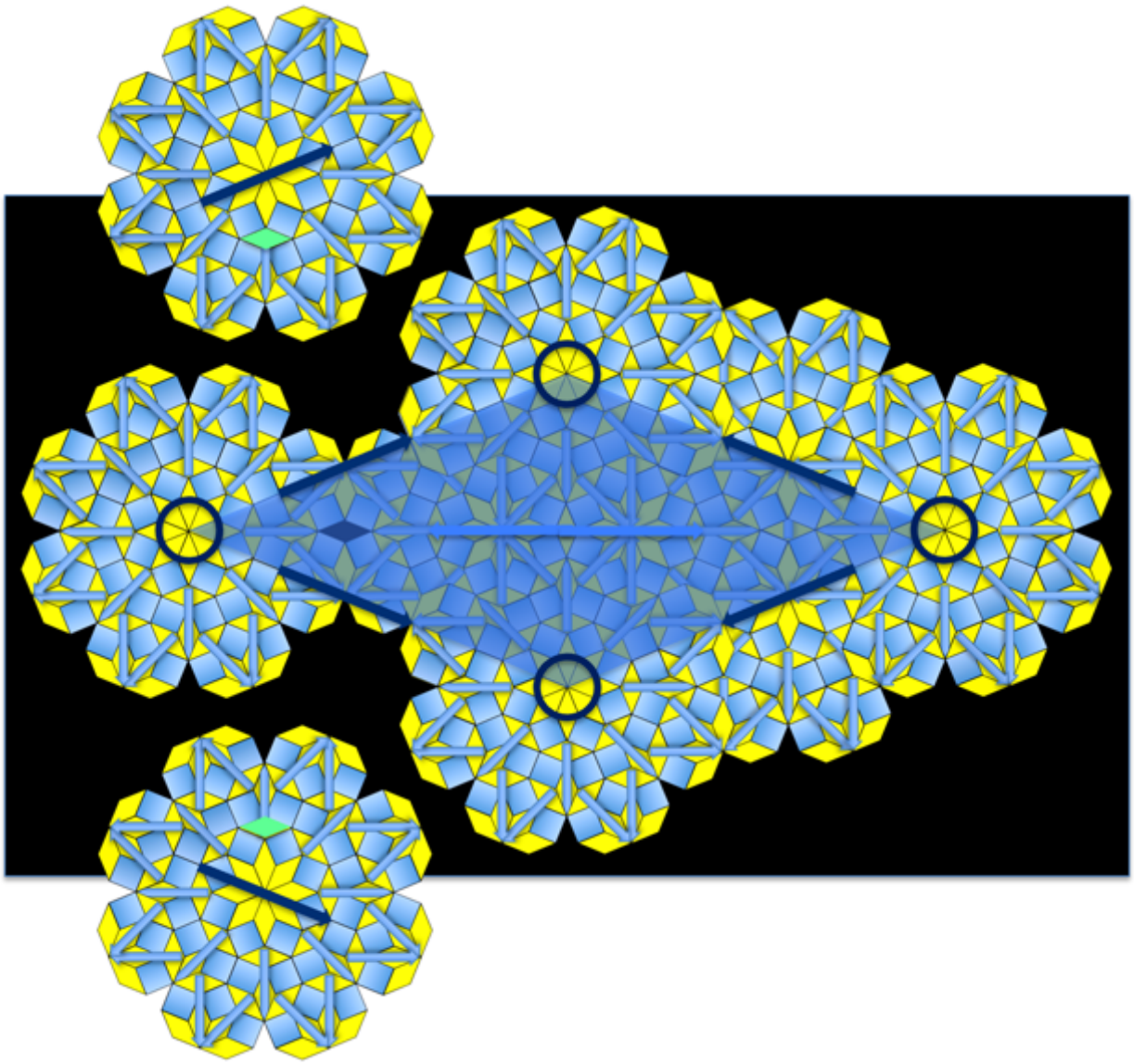

**Figure 3.20:** This image shows the construction of a second-order rhombus made from first-ring octagonal motifs. On the left side, two of the dark blue first-ring octagonal motifs have been pulled out, leading to the creation of a rhombus hole. This shows that for the first-ring octagonal motif construction, the dark blue octagonal motifs are still required. This can be changed, however. Green rhombuses have been colored into the octagonal motifs that were removed, showing which rhombus fills in the hole. In this respect, the dark blue octagonal motif is made entirely from the octagonal motifs that are nearby and the space-filling constraint is satisfied without explicitly requiring it.

### Second-Ring Expansion

In the first-ring expansion, a significant problem with space-filling was resolved by simply expanding the ring to include another ring of sixteen additional characteristic octagons. In this section, we will see that another problem—but one more related to reducing the complexity—can be solved by adding yet another ring of sixteen characteristic octagons (***Figure***

***3.21***). The octagonal motif now contains forty-eight characteristic octagons. A reader might also note that this is actually the **third** ring expansion, as the original octagonal motif already contained two rings (with one being the core), with eight characteristic octagons each. But for sake of clarity, I will just continue referring to it as the second-ring expansion.

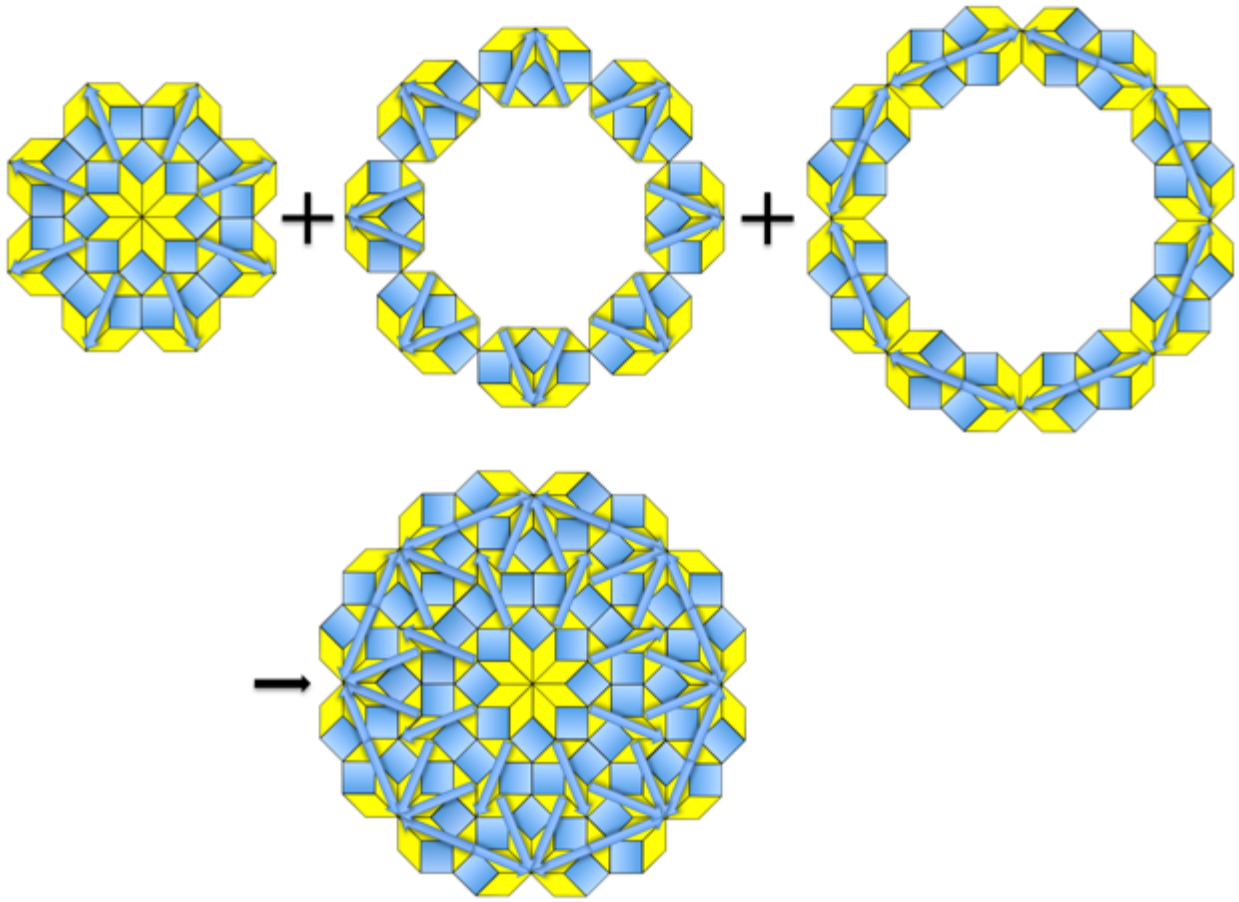

**Figure 3.21:** Unlike the Penrose tiling, we can continue expanding the octagonal motif until it contains not just the first additional ring, which retained the space-filling property, but a second additional ring. This second ring, shown in the upper right corner of this figure, allows the removal of the fourth dark blue octagonal motif, as shown in ***Figure 3.20***.

Expanding the ring out a second time provides an interesting option—it allows us to reduce the total number of octagonal covering motifs from four to three (or equivalently, the number of layers from four to three) (***Figure 3.22***).

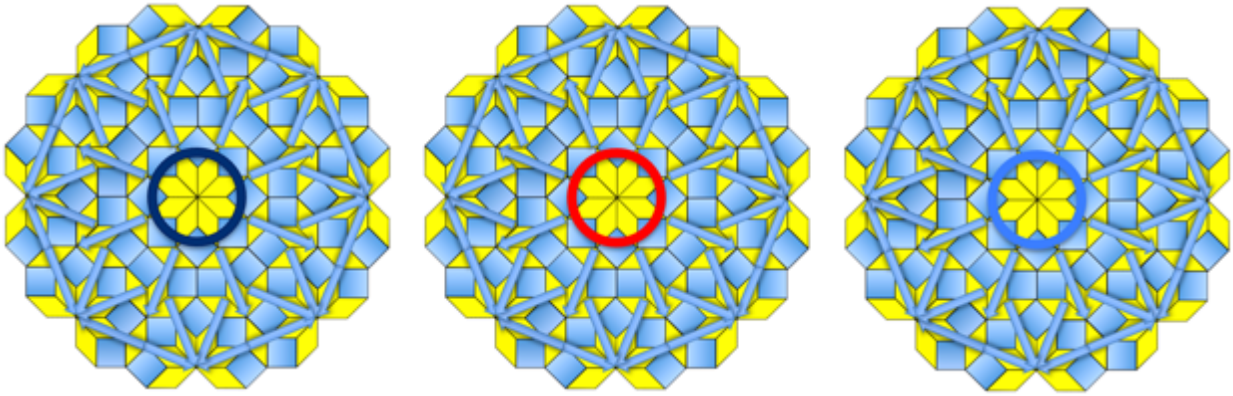

**Figure 3.22:** These three octagonal motifs all have the same tiling, but have been marked with different colors to indicate which layer they belong to. Blue will be in the top layer, red in the middle, and light blue on the bottom.

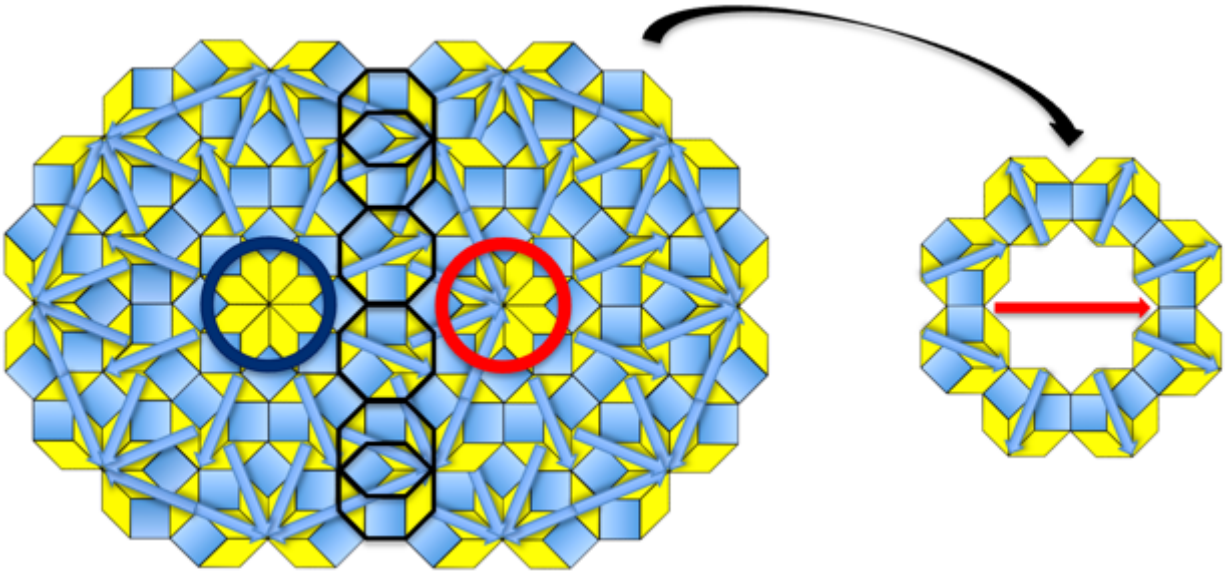

**Figure 3.23:** The second-ring red octagonal motif can be constructed with a dark blue octagonal motif and a red octagonal motif from ***Figure 3.22***. Black octagons highlight the octagons that undergo a phason rotation when this layering is performed. A curious point is that because the red octagonal motif only occurs once in a second-order octagon (***Figure 3.26***), it is quite rare and you may spend quite a while searching for one in any given perfect octagonal quasilattice tiling. The red arrow in the rightmost figure designates the line of symmetry and points in the direction of highest rotational symmetry/fewest number of rotated characteristic octagons.

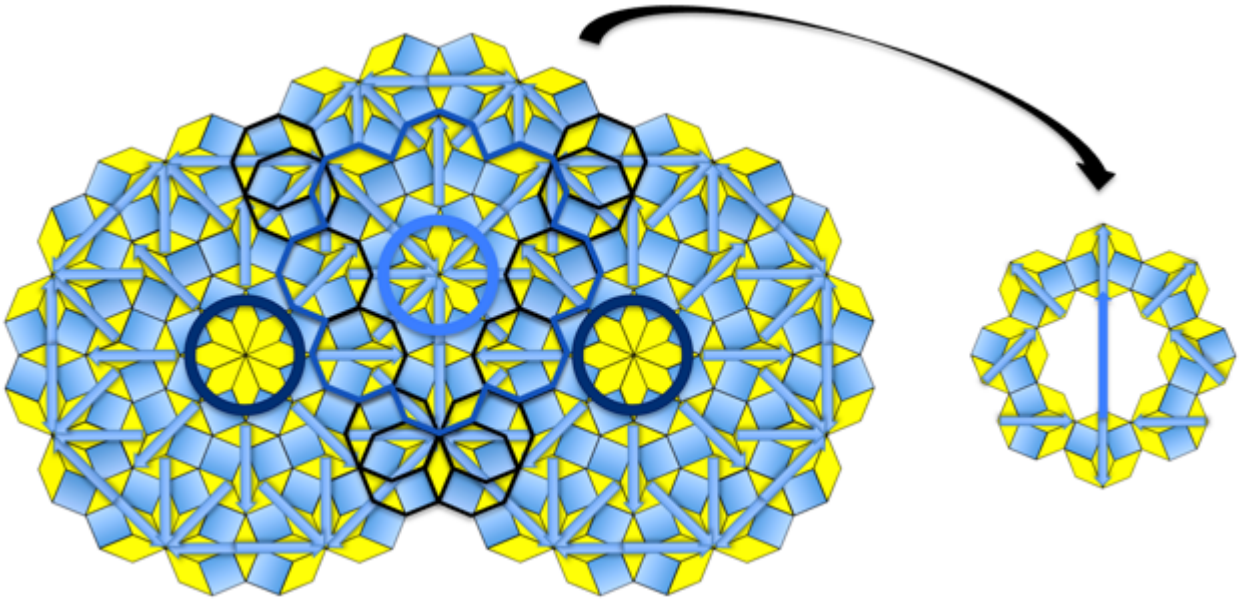

**Figure 3.24:** The second-ring light blue octagonal motif is constructed from two dark blue octagonal motifs and one light blue octagonal motif from ***Figure 3.22***. Black octagons highlight the octagons that undergo a phason rotation when this layering is performed. Two of these light blue octagonal motifs occur in both the second-order square and the second-order rhombus, making them relatively common in a perfect octagonal quasilattice tiling.

Unlike the layerings done with the original octagonal motif (***Figure 3.13***) that produced only two characteristic octagon rotations, the second-ring layerings produce six characteristic octagon rotations (for two motif layerings) (***Figure 3.23, Figure 3.25)***. This line of rotating characteristic polygons will also come into play for the Tübingen triangle tiling, which will be covered in *Chapter Four*.

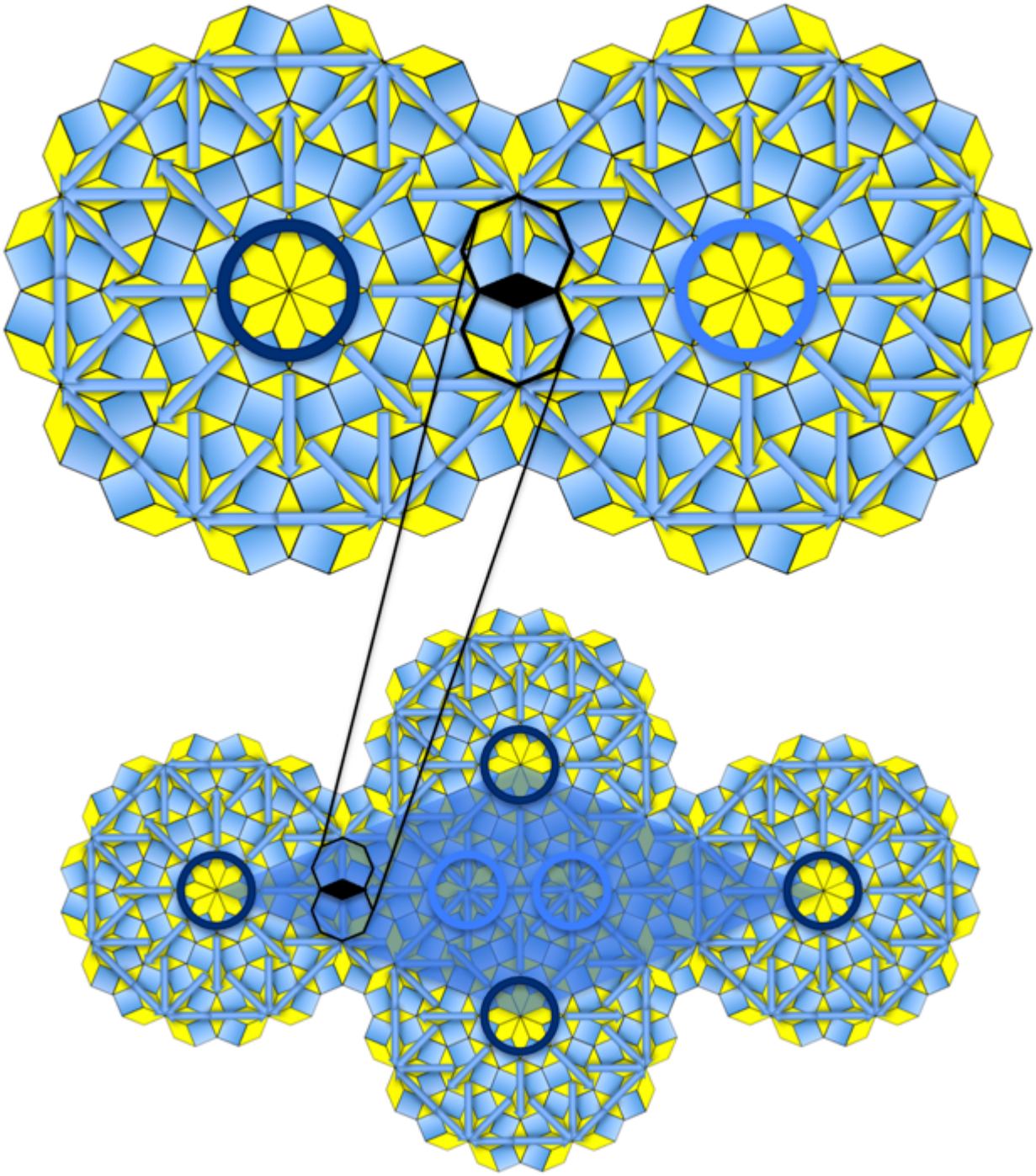

**Figure 3.25:** The space-filling condition is satisfied if second-ring octagonal motifs are used to create a new second-order rhombus.

If we remove the dark blue octagonal motif from our new second-order rhombus creation, a rhombus hole would open, as shown in ***Figure 3.20***, and our second-order rhombus would no longer be space-filling. If, however, we expand the ring like those shown in (***Figure 3.21***), then

this farthest distance interaction between the octagonal motifs can still fill in that rhombus hole, as shown in the dual black octagonal inlays of ***Figure 3.25***. **Since our tiling is still space-filling within the bounds of the second-order rhombus, it shows that the second-ring octagonal motif will bridge the gap and provide a space-filling of the entire tiling when combined with the second-ring square.** Interestingly, this overlap required no rotations of the characteristic octagons. The characteristic octagons that overlap completely, also happen to be in the same orientation. Therefore, at this interaction distance, these two octagonal motifs can co-exist at the overlap without layer modifications—which introduces the concept of a *sublayer.* This property also plays an important role in understanding the Ammann-Kramer-Neri icosahedral quasicrystal, which will be covered in *Chapter Six*. It is important to note how this works in two dimensions, as it will become significantly more difficult in the three-dimensional case. This kind of interaction starts to reveal how dauntingly complex a quasicrystal can become if visualized in less simple ways. After the second-ring expansion of the octagonal motif, no additional rings can be added. The same is true for the Penrose P3 tiling motif at a much earlier radius, as described in ***Figure 3.19***.

The fundamental underlying idea in this process is that there is a single petal motif that overlaps with itself to produce a space-filling tiling—but we must check that it is really space-filling, and fix it if not. To that end, the first ring has been added to our basic octagonal motif. An additional overarching goal in these chapters is to present this process in as simple a way as possible. But of course, the easiest way to understand these concepts is to move the tiles and motifs around by hand in a graphics editor! In this octagonal quasilattice tiling, we see that we can make the octagonal motif more complex by adding another ring of characteristic octagons, and we see that we can remove an entire type of octagonal covering motif altogether (the octagonal motif with the dark blue arrow shown in ***Figure 3.20***). Alternately, we could reduce the complexity of the octagonal motif, and retain the fourth dark blue octagonal covering motif (or layer of blue octagonal motif). I think it is interesting that both approaches work, and it is interesting to me that this process can be taken to different levels for different quasilattice tilings. In that mode of discovery, then, I urge the continuation of this ring addition process until it must stop at a ring conflict (***Figure 3.19***), to give the reader a full appreciation of the ubiquity of this process. But if a reader should prefer having a less complex petal motif and instead have additional covering motifs, then I see no strong reason to object. I do think, however, that

having fewer covering motif coordinates is overall a better choice in this aim of a simple-as-possible description of quasilattice tilings.

## New Second-Ring Polygons

Once we are at the stage of building a new hierarchy of second-order polygons, the next step of construction is relatively simple. We take these second-order polygons and arrange them into the second-order characteristic octagon of ***Figure 3.2***. Once this is done, the entire process repeats cyclically. In essence, this is what a quasilattice is—at least in the context of these chapters. Many methods exist for generating quasilattices, but I propose that none of these let you visualize what a quasilattice actually **is**. The other methods show a hierarchy, through the use of substitution methods, for instance—but what is the global picture? Deflation is like peering through a hole that lets you see more and more of the tiling, but never lets you see the underling structure. The cut-and-project method shows that it can be represented as a cut through a higher-dimensional lattice, but how does this help us understand how to visualize it? Or we also know, for instance, that two crossed periodic lattices, at the right angle, can generate a quasilattice in its moiré pattern, but again, does this help us actually visualize the hierarchical structure? To this end, I have written these chapters in the hope of providing, in addition to opening analysis options, a deeper understanding of the hierarchical structure of a perfect quasilattice.

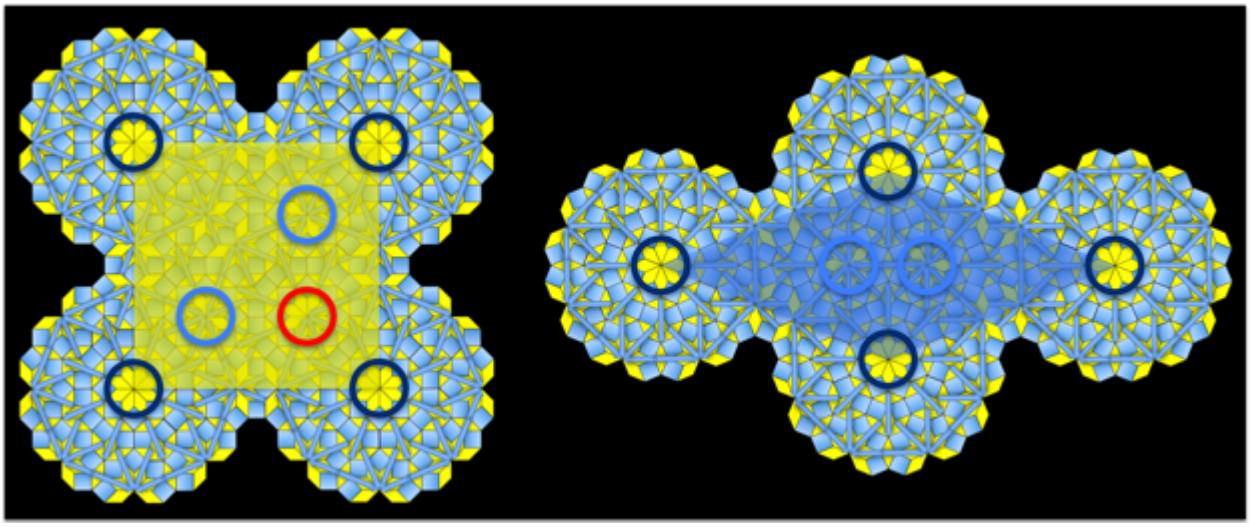

**Figure 3.26:** The three second-ring octagonal motifs from ***Figure 3.22*** can be used to construct a new second-order square and second-order 45°-135° rhombus. This second-order square has four blue, one red, and two dark blue octagonal motifs. The second-order rhombus has four blue, and two dark blue octagonal motifs. A black backdrop has been provided to show that these

shapes are also space-filling within the bounds of the new second-order polygons—the necessary condition to prove the covering or layering will be space-filling.

## The Last Step of the Octagonal Quasilattice Assembly

Like the other quasilattice tilings, this is the end of the cycle. Once we have this new second-order octagon, we can build a new second-ring octagonal motif (***Figure 3.22***). Although the rotationally symmetric octagonal motifs "spill out" from the boundary of the original octagon (made from the centers of the first ring of characteristic octagons around the core), they will still cover together correctly into new second-order polygons. Like the characteristic octagons used for the rotationally symmetric octagonal motifs, the second-order polygons will assemble according to covering rules—each fundamental square or rhombus will match the fundamental square or rhombus below it. Likewise, each of the rings in a given octagonal covering motif will neatly *cover* the rings in another octagonal covering motif. As was the case for *Chapter Two* and *Chapter Three*, assembling rotationally symmetric octagonal motifs into second-order polygons will instead follow layering rules (since they are not coverings). The hierarchical polygon cycle using either coverings or layerings will produce ***Figure 3.27***.

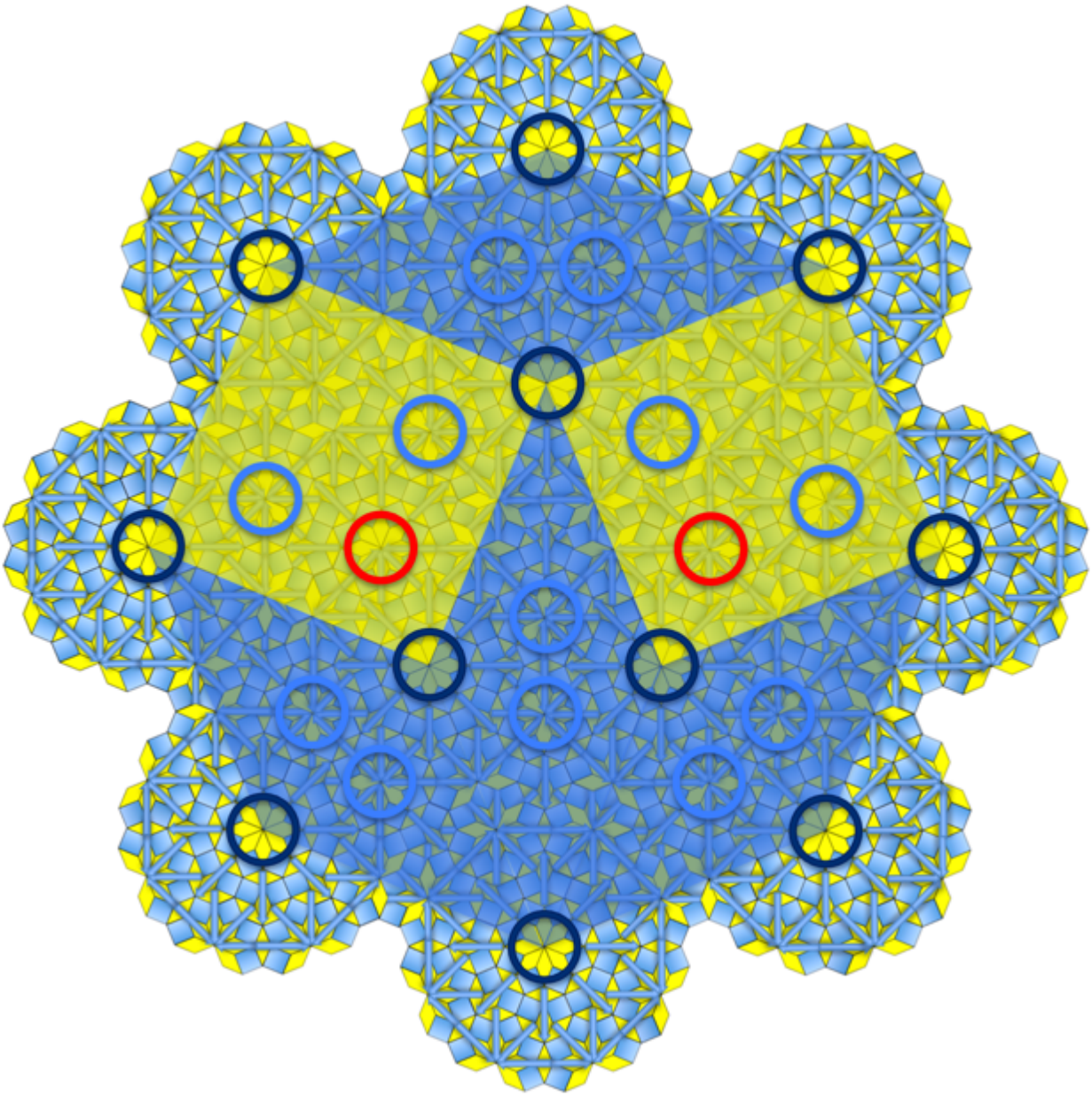

**Figure 3.27:** The final octagonal motif can be constructed from two of the second-order squares and four of the second-order rhombuses from ***Figure 3.25***. If the second-order polygons were assembled as layers and not coverings, the final step must be to put each respective octagonal motif into its correct layer, independent of which second-order polygon was placed first.

The petal motif for the Ammann-Beenker tiling is comparable in complexity to those for the Penrose tilings.

## An Algorithm for Constructing the Ammann-Beenker by Layering

For any reader interested in understanding or programming the Ammann-Beenker octagonal tiling via a mathematical algorithm that uses layering, an abbreviated description has been provided here. Positions, orientations, and translations are given for the assembly and placement of each motif.

***Figure 3.6*** forms the core of the octagonal motif (which is generically referred to as a petal motif). From there, we add a ring of characteristic octagons in ***Figure 3.5***. These two rings overlap by a set of eight rhombuses. The three edge-adjacent rhombuses of the characteristic octagon face inward for the core, and outward for the first ring.

***Figure 3.17*** shows the addition of the next ring, which has sixteen characteristic octagons in total. The sixteen octagons are arranged into pairs, each of which overlaps the hexagon outlined in ***Figure 3.29***. When placed over the core and first ring, there are sixteen rhombus overlaps in total.

If we want to use three instead of four types of petal motif, we can expand it again with another ring, as seen in ***Figure 3.21***. This ring has sixteen characteristic octagons, arranged into eight pairs. Each of these pairs are arranged such that the vertices of the characteristic octagons with three edge-adjacent rhombuses will mutually point away from each other. These are then formed into a ring which overlaps with the second ring, such that there are sixteen total hexagon overlaps.

### Formation of the Second-Order 45°-135° Rhombus

The second-order 45°-135° rhombus is formed by first taking a second-ring octagonal motif (***Figure 3.22***) and rotating it (CW or CCW) 45°/2 (the rhombus star in the core now has rhombuses with vertices that point straight up and down). Copy this 1st octagonal motif and translate it a distance of $7 + 5\sqrt{2}$ at an angle of 45°/2 above the horizontal. Copy this 1st octagonal motif again and repeat this translation distance for an angle of 45°/2 **below** the horizontal. Take the 2nd octagonal motif and translate it the same distance at an angle of 45°/2 below the horizonal. These four octagonal motifs form the vertices of the new second-order rhombus. They are all on the top of the layering—they are all rotationally symmetric, corresponding to the octagonal motif with the dark blue circle.

If the edge length of the 45°-135° rhombus has a unit length of one, then the long axis has a length of $5\sqrt{2+\sqrt{2}}$ and the short axis has a length of $5\sqrt{2-\sqrt{2}}$ [27]. To place the 5th and 6th octagonal motifs, we will copy the 1st octagonal motif. Translate it to the right by $2\sqrt{2-\sqrt{2}}+5\sqrt{2+\sqrt{2}}$ [28]. This is the location of the first interior octagonal motif. Copy the 1st octagonal motif again and translate it to the right by $\sqrt{2-\sqrt{2}}+2\sqrt{2+\sqrt{2}}$ to place the second interior octagonal motif. These two octagonal motifs sit on the third level of the layering—the second-order rhombus has no octagonal motifs that belong to the second level. The second-order rhombus is now complete.

**Formation of the Second-Order Square**

Begin with the octagonal motif from ***Figure 3.22***. Copy and translate it by $7+5\sqrt{2}$. Copy the 1st octagonal motif again and translate it $7+5\sqrt{2}$ to the right. Copy this 1st octagonal motif again and copy it to the right by $7+5\sqrt{2}$ and up by $7+5\sqrt{2}$. These four octagonal motifs will all sit on the first layer and form the vertices of the new second-order square (***Figure 3.26***).

The second-order square has seven octagonal motifs, four of which are vertices and three of which are internal. To place these internal octagonal motifs, we first copy the 1st octagonal motif. Translate it by $3+2\sqrt{2}$ at an angle of 45° above the horizontal. This octagonal motif will sit on the third layer. For the second internal octagonal motif, copy the 1st octagonal motif again and translate it by $7+5\sqrt{2}$ at an angle of 45° above the horizontal. This octagonal motif will also sit on the third layer. Lastly, copy the 1st octagonal motif again and translate it by $2\sqrt{2-\sqrt{2}}+5\sqrt{2+\sqrt{2}}$ at an angle of 45°/2. This final octagonal motif will sit on the second layer. This completes the construction of the second-order square.

**Creating the Second-Order Octagon**

This section will show how to assemble the second-order octagon of ***Figure 3.27***. We will start with the second-order square as oriented in ***Figure 3.26***. Rotate this square CW 45°/2. Copy this 1st square and rotate it again by CW 45° with respect to the bottom right vertex (closest to the octagonal motif with the red circle). Next, translate this copy of the square by

[27] The silver mean has a value of $1+\sqrt{2}$ so it is not surprising to see that the dimensions involve $\sqrt{2}$.

[28] These distances are found with the trigonometric half-angle formulas for sine and cosine.

$2\sqrt{2-\sqrt{2}}+5\sqrt{2+\sqrt{2}}$ to the right with respect to that bottom right vertex[29]. This will place the two second-order squares onto the second-order octagon. The two second-order squares will share a single top vertex, which can be taken as the origin (0,0).

Next, take the second-order rhombus from ***Figure 3.26*** and rotate it by 90° so that its 45° vertices point straight up and down. Place the second-order rhombus so that its top vertex overlaps the single vertex that the two squares already share[30]. Copy this second-order rhombus and rotate it CCW 45° with respect to its bottom vertex[31]. Copy this second-order rhombus again and rotate it CW 45° with respect to its bottom vertex. Finally, copy the first second-order rhombus again (the vertically aligned second-order rhombus with the top vertex located at (0,0)), rotate it by CCW 90° with respect to its top vertex and then translate it left by $7+5\sqrt{2}$ at an angle of 45°/2 above the horizontal. This completes the construction of the second-order octagon.

The Ammann-Beenker tiling is assembled in much the same way as the Penrose rhombus tiling. One notable difference is that the octagonal motifs with the dark blue circles—corresponding to the octagonal motifs with the highest degree of rotational symmetry—always sit on a vertex of the higher-order square-rhombus network and there is no vertex without one. The Penrose rhombus tiling differs in that although the pentagonal motifs with the highest rotational symmetry do sit on vertices of the higher order rhombus network, there are many vertices without one.

## Phasons and Octagon Rotations

In a covering, overlaps must match top and bottom. The core of the motif in ***Figure 3.7*** was created by this kind of overlap. In ***Figure 3.9***, however, we suspend this rule to instead create a layering. The layering protocol, as described in previous chapters, allows the top and bottom tiles to not match, **but only if they take the form of a complete octagon overlap**.

---

[29] Alternately, you can copy the first second-order square, rotate it CW 45° with respect to its center, and then translate it to the right by $3\sqrt{2-\sqrt{2}}+8\sqrt{2+\sqrt{2}}+\frac{\sqrt{2-\sqrt{2}}+\sqrt{2+\sqrt{2}}}{2}$ (the total of which is half of the vertex-vertex diameter of the second-order octagon).

[30] Alternately, place this vertically aligned rhombus so that its center is at (0,0), and translate it down by $2.5\sqrt{2-\sqrt{2}}+6\sqrt{2+\sqrt{2}}$).

[31] Located at $5\sqrt{2-\sqrt{2}}+12\sqrt{2+\sqrt{2}}$.

Consequently, the **layering produces an effective rotation of the octagon** in question. When we take an octagonal petal motif and rotate specific sets of characteristic octagons—those that overlapped completely between the two sets of rings in each respective petal motif—a special scenario is created whereby new correct petal motifs are generated. **Partial overlaps, alternatively, will obey covering rules.** Because of the special nature of the characteristic octagon, partial overlaps are possible which do not require a re-orientation of the characteristic octagon. In two dimensions, this is relatively clear to understand. It is important to understand it here, however, as the situation will become more complex when we later consider the three-dimensional analogues in the Ammann-Kramer-Neri (AKN) tiling. **Partial overlaps of fundamental polygons/polyhedra do not require a re-orientation with respect to one blue petal motif, but full overlaps will.** This is a special feature of quasitiling motifs and appears to be largely responsible for what allows their unique existence.

**Octagonal Tiling Phason Flips**

In the case of the octagonal tiling, we see that the octagons rotate by 135° during a layering. As seen from previous chapters, this is no coincidence—this is the internal angle of an octagon.

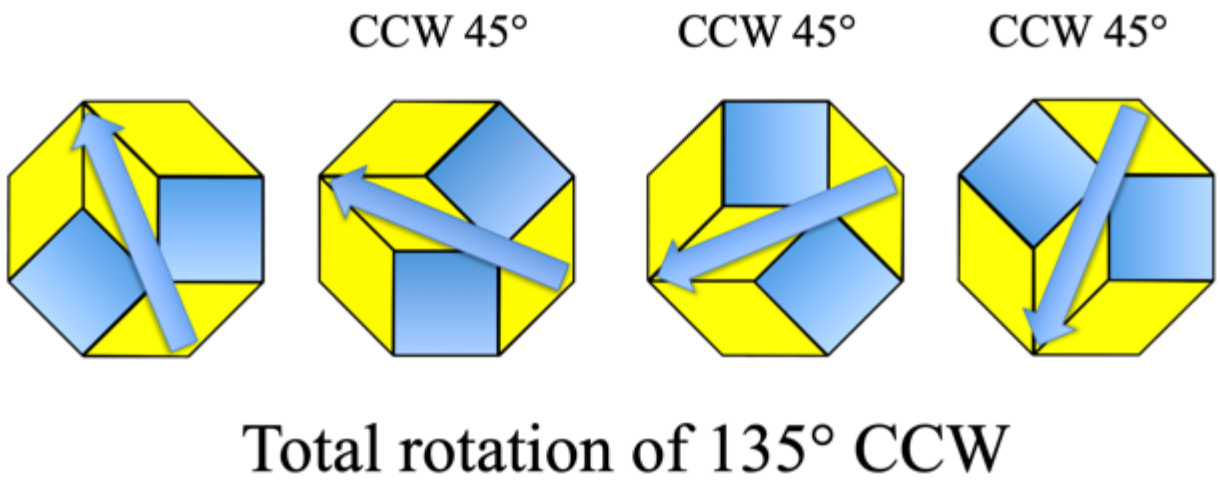


**Figure 3.28:** Rotating an octagon by 135° will reproduce the rotation seen when layering two octagonal ring motifs.

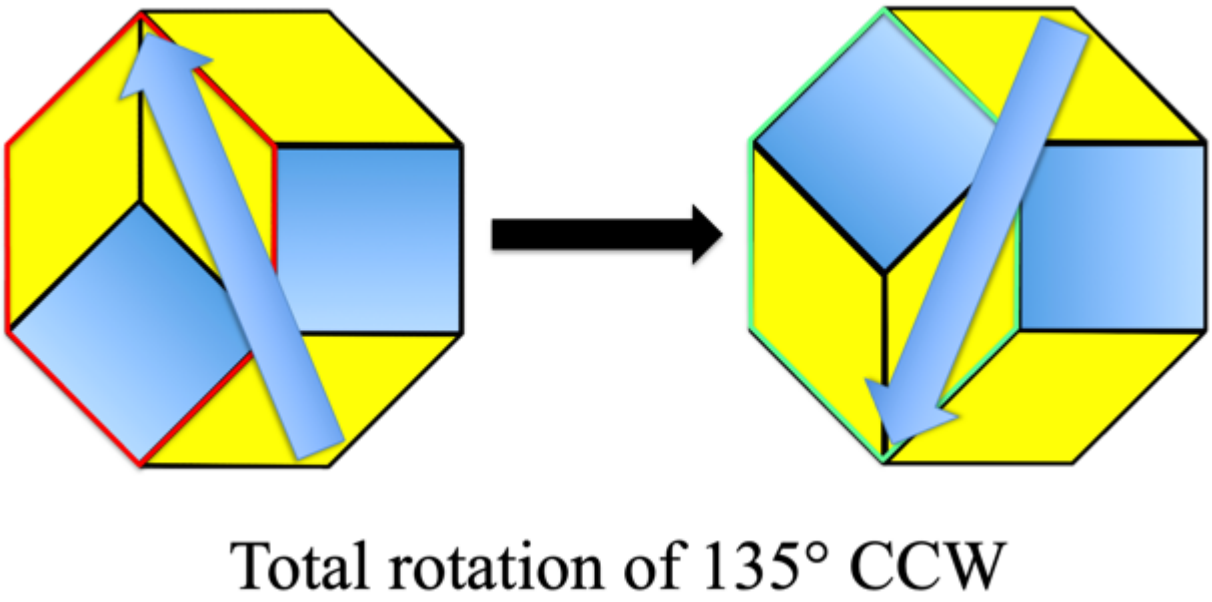


**Figure 3.29:** The 135° octagon rotation produces the phason flip of the Ammann-Beenker tiling. One of the internal hexagons (red and green outlines) experiences a 180° rotation, which is the phason flip for this tiling.

A phason flip can be seen in as a 180° rotation of a hexagon (two rhombuses and a square), or as a flip of the single vertex inside of the hexagon. Ring overlaps, as we saw in *Chapter Two*, produce the unit of phason flip for that tiling. We can also think of phason flips as what create the other octagonal motifs from the default "blue" motif. Now that we have the "red" motif, we can go on to create the others by layering on additional rings (***Figure 3.10*** and ***Figure 3.11***).

## Conclusion

In conclusion, we see that the hierarchical polygon cycle can be successfully applied to the Ammann-Beenker tiling, either via layering or covering motifs. A new concept—rings—has been added to the method to maintain the space-filling characteristic of the quasilattice. Although adding a ring increases the complexity of the petal motif, it reduces the number of petal motifs (or layers) needed for the total assembly, thereby reducing the complexity along another dimension. Rings can be added until there is a *ring conflict*, where the two petal motifs on the top (blue) layer have been expanded too far and create a mismatch in the tiling. This tradeoff presents an interesting opportunity for adjusting the level at which we understand the tiling. We can make the tiling from a more complex petal motif with fewer covering motifs (or

layers), or we can make it from a simpler petal motif with more covering motifs (or layers). In either case, the hierarchical polygon cycle works and we can use it to understand the fundamental idea behind creating a quasilattice tiling.

This chapter also introduced a concept in ***Figure 3.12*** that proposed a possible geometric origin for the number of covering motifs (or number of layers). In the construction of the petal motif, there are only so many ways of attaching new petals before creating incompatible overlaps between petal motifs, and this may underlie the origin of the layer number. All of the tilings in this thesis follow this general rule.

In the next chapter, we will look at the most complex 2D tiling in this thesis—the Tübingen triangle tiling. This tiling has 13 covering motifs, rings, and chirality, but there are no further concepts developed.

## Chapter Four

## A Layering Construction of the Tübingen Triangle Tiling

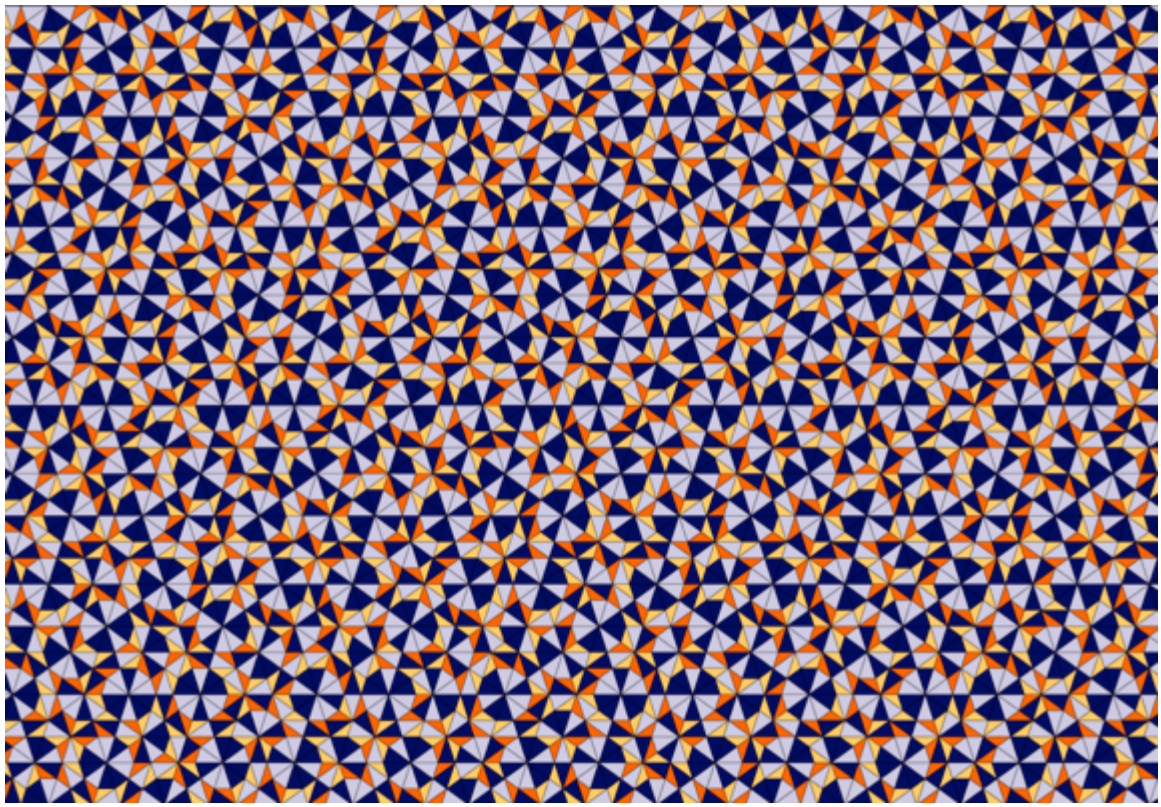

**Figure 4.1:** The Tübingen triangle tiling as shown in the Tilings Encyclopedia which can be found at https://tilings.math.uni-bielefeld.de/substitution/tuebingen-triangle/

## Introduction

As in *Chapter Two* and *Chapter Three*, the goal of this chapter is to show that the hierarchical polygon cycling works, either via covering or layering, and that it can greatly simplify our understanding of quasilattice tilings by explaining the tiling in real-space terms. Concepts that were previously largely restricted to hyperspace descriptions are also given real-space meaning in a non-arbitrary fashion—the real-space description of the phason falls naturally out of the layering model, for instance. The Tübingen triangle tiling is certainly one of the more complicated tilings that is analyzed in this thesis. The tiling has two types of covering pentagon,

for instance, and each type has a chiral twin. This will be the first chapter in this thesis to cover a tiling with either of these properties. The petal motif is then made from both kinds of pentagon and both of their chiralities, leading to a particularly complex form. Like the Ammann-Beenker tiling before it, we will make use of the ring concept to expand the petal motif and ensure that it fills space. The thirteen coverings (or layers) in the Tübingen triangle tiling thus present some interesting features for the model.

The Tübingen triangle tiling is fairly ubiquitous across many types of decagonal quasicrystals. It is an axial (quasiperiodic in 2D but periodic along a single 3D axis if in a real material) quasilattice. It has two primary presentations as tilings—one with two types of triangles, and another as a degenerate case, containing no triangles, which can be seen in simulation (Damasceno et al., 2017; Engel & Trebin, 2008; Ryltsev et al., 2015), experimental research (Burkov, 1991; Duneau & Gratias, 2007) and even in nature (Bindi et al., 2015). The latter has only been found in a specific type of chondrite meteorite (Bindi et al., 2015).

## Gummelt Motifs

Gummelt proved that the Penrose tiling contains a constant shape in the form of an extended decagonal patch which covers the infinite tiling (Gummelt, 1996). The Tübingen triangle tiling has a similar property, but has two covering structures instead of one (Gähler, 2000). Inspired by the previous work in this thesis to create a real-space model of the Penrose tiling, and motivated by collaborative work that was done with a Tübingen triangle 3D-axial quasicrystal simulation (quasiperiodic in XY and periodic in Z) (Han et al., 2021), I set out to create a similar real-space model for the Tübingen tiling. In analogy to the Penrose tiling, I first looked for the most rotationally symmetric cluster I could find, which is illustrated in detail later in the chapter. I then took a large ideal tiling and broke it up into many similar structures that overlap in such a way that the clusters match each other at each level. Like the Penrose tiling, these other structures can be generated as rotations of the outer pentagons that form the new decagonal ring motif. By allowing these outer pentagons to overlap, a covering of the ideal Tübingen tiling can be created. Not only that, but a *layering*, discussed previously for the Penrose tiling, can also be produced.

A real-space model for a quasilattice holds significant promise for developing intuition for quasicrystal phenomena, and it is important to show that it also works for the Tübingen tiling. To do this, we want to find a candidate for this new tiling that has the same general properties as

the Penrose tiling. These new properties are that (1) the entire tiling can be described with this one motif. (2) The motif overlaps with itself and changes, using phason flips, into the other cluster motifs seen in the tiling. (3) These clusters together will create new base motifs from which the original layering cluster was constructed, thereby enabling the construction of a yet-larger tiling. (4) This process can be repeated indefinitely to yield the infinite perfect tiling.

As shown by Gummelt (Gummelt, 1996), there is a surrounding region that is constant for each of these decagons, including two of the ten pentagons that also surround each decagon—illustrated and discussed later in the chapter. Because of this, we note an asymmetry in the decagon's local environment, which we can represent with an arrow facing to the left of the lone dark blue golden triangle. These pentagons also come in two chiral types.

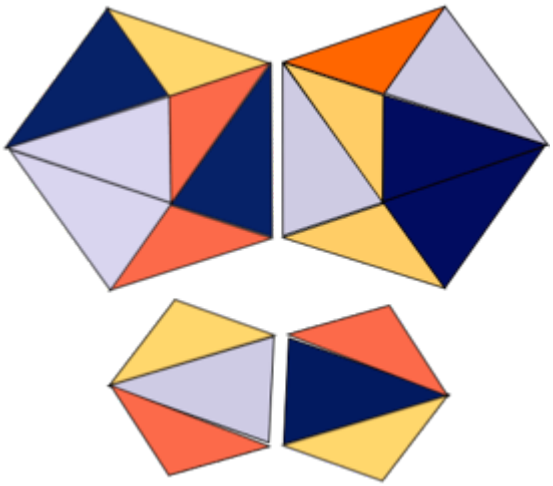

**Figure 4.2:** These are two pairs of chiral pentagons made from golden triangles and golden gnomens. The mirror image triangles, grey and dark blue, or orange and yellow, reflect the different but chiral ways that these triangle pairs are deflated.

As noted by Gummelt, two of these pentagons are constant for each of the decagons, but the others are variable, so no consistent Gummelt motif could be created. However, in analogy with the Penrose and other quasilattice tilings, we can still use either the covering model, where different clusters (most research is focused on finding **one** or **two** covering motifs) can be converted into each other through phason flips, or the layering model, where clusters exist on different layers or sublayers depending on what phason flips are necessary to bring them up to the "surface" of the layering stack.

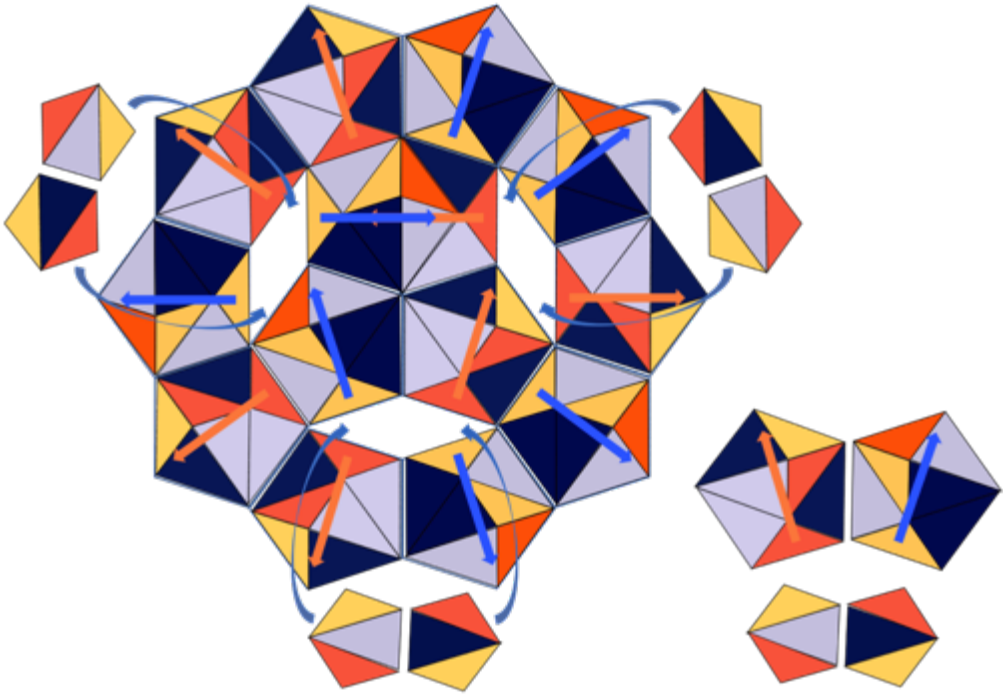

**Figure 4.3:** The two types of covering pentagon can be used to construct a larger decagon. The figure on the left is made from the four figures on the right, which itself contains a large and small pentagon along with their mirror twins. This chapter shows that the entire Tübingen tiling is made from the figure on the left (as a *layering*), and so it would follow that the four pentagons on the right constitute a covering for the tiling.

As noted previously, the Tübingen triangle tiling has two covering motifs instead of one. The orange and purple arrows have been added to help guide the eye with regard to orientation, and have been placed in such a way that, for the outer ring of ten pentagons, all of the arrows point outward for the illustrated cluster. This satisfies the requirement that the base, or "blue" decagonal motif, has the highest degree of rotational symmetry among all of the decagonal covering motifs. The reasoning behind this relates to the layering model and will be discussed later in the chapter.

The Tübingen is somewhat deceptive, as it is possible to create a set of five tiles which, at first glance, look as though they produce a covering. The first tiling motif, the "blue" tile, has the highest degree of rotational symmetry with respect to its phason units—the fat Penrose rhombus made from two golden triangles and two golden gnomens. It is also interesting to note that because the deflation is chiral, we can envision a tiling that has a right-handed deflation protocol instead of the left-handed one that exists in the Tübingen tiling. Specifically, this means

that although the simplest level of tiling is mirror symmetric, any higher order deflations of clusters will break mirror symmetry with additional chiral forms. These clusters are all interchangeable with each other by performing a phason flip. The phason flip[32] in the Tübingen tiling is known from the literature (Suck, 2002). The phason flip, like many other phason flips in other quasilattices, is executed by a 180° rotation of the composite prototile. We start with the blue motif, which is the decagonal motif with the highest rotational symmetry, and phason flip the top rhombus into a "red" cluster.

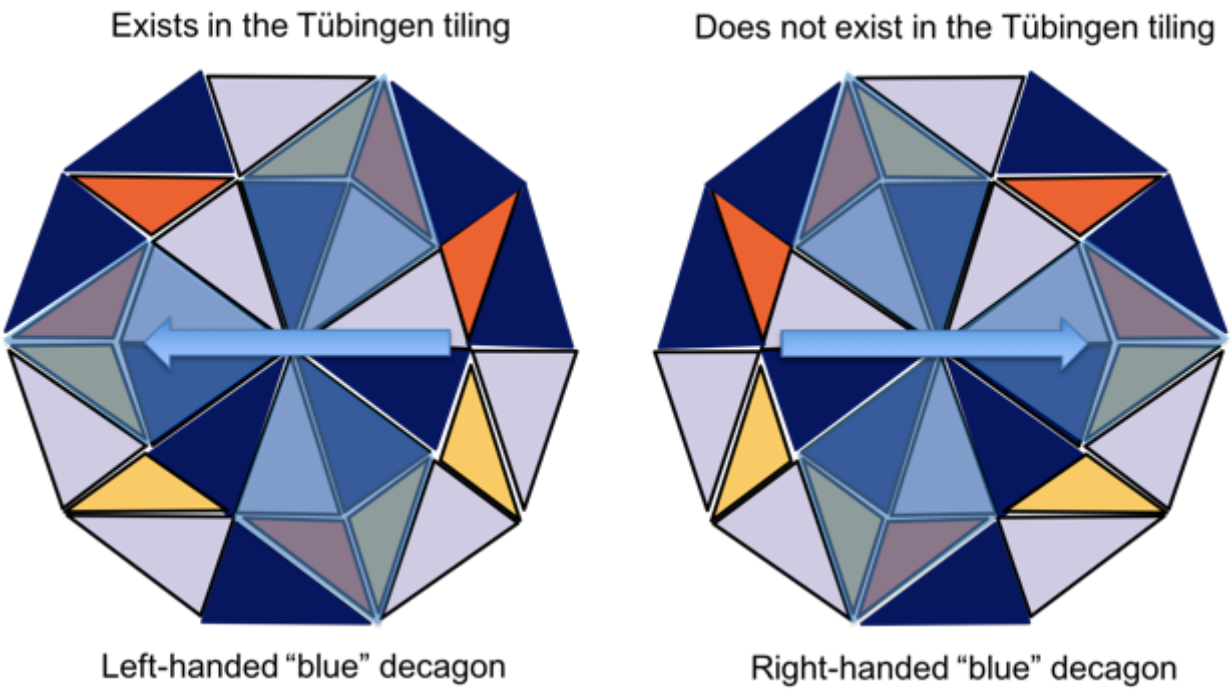


**Figure 4.4:** Two chiral versions of one primary motif in the Tübingen tiling are shown. The left image occurs in the tiling, whereas the right does not. A tiling made from the right-handed tiling is possible. Blue rhombuses highlight the tiling motif that can be flipped as a phason, and also serve to guide the eye.

In ***Figure 4.4***, the blue arrow has been chosen to point left, along the mirror axis of the rhombus phason units. The phason units are rhombuses made from all four types of golden triangle and golden gnomen (highlighted in blue in ***Figure 4.4***). Because of this symmetry, I can

[32] Although phason flips naturally emerge from the layering picture, it is helpful to first apply the simple literature phason concept to some simplified examples. Both phason flips and petal motifs are more complicated in the real analysis presented later in the chapter, so it is worthwhile to see the concept explored here first.

create a mirror-flipped tile which points to the right with respect to its chiral decoration. This right-handed configuration does not exist in the left-handed Tübingen tiling. Additionally, since the vertex configuration is the same, this difference would only be apparent at the next order of deflation. Said more explicitly, the different colors of golden triangle represent different ways of deflating the tile—not an intrinsic difference in the tile itself. But since the quasicrystal tiling is an infinitely recursive structure, these tiles are necessarily different colors in that representation. Interestingly, a similar chiral duality exists in the Ammann-Kramer-Neri tiling, **but both chiral forms are used in the construction**.[33] **The Tübingen tiling is therefore our first exposure to the partial use of chirality in a quasilattice.**

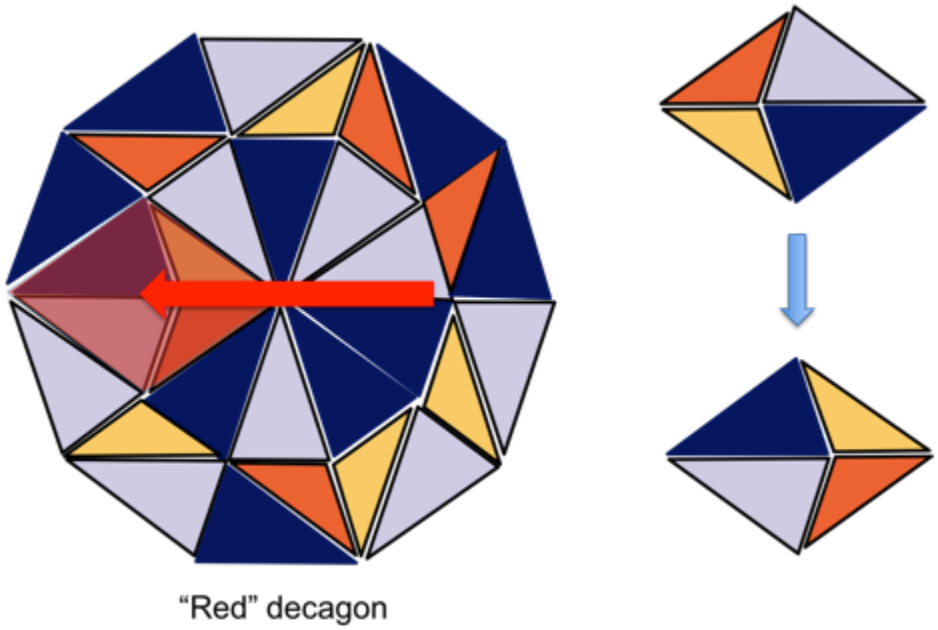


**Figure 4.5:** This motif has been created by simply flipping (highlighted in red) one of the rhombus units by 180°. It is second in the hierarchy of decreasing rotational symmetry.

[33] It may be interesting to some readers to note that the Tübingen tiling is actually a cross-section of the Socolar-Steinhardt tiling of the icosahedral quasicrystal. This icosahedral tiling is generated from a cut through an FCC hypercubic lattice, as opposed to a cut through a simple cubic lattice that generates the Ammann-Kramer-Neri tiling. A reader familiar with the Tübingen tiling can find some beautiful and familiar illustrations of the Socolar-Steinhardt tiling in Madison (A. E. Madison, 2014).

Now, keeping that first rhombus flipped, we choose either the left or right side, to create either a left-handed green decagon (pale green), or a right-handed green decagon (bright green). Unlike the Penrose tiling, the Tübingen tiling contains chiral proto-tiles, and so will contain chiral composite tiles. At this level of description, the tiling contains only two types of chiral cluster, but there are more to follow.

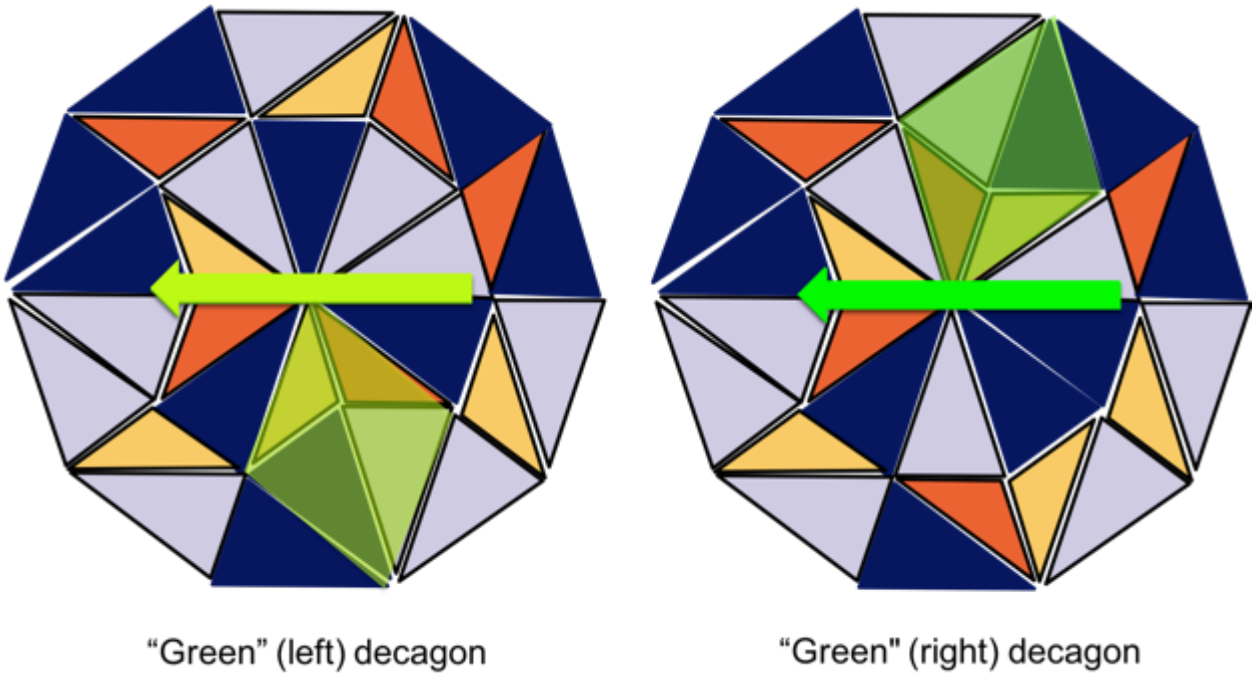


**Figure 4.6:** The green tile is the second most rotationally-symmetric decagonal motif, but has two mirror symmetric forms. The left motif has a flipped rhombus unit (highlighted in pale green) to the left of the pale green arrow, whereas the right motif has a flipped rhombus unit (highlighted in bright green) to the right of the bright green arrow.

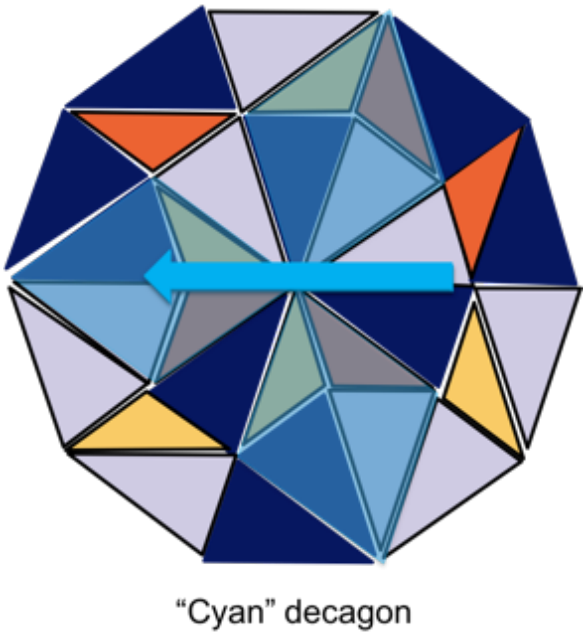


**Figure 4.7:** The cyan decagonal motif is the least rotationally symmetric decagon. This fifth decagonal motif has all three phason rhombuses flipped.

In previous chapters, I have shown that the covering motifs can be generated by rotations of the composite characteristic polygons. If, for instance, we take a pentagonal motif from the Penrose tiling and rotate the correct number of decagons in the correct 108° clockwise or counterclockwise direction, we can turn a blue pentagonal motif into a red pentagonal motif, and so on. In this first inflation of the blue decagonal motif, it is apparent that I can change blue to red, green, or cyan, simply by swapping red for blue.

If, however, the Tübingen tiling works the same as the Penrose tiling, then the layering method should also work to construct the different covering clusters. First take a single blue decagonal motif, for example, and place another blue decagonal motif on top, such that their inner phason rhombuses overlap.

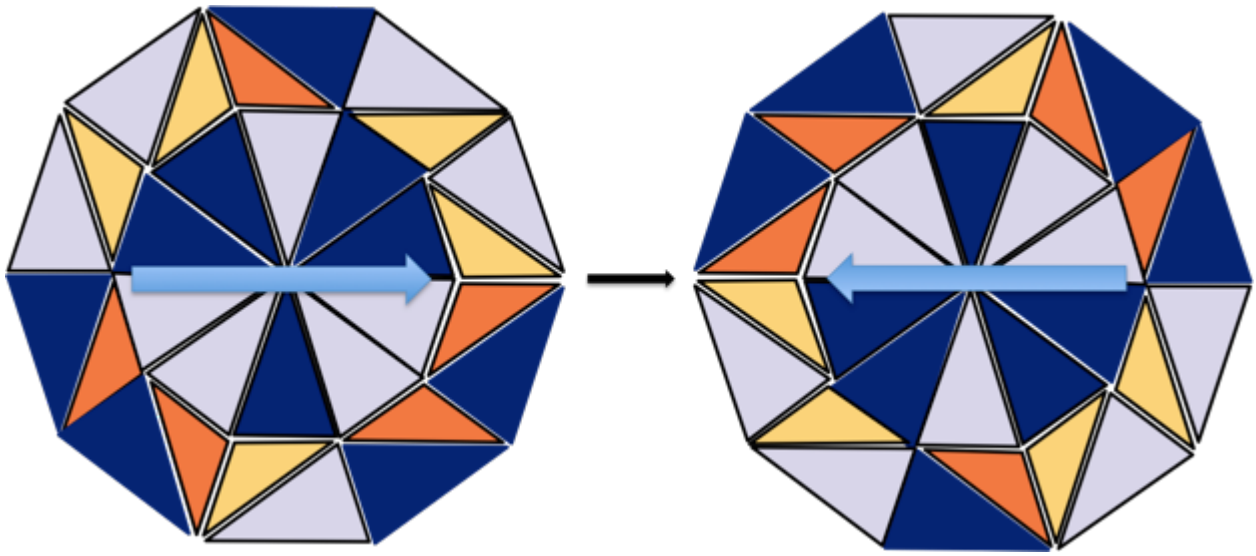

**Figure 4.8:** Layering the blue decagonal motifs

This process can be used to create the red decagonal motif, two types of green decagonal motif, and cyan decagonal motif, as seen in ***Figure 4.9***. Note that this is not a proper layering as was seen in the Penrose tilings. In order to satisfy that process, the top and bottom tile would have to match exactly except for the regions that underwent the phason flip. Although the rhombus unit does flip, the corner regions are no longer related anymore by the simple flip considered here. This will be addressed later on in the chapter.

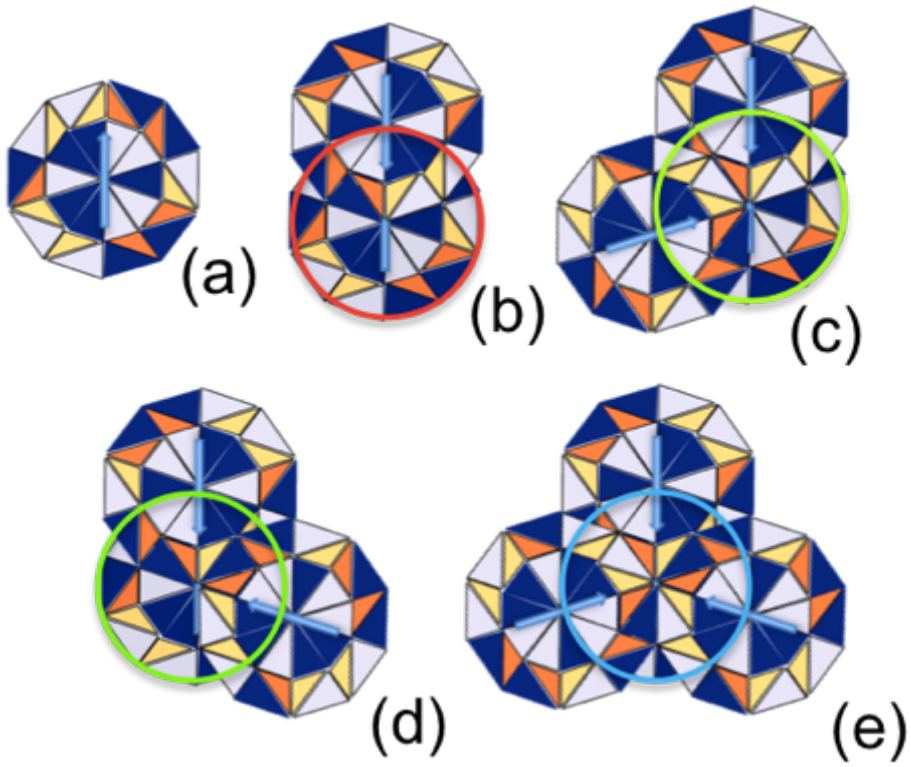


**Figure 4.9:** A blue decagonal motif (a) is rotated by 180° and placed over another blue decagonal motif to produce a red decagonal motif (b). Likewise, an additional blue decagonal motif is rotated 72° and placed over the lower left of the blue decagonal motif to produce a left-handed pale green decagonal motif (c), or over the lower right of the same blue decagonal motif to produce a right-handed bright green decagonal motif (d). In (e), three blue decagonal motifs over an underlying blue decagonal motif will produce a cyan tile.

Similar to the Penrose tiling, all of the possible covering motifs are produced by placing as many blue decagonal motifs around a central blue decagonal motif as will fit without overlaps between the surrounding decagonal motifs. This is a significant point, since it lets us understand the geometrical restrictions that set the number of allowed decagonal motifs. This is detailed in *Chapter Two* and *Chapter Three* because of the relative simplicity of those tilings. Once we know how to construct the different covering motifs by using a layering, we no longer need to use the covering motifs. Instead, we can assign different colors to the same original blue decagonal motif, so that we know where to put each respective decagonal motif in the layering.

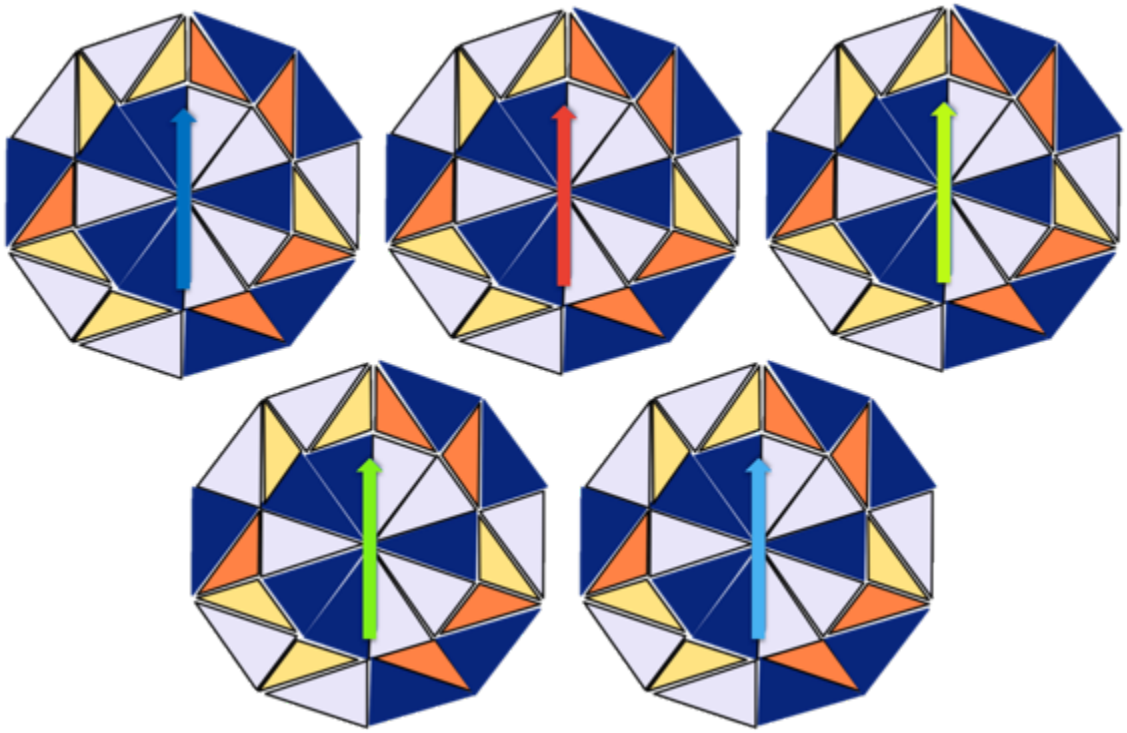

**Figure 4.10:** Five identical decagonal motifs with differently colored arrows used in the layering method

Now that we have all of the decagonal motifs marked, we can construct a larger motif.

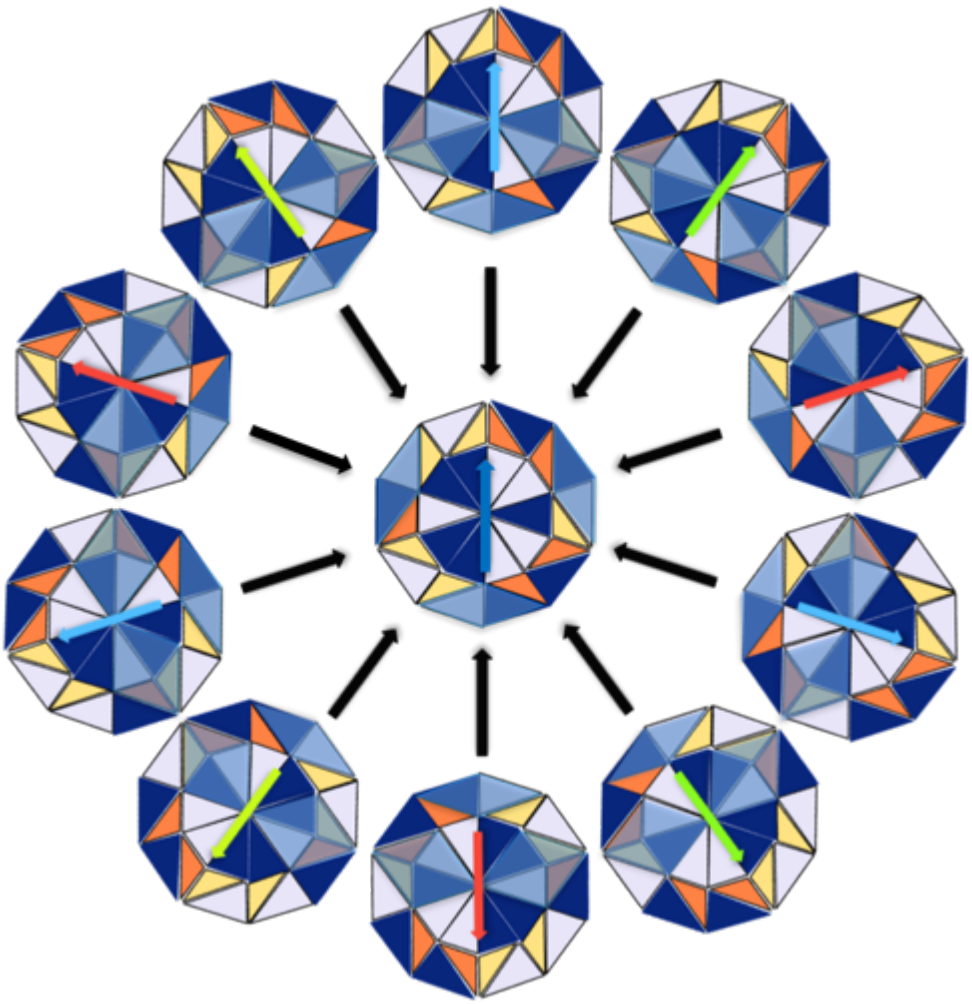

**Figure 4.11:** This is the first stage of my first attempt at a layering construction. A single blue decagonal motif is placed at the center. Ten additional decagonal motifs, identical except for the color of their arrows, are placed around the central decagonal motif with their arrows facing outwards. The oblate blue rhombuses indicate where decagonal motifs in the ring will layer with each other and produce respective 180° rhombus phason flips. The acute blue rhombuses show where the outer ring of decagonal motifs will overlap in area with the central decagonal motif. Interestingly, only the red decagonal motifs overlap in a covering, although they do not obey chirality matching.

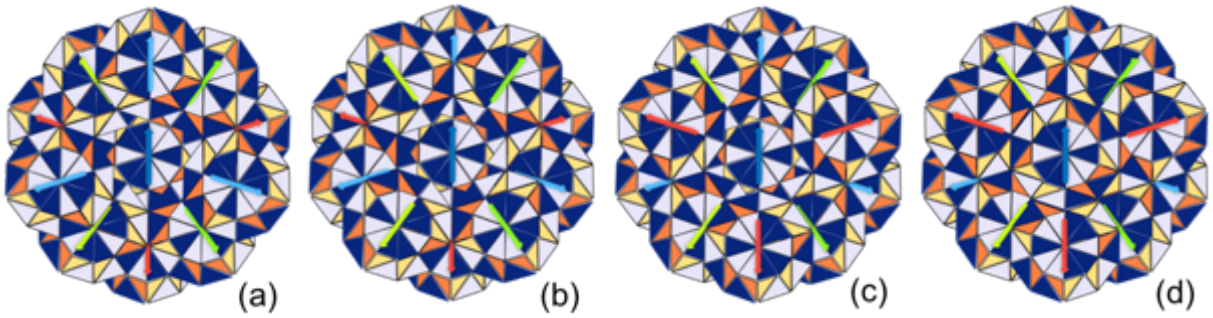


**Figure 4.12:** Only (d) has the correct layering order. The other tilings (a)-(c) show the results of incorrect layering order.

The layering method works by placing copies of the same blue decagonal motif, which has the highest degree of rotational symmetry, into the correct sequence of layers. In this labeling of the Tübingen layering motif, the hierarchy requires blue on top, followed by red, green (chiral twins being on the same layer), and then cyan, respectively. Different motifs result from alternative layer ordering. In ***Figure 4.12***, (a) cyan is on top, (b) green is on top, (c) red is on top, and finally, (d) blue is on top. Since they have been brought together in the correct sequence, only the motif represented by (d) is correct for the Tübingen tiling, whereas (a)-(c) produce incorrect patternings. Because this layering motif is still incomplete, the incorrect orderings can reveal tilings that do not obey the layering rules observed in the Penrose tilings, seen as small triangles inconsistent with the proto-tiles used for the Tübingen tiling.

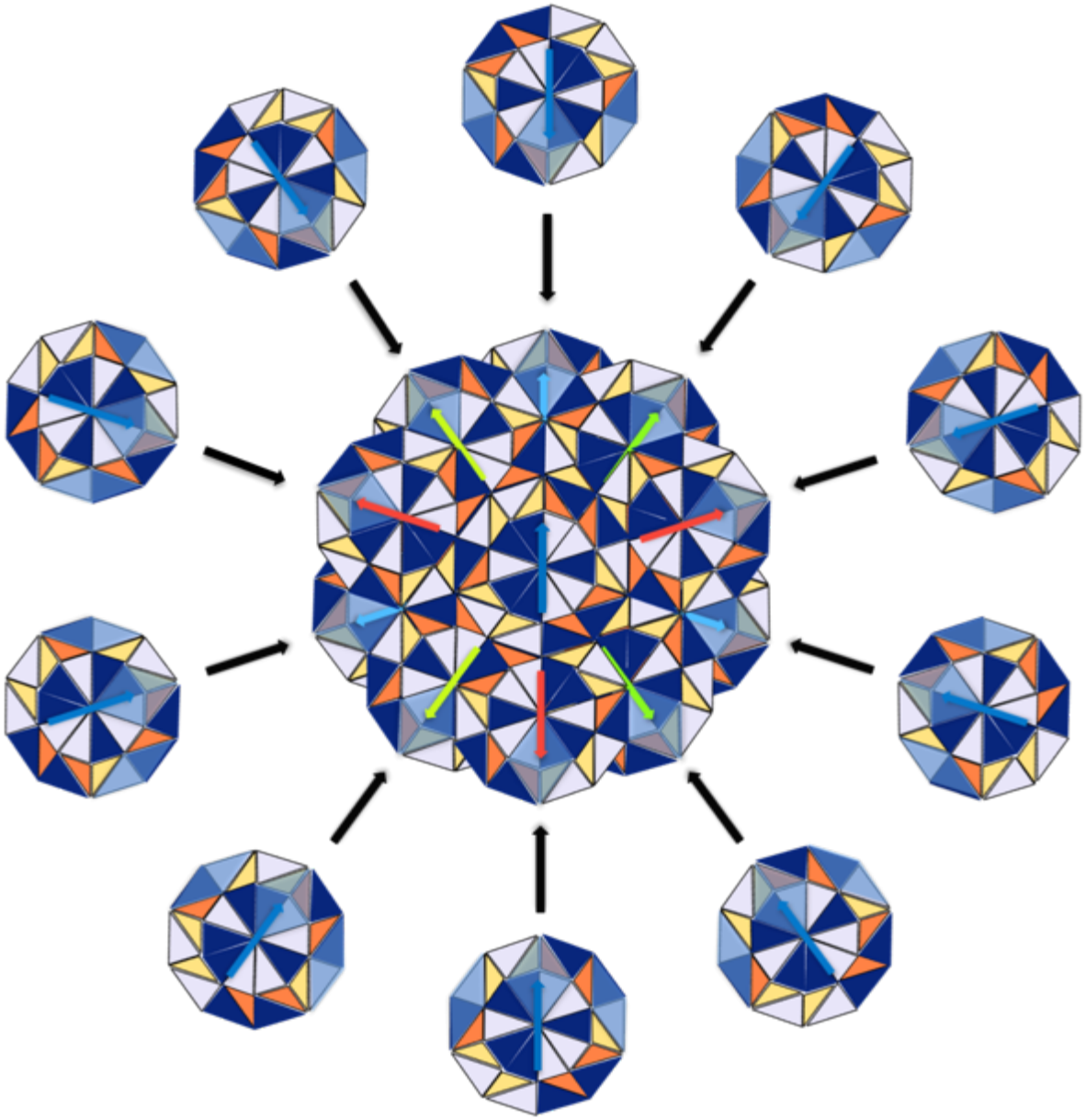

**Figure 4.13:** The second ring is added to the expanding motif. Oblate blue rhombuses indicate regions where the 180° rhombus phason flip will take place. Acute blue rhombuses indicate an overlap covering shared by the decagonal motifs, but which do not obey chirality matching.

Once the inner ring is complete, another ring of blue decagonal motifs is placed around that first ring. For this outer ring, all of the decagonal motif arrows will face inwards. Note that because the inner decagonal motif does not overlap with any of the first ring rhombuses, there will be no phason flips—at least not of the kind illustrated earlier in ***Figure 4.5***—taking place to

redefine the motifs. Instead, the second ring is defined entirely by rhombus overlaps with members of the first and second ring.

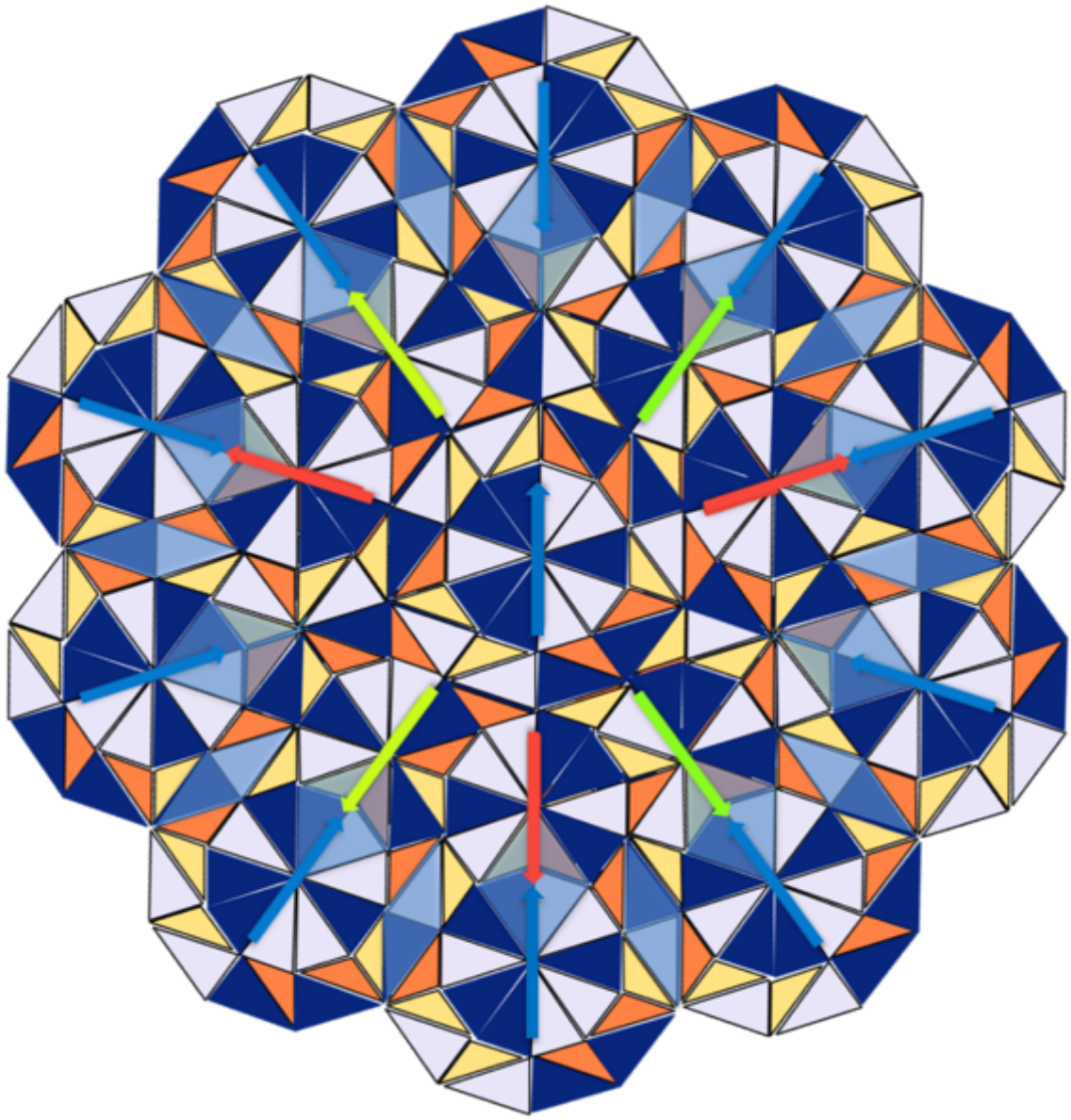

**Figure 4.14:** The first ring of the new decagonal motif is assembled. The center contains a single blue decagonal motif. The inner ring contains four green, three red, and three cyan decagonal motifs. The outer ring comprises only blue decagonal motifs in this representation of the tiling—but we will later see that this is an oversimplification. There are now twenty-one decagonal motifs. Eleven of them are blue, three are red, two bright green, two pale green, and three cyan. All of the non-cyan arrows have been brought to the top of the image for clarity. The cyan arrows, and, indeed, the entire cyan decagonal motif, are completely layered over by the other motifs. Like the yellow motif of the Penrose tiling, which has the inverted star of oblate rhombuses, this covering cluster turns out to be unnecessary for the creation of Tübingen motifs, as it is created entirely by the overlaps of other motifs. Note that although the outer ring of blue decagonal motifs obeys an overlap covering, embodied by the skinny blue rhombuses, the chirality matching is not obeyed. The decagonal motifs have been placed with arbitrarily chosen layering

hierarchy, as can be noted in the positions of the blue and grey golden triangles that make up the skinny blue rhombuses. Some of the skinny rhombuses have their dark blue triangle pointing inwards while others have them pointing outwards. One or more decagons must sit on top of the other members of the second ring, so there will always be at least one skinny rhombus with either a grey or dark blue triangle pointed inwards or outwards, respectively. This inconsistency suggests something is missing, which will be resolved later.

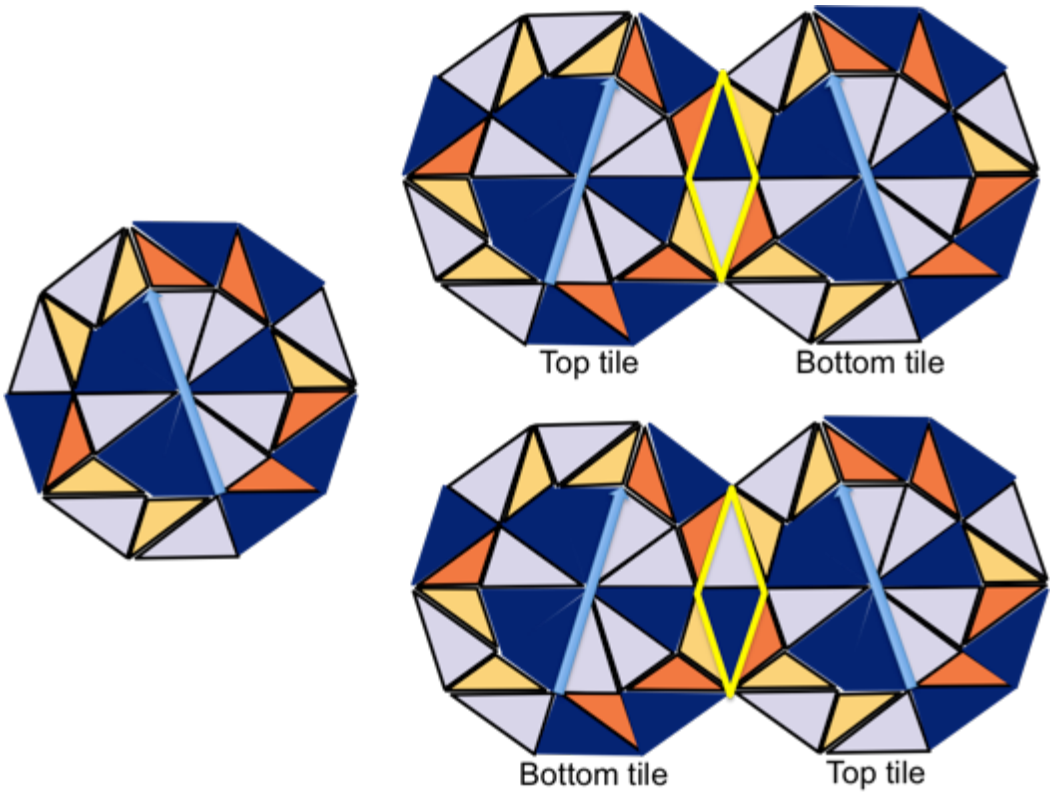


**Figure 4.15:** The orientation of the skinny rhombus overlap is determined by which blue decagonal motif is on top. Since this appears to be an arbitrary decision with this level of description, it suggests that a more complex motif is needed for the tiling.

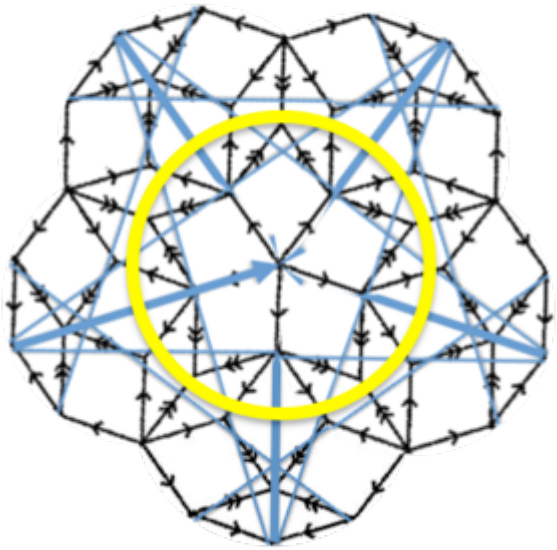

**Figure 4.16:** This pentagonal motif from the Penrose rhombus tiling is emergent in the same way as the cyan tiling for this description of the Tübingen tiling. In the Penrose tiling, this motif only emerges as a consequence of the overlaps of the blue pentagonal motif (not shown in its entirety) with itself, but never exists as an independent motif. Likewise, the cyan decagonal motif emerges as a consequence of the overlaps of the other decagonal motifs and is not needed during assembly as a separate decagonal motif. The light blue bars are Ammann bars, which are continuous (broken) lines for an ideal tiling.

Since the layering order of the suspiciously identical blue decagonal motifs will control the chirality of the skinny blue rhombuses, there must be some further underlying principle behind the process. This lack of determinism is the next indication that there is more required for this picture than presented thus far. The resolution of this inconsistency will be revealed later in the section.

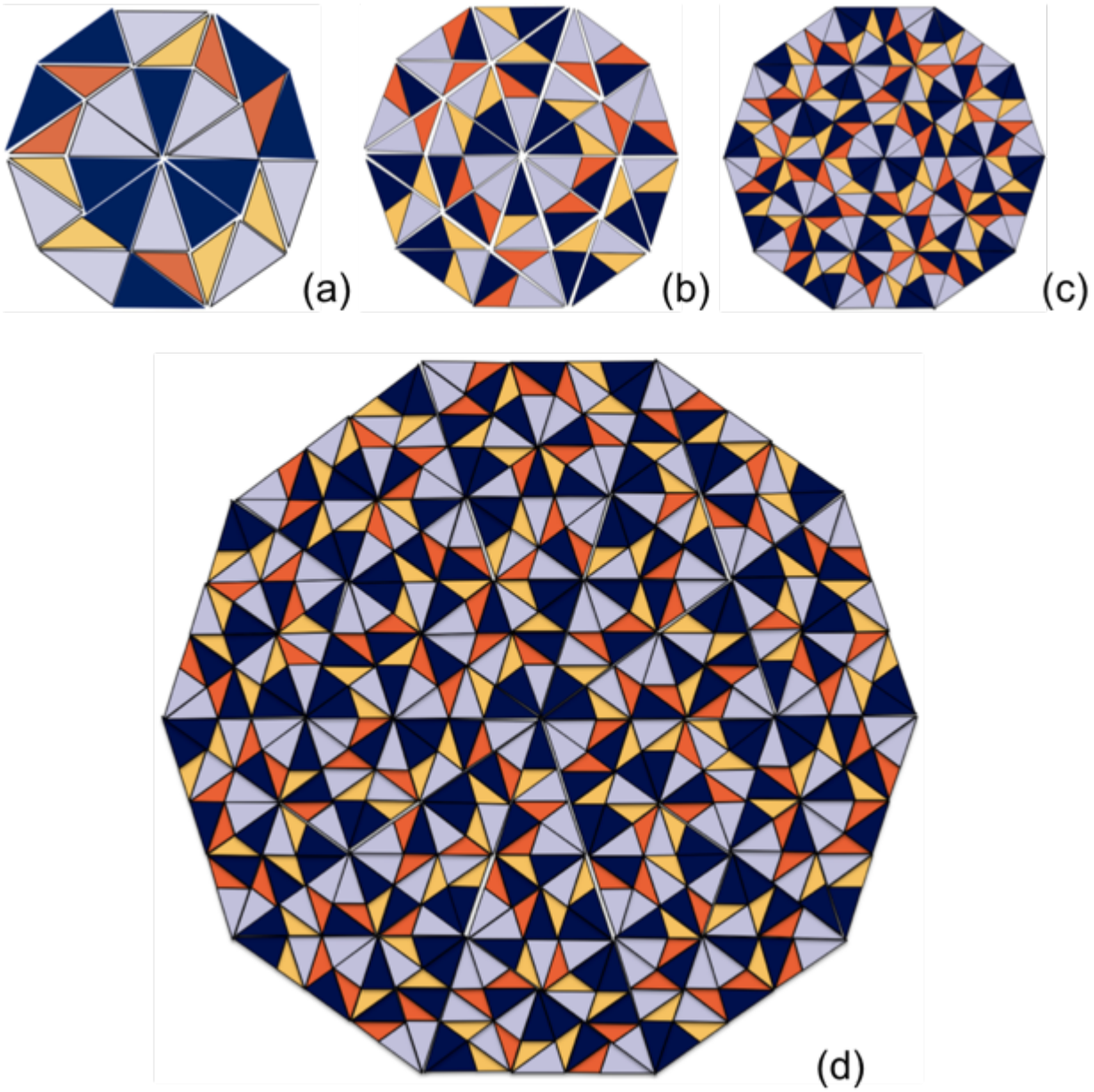


**Figure 4.17:** Three stages of substitution of a decagon, (a), (b), (c), (d): Note that although it almost contains the second-order decagon, it is still missing the 3/5ths of the outermost ring. The two processes are different in the boundary of the tilings they produce. Deflation, despite producing similar types of motifs, is a fundamentally different type of process than the hierarchical motif assembly process (layering) detailed in this chapter for the Tübingen tiling.

The same method can be used to turn this blue decagonal motif into one of the other red, green, or cyan decagonal motifs. But let's look more closely at the cyan decagonal motif. Having all three rhombuses flipped would suggest that it sits at the very bottom in the layering

hierarchy. But what happens when we assemble the second-order decagon? We note that, upon removal, the cyan decagonal motif has no effect.

## Second-Order Decagons

We now turn to the creation of second-order decagons using the layering method.

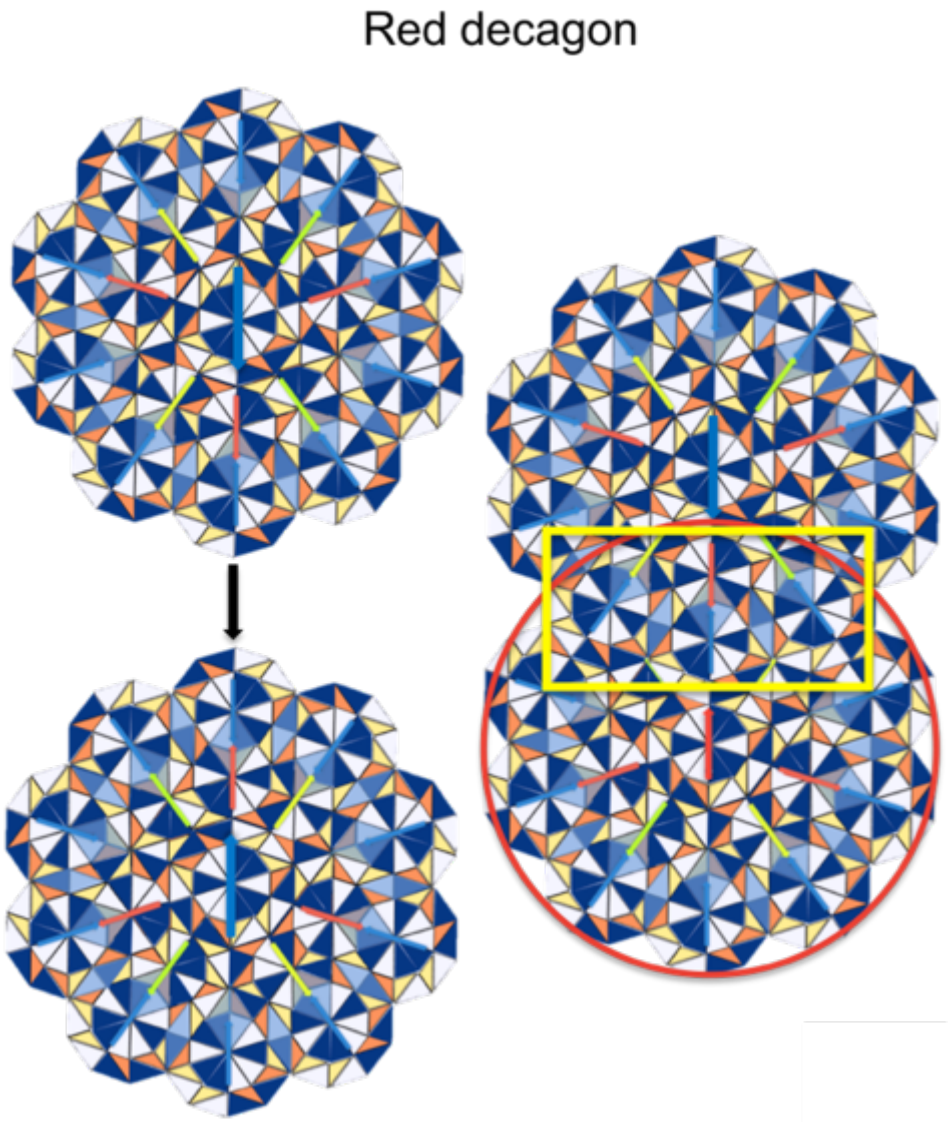


**Figure 4.18:** Two second-order decagons can be layered to produce a second-order red decagon. The yellow box highlights the region of overlap. From the point of view of the red decagon, an outer ring decagon has swapped places and orientations with an inner ring red decagon. In materials or simulation, this corresponds to the first-order phason flip of a rhombus rotating 180°.

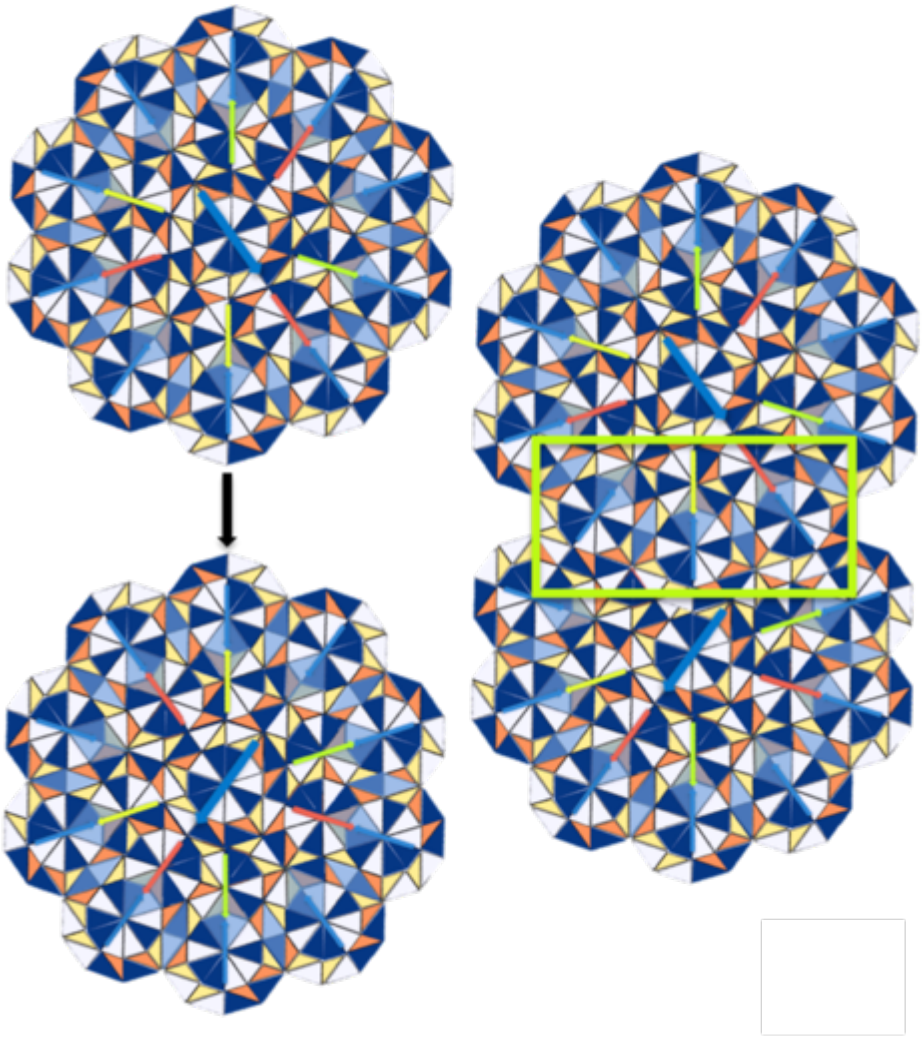

**Figure 4.19:** This layering represents the creation of a decagonal motif that is not present in the Tübingen tiling. Note the direction of the center blue arrows.

We can try to do a layering overlap with decagonal motifs other than red, such as pale green as seen in ***Figure 4.19***. The overlap produces a kind of phason flip that rotates and chirally flips the smaller covering pentagon. But it also creates rhombus phason flips, which are not seen in the creation of the second-order red decagon. In any case, it produces a motif configuration that is not seen at any scale in the full Tübingen tiling—blue decagonal motifs are never seen with a red-blue phason swap at a 36° angle CW or CCW of their tail.

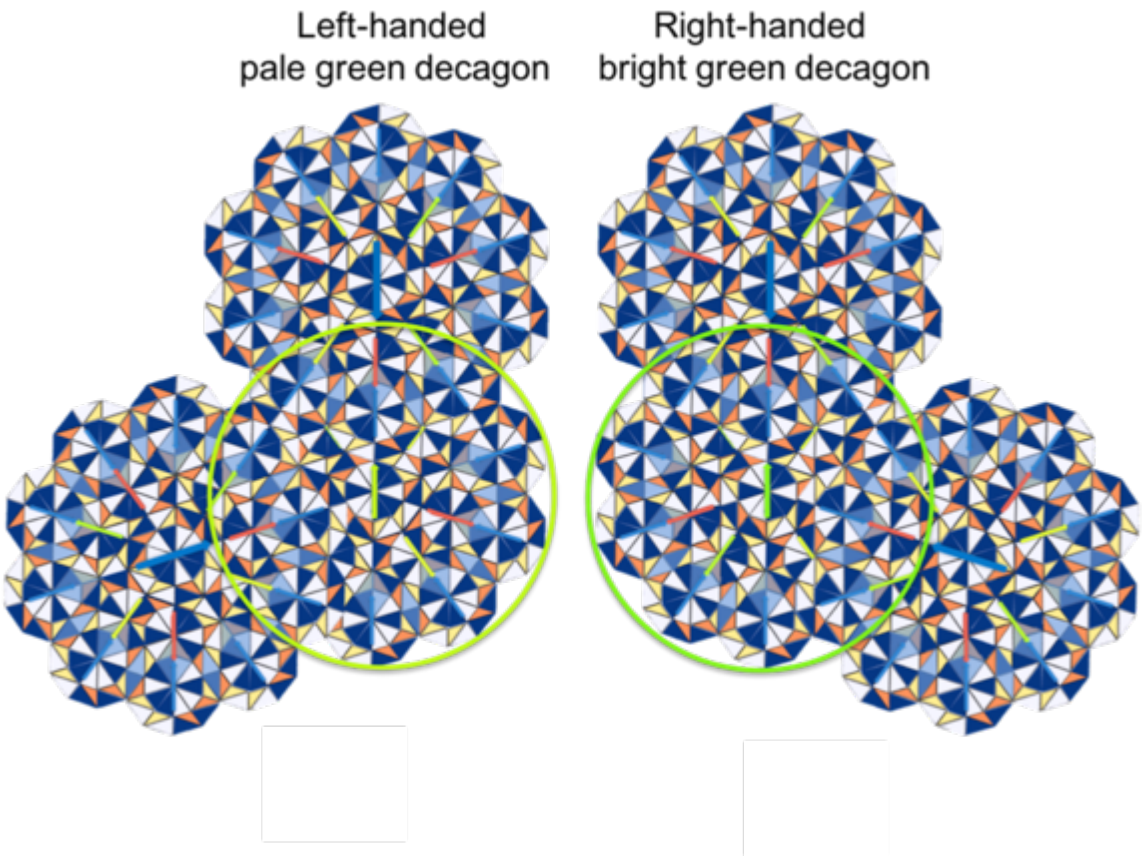


**Figure 4.20:** Two second-order decagonal motifs have been layered over a third to produce a pale green (left) and bright green (right) second-order decagon, respectively.

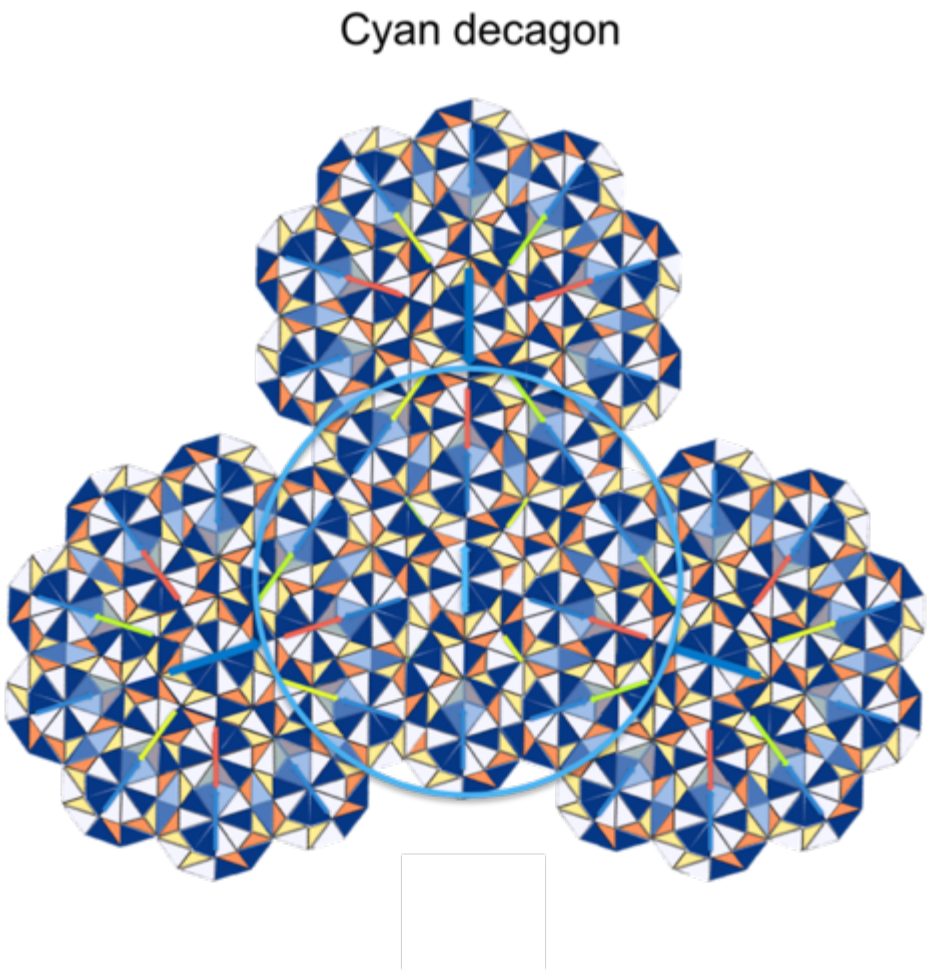


**Figure 4.21:** This cyan decagon has been created by layering three second-order decagons onto the sides of another blue second-order decagon.

These new second-order decagonal motifs (***Figure 4.18***, ***Figure 4.20***, ***Figure 4.21***) are created by layering the second-order blue decagon with itself in the same manner that was used to produce the other first-order decagons. The creation of the second-order red decagon can be clarified by noting that a blue and red first-order decagon have swapped positions, and their two nearest first-order blue decagons have rotated 72° CCW and CW for the left and right positions, respectively. As can be seen later in ***Appendix Figure .7***, this differs with respect to the Penrose tilings where higher-order clusters are created by simply rotating ring members. It also provides insight into exactly why only specific particles within the decagonal motif can undergo a phason flip; they must correspond to a decagonal motif moving between layers in the hierarchy.

The chiral directionality of the decagon flips 180° at each higher order, so the arrows have been flipped accordingly. Recall that the arrow has been arbitrarily decided to point in the direction of the central rhombus. Looking at the construction of the center of the second-order blue decagon in ***Figure 4.22***, it becomes obvious why. The skinny blue rhombuses on the tails of the red decagons must fit into the skinny blue rhombuses of the blue decagon. This new pattern establishes an arrow that must now point in the opposite direction toward the new central rhombus of the second-order blue decagon.

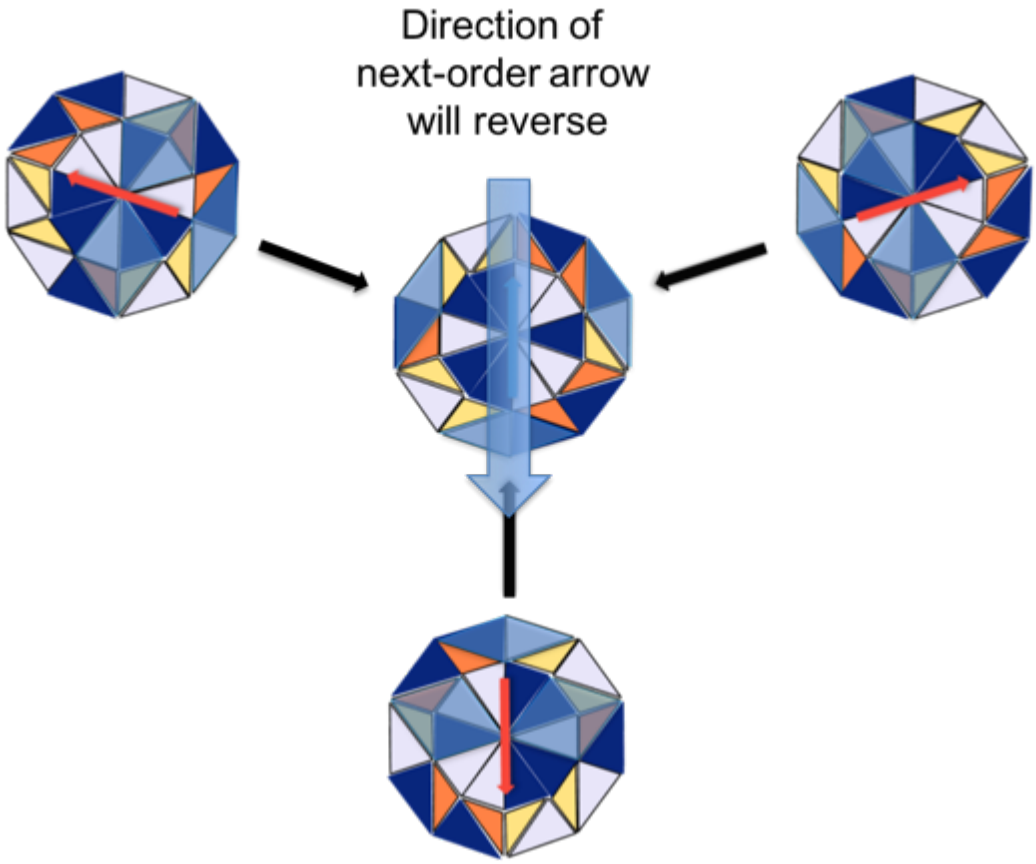


**Figure 4.22:** As can also be observed during the process of deflation/substitution, the orientation of the motif flips by 180°. This figure illustrates the cause of the flip—the next successive shell must fit over the central decagonal motif in such a way that the symmetry is reversed by 180°. Understanding this from a deflation point-of-view is decidedly murkier (at least to this author).

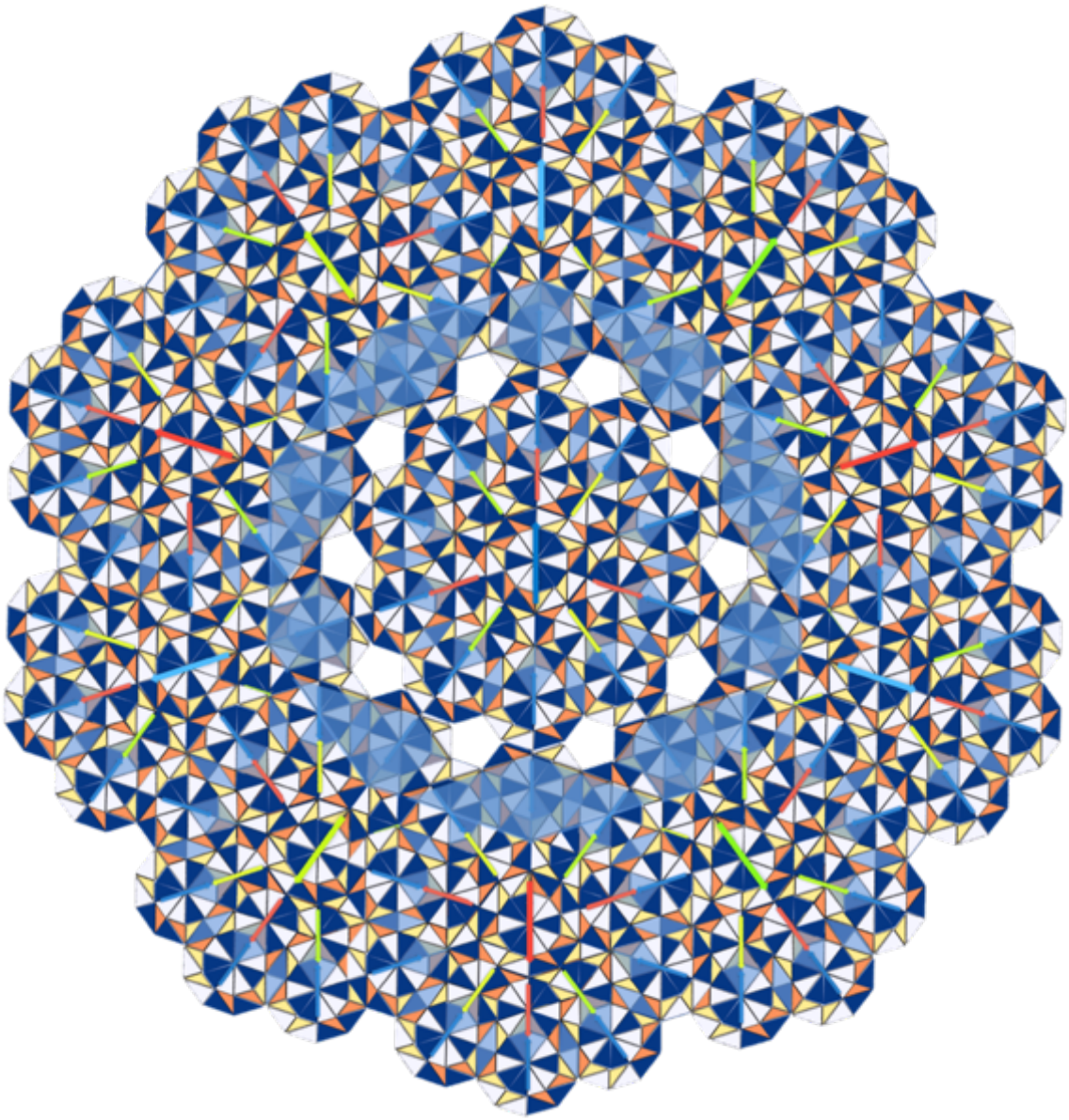

**Figure 4.23:** Inner ring of attempted third-order decagon. Note the missing pentagonal regions. The inner ring second-order decagons are still incomplete—they require the presence of the overlapping second ring for their motifs to match their arrow color designations.

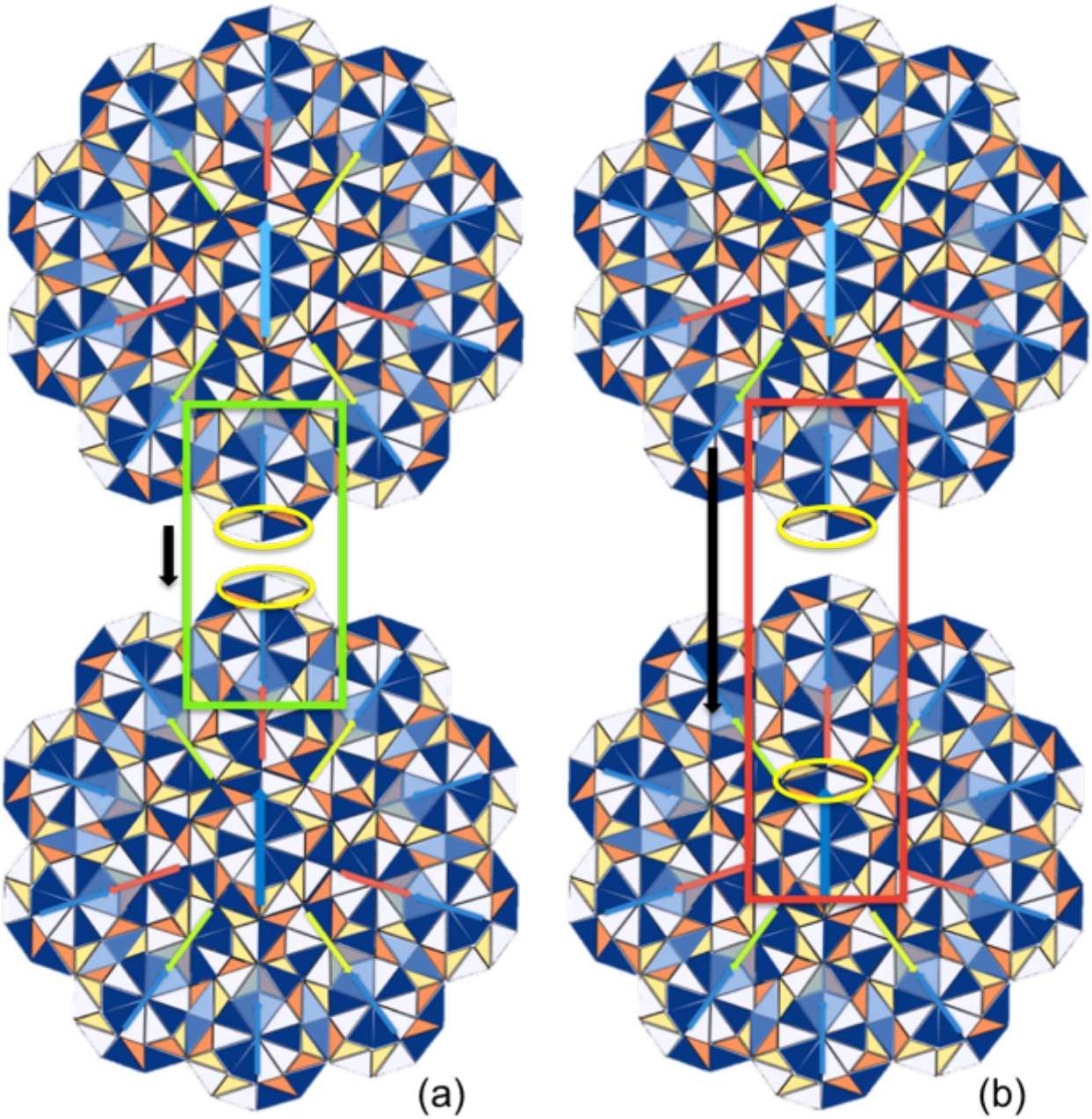


**Figure 4.24:** When overlapping two of the incomplete second-order decagons, pay heed to overlapping only the first two skinny rhombuses (yellow ovals in the green rectangle in (a)). Overlapping the top skinny rhombus (yellow ovals in the red rectangle in (b)) will produce the expected rhombus phason flips and chirality flips with the central blue motif, but will produce a significant degree of inconsistent spacing in the other inner-ring second-order decagons.

When constructing the third-order decagon, it becomes clear that there is a problem! The decagonal motifs that I have chosen here are clearly not large enough to tile space. As we saw in *Chapter Three*, the solution is straightforward, but adds more complexity to the picture. Each of

these decagonal motifs is surrounded by an additional decagonal ring of pentagons. These are the larger of the two pentagons that cover the Tübingen tiling seen below in ***Figure 4.25***.

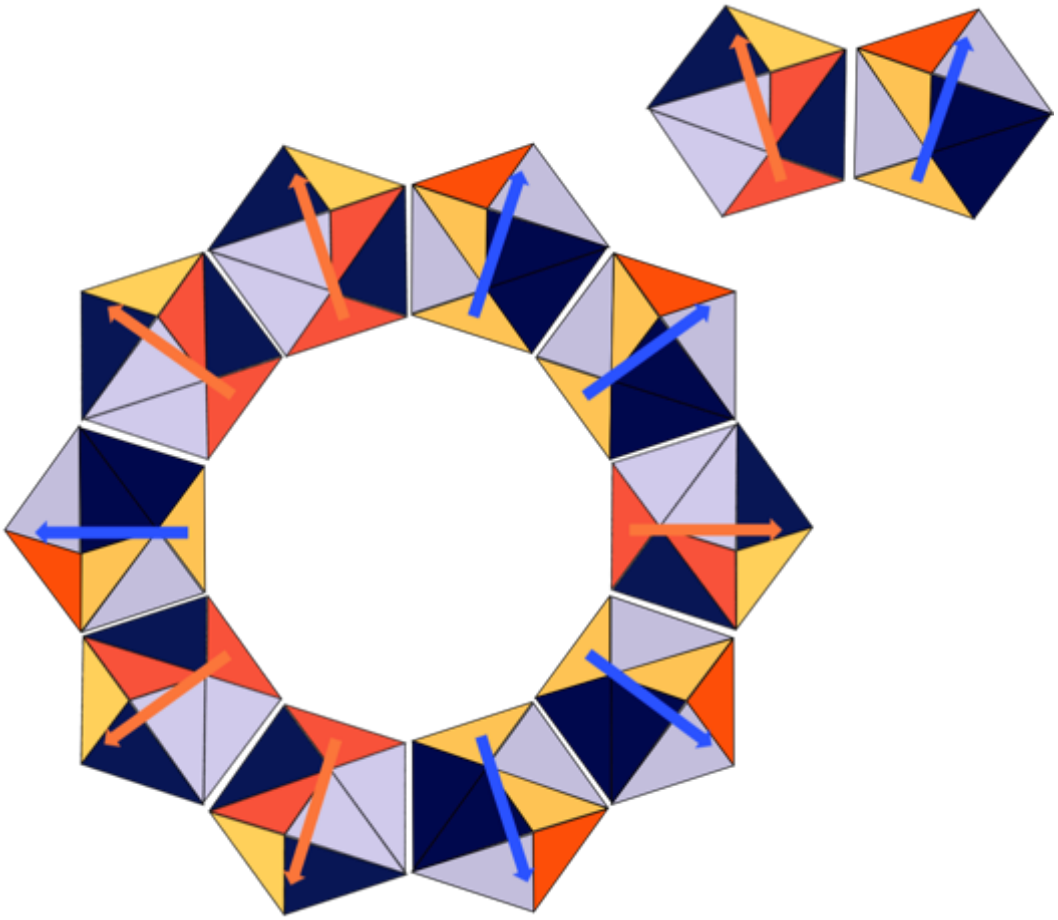

**Figure 4.25:** This is the larger of the two covering pentagons in the Tübingen tiling. Each chiral form is shown (upper right), and five of each type are used to construct an outer decagonal ring of pentagons (lower left).

Each of the previous smaller decagonal motifs is surrounded by a ring of these decagons, as was noted by previous work (Gummelt, 1996)[34]. Gummelt points out that two of these

[34] Gummelt was simply pointing out that her covering motif could not be extended further because only two of the pentagons are constant in the 10-pentagon ring. This section is pointing out that this is ok, if we are allowed to have multiple covering motifs. Moreover, in the layering picture, the number of motifs is again reduced to one—as we will soon see.

pentagons are fixed for every type of first order decagon. Because of this, she argued that a single covering motif does not exist for the Tübingen tiling.

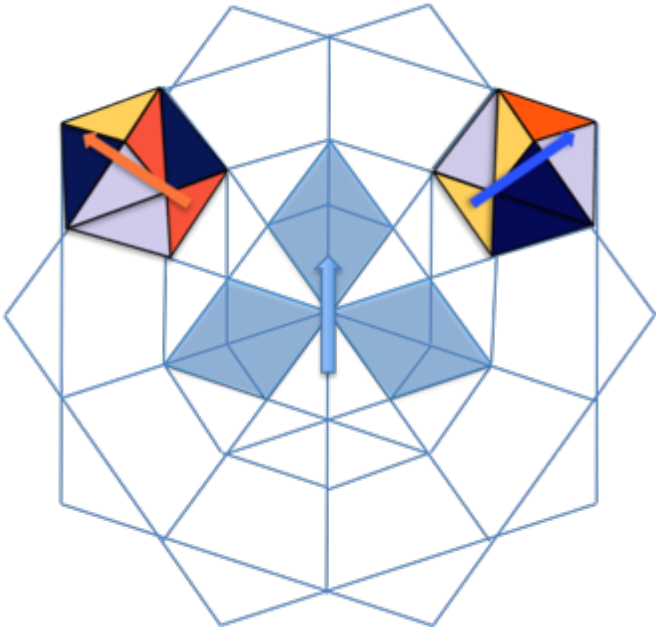

**Figure 4.26:** The blue lines here denote the boundaries of the tiles that are fixed across every type of first-order decagon in the Tübingen tiling. The blue arrow indicates the position of the central rhombus phason, highlighted with oblate blue rhombuses. Bolded black pentagons show the position of the two larger covering pentagons that are fixed in chirality and orientation with respect to the arrow orientation.

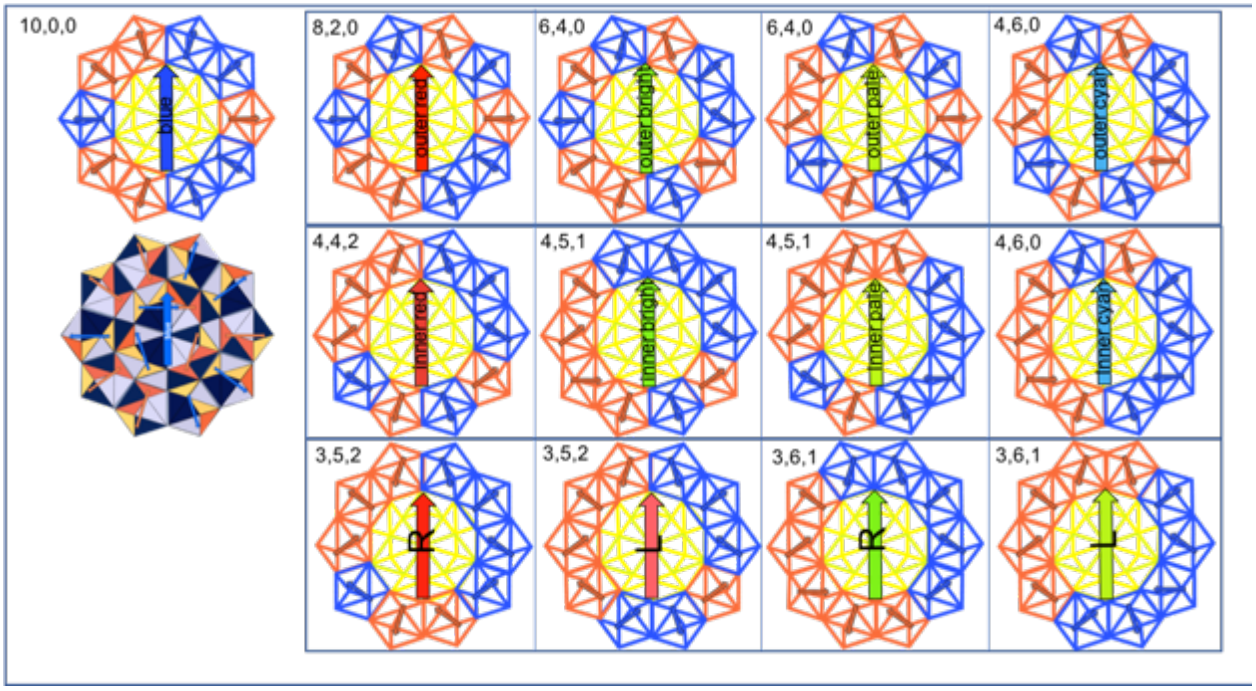


**Figure 4.27:** Thirteen of the covering decagonal motifs: Coverings fill all of space, and each of these has a specific role in the tiling. A colored tile version of the blue decagonal motif is added for comparison (left, middle). Note that all of the pentagons in ***Figure 4.26*** remain unchanged in each of these new motifs.

Instead, I find that there is not only a set of covering motifs, but, as we will see, also a single layering motif that also tiles space. There are thirteen covering motifs in total (***Figure 4.27***). The rotationally symmetric one is shown above on the far left of ***Figure 4.27***. All of the others involve either a rotation of a blue or orange pentagon, or a chirality flip from blue to orange or vice versa. Each of these covering motifs can be used to make a larger second-order decagon.

In ***Figure 4.27***, each decagonal motif has an index in the upper left. This is a count of how many pentagons are in each of the three types of possible positions. The first index is a pentagon that points outward, the second a pentagon that points inward to a corner, and the second is a pentagon that points roughly left or right, at a corner 72° above a bottom corner. These should roughly capture the ordering of the layering hierarchy, where the index on the right is most important. This picture is complicated by the fact that, unlike the Penrose tiling, the pentagons in the outer ring can remain in the same outward position if they land on the same orientation of pentagons in the **core** of a pentagon that sits on top, so the simple metric that worked for the Penrose and Ammann-Beenker tilings is not as straightforward here.

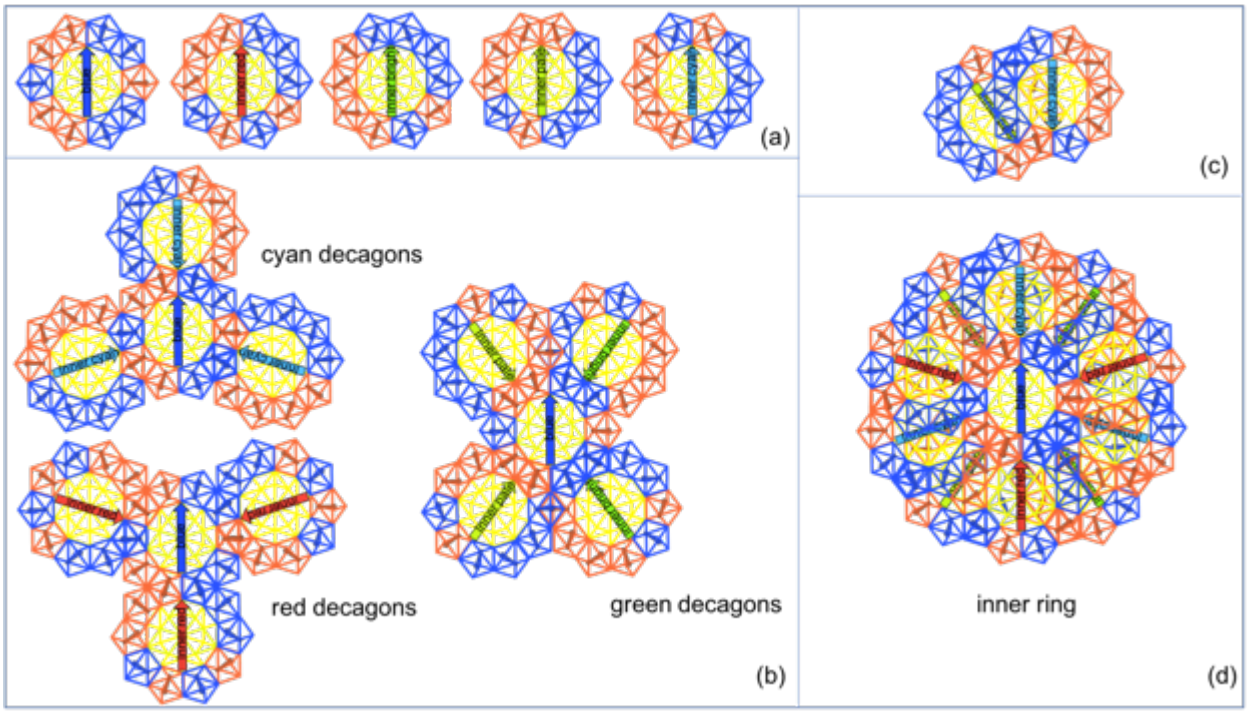


**Figure 4.28:** The blue decagonal motif combined with the set of inner decagonal motifs can be used to form the inner ring of the second-order decagon. The decagonal motifs are shown in wireframe so that any deviation from a covering structure will be readily visible. This will appear in the form of a mismatch between the bottom and top pentagon wireframes. Note also that any complete pentagon rotation will also involve a chirality flip, so there would be mismatched orange and blue lines in the event of an error.

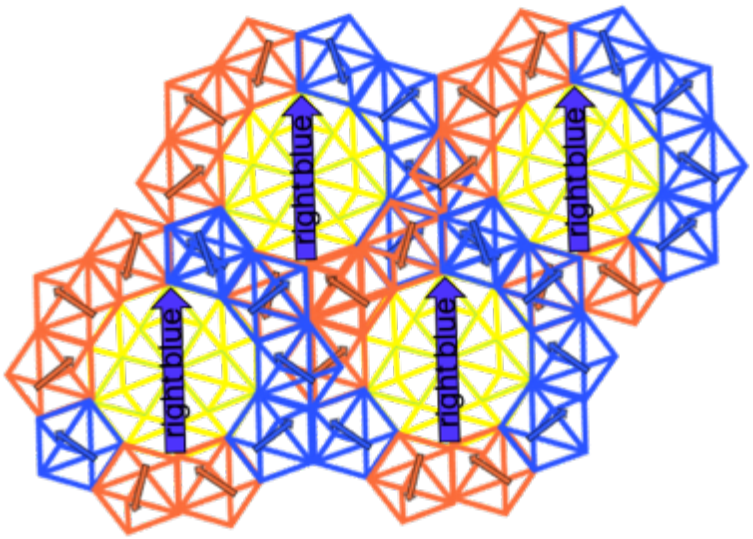


**Figure 4.29:** The "right blue" decagonal motif (bottom left of ***Figure 4.27***) has been placed into a periodic array. Note the many disagreements between the overlapping blue and orange pentagons.

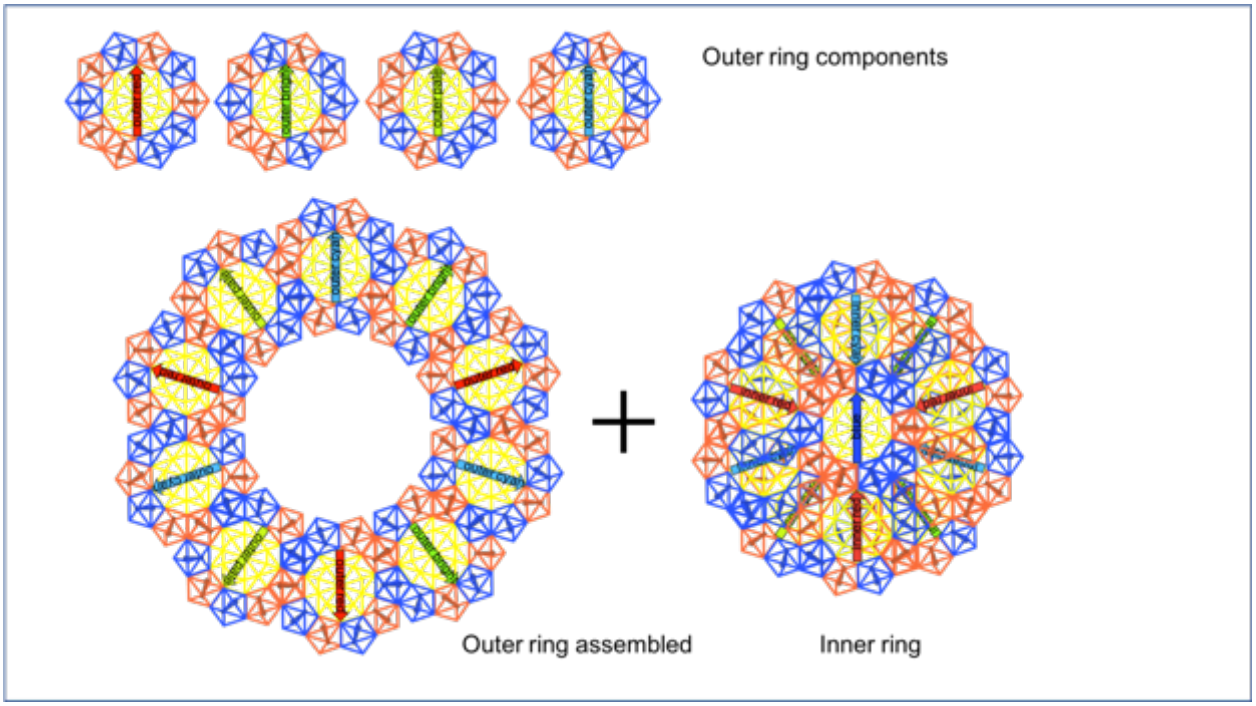


**Figure 4.30:** The outer ring components are used to assemble the outer ring. These decagonal motifs overlap with each other only by their ring of pentagons, just like the characteristic decagons of the Penrose tiling, but overlap with the inner ring in a way that mutually co-creates their respective cores. This mutual co-creation of cores also plays a large role in *Chapter Six*.

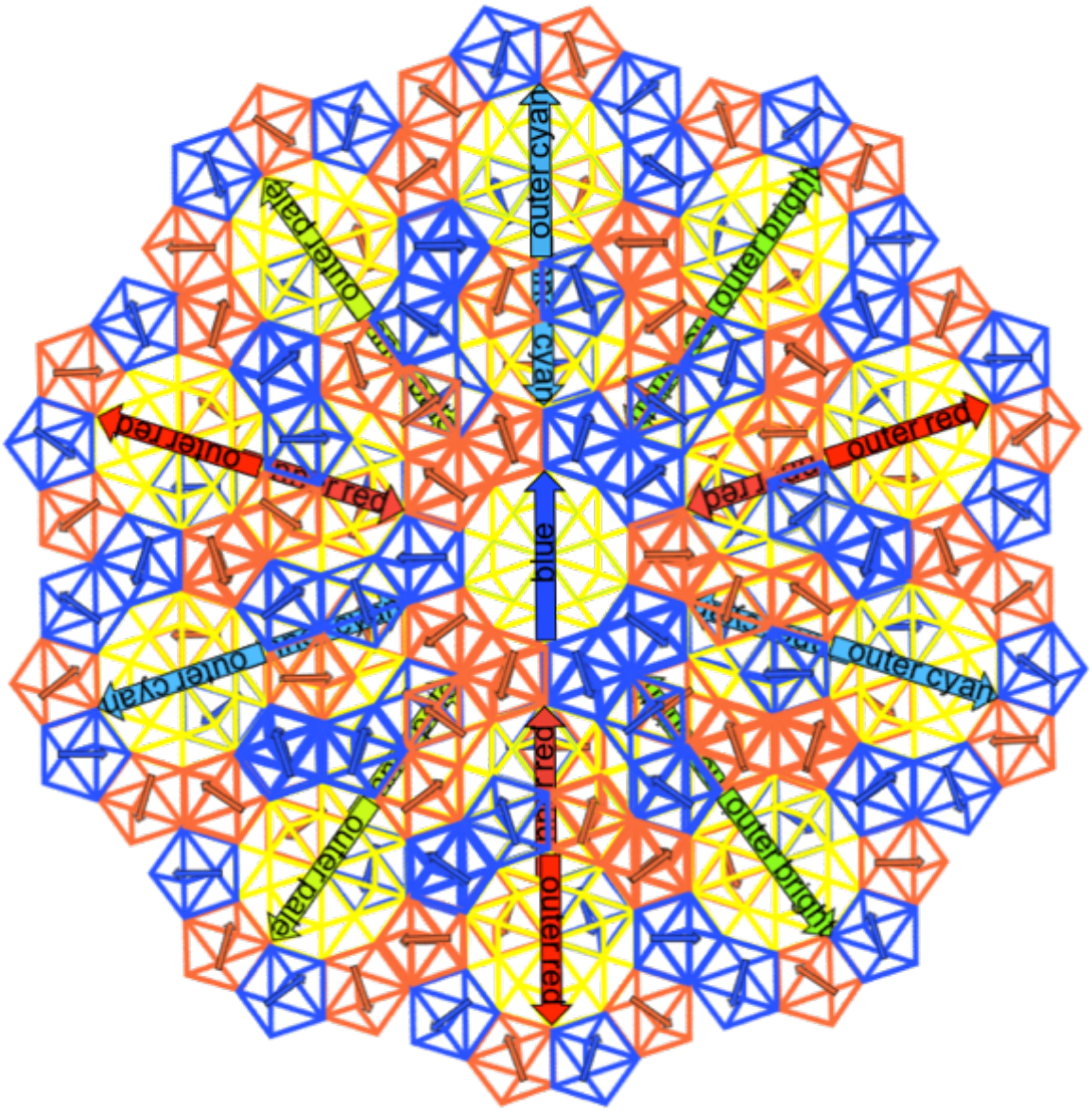


**Figure 4.31:** This shows one type of second-order blue decagon. Here, each specific covering motif has been used, which means that the outer pentagon color and arrow can change configuration. Like before, there is a central decagonal motif, an inner ring, and an outer ring, with the rings each having ten decagonal motifs apiece. Note the agreement for each pentagon with both color and arrow direction.

These decagonal motifs have been drawn as wireframes to reveal the covering nature of the motifs. Any non-covering portions will be readily visible with these wireframes, as can be seen in ***Figure 4.31***. The inner ring surrounds the blue decagonal motif, and contains three cyan, three red, and four green of the inner decagonal motifs. These are all arranged so that they point inwards with respect to the arrow that points toward the central phason rhombus (***Figure 4.28,***

***(b) (d)).*** Although they overlap with the blue decagonal motif in such a way that they only share pentagons from their ring, they overlap with other neighboring ring components in such a way that they mutually co-create their respective cores (***Figure 4.28 (c)***). The outer ring, similarly, contains three cyan, three red, and four green of the outer decagonal motifs. The outer ring components are arranged, and named, such that they line up with their respective inner partners[35].

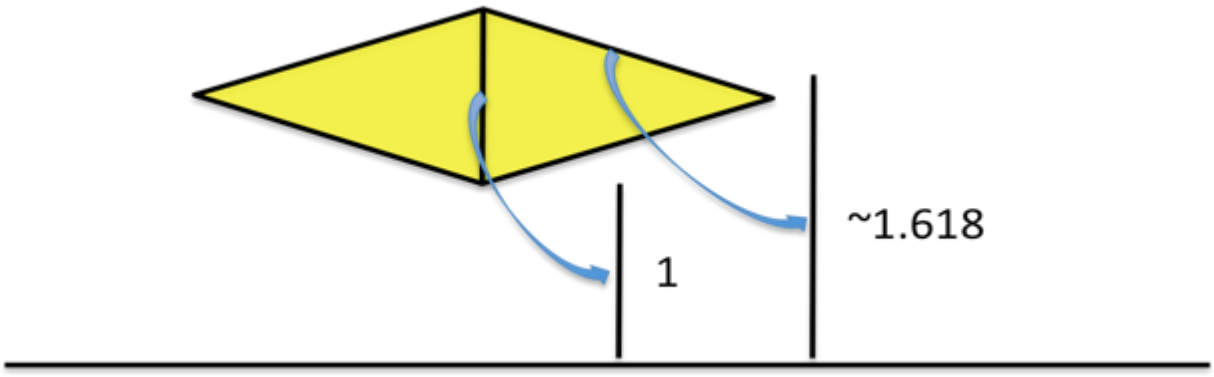


**Figure 4.32:** Incommensurate length scales are a common theme in any quasilattice tiling. This is a rhombus from the Penrose tiling with a comparison of the edge length and short cross-sectional distance, showing a proportion of the golden ratio. Similar kinds of geometric relationships can be found in the Tübingen triangle tiling.

Quasicrystals can be understood though the existence of two incommensurate length scales (Socolar, 1986). A quasilattice like the Penrose tiling will have two length scales that describe, for instance, the ratio of the edge length to the short cross-sectional distance of the acute Penrose rhombus (***Figure 4.32***). An example of this incommensurate length scale for the Tübingen triangle tiling is shown in ***Figure 4.33***. An incommensurate length scale means that

[35] The second-order blue decagon is also the cross-section of what is called the Tsai cluster (Jazbec, 2009; Kramer, 1999; Takakura et al., 2007; Yamamoto et al., 2003). This forms an interesting parallel with the Penrose rhombus tilings and the Wierenga roof (de Bruijn, 1981; Grünbaum & Shepherd, 1986), where a cross-section of the five-fold axis of the Ammann-Kramer-Neri tiling produces something like the Penrose tiling, depending on where the cut is made perpendicular to one of the five-fold axes. Likewise, taking a correct slice through a face-centered cubic icosahedral quasicrystal along one of the five-fold axes will also produce a Tübingen tiling. To my knowledge, there is no tiling description for either the body-centered cubic icosahedral quasicrystal, nor the 2D cross-section taken along one of its five-fold axes. Figures detailing this process for an icosahedral quasicrystal are in *Chapter Six*.

the two lengths cannot be expressed as a fraction made from whole numbers. The golden ratio scaling of these two length scales is ultimately what gives rise to the pentagonal symmetry seen here—lengths with golden ratios make pentagonal shapes when put together in the right way. These two length scales are apparent even when assembling the tiling. Here we see that one length scale, which separates decagonal motifs when they overlap only by their ring of pentagons, is allowed between some motifs at some orientations, but not others. Similarly, the shorter length scale is allowed by some motifs at some orientations, but not others. This ultimately generates the same length scales we would find if we decorated each vertex of the new lattice with yet another smaller set of decagonal motifs, scaled down by a factor of the golden ratio. This reflects the self-similarity property demonstrated by the deflation/substitution protocol described earlier.

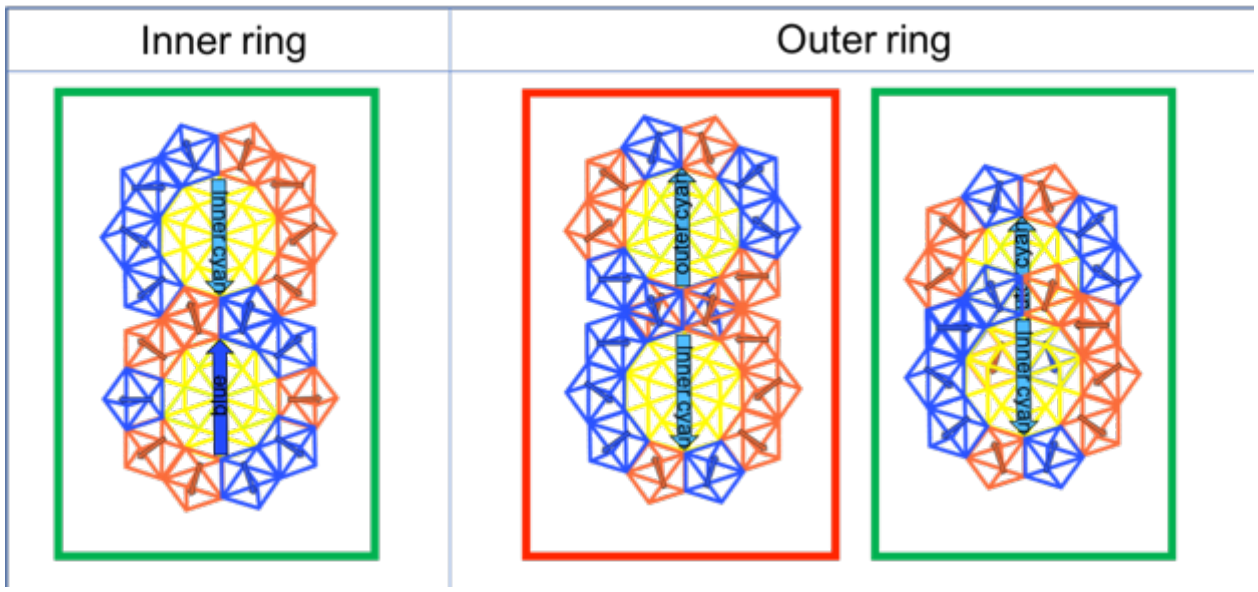


**Figure 4.33:** The inner ring components overlap perfectly with the ring of pentagons of the blue decagonal motif (left, green box) when the decagonal motifs are mutually pointing toward each other. In contrast, the outer ring cannot overlap at this distance and orientation (right, red box) when the decagonal motifs are pointing away from each other. Instead, each inner and outer component must further overlap so that their respective rings of pentagons partially complete the core of the other decagonal motif (right, green box).

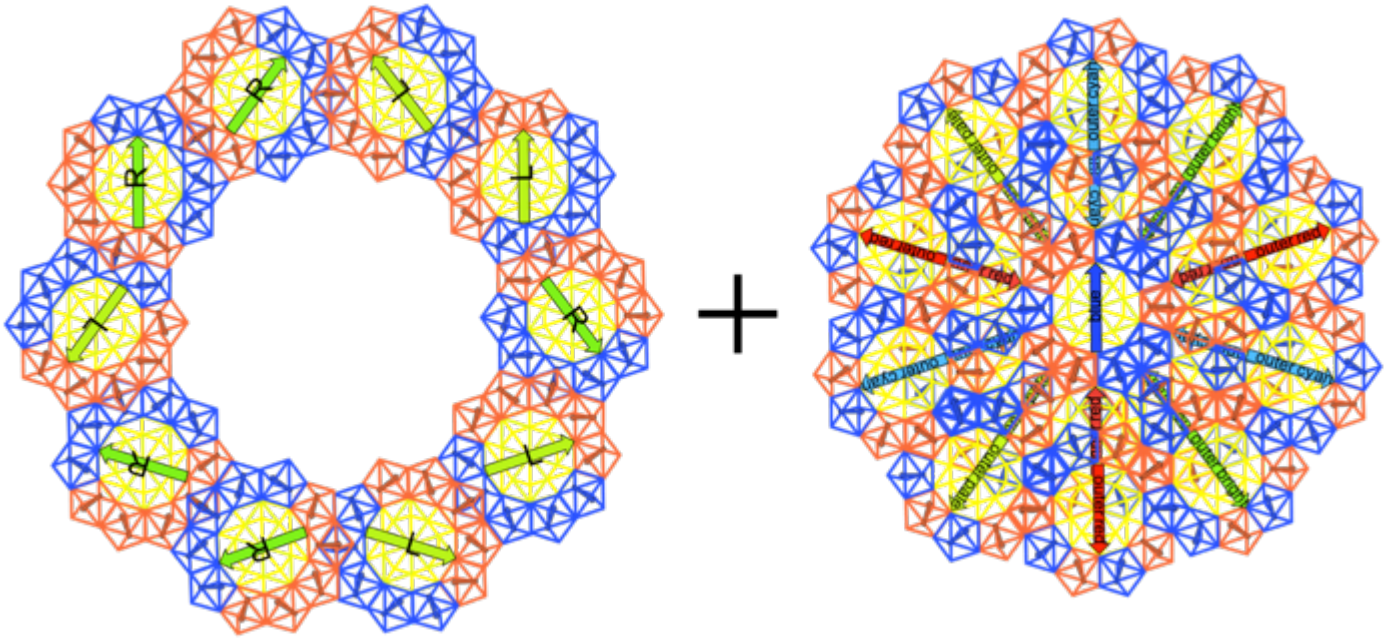


**Figure 4.34:** The leftside outer ring and rightside core combine to produce the image in ***Figure 4.35***.

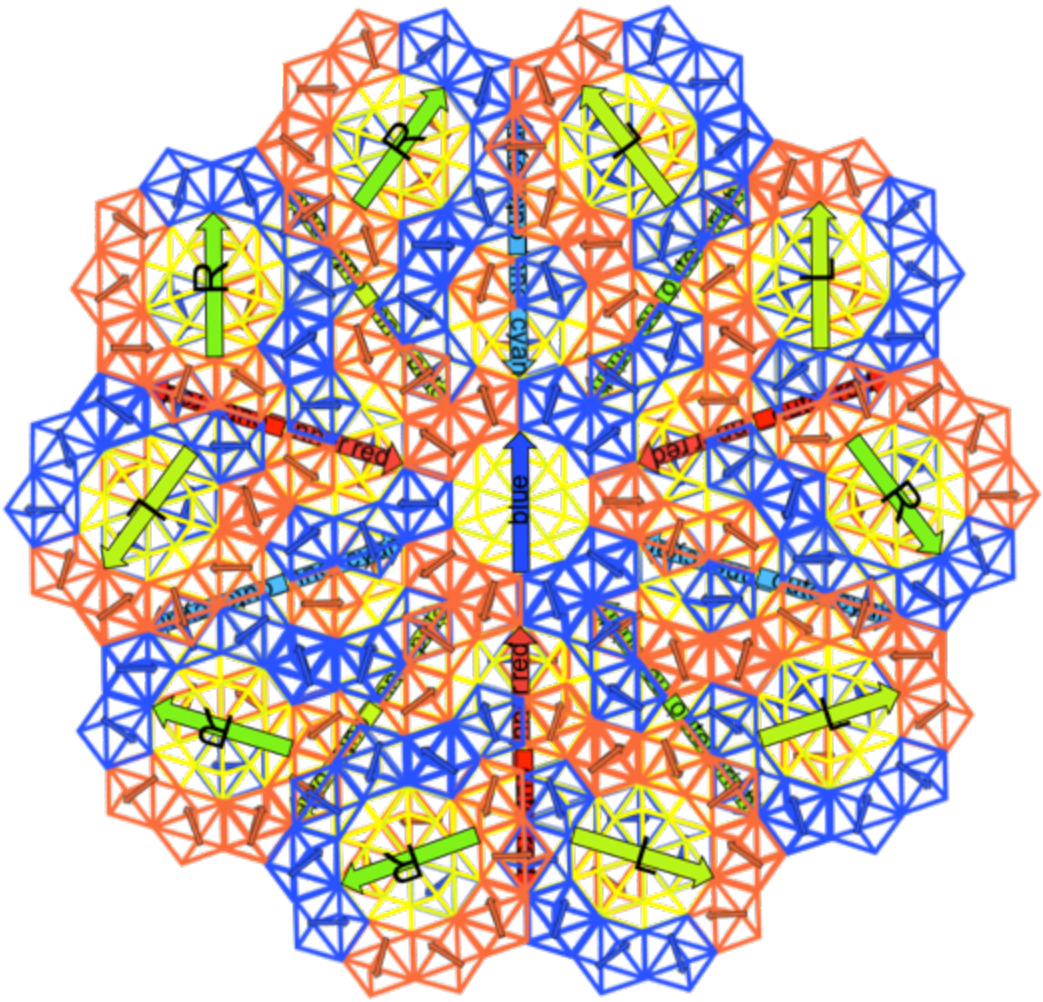


**Figure 4.35:** These are wireframe shapes. Since they are coverings and not layerings, the wireframes will overlap precisely. Each phason flip induces a chirality change, which changes blue to orange and vice versa. This means that any errors would produce crossed blue and orange lines—but none are visible. The entire assembly fits perfectly together. The right and left green decagonal motifs create a third outer ring, and they are one of the bottommost decagonal motifs in the layering hierarchy. **This image would be difficult to decipher without the new covering model introduced in this chapter.**

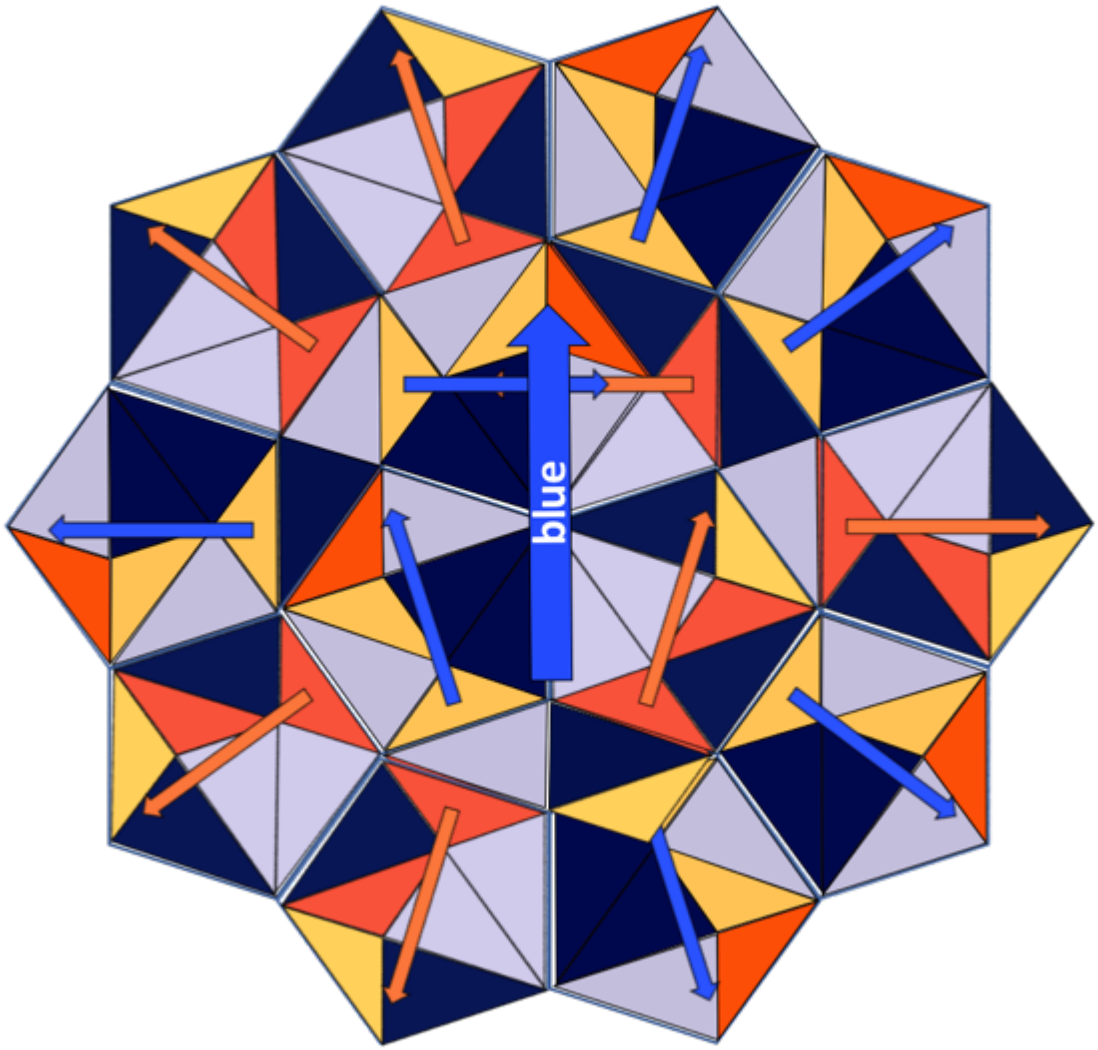


**Figure 4.36:** Tübingen tiling layering motif: Note how two of the blue and orange pentagons in the center are allowed to partially overlap (in the top of the core, there are two arrows, one orange and one blue, that face each other and overlap with an entire rhombus). This is an overarching theme in quasilattice tilings and plays an important role in quasilattice covering models.

## Tübingen Layering Model

We next present the new layering cluster for the Tübingen tiling. The idea of the layering model is that instead of creating new covering motifs, we ignore the covering requirement and simply place one motif over another in such a way that the bottom one is hidden. For the Tübingen tiling, there is only one layering motif (***Figure 4.27 (left, top)***), so we only need to layer this motif over itself to produce the entire tiling. **The complexity of the covering motifs is then stored instead as information in the hierarchy of layers.**

When a layering motif overlaps with itself, it produces phason flips—in any tiling. In this case, the phason flips are represented by rotations of the large covering pentagon and its chiral twin. If we want to rotate a pentagon, we can perform a series of rhombus flips to flip some of the vertices of the tiles. Other kinds of flip are not represented by rhombus flips at this scale, but would be at a lower series of deflation.

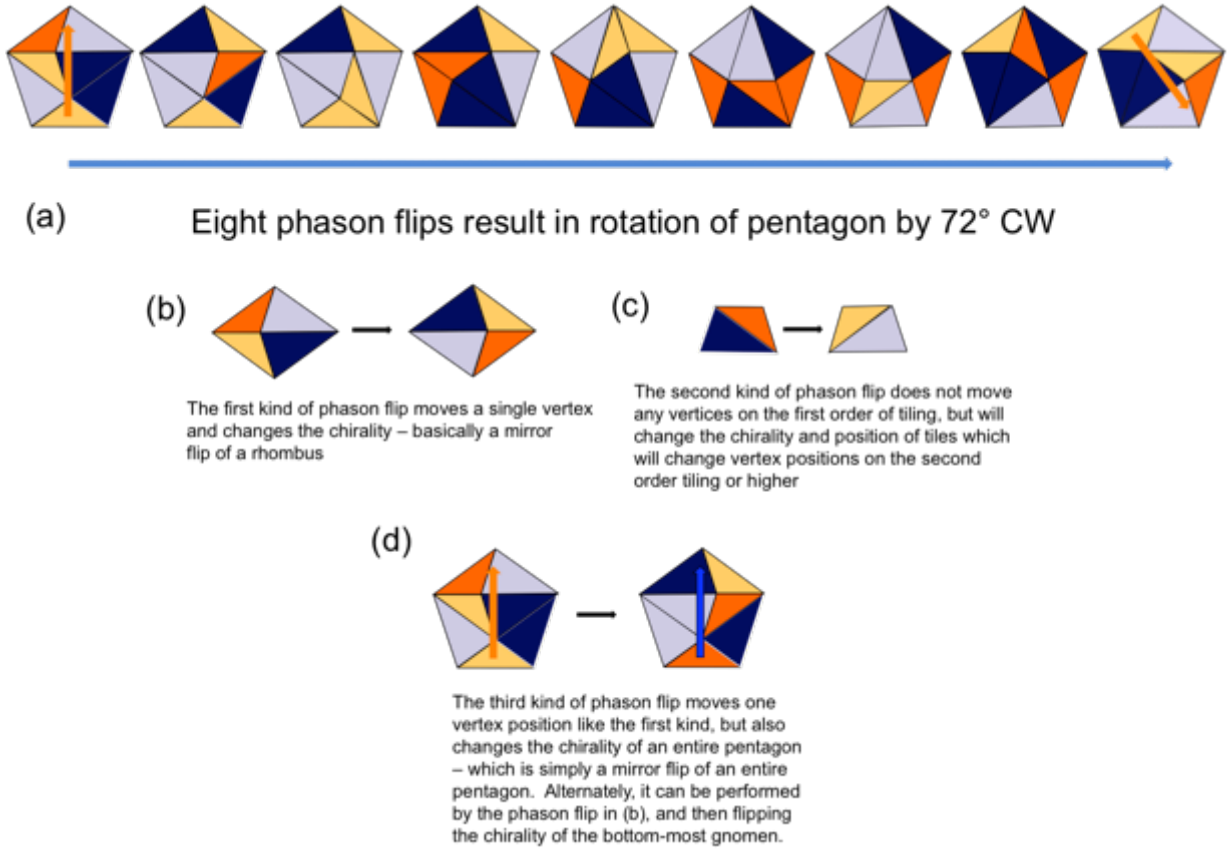


**Figure 4.37:** Phason flips which are possible in the Tübingen tiling. These can be used to introduce phason strain into a pentagon, change its orientation, or change its chirality entirely.

In ***Figure 4.37, (b) (c)***, we see the two allowed phason flips (Suck, 2002) for the Tübingen tiling. The phason flip in (b) is both a chiral flip as well as a vertex swap—the central vertex in (b) changes location during the phason flip[36]. After twelve combined phason flips from (b) and (c), the pentagon returns to the same state except rotated by 144°. The rotation of the

[36] If we are looking at an atomistic quasicrystal simulation, for instance, and only have a single species of particle, then we will not actually see the phason flip represented in (c). However, both (b) and (c) are used to rotate pentagons, as can be seen in (a).

pentagon is important because the same analogous process can be seen in other tilings. The structure that rotates when layering the blue decagonal motif with itself correlates with the definition of the phason flip in the other quasicrystalline tilings I have looked at, so it is not surprising that it is also the same here. Since we can rotate a given pentagon with the phason flips in (b) and (c), then we can interpret the pentagon rotation resulting from the layering as actually involving these phasonic flips. The final phason flip shown in (d) is the chiral flip of an entire pentagon, which does not correspond to the phason flips in (b) and (c). Though, we can produce the same effect as (d) with the phason flip in (b), and a chirality flip of the bottommost golden gnomen.

It is also worth noting that because the phason flip in (c) produces a chirality flip, but not a vertex flip, it also produces a change at the next higher order of deflation. At that next higher order of deflation, the requisite changes can be entirely described by the phason flips. Additionally, any change of one triangle to its opposite type is entirely defined by flipping the chirality of each triangle—at any stage of deflation.

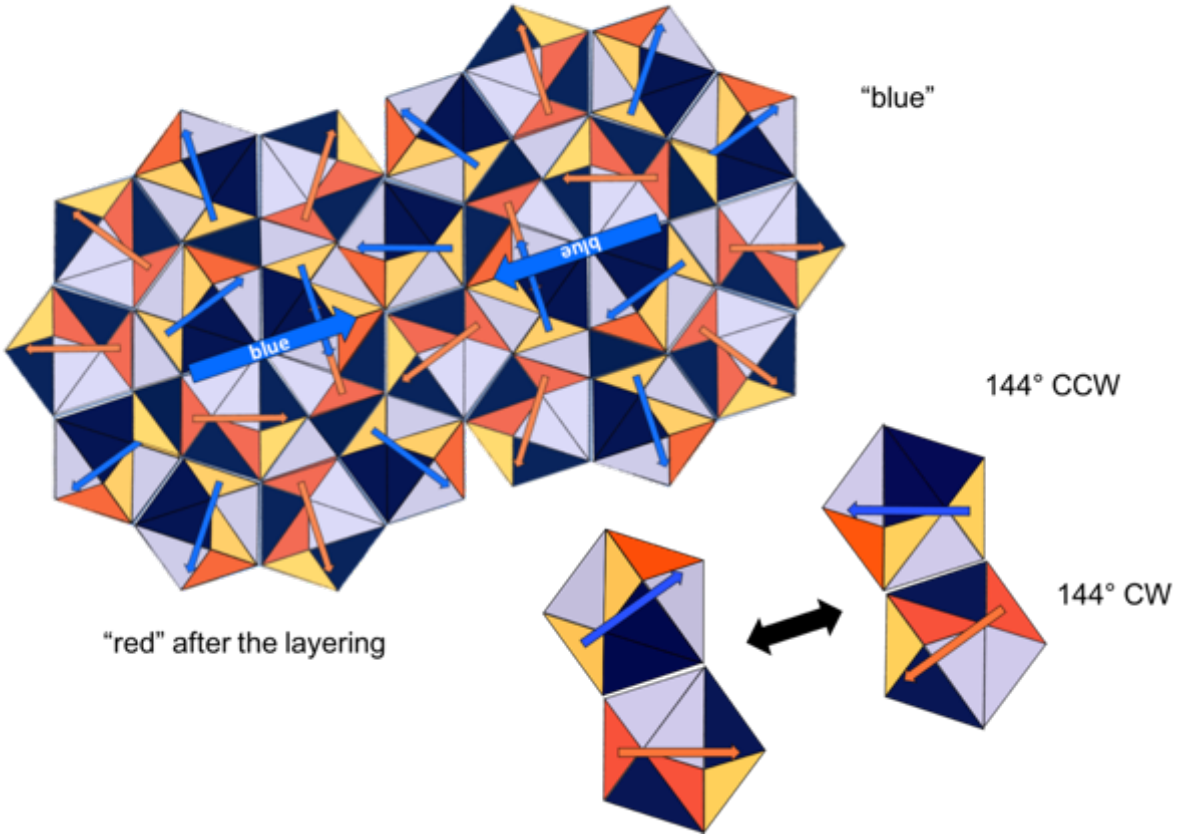


**Figure 4.38:** A blue motif (right) is layered over itself (left). This effectively accomplishes a phason flip in the overlapping blue and orange pentagons.

### Long Distance Overlaps

In the above figure, I have layered the blue decagonal motif on the right with the blue decagonal motif on the left. They overlap with two pentagons—a blue and orange, respectively. The chirality of the pentagons has been changed, in addition to their orientations. The decagonal motif on the left would now be considered an outer red decagonal motif! As decagonal motifs overlap each other, the number of chiral types remains constant—five of the orange and five of the blue. As each decagonal motif is concealed by additional higher-layer decagonal motifs, it sinks lower in the layer hierarchy. Roughly, if we want to know where in the hierarchy a given covering decagonal motif sits, we can approximate it as the number of changes that separate it

from the original blue decagonal motif[37]. **This is an overarching feature that is discovered to be true for all tilings in this thesis.**

Decagonal motifs that are chiral twins, like the pale and bright green decagonal motifs, are not allowed to overlap, or only partially, and so would sit on the same layer, or sublayer, respectively. Though unlike the sublayer definition I create for the Ammann-Kramer-Neri tiling in *Chapter Six*, this sublayer exhibits no hierarchy. The assembly of the pentagons is quite intriguing—they are allowed to partially overlap without any change to their pentagon orientations and chirality. This means that if two decagonal motifs are overlapping, only the complete pentagon overlaps need to make a choice—does it point away from this decagonal motif or the other decagonal motif? This would alternate the definitions in the above example, switching right from blue and left from red, and vice versa, by only rotating the two decagonal motifs by 144° CCW for the blue, and 144° CW for the orange, going from right to left. This angle is no coincidence—it is the interior angle of a decagon. This exactly parallels the analysis of every proceeding chapter.

[37] An ongoing theme in this thesis is that the rotations that result from these overlaps are phason flips, in a different sense than the hyperspace definition. Phason flips are then understood as a tile re-arrangement that moves motifs between layers in the layer hierarchy. **This is a convenient definition, as it moves phason flips into real space, and away from their traditional, but complex, definition in higher-dimensional space where they are defined as lattice points that fall outside of the cut window during the lifting protocol** (they would be outside of the blue rectangle in ***Figure 1.4***).

## Short Distance Overlaps

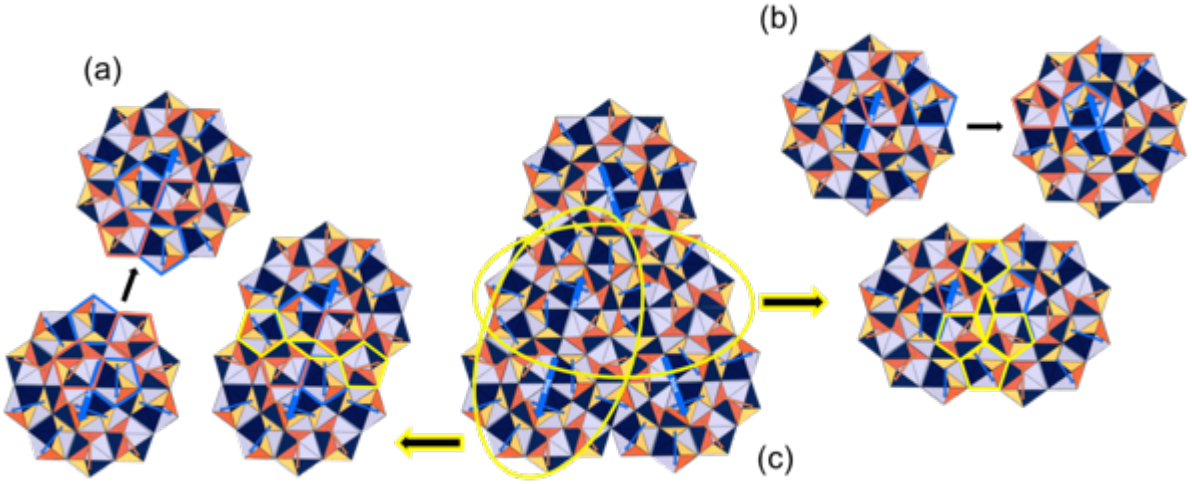


**Figure 4.39:** This image shows two ways that decagonal motifs can layer with a short interaction distance. In (c), a wedge has been removed from the second-order decagon in ***Figure 4.35*** that contains five decagonal motifs. From here, we can see the location of the decagonal motifs removed and disassembled in (a) and (b). In (a), an outer ring decagonal motif (bottom) layers over an inner ring decagonal motif (top). In (b), an inner ring decagon motif (left) layers over another inner ring decagonal motif (right).

Just as there are two incommensurate distances between the vertices of the original triangle tiling, there are also two incommensurate distances in the layering picture. ***Figure 4.39*** shows the placement of two types of short layering distance. In part (a), we see two tail-to-tail decagonal motifs that have been layered at the short distance. Pentagons with a blue or orange outline indicate that these pentagons do not change after the layering. They are the same on the top decagonal motif as they are on the bottom. Pentagons marked with yellow pentagons, however, do undergo a change when layered. Whenever a pentagon is completely layered over by the top decagonal motif, it undergoes a chiral flip. So, orange will turn to blue, and blue will turn to orange. **This is a simpler version of the same phenomenon seen in the three-dimensional Ammann-Kramer-Neri tiling (AKN), which will be discussed in *Chapter Six*.** The rhombus made from two different chirality golden triangles also undergoes a chiral flip during the layering. Remarkably, the decagonal motifs are constructed and layered over each other in such a way that the pentagons will neatly flip between blue and orange for every additional pentagon that layers over them.

In ***Figure 4.39 (b)***, two inner ring decagonal motifs are shown which, instead of being tail-to-tail or 180° separated, are 36° rotated, such that their blue arrows both face the central decagonal motif of the second-order decagon. In this layering, the same rules are followed, but in a different way. Whereas the 180° case had only two chirally flipped pentagons, the 36° case has four. ***Figure 4.31*** describes the same distance of overlaps, but with covering motifs instead. No chiral flips are produced there because the covering motifs already have the necessary chiral decoration. The layering method is interesting because these decorations are automatically produced simply by layering the blue decagonal motifs in the correct order.

**Identification and Role of Different Green Decagonal Motifs in the Covering and Layering Pictures**

The inner pale green and inner bright green decagonal motifs exist in the inner ring of the second-order decagon. The inner pale decagonal motif is defined as the decagonal motif with no flipped phason units that sits just outside of the decagonal motif with two flipped phason units, where the front-most unit is flipped by this same inner pale decagonal motif, and the left phason unit is flipped by the tiling that belongs to the neighboring red decagonal motif. Likewise, the inner bright decagonal motif is defined in the same manner, but with the singly flipped decagonal motif placed on the right, which can be seen in ***Figure 4.40*** below.

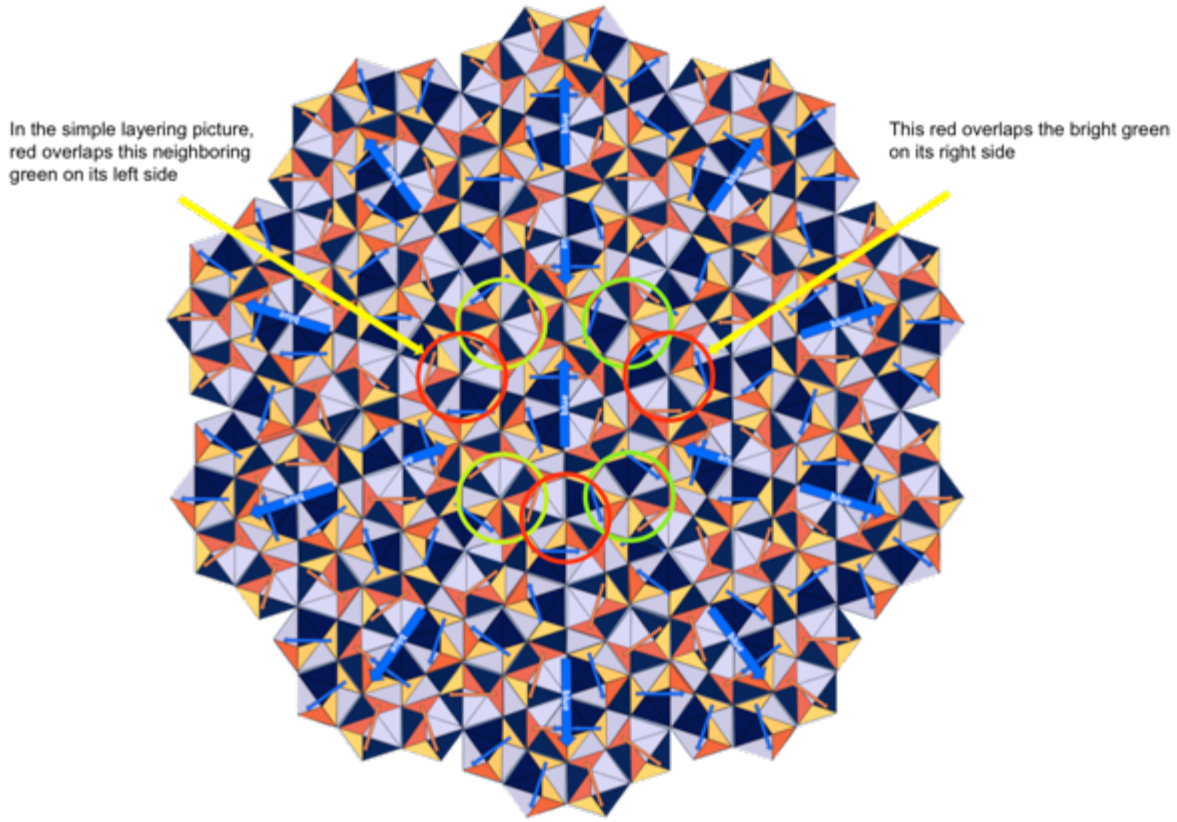


**Figure 4.40:** In the simpler layering picture outlined earlier, the decagonal motifs in the green and red circles were treated as real covering entities. However, we saw that expanding the decagonal motifs with an outer decagonal ring of pentagons led to the automatic tiling of these pieces when only the decagonal motifs with unflipped phason units were included in the assembly. These are the decagonal motifs with blue arrows in the above figure—also note that some of them are partially or wholly covered in this version of the layering. **This has been a theme of the thesis since *Chapter Three*, where we see that expanding our motifs with rings can reduce the number of necessary covering motifs.**

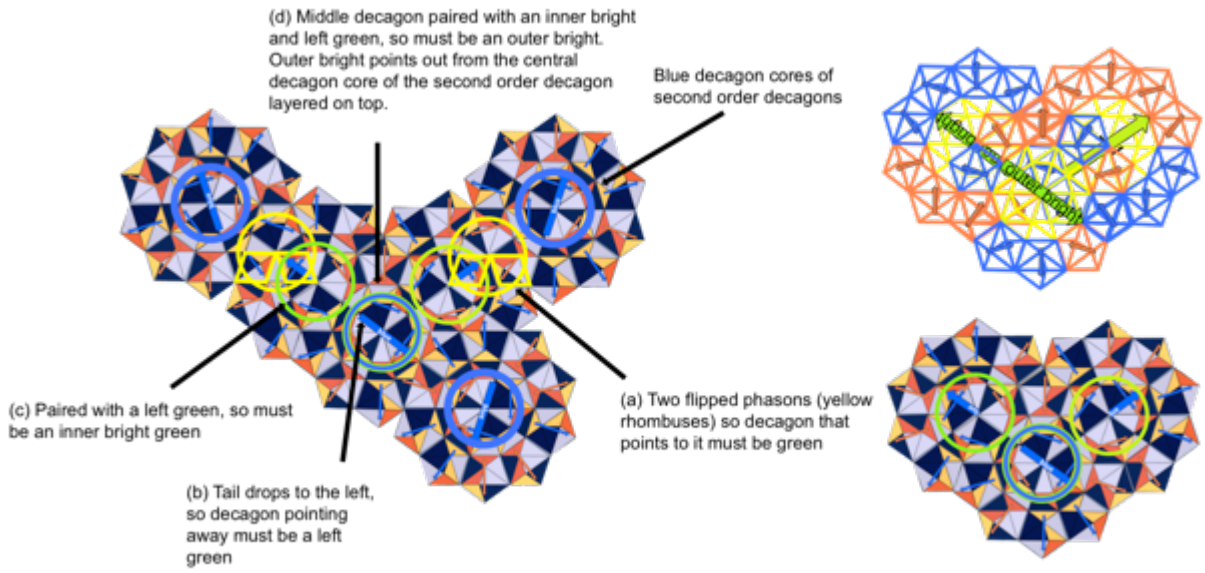


**Figure 4.41:** Green decagonal motifs are defined by the type of phason-flipped decagonal motif they point at, and the orientation of the decagonal motif they point away from.

Although green decagonal motifs had previously been defined as either pale green or bright green, depending on whether there was a decagonal motif layered on top of it from the left, or the right, with respect to the central decagonal motif, I know from later examination that these simple red, green, etc., decagonal motifs are not "real", in the sense that expanding the size of the motif around a decagonal motif with no phason flipped units will work to create the same tiling without requiring these simple decagonal motifs. In the terminology of previous chapters, these are *secondary clusters* (or secondary motifs, in the terminology of this thesis). This was done originally to fill in the holes that would otherwise exist in the tiling, but it also redefines what decagonal motifs are used in the covering, as can be seen in ***Figure 4.27***. With this new definition of the decagonal motif, there is also another way of defining its type. It is quite straightforward—decagonal motifs can be classed into types by first looking at what decagonal motif their arrow of mirror symmetry points toward, and then which decagonal motif they point away from.

Consequently, each green decagonal motif is likewise defined by the configuration it points toward, and the configuration it points away from. The green decagonal motifs in ***Figure 4.41*** point toward a decagonal motif with two flipped rhombus phason units, which are seen in the yellow circles. In (a), we see a decagonal motif that is pointing toward another decagonal

motif with two flipped phason units. This means that this is some kind of green decagonal motif, but we do not know which one yet. The decagonal motif that it is pointing away from is itself pointing toward a decagonal motif with three flipped phason units, so it must be a cyan decagonal motif. In (b), we look at the tail of the cyan decagonal motif and see that it is dropping to the left. This is one way of defining the green decagonal motif as a *left* decagonal motif. As shown in ***Figure 4.41 (d)***, left green decagonal motifs are always paired with either an inner bright decagonal motif at a 108° angle, or a right green decagonal motif at an angle of 144°. Since the angle here is 108°, we know that the other decagonal motif pointing away from the cyan decagonal motif must be an inner bright decagonal motif (c), since these are the only configurations that exist in the tiling. In (d), we can identify the cyan decagonal motif as an outer bright decagonal motif, since it is pointing away from the inner bright decagonal motif. This means that these two decagonal motifs are part of a second-order decagon that is layered on top of the other second-order decagon that contains the left green decagonal motif. This chiral pair of left and right green decagonal motifs serves an important role by allowing the inner green decagonal motifs of two overlapping second-order decagons to both point away from the same cyan decagonal motif. Without this second pair of decagonal motifs, the decagonal motifs could not tile space without overlap errors. The above explanation then justifies the existence of these other covering motifs (L and R in ***Figure 4.42***), which might otherwise be mysterious. This is illustrated in ***Figure 4.42***.

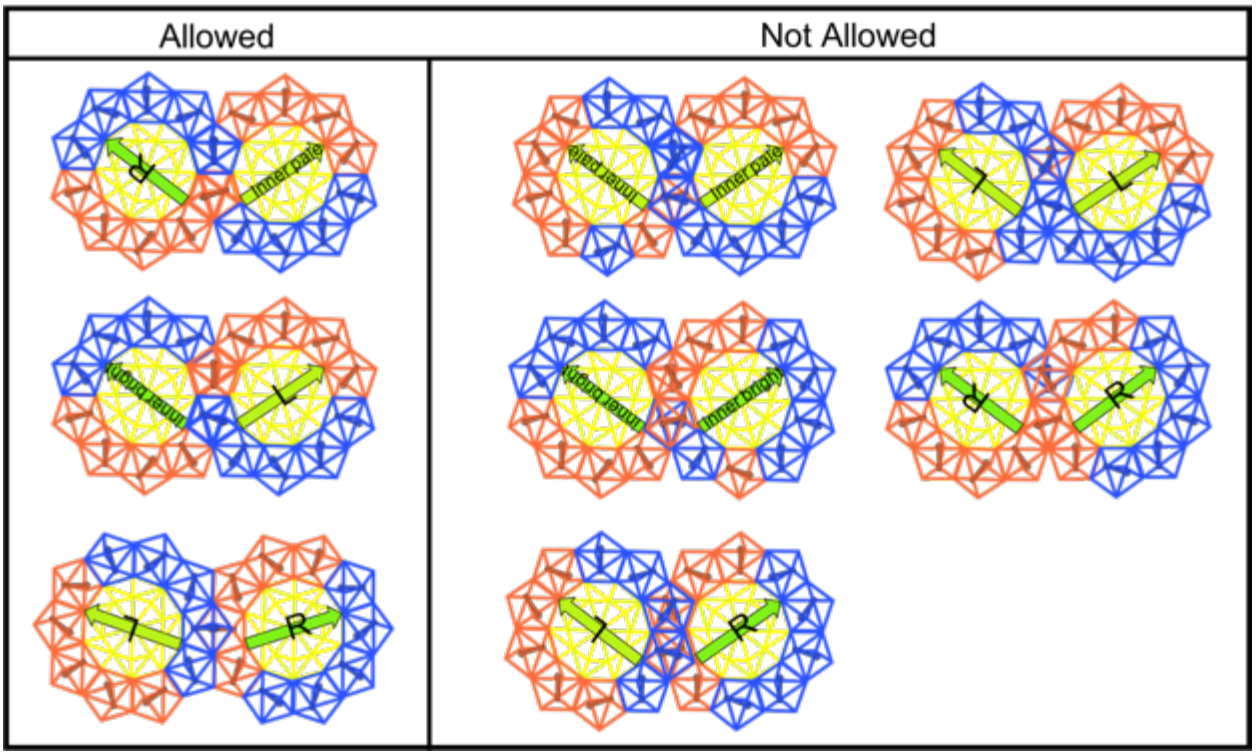


**Figure 4.42:** The left panel illustrates the coverings allowed by the left and right pair of green decagonal motifs, in combination with the inner pale decagonal motif and inner bright decagonal motif, while the right panel illustrates those configurations which are not allowed due to incompatibility between their outer ring of pentagons.

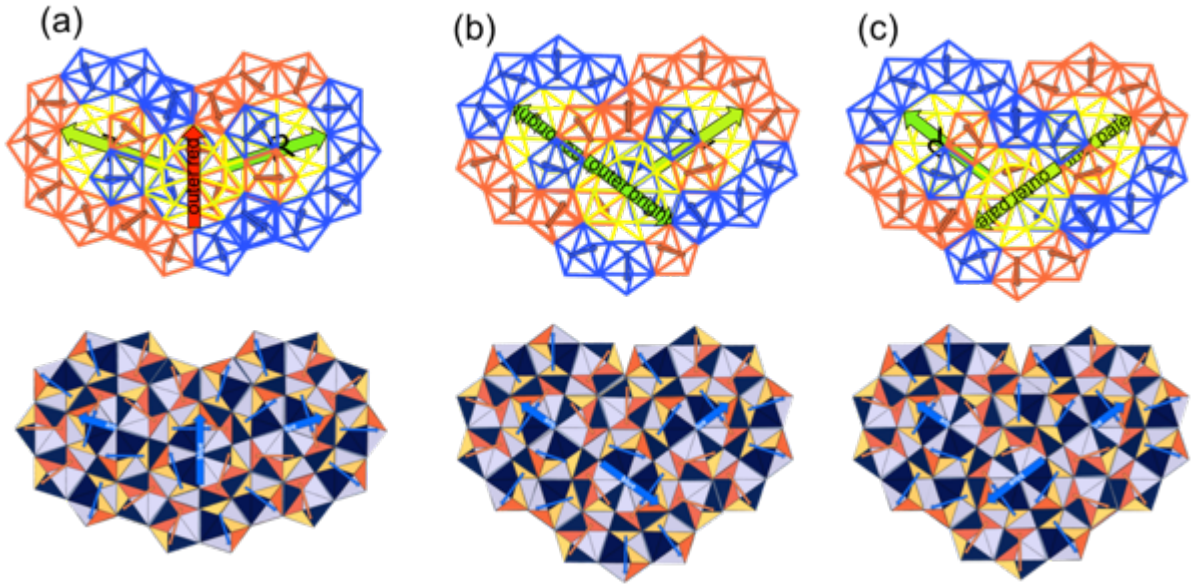


**Figure 4.43:** The left and right green decagonal motifs exist in three configurations across the tiling and these three pairs of figures show their (partial) creation with the single layering motif. By nature, any tiling created by the single layering motif will be incomplete if the outermost tiles do not sit on top.

## Conclusion

With these rules, we have a real space method of generating a quasicrystal tiling of arbitrarily large size. The tiling is then seen as the same quasi-unit cell existing in a unique place in the layer hierarchy. Moving a quasi-unit cell around will occur by means of phason flips that flip it between one of the thirteen decagonal motifs displayed in ***Figure 4.27***. These new motifs are then placed on the lattice points of a new quasi-unit cell. For every overlap between blue-type decagonal motifs, a series of phason flips takes place that moves it into either a new covering motif, if we work with the covering picture, or a new layer hierarchy, if we work with the layering picture. **The layering picture works for the Tübingen triangle tiling, provided that we always move any blue decagonal motifs in a second-order decagon back to the top of the layering when we are done with the layering process. This makes sense, as it is just reiterating the idea of the layering process itself, but a user may encounter this detail if treating a second-order layer as its own layer unit, which it is not. It is simplest to define the 2D position and orientation of each polygonal motif, and then put them all into their correct respective layers as a single final step. This same requirement is noted in the**

***Algorithm* sections for *Chapter Two* and *Chapter Three*, and is a potential source of confusion.**

The goal of this chapter was to show that the hierarchical polygonal cycling method works for the Tübingen triangle tilings, whether by covering or layering rules, and can greatly simplify our understanding of quasicrystal tilings by producing a real-space model for the lattice or structure, as well as provide a real-space model for concepts which are classically restricted to hyperlattice mathematics, such as phason flips. Madison (A. E. Madison & P. A. Madison, 2019) says of the FCC icosahedral quasicrystal, for instance, "Phasons are intrinsically linked with the higher dimensional picture. Further investigations are thus needed to incorporate them into the essentially 3D description." **An approach like the one listed here may turn out to be what Madison is looking for.**

In the next chapter, I introduce the layering picture for the Niizeki-Gähler tiling. This tiling holds a special place in this thesis because of its close ties to the Liao, 2013 publication—there are no analogues to this research in the literature, but this paper comes close to describing the petal motifs. The layering picture gives us an entirely different way of understanding Liao's work.

## Chapter Five

### A Layering Construction of the Niizeki-Gähler Dodecagonal Tiling

## Introduction

The Niizeki-Gähler tiling (NGT) is a quasilattice tiling similar to those previously discussed. It has three fundamental polygons, which are combined into a fundamental polygon—a dodecagon. These fundamental dodecagons are then combined into a rotationally symmetric dodecagonal ring, which is then used to construct yet-larger fundamental polygons. Like some of the previous tilings, the ring is not so simple, but is still straightforward to implement with the layering method once it has been assembled. Each quasilattice tiling looked at so far has introduced unexpected quirks, and this one is no outlier.

Remarkably, there are publications (Hong et al., 2009; Liao et al., 2010, 2013) that contain some of these motifs. Although there is no hierarchical work in these publications, they still highlight the interest that researchers have in this field and make apparent the contribution and context of this thesis. In this chapter, I outline the same layering process as shown in previous chapters, and then compare and contrast the work done in the 2013 publication to better understand both their work and mine.

**Fundamental Polygons**

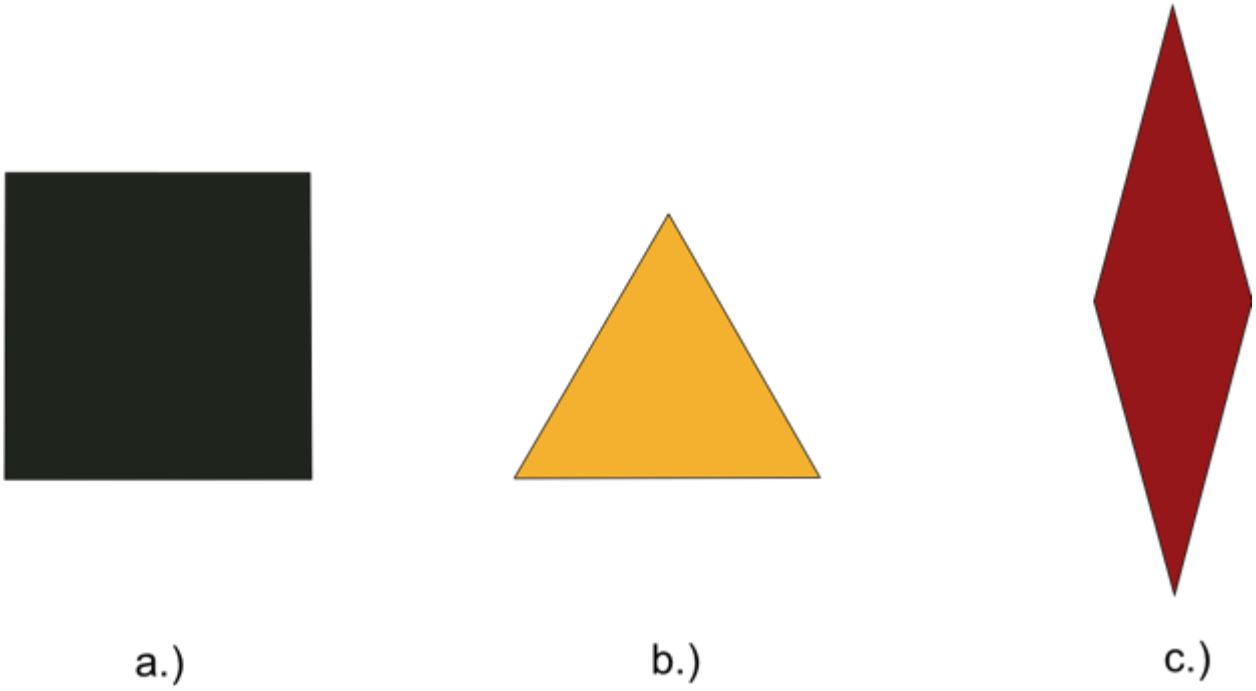


**Figure 5.1: The Niizeki-Gähler tiling comprises a square, an equilateral triangle, and a 150-30 rhombus.**

The Niizeki-Gähler tiling (Hong et al., 2009; Liao et al., 2010, 2013; Liao et al., 2013), also known as the dodecagonal ship tiling (Liao et al., 2010), is an axial (as a real material, it would be quasiperiodic in 2D but periodic along a single 3D axis) dodecagonal quasi-lattice tiling that has three components—a square, an equilateral triangle, and a 150-30° rhombus. These components have the same edge length and exist in the ideal tiling in a ratio of 2.73: 1: 0.37 for the triangles, squares, and rhombuses, respectively (Schenk et al., 2019). Similar to the other quasilattice tilings that have been discussed in this thesis, these tilings can be broken apart into composite dodecagonal motifs (characteristic polygons) which can then be assembled into a larger dodecagonal petal motif, and which then overlaps itself in a layering protocol to iteratively produce the entire tiling. There is also a known Gummelt-like single-cluster covering (Schenk et al., 2019). In this chapter, I will show how to construct the layering protocol for the tiling and, going a bit further, show that the same methodology will create a route for understanding the single-motif covering that is different from the Liao paper. Additionally, this work will highlight an element that is missing from other work from the same authors (Liao et al., 2013).

## Characteristic Polygon

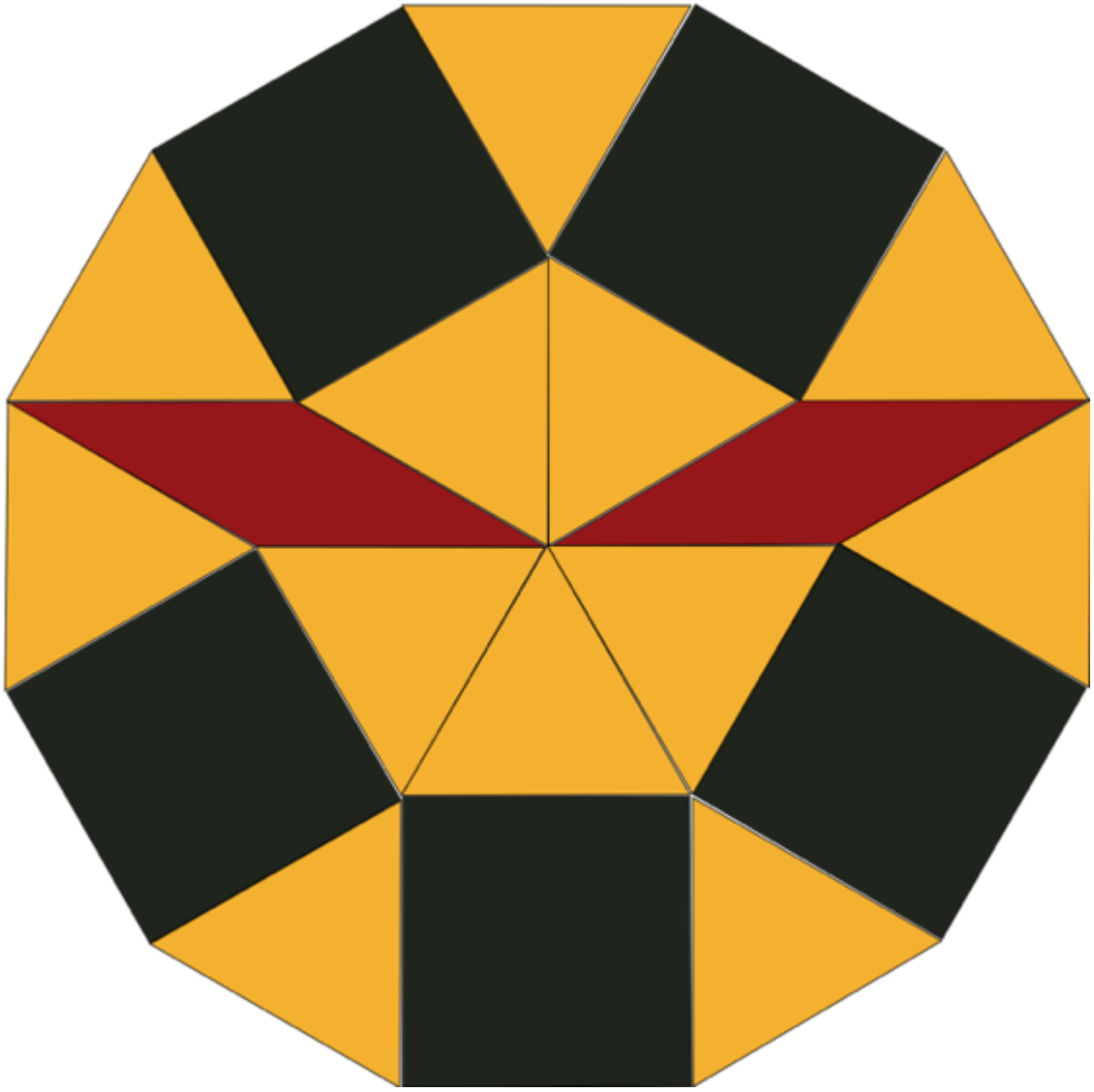

**Figure 5.2:** The three fundamental polygons can be assembled into a dodecagon, as seen here, which has twelve triangles, five squares, and two rhombuses.

## Phason Flips

**Figure 5.3:** The square-triangle tiling (which is not pictured and does not contain rhombuses) does not have a phason unit, but the Niizeki-Gähler tiling does. Here it is removed from the dodecagon. 60° rotations of this shield represent a phason flip.

Although the phason flip emerges from the layering picture described layer in this chapter, it is important to understand the motifs that can be generated via these phason flips to understand the motif assemblies first presented here. Most quasicrystal tilings have a phason unit that uses a 180° flip to rotate a group of tiles. The Niizeki-Gähler tiling uses a 60° rotation instead. This shield motif, comprising a single rhombus, two triangles, and a single square, can undergo 60° rotations to produce a phason flip. Likewise, rotations of this shield will produce the other dodecagonal motifs that cover the tiling. Two examples of these other dodecagonal motifs are presented in ***Figure 5.4***. Note that in the original dodecagon, as seen in the left image of ***Figure 5.4***, two shields can share a single rhombus. If one of these shields undergoes a phason rotation, then the other shield is destroyed. In this way, the rhombus could conceivably travel throughout the tiling. Rotation of the top or bottom shield will produce ***Figure 5.4 (c)*** or ***Figure 5.4 (b),*** respectively.

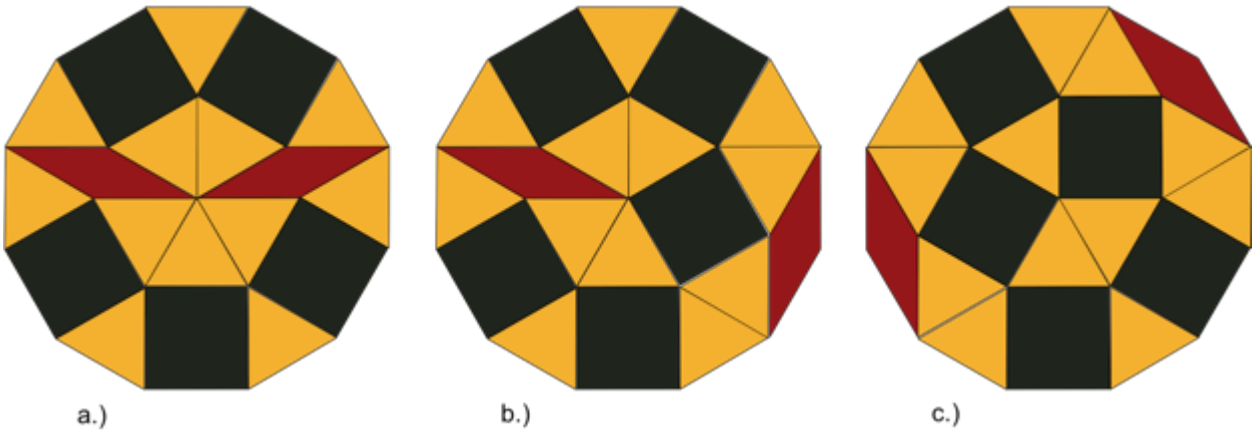


**Figure 5.4:** The phason flip can be used to generate two other dodecagons that occur in the tiling. These can be used to create additional rings around the central dodecagon, and they can also be used to migrate the rhombus throughout the tiling.

As in the other two-dimensional tilings of this thesis, there is a characteristic polygon. The Penrose tiling has, for example, a decagon and the Ammann-Beenker tiling has an octagon. Likewise, the Niizeki-Gähler tiling has a dodecagon. Creating this dodecagon (***Figure 5.2***) is the first step in building the tiling. Interestingly, this dodecagon—in the abstracted picture of the layering model—makes up the entire tiling. This is a different concept than the single-covering T-cluster that will be discussed later. Like the other characteristic polygons, it also contains a line of mirror symmetry. I will make note of this line of mirror symmetry later when constructing the additional motifs.

## First-Ring Dodecagonal Expansion

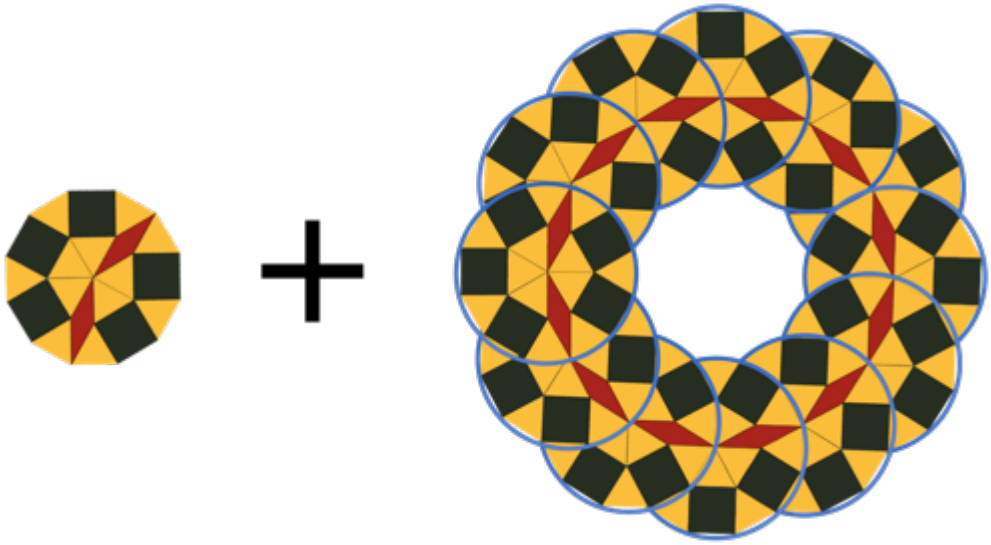

**Figure 5.5:** Take the dodecagonal motif from ***Figure 5.2*** and create a ring of twelve of them around another copy. This is the fundamental motif of the Niizeki-Gähler tiling and forms our first "blue" dodecagonal motif, in analogue with the "blue" pentagonal motifs from *Chapter Two* that contain the highest rotational symmetry with respect to the other motifs.

Twelve of the characteristic dodecagons are arranged into a ring as shown in ***Figure 5.5***. A single characteristic dodecagon is placed inside of this ring, as shown in ***Figure 5.6***.

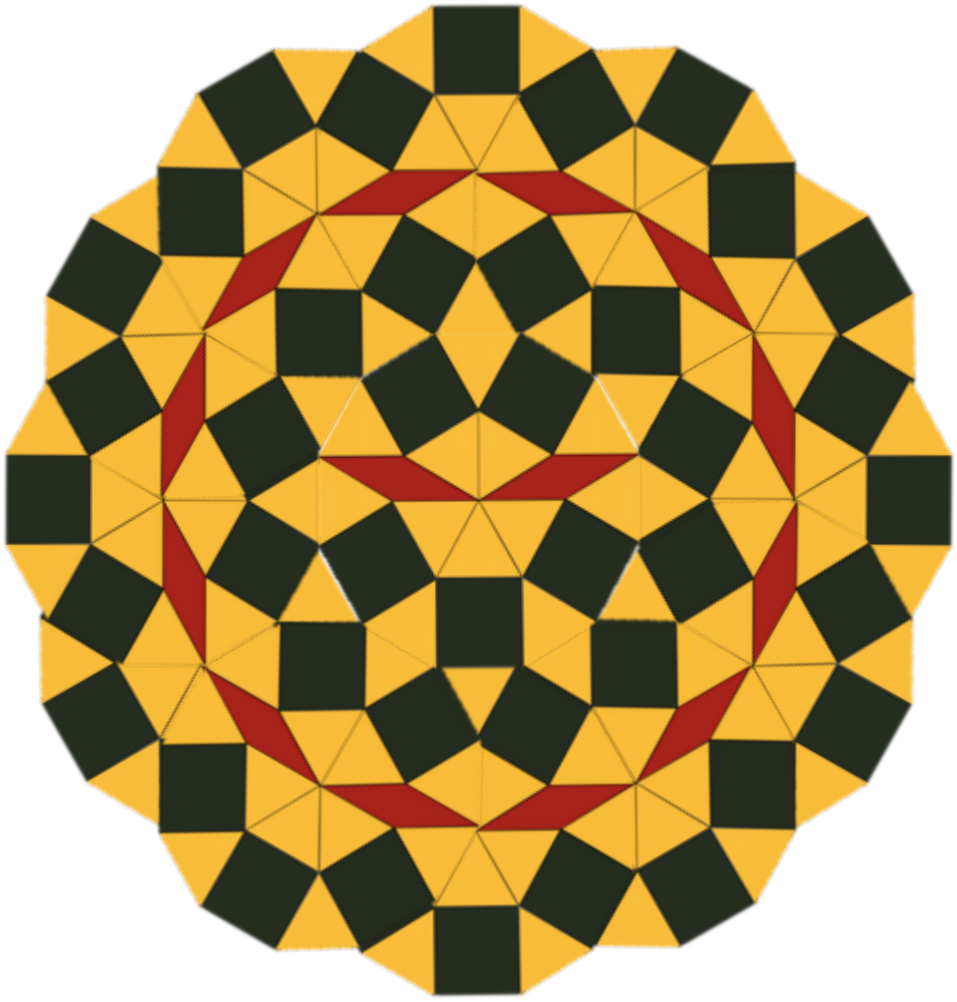

**Figure 5.6:** This dodecagonal motif has one ring of characteristic dodecagons around a central characteristic dodecagon, so I call it the first-ring dodecagonal motif. In this expansion of the tiling, it will serve the same role as the blue pentagonal motif in the Penrose tilings.

The dodecagonal motif shown in ***Figure 5.6*** is special because, in the layering picture, this motif creates all of the tiling. It is also special in the covering picture, because it can transform into any of the other dodecagonal motifs by simple phason rotations, brought about by the layering procedure. This motif, similar to other petal motifs described in this thesis, contains the instructions for building the entire infinite Niizeki-Gähler tiling.

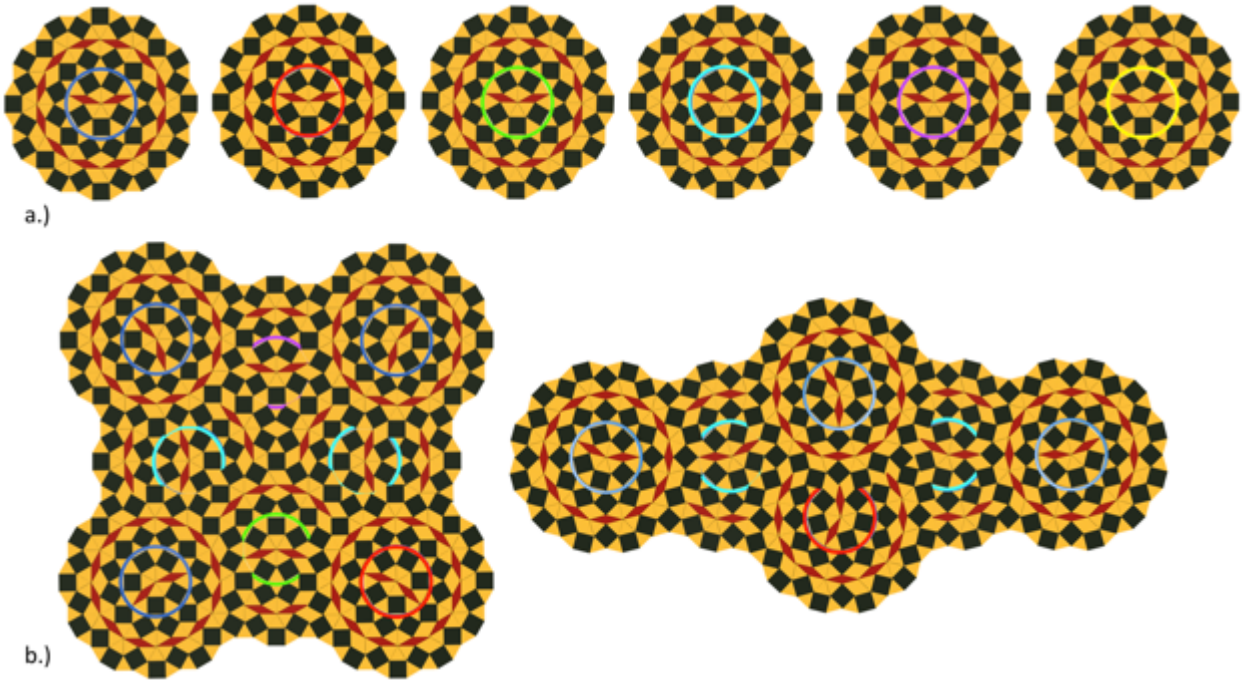


**Figure 5.7:** Here is an example of a square and rhombus that have been tiled with the dodecagonal motif in its first-ring expansion. The square and rhombus shown also have chiral twins which are also used in the second-order motif assembly. There are now six layers of dodecagonal rings—blue, red, green, cyan, purple, and yellow—in descending order. Note the lack of a purple dodecagonal ring in the larger rhombus construction. The dodecagonal motif with the yellow ring (right(a)) is used for the triangle construction in ***Figure 5.8***.

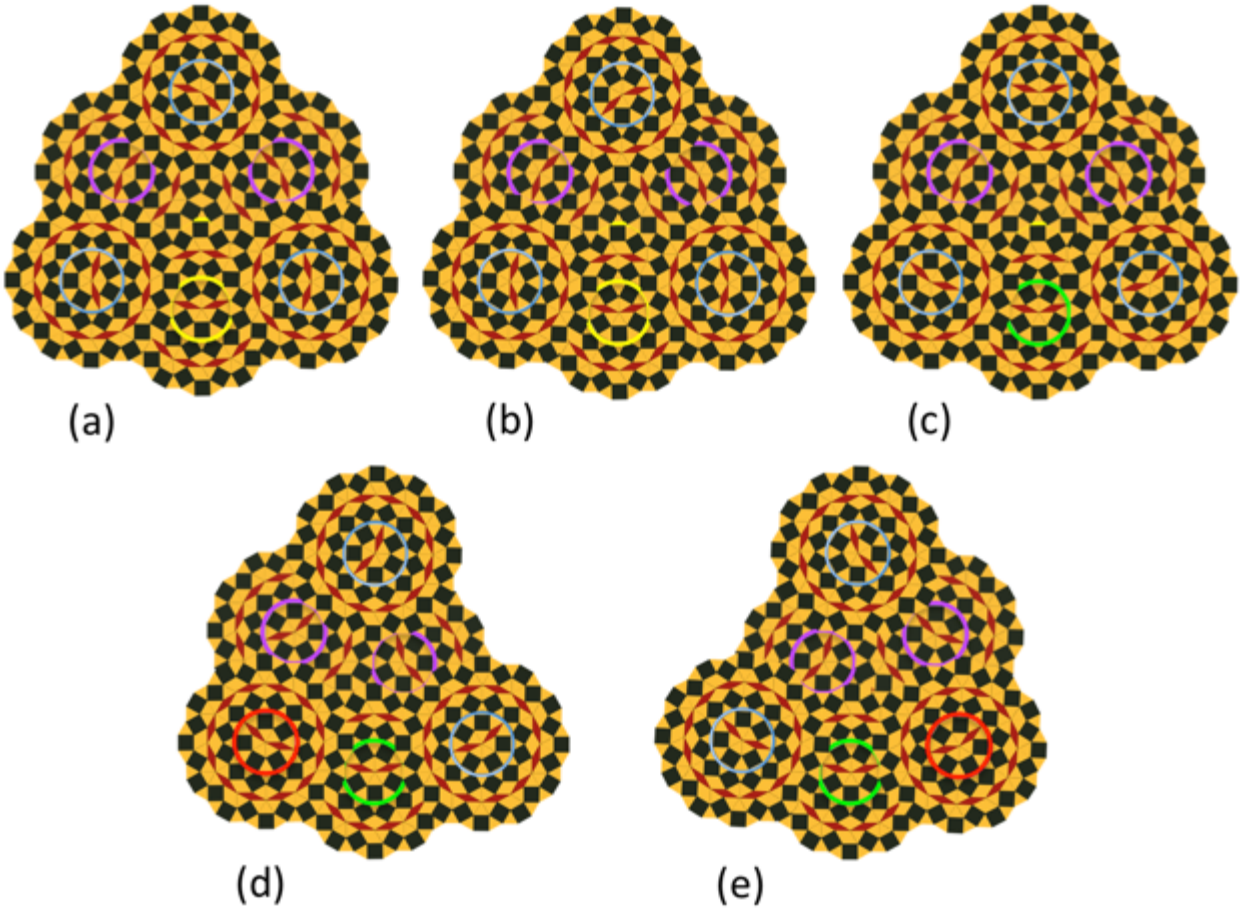


**Figure 5.8:** Here are some examples of the triangle construction in the picture of the first-ring dodecagon layering. (a) and (b) are chiral pairs, as are (d) and (e). Note that if a shape is, e.g. purple, but is only layered with two other dodecagons, then it implies that more dodecagons are layering it in the complete tiling.

In a fashion similar to the Penrose tiling from *Chapter Two*, we see the construction of the fundamental polyhedra from composite polyhedral petal motifs—dodecagonal ones in this case. This process creates a new square, triangle, and rhombus, which can then be used to build new second-order dodecagons, as seen in ***Figure 5.9***. Since there is a dodecagonal motif at each vertex, each of the polyhedra meet with complete characteristic dodecagon overlaps. In similar fashion to other quasilattice tilings, rotations of the characteristic dodecagon will produce a phason flip. Hence, constructing a new covering motif is accomplished by a series of these simple phason flips.

## Construction of Larger Characteristic Dodecagon

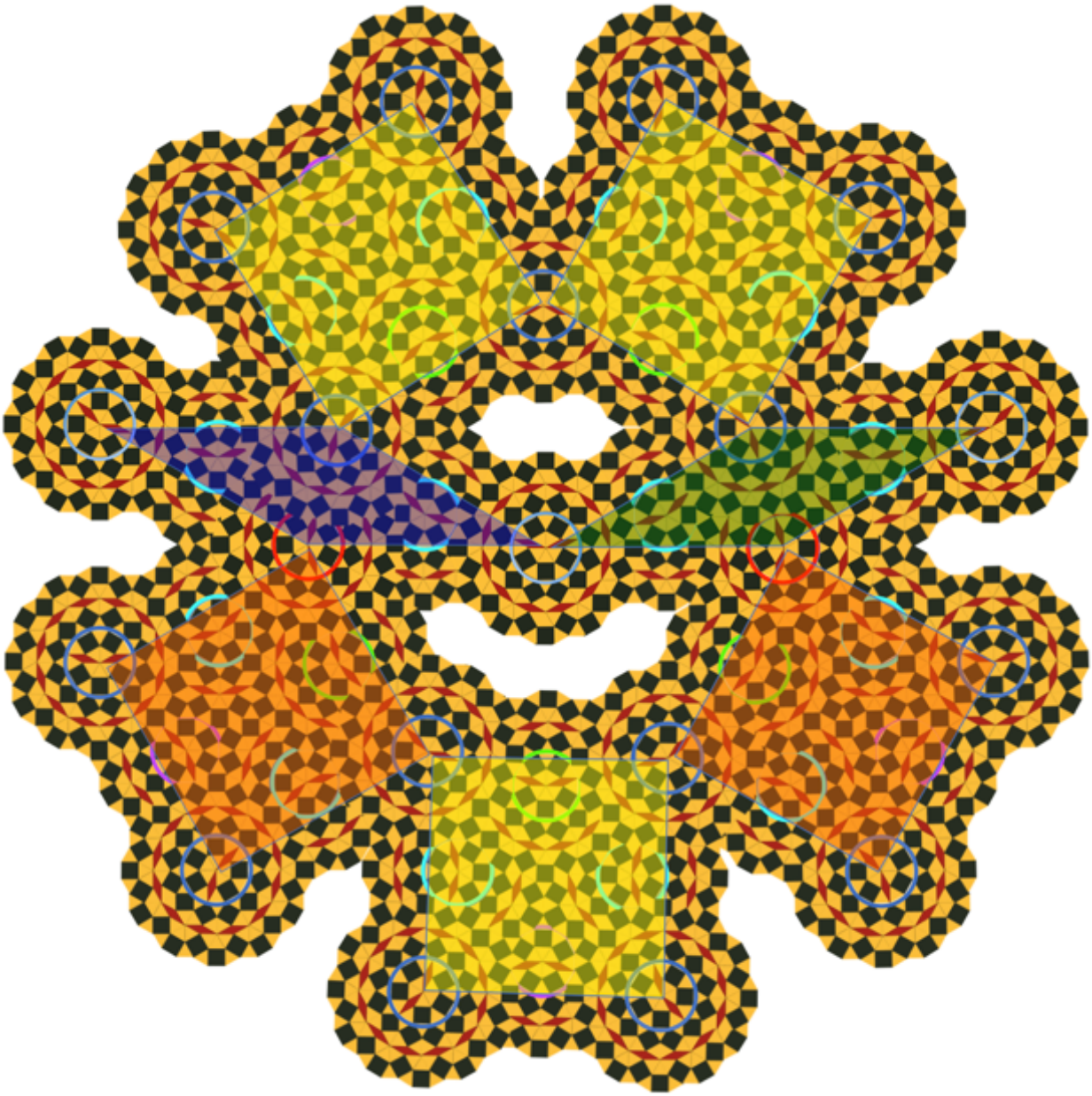

**Figure 5.9:** Two types of square and two types of rhombuses combine to form a new second-order dodecagon. The triangles of ***Figure 5.8*** have not been included for clarity.

### Second-Ring Dodecagonal Expansion

As seen in some of the other quasicrystal tiling chapters, we can also sometimes reduce the complexity of our layering hierarchy if we expand the motifs with new rings. Although this increases the complexity of the single motif, it can reduce the number of layers needed in total.

Regardless, this tradeoff is an interesting concept to explore by adding additional rings to see how the tiling process changes—especially since this is the general protocol that can be used to create this kind of ring for any of the quasicrystalline tilings shown in this thesis. The Niizeki-Gähler tiling is interesting with respect to its additional rings, as these additional rings are not made from the original dodecagon of ***Figure 5.2***, but rather versions of it that contain phason flips, as seen later in Figure 5.4.

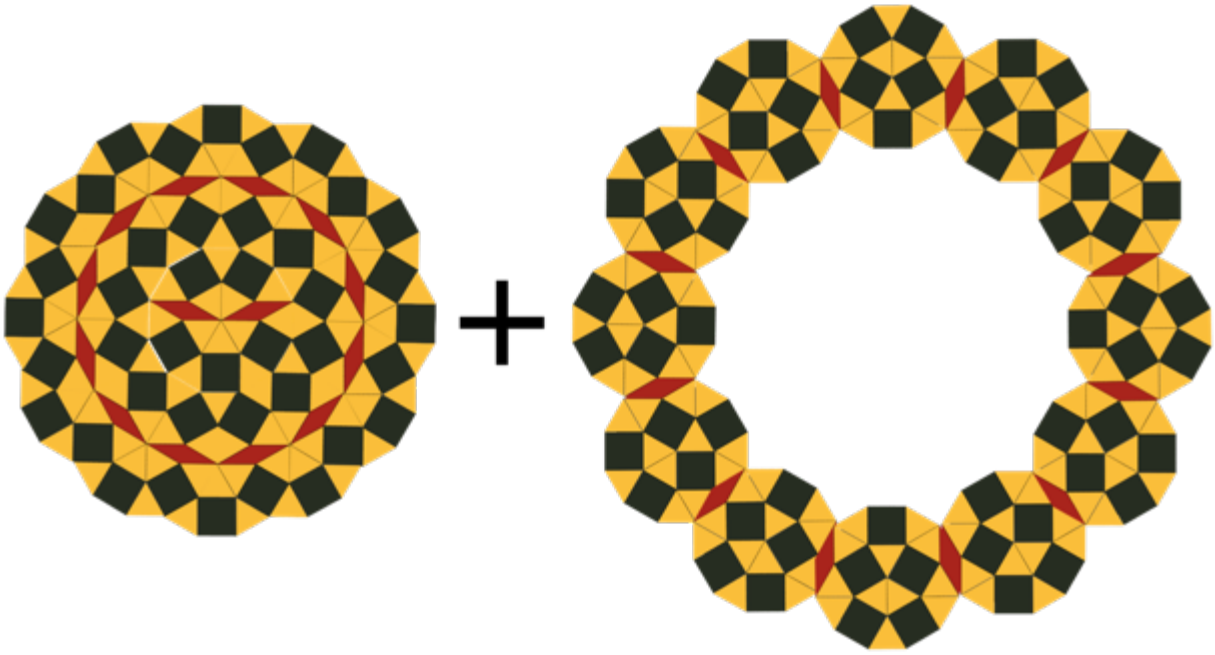

**Figure 5.10:** A second ring can be added to the dodecagonal motif. Take ***Figure 5.6*** and add a 12-fold ring of the (phason flipped) characteristic dodecagons from ***Figure 5.4 (c)*** to create the second-ring dodecagonal motif. These dodecagons can be generated by phason flips using a shield rotation, which is discussed later in the section on phasons.

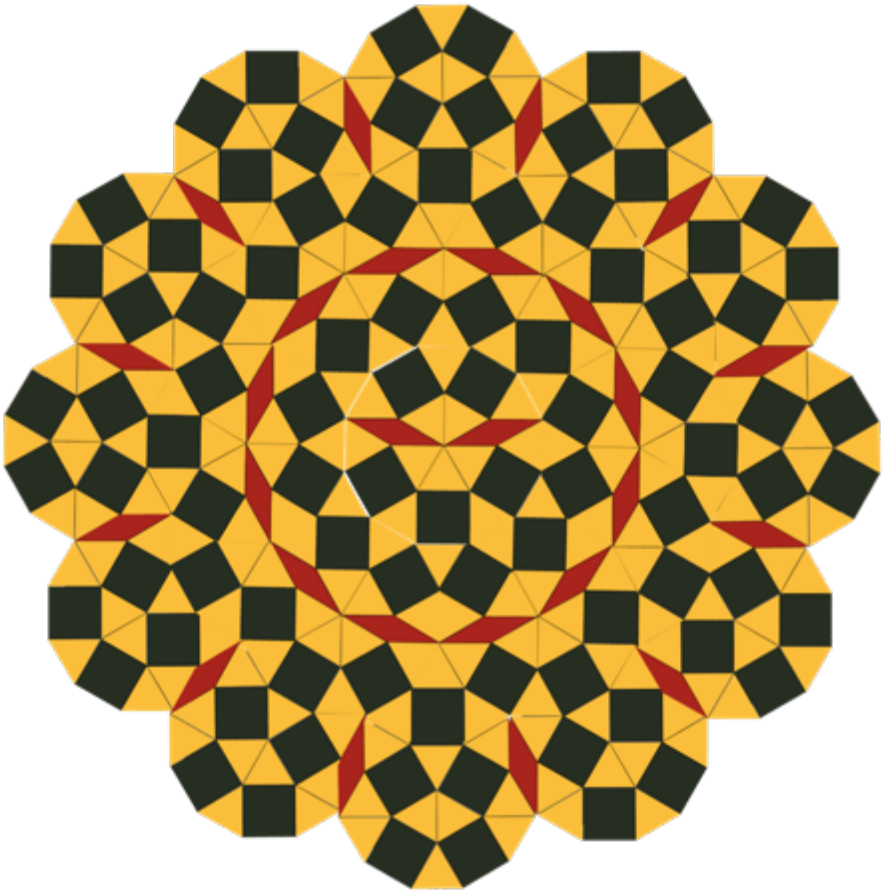

**Figure 5.11:** This is the second-ring dodecagonal motif. But note that it is not made entirely from the same characteristic dodecagon, but rather the original from ***Figure 5.6*** and ***Figure 5.4 (c)***. There is also the characteristic dodecagon from ***Figure 5.4 (b)***, but it is a composite characteristic dodecagon made from the other two, so we do not need to explicitly include it.

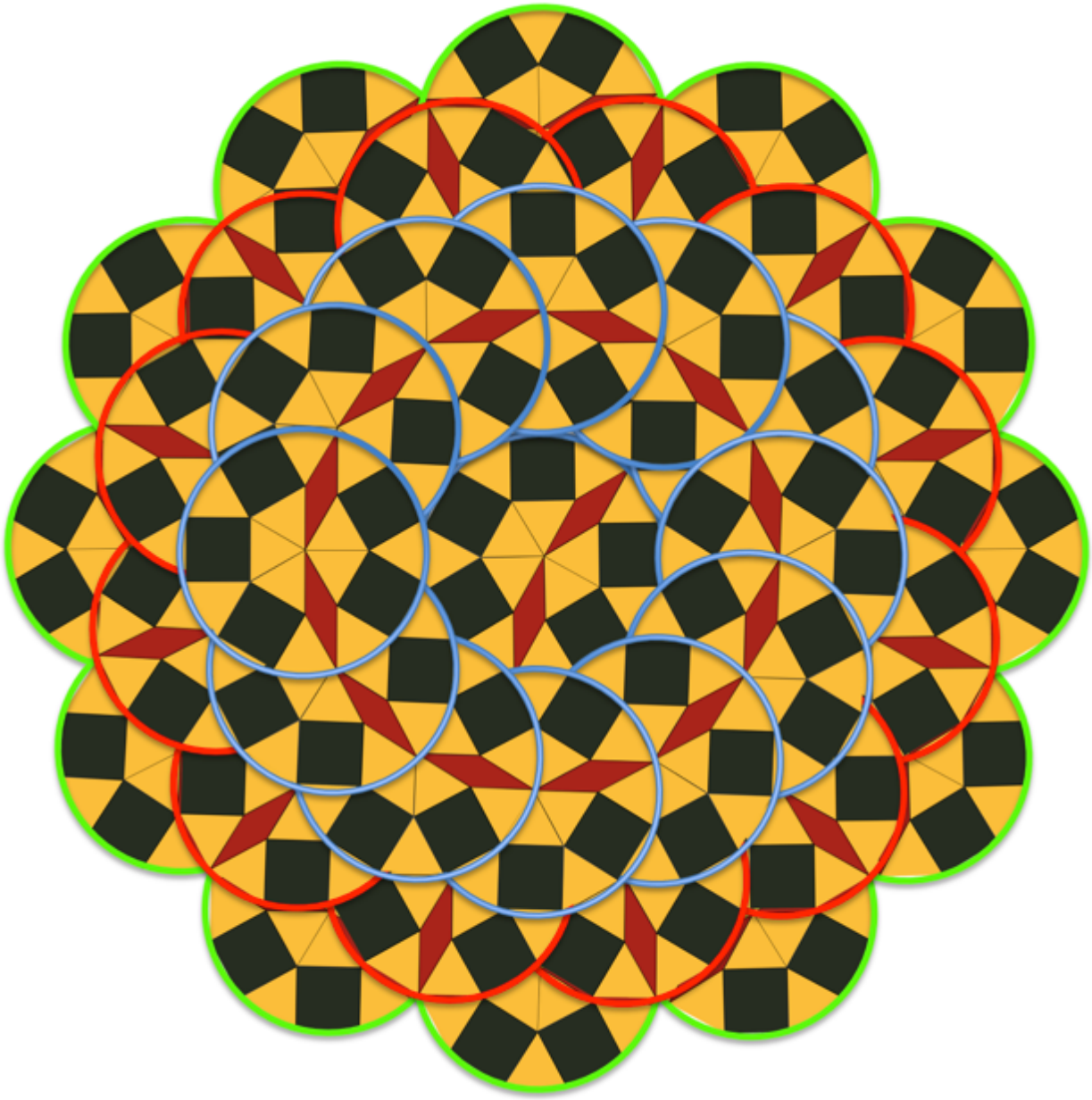

**Figure 5.12:** We could refer to this motif as either the second or third-ring expansion, depending on how we want to think about it. But since the second ring (red outlines) is automatically created by adding the third ring (green lines), it's easy enough to just call it a second-ring expansion. In any case, all three dodecagons from ***Figure 5.4*** are used in the construction of this motif.

The second-ring dodecagonal motif can serve the same role as the blue pentagonal motif in the Penrose tilings, but now we only have three dodecagons vs. the six in ***Figure 5.7***. In this respect, it is a simpler tiling.

**Figure 5.13:** These three second-ring dodecagonal motifs are sufficient to layer the tiling. Note they are all the same—these are the layering motifs, and not covering motifs. The set of coverings can be made by creating edge-to-edge dodecagons, such that there are two complete overlaps of the composite characteristic dodecagons. Each additional edge-to-edge dodecagonal motif will produce a covering that corresponds to a dodecagonal motif that is deeper in the layering hierarchy, as detailed in *Chapter Two*.

## Phason Flips in the Second-Ring Dodecagon

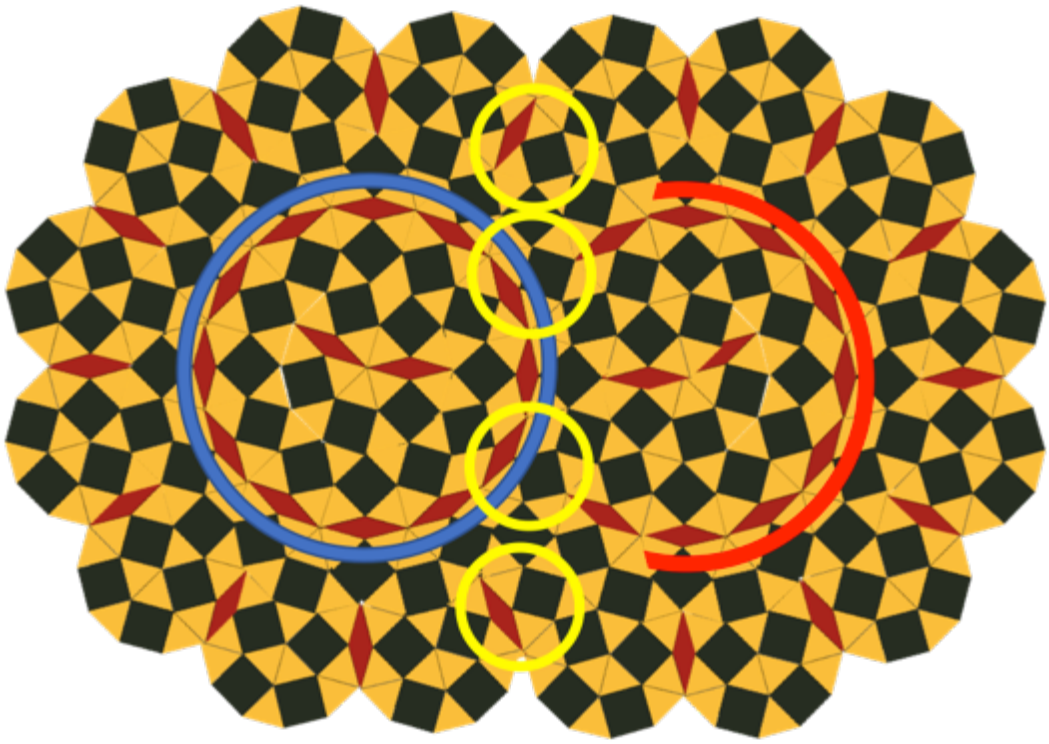

**Figure 5.14:** Layering a blue second-ring dodecagonal motif (left) over another copy of itself produces a red second-ring dodecagonal motif (right). Note that the red motif is identical in the layering picture, but would correspond to a different

dodecagonal motif entirely in the covering picture. The yellow circles highlight the only regions of the red motif that change when the blue motif is placed on top of it, and these correspond to rotations of the shield tiling as seen in ***Figure 5.3***, which also corresponds to the phason flip in the Niizeki-Gähler tiling.

As seen in ***Figure 5.9***, yellow circles have been used again in ***Figure 5.14*** to denote the shield rotations that correspond to phason flips. This shows the phason flips that take place from the original blue-red layering in ***Figure 5.9***, in addition to two new ones.

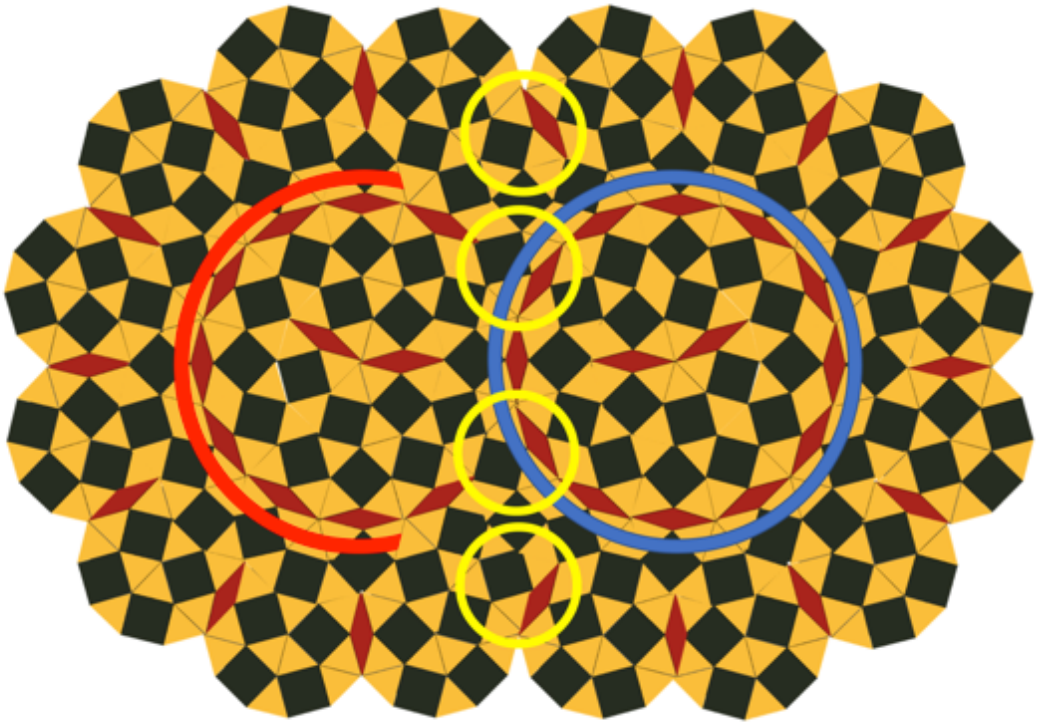

**Figure 5.15:** Interestingly, the red second-ring dodecagonal ring also has a chiral twin. This is an uncommon feature in comparison to other quasicrystalline tilings (compare with the different types of green decagonal motif from *Chapter Four*). One square is shown in ***Figure 5.7***. There are two squares, each made from one of these chiral red second-ring dodecagonal motifs.

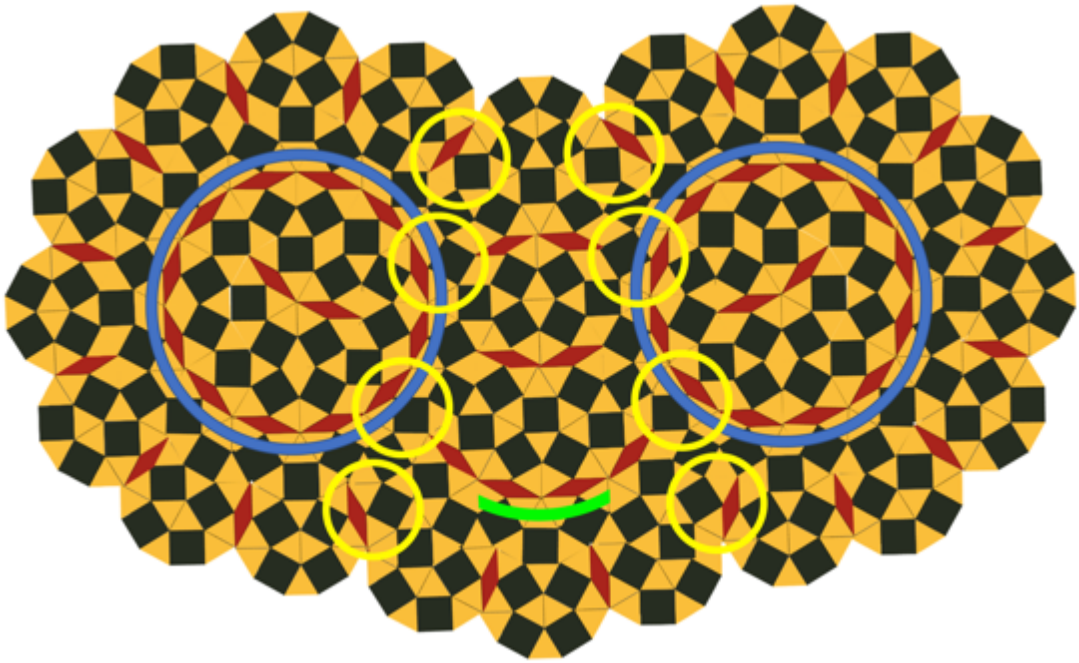

**Figure 5.16:** Two blue second-ring dodecagonal motifs can be layered onto a third in the center. The only tiles to change are those in the yellow circles, which are rotations of the shield phason unit. This creates a green second-ring dodecagonal motif, whose ring can be partially seen in the bottom of the figure.

## Larger Polygon Construction with Second-Ring Dodecagons

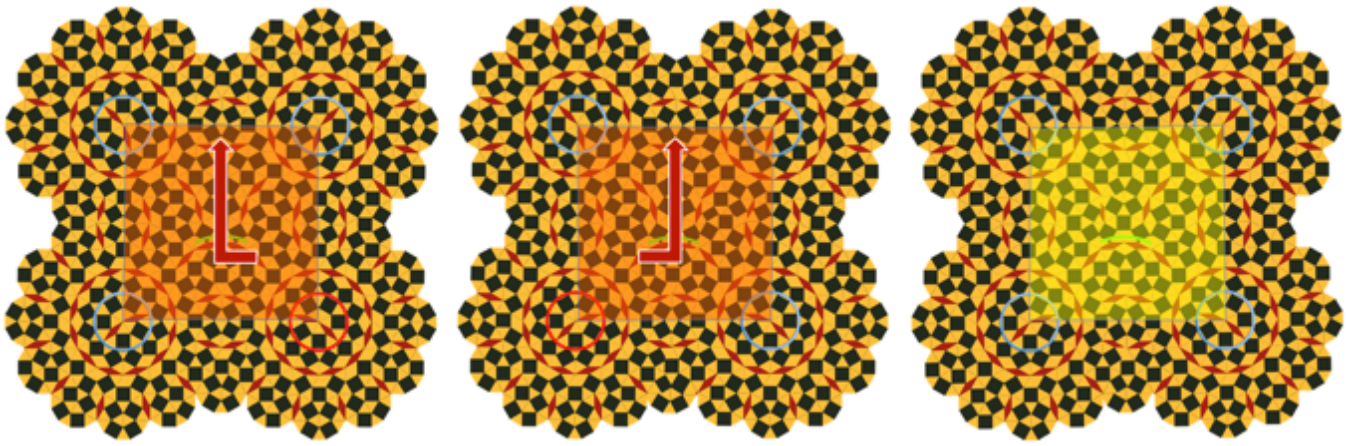

**Figure 5.17:** There are three different kinds of second-order squares that can be constructed from the three different second-ring dodecagonal motifs. The yellow-shaded square (right) has blue motifs for each corner, but the two orange squares (left, middle) have a red second-ring dodecagonal motif on one corner. These two orange second-order squares are a chiral pair. Note that the green second-ring dodecagonal motif occupies a near-central position in each square. Without it, each square would have a hole.

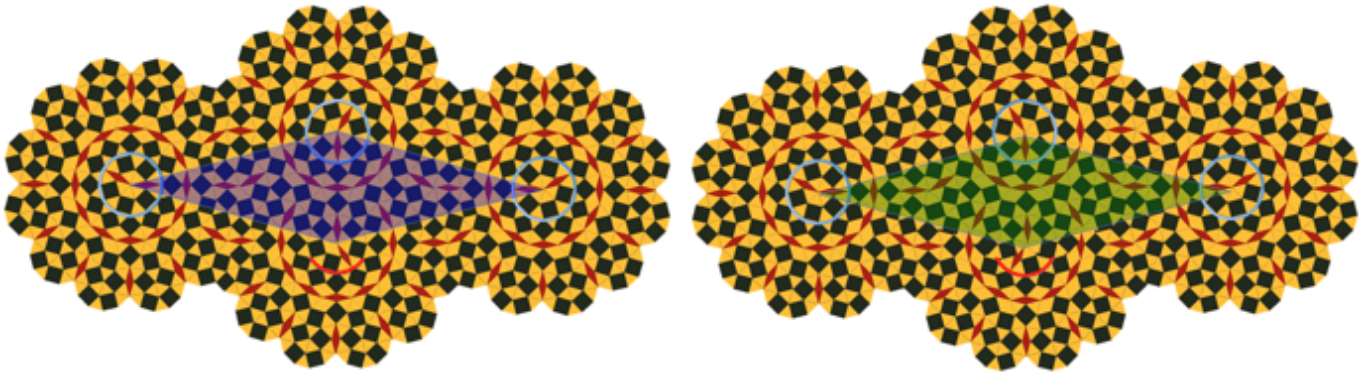

**Figure 5.18:** Only red and blue second-ring dodecagonal motifs are necessary for the construction of the larger second-order rhombus tilings. Like the two orange second-order squares from ***Figure 5.15***, they form a chiral pair!

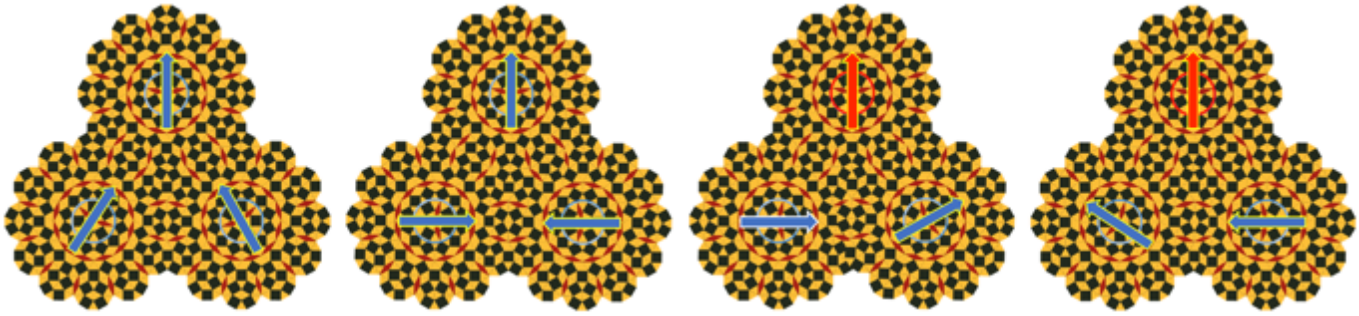

**Figure 5.19:** Here are four examples of the second-order triangle motifs that are needed in the second-ring construction of the tiling seen in ***Figure 5.20***. There are two types comprising only blue second-ring dodecagonal motifs (left and second from left), and two types comprising two blue and one red second-ring dodecagonal motif (right and second from right). In the second-ring construction, these triangles are no longer needed as the second-ring dodecagonal motifs are now large enough to fill in any tiles previously provided by the triangles—the square and rhombus, when made from the second-ring dodecagonal motif, will act to space-fill the remaining triangle voids. **This is a common feature in quasicrystal tilings when constructed with this method. Consequently, we do not actually need to define the triangle motifs to define the layering protocol in the second-ring expansion**.

## Construction of Characteristic Dodecagon with Second-Ring Dodecagons

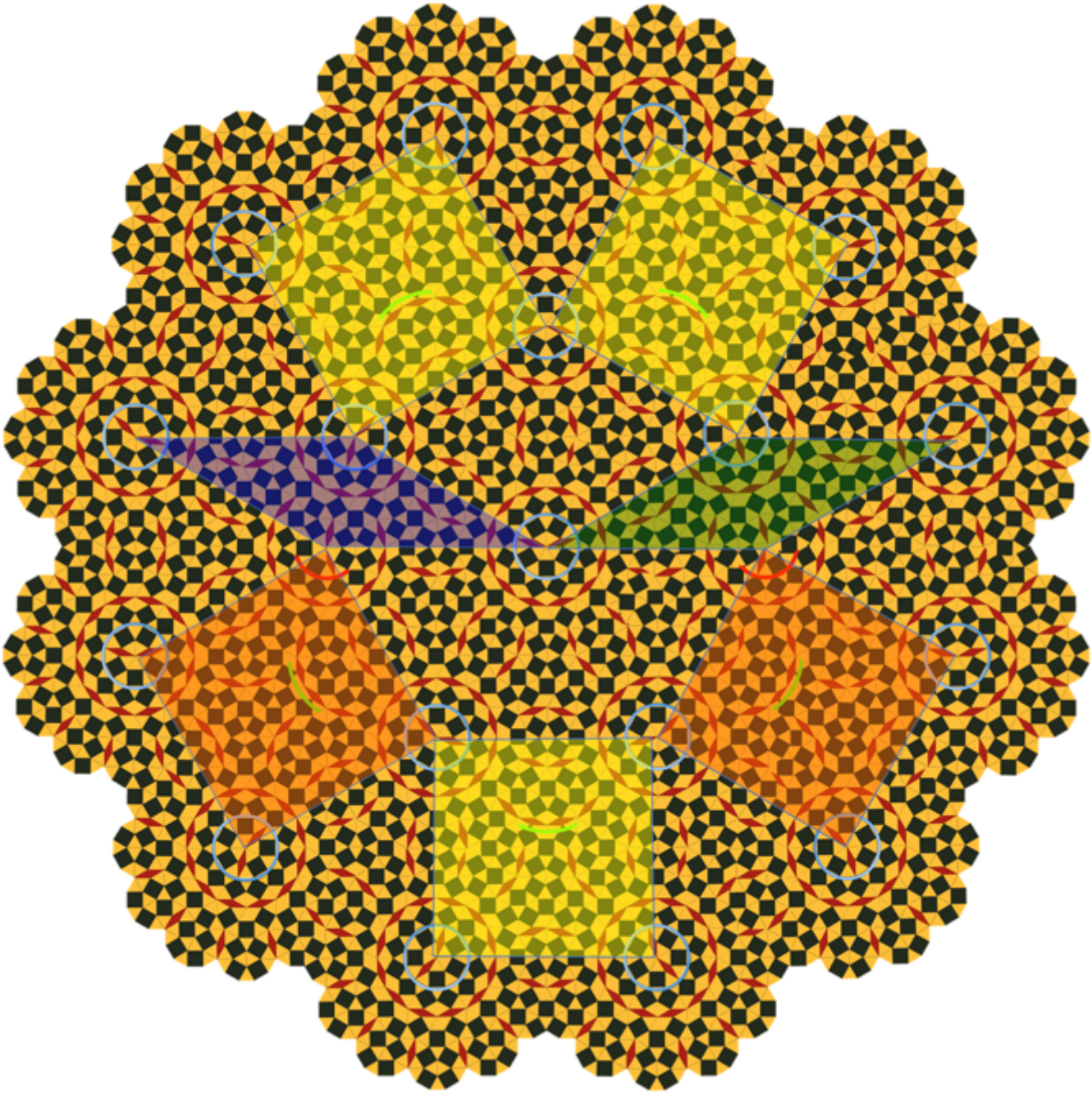

**Figure 5.20:** These new larger second-order squares and second-order rhombuses can be formed into a yet-larger second-order dodecagon. Note how the triangles in ***Figure 5.8*** are automatically generated in this scaling of the tiling. In this respect, they are secondary tilings (Steurer & Deloudi, 2009). **This is the only tiling in this thesis to show the effective erasure of an entire second-order polygon by a ring-expansion!**

## Third-Ring Expansion and Relation to the T-Cluster

***Figure 5.20*** shows the completion of the hierarchical cycle using the second-ring expansion of the dodecagonal motif. Once we have this second-order decagon, we can go about creating yet-larger versions of the second-ring dodecagonal motifs and build yet-larger squares and rhombuses. This demonstrates the concept that expansion of the rings leads to fewer layerings—which can generally be considered a simpler version of the tiling. This second-ring expansion has four layers, for instance, and can be contrasted with the first-ring expansion of ***Figure 5.7,*** which has six layers. Although this often results in a simpler tiling, the dodecagonal tiling shown here becomes more complex in an unexpected way. The outer rings are not made simply from the characteristic dodecagon shown in ***Figure 5.4 (a)***, but also involve ***Figure 5.4 (b)***. For this reason, I would argue that the simplest tiling is actually that shown in ***Figure 5.7*** and ***Figure 5.8***. These are made purely from the simple characteristic dodecagon, have six layers, and have a relatively simple construction protocol for the second-order square, second-order triangle, and second-order rhombus. In contrast to the T-cluster from ***Figure 5.21 (b)***, we only require the simple characteristic dodecagon and so I think it achieves an easier single-covering motif than the T-cluster. In this respect, the layering protocol offers a very straightforward picture of the infinite Niizeki-Gähler tiling.

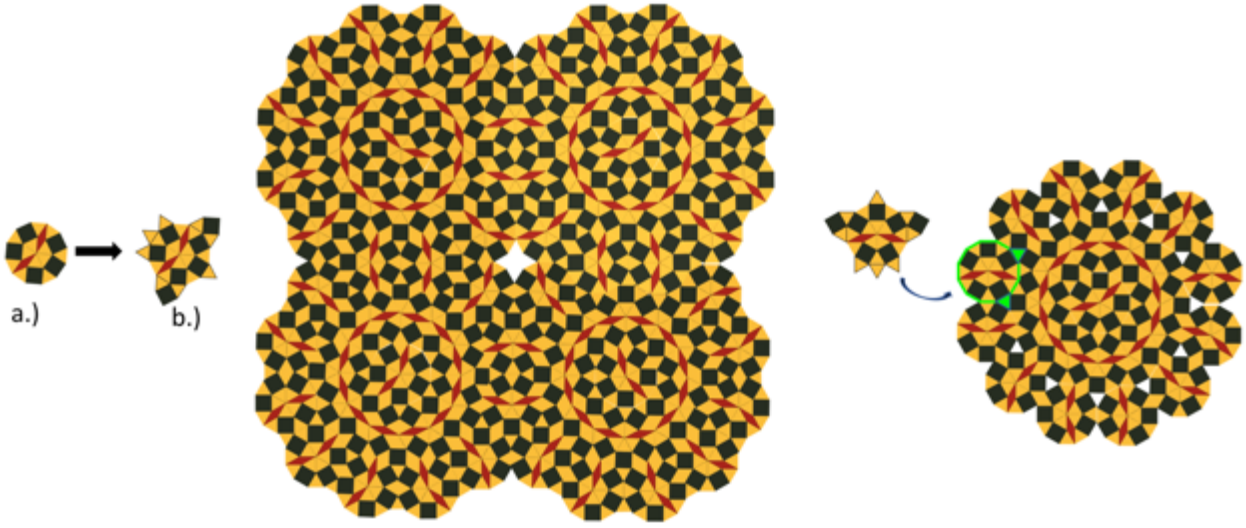


**Figure 5.21:** In this figure, (b) shows the T-cluster motif that Liao (Liao et al., 2010) discovered to complete the tiling in this third-ring expansion (another ring of characteristic dodecagons has been added to correspond with the figures of Liao). Although their proof rests on an argument using inflation, they use motifs somewhat comparable to the one presented here.

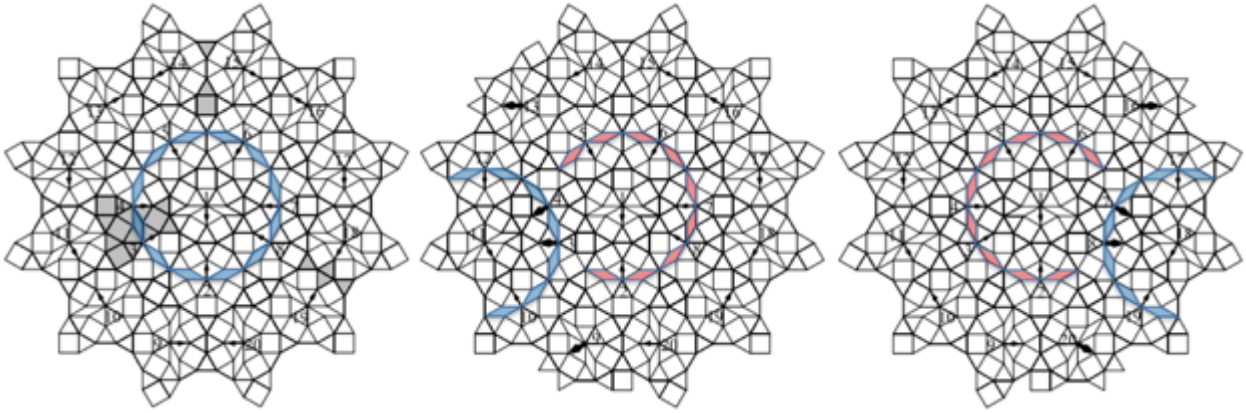

**Figure 5.22:** These are three images from Liao (Liao et al., 2013) overlain with my own blue and red highlights. These highlights show (left) a blue third-ring dodecagonal motif decorated in the manner of the T-cluster, and the chiral twin pair (middle and right) for the red third-ring dodecagonal motif.

The Liao paper referenced in ***Figure 5.22*** comes closest to capturing the essence of the ideas discussed in this thesis, insofar as they build larger motifs and compare and contrast them. What was not referenced in the Liao paper is the fact that these red second-ring dodecagonal motifs are in fact just two blue second-ring dodecagonal motifs layered on top of one another. But because they come so close, I would like to especially make note of their work. Their proof of the T-cluster rests on an understanding of the allowed vertices in the tiling, and the fact that the T-cluster emerges at the center of each of these during deflation. **Because it is such a different approach than the one presented here, the layering approach may provide a different technique for exploring the same ideas in other non-dodecagonal quasilattice tilings.**

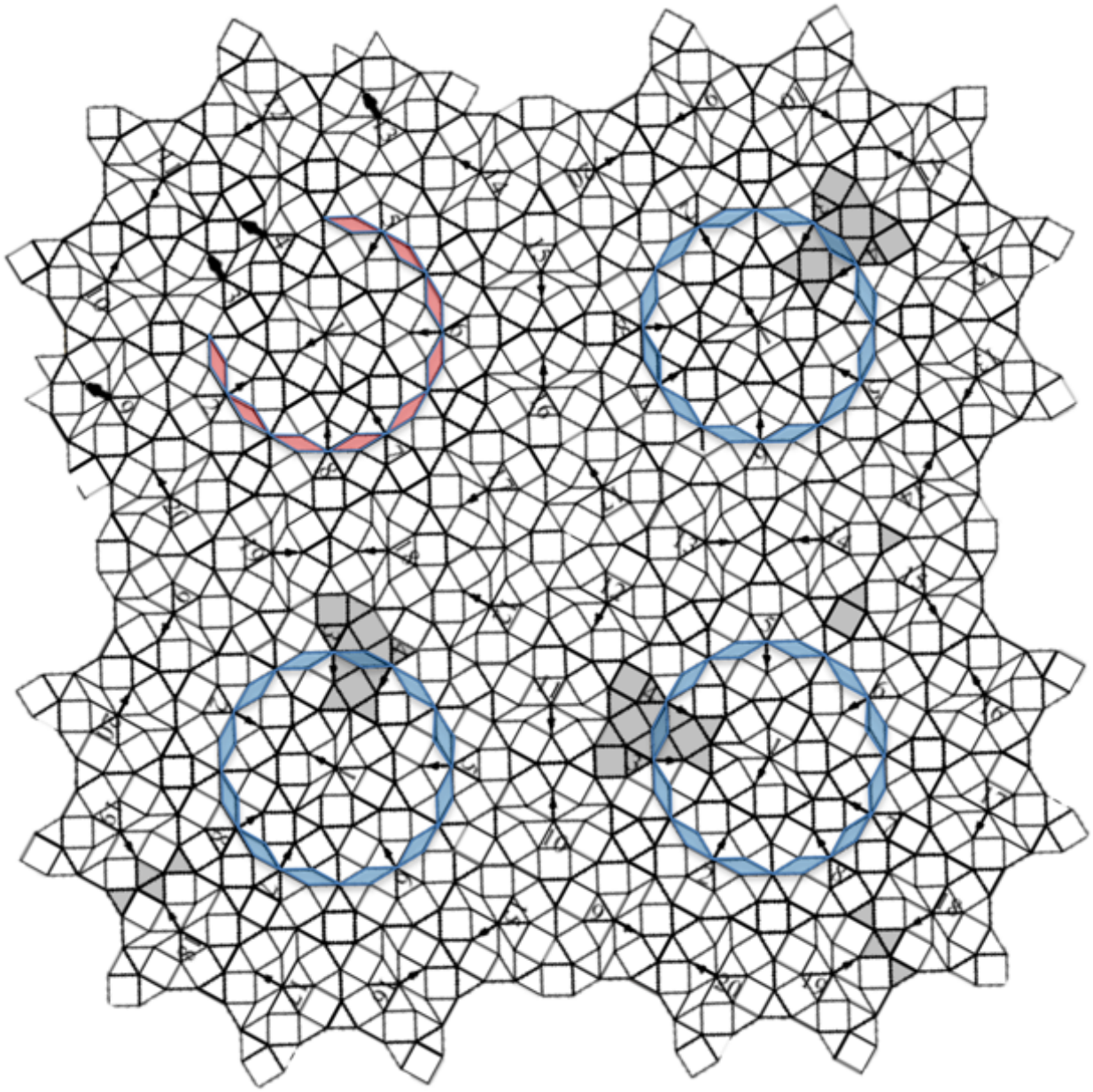

**Figure 5.23:** The third-ring dodecagonal motifs of ***Figure 5.22*** can be used to construct a new square motif, as I have done for this figure. Note that because of the T-cluster decoration of the dodecagon (***Figure 5.21***), there is no gap in the center of the square. Because of this, the T-cluster decorated decagons only need three third-ring motifs instead of five, which is explained later in ***Figure 5.25***.

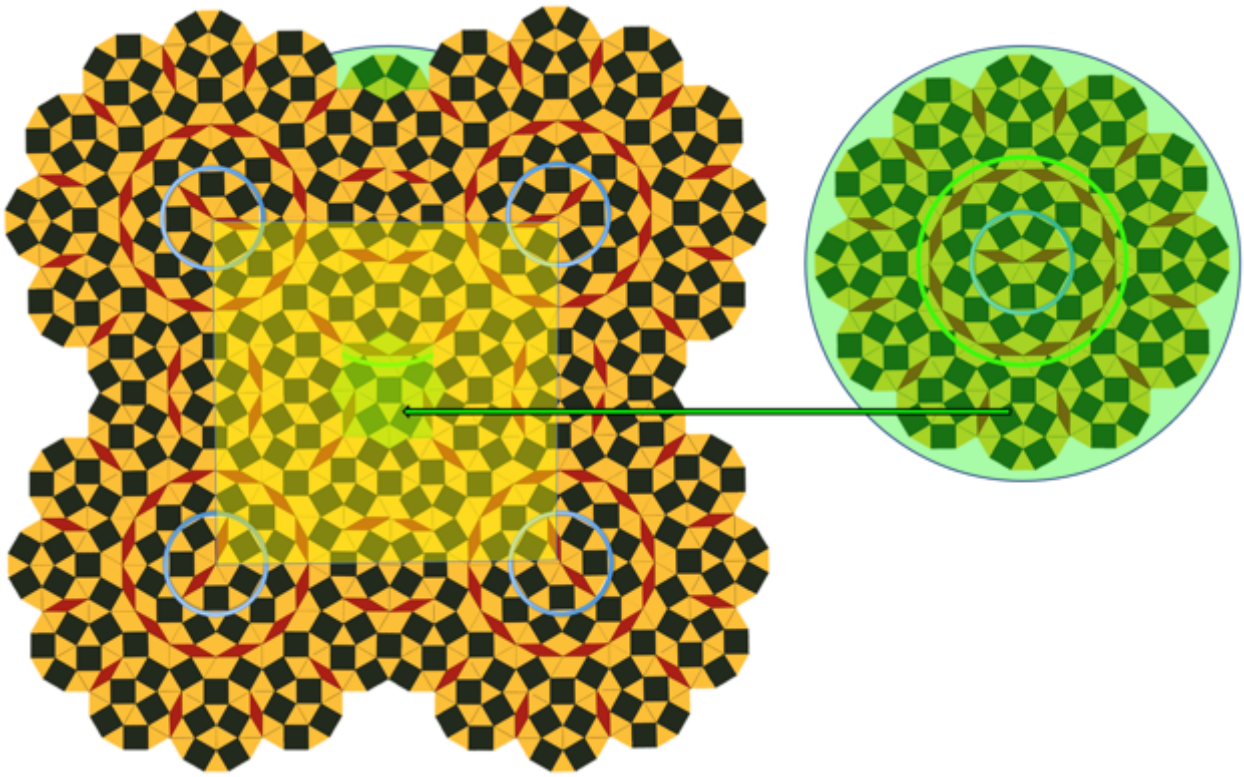

**Figure 5.24:** If we simply use the second-ring dodecagonal motifs, we see that the T-cluster modification in ***Figure 5.25(b)*** is not sufficient to close the gap left the center of the second-order square. This motivates the creation of the third-ring dodecagonal motif.

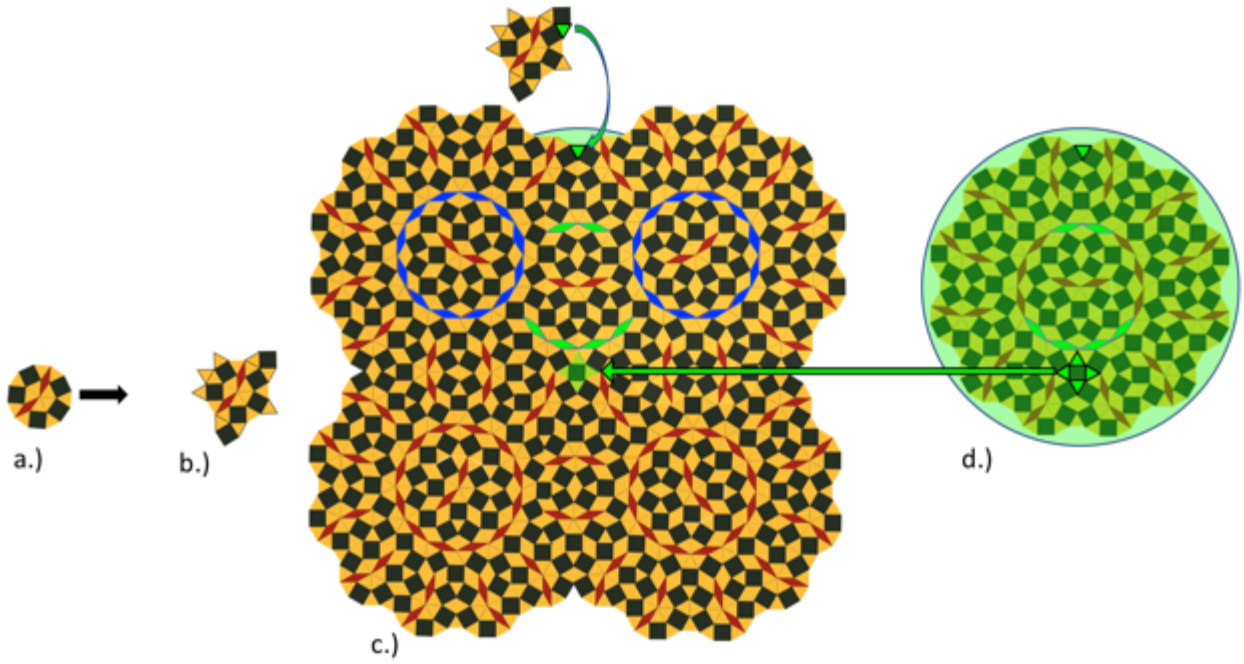


**Figure 5.25:** Part (a) shows the original characteristic decagon. (b) shows the T-cluster discovered by Liao (Liao et al., 2010). (c) is a second-order square created by the third-ring dodecagonal motif created with (a). (d) shows the green third-ring dodecagonal motif that is present in (c) but difficult to see. **Instead of decorating the decagon with the additional polygons shown in the T-cluster, it's also possible to just include a green third-ring dodecagonal motif.** This green dodecagonal motif will fill in the polygons that are missing from the center of the second-order square—a square surrounded by four triangles.

***Figure 5.25*** contrasts the solution of Liao using the T-cluster with a different kind of third-ring dodecagonal motif. We know that the decoration of the simple characteristic decagon in (a) will cover space in (c), if the T-cluster is used to construct the motifs instead of (a). However, instead of using the T-cluster, we could also choose to use a fourth layer—giving us blue, two chiral forms of red, and finally a green layer. This green dodecagonal motif is shown in (d) for clarity—it has been moved out from under the second-order square (c), and is at the same vertical height as the copy that is still under the second-order square (c). This green third-ring dodecagonal motif is barely seen in (c), and has been highlighted in green to make it easy to see the six tiles (five triangles and one square) that it contributes to the second-order square. The rhombus and triangle are already space-filled by the second-ring dodecagonal motif, so are not treated here with the T-cluster.

## Phason Flips in the First-Ring Dodecagon

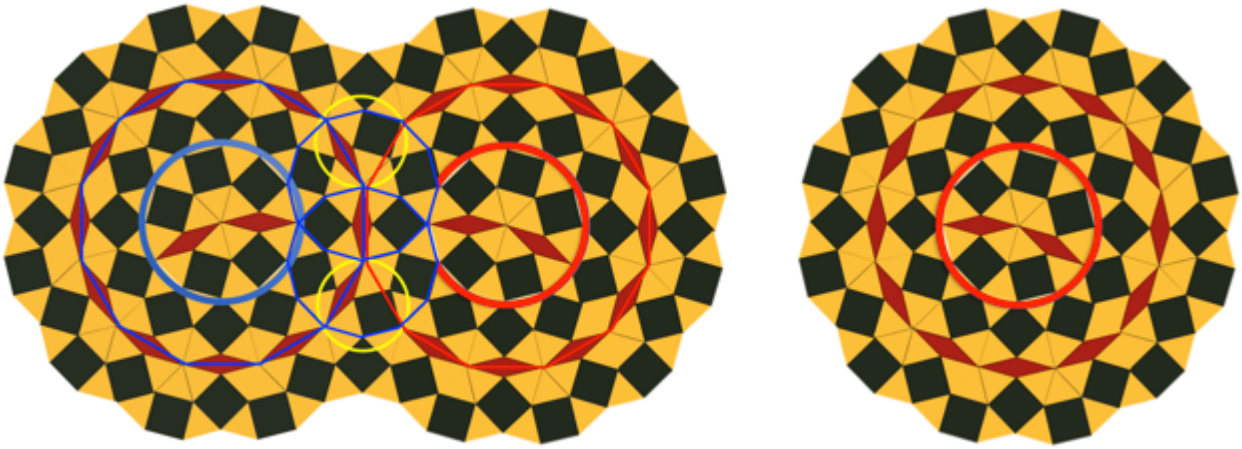


**Figure 5.26:** When a blue dodecagonal motif layers over a copy of itself, it creates a red dodecagonal motif. Shields that have been rotated to perform a phason flip have been circled in yellow. On the right, the original dodecagonal motif is shown before its shield components have been rotated into place. Note how the red rhombuses create a ring, which is superseded by the rhombus ring from the blue dodecagonal motif. The unmodified red dodecagonal motif (and hence not yet configured like a red dodecagonal motif) is shown in (b) for comparison.

Just like the Penrose tiling, the dodecagonal motifs meet together edge-to-edge when the dodecagon is drawn from the center of the first ring of characteristic dodecagons. In ***Figure 5.26 (a)***, a large blue dodecagonal line and a large red dodecagonal line together map the perimeter of the two dodecagonal motifs. Where the blue and red dodecagons meet face-to-face, there are two vertices and hence two of the small characteristic dodecagons from ***Figure 5.2***. Yellow circles mark the only regions of the underlying red dodecagonal motif that have changed with the addition of the blue dodecagonal motif, which also corresponds to a phason rotation. An original red dodecagonal motif has been provided in ***Figure 5.26 (b)*** to show the unmodified version. But recall from *Chapter Two* that the phason rotations were actually just characteristic decagon rotations. The same is true here—the shield rotations correspond exactly to dodecagons that have rotated to face "toward" the blue dodecagonal motif instead of the red dodecagonal motif. This may be a good description of a phason in general. Phasons in a real material are rotations of the shield. But we produce the components of an ideal tiling by phason flipping, in this sense, the dodecagonal motif in such a way that it can form a covering with itself when it meets edge-to-edge. This contrasts significantly with the hyperspace interpretation of a phason, where a phason is a particle position whose hyperspace location falls

outside of the cut window (blue rectangle of ***Figure 1.4***). An ideal quasilattice tiling would therefore not have phason errors since all of its projections originated within the cut window. The layering perspective is an expansion of the geometric understanding of a phason flip.

With six layers of dodecagonal motif, we can create yet-larger second-order versions of the square, triangle, and rhombus. Although we will see there is no need to produce a second-order triangle in the second-ring expansion (to be discussed soon), there is still a need for a second-order triangle in the first-ring expansion. This second-order triangle displays significant complexity when compared to the second-order squares or second-order rhombuses. If we just want to understand the layering protocol, we could stop here. But we will continue forward to gain new insight into the single-covering motif discovered in Liao (Liao et al., 2013).

## Conclusion

In summary, we showed in this chapter that the layering method offers a new perspective of the Niizeki-Gähler quasicrystal tiling that simplifies it from both a construction point of view, and from a single-cluster covering point of view. Higher-dimensional cut-and-project methods offer a powerful means of both creating and analyzing quasicrystalline tilings, but do not offer a real-space perspective for tiling *construction* or analysis. A real-space understanding of the tiling will open up an entirely new way of determining whether a given motif is correct, and what exactly would need to change to bring that tiling closer to a perfect tiling on the random-ideal continuum. If we want to build shapes that are better at self-assembling, then this kind of perspective opens up an entirely new world of engineering possibilities to achieve those goals. Some hint of this approach is provided in the next chapter where I take a mathematically ideal icosahedral quasicrystal and show that this approach provides, for the first time, an exact mental picture for how to build the different kinds of motif seen in the icosahedral quasicrystal, as well as a series of tools to break down the motifs and analyze exactly in what sense they are correct.

## Chapter Six

## A Layering Construction of the Ammann-Kramer-Neri Icosahedral Tiling

### Introduction

The icosahedral quasilattice is by far the most complex of the quasilattices discussed in this thesis. In part, *Chapters Two* through *Chapter Five* exist to provide a template in which to better understand *Chapter Six*. These chapters introduce many of the different concepts like phason flips, chirality and chiral flips, coverings, and so on. Because *Chapter Six* deals with a three-dimensional quasilattice, these concepts all exist in a slightly different way. Hopefully enough groundwork has been laid by now that the reader will form a seamless mental picture of the Ammann-Kramer-Neri tiling. To my knowledge, this is the first time anyone has attempted to lay out a detailed picture of an icosahedral quasicrystal that extends to something more visually intuitive than the basic deflation or multigrid description.

The icosahedral phase of matter, known as an icosahedral quasicrystal, has 5-fold, 3-fold, and 2-fold rotational symmetries corresponding to the icosahedral point group (m53) in reciprocal space. There are three corresponding Bravais lattices for this point group that exist in six-dimensional space (Rokhsar et al., 1987). There are three possible cubic lattices—simple cubic (SC), body centered cubic (BCC), and face centered cubic (FCC)—which, after projection onto irrational orientations of 3D space, can give rise to the SC, FCC, and BCC icosahedral lattices, respectively (Mukhopadhyay et al., 1996). The Ammann-Kramer-Neri tiling (AKN) represents the primitive or simple cubic version of the icosahedral quasilattice.

Alternately, the Socolar-Steinhardt tiling (SS) (Socolar & Steinhardt, 1986) is created by projecting an irrational-angle cut of a 6D FCC lattice onto 3D. It contains four tiles—the golden rhombic triacontahedron, golden rhombic icosahedron, golden rhombic dodecahedron, and prolate golden rhombohedron (Steurer & Deloudi, 2009). These four tiles can be created by pairs of triacontahedra with different degrees of overlap. Consequently, the Socolar-Steinhardt

tiling can be thought of as overlapping triacontahedra, which is also an important component of the AKN tiling. Unlike the AKN tiling, the SS tiles do not have chiral twins, and the tiling as a whole also has a closed deflation protocol (Hann et al., 2016; A. E. Madison, 2015; Steinhardt & Ostlund, 1987). Like other quasicrystal tilings, this deflation protocol consists of taking any one of the four tiles and subdividing it into parts comprising the original four tiles in a way that preserves the overall aperiodicity of the tiling. The procedure for doing this was spelled out as early as Levine and Socolar's work (Levine & Steinhardt, 1986b; Socolar & Steinhardt, 1986), but were only confirmed with 3D models by Madison (A. E. Madison, 2015). As mentioned earlier, the AKN does not have a closed deflation protocol (Steinhardt & Ostlund, 1987), which is in contrast to the Penrose or Ammann-Beenker tilings. A potential visual method for understanding why is given by the work detailed here. It is known that there is a base for deflating a given rhombohedron (Lück, 1990; Yamamoto et al., 2003), but the exterior of the deflated rhombohedron changes and is dependent on the local environment (Levine & Steinhardt, 1986b; Eric A. Lord et al., 2006). One can best visualize this unchanging rhombohedral core with the four tiles of the Socolar-Steinhardt tiling and not whole triacontahedra.

The BCC icosahedral lattice has no known tiling projection, but it would be very anomalous for one to not exist. Every quasilattice comprises a space-filing tiling. While the simple cubic and face-centered cubic projections are well-known from experimental quasicrystals, the body-centered cubic projection has been found only in simulation (Engel et al., 2015). Developing a real-space quasilattice model is of interest for all three of these projections, but this chapter will focus on the AKN SC projection. The AKN is also a binary system of acute and oblate golden rhombohedra. This raises the possibility that the AKN, with appropriate matching-rule patches, or some other potential rules, could be self-assembled. It is known (but unpublished by Dr. Sangmin Lee, a former Glotzer group PhD student) that systems of these two rhombohedra in the appropriate stoichiometry do not self-assemble, so it is apparent that a decoration with attractive potential patches may be necessary.

The icosahedral quasilattice has many commonalities with the other tilings in this thesis, except it is in 3D. In fact, the icosahedral quasilattice is the only kind of 3D quasilattice allowed (Liao et al., 2010). There are two fundamental polyhedra that combine into another characteristic polyhedron—a rhombic triacontahedron in this case—which is then arranged into a

petal motif in the shape of an icosahedron, and which can then be arrayed into $n^{th}$-order versions of the fundamental polyhedron. But are there three covering icosahedra, analogous to the three covering pentagonal motifs in the Penrose tiling? That is part of what this chapter sets out to answer. This quasicrystal turns out to be substantially more complex than the other tilings—perhaps because it is in 3D! Here we will show that there are 26 versions of the covering icosahedral motif, each of which can be arrayed into 106 acute, and 56 oblate, second-order rhombohedra, respectively. We show that these can then be used to construct a significantly larger subset of second-order triacontahedra—the number of which is still unknown. This is quite different from the other quasilattices discussed in this thesis, and I think it is related to the fact that the Ammann-Kramer-Neri tiling does not have a deflation protocol in the usual sense (Steinhardt & Ostlund, 1987). This chapter also then serves to highlight the difference between the layering method and the deflation protocol, since the former exists for the AKN.

For the purposes of simulation, this chapter represents the development and application of a new kind of order parameter developed from the layering model. This is applied as a proof-of-concept to a perfect icosahedral tiling in the form of the Ammann-Kramer-Neri binary rhombohedral packing.

## Ammann-Kramer-Neri Tiling

Although there is no way to pack icosahedra into a space-filling tiling, the re-mapping of the Ammann-Kramer-Neri (AKN) tiling to the layering model provides a way of visualizing the overlapping icosahedral motifs specific to this structure. **It is worth noting that a recent paper argues that a single *covering* motif does not exist for a material based on the AKN (Buganski et al., 2020).** Like the chapters before this, *Chapter Six* will walk the reader through the geometry of the AKN to establish the existence and nature of a single *layering* motif (and its chiral twin!), as well as proposing a set of 26 covering clusters. I believe these layering and covering descriptors will be as useful as, or even more useful, than a single-covering motif description. By taking each icosahedral motif, each of which comprises twelve rhombic triacontahedra (RTC), and drawing an icosahedron whose vertices lie at the center of each RTC, a quasiperiodic network of icosahedra can be generated that is analogous to the pentagonal Penrose P1 tiling. In this AKN quasilattice, I have found that each icosahedral motif overlaps with its neighbors in two ways, or shares an edge. In the overlap cases, the accompanying RTC

mesh seamlessly in a way that is not easily visualized. This is only possible because the RTC is a golden zonohedron—the boundaries between the rhombic dodecahedron, rhombic icosahedron, and oblate rhombohedron provide for the possibility of two overlapped RTC that still maintain their original orientations. RTC along their 5-fold axes can only overlap with the shared volume of a rhombic icosahedron. Along the 3-fold axis, it is an oblate golden rhombohedron. For their 2-fold axes, the shared volume is a rhombic dodecahedron (Steurer & Deloudi, 2009). In this way, the original motif type, as defined by the orientation of each of the twelve RTCs, can be entirely preserved during these first two overlaps. In the third icosahedral motif overlap—corresponding to icosahedra that share edges if viewed in the P1 equivalent manner—the RTC must overlap completely. In this case, the system must choose which icosahedral motif to define, as the composite RTC cannot have their axis of highest rotational symmetry point in two different directions. In this way, the AKN is constructed at the most basic level—and in a way completely analogous to the comparatively simple description of the Penrose rhombus tiling.

Each icosahedral motif sits at the vertex of a new, higher-order, AKN tiling. But at this higher level, there are 106 second-order acute rhombohedra (AR) and 56 second-order oblate rhombohedra (OR) combinations of the twenty-six icosahedral cluster motifs (IC) to choose from—as this chapter will discover. At this point, it becomes clear why there does not exist a deflation protocol for the AKN. Each OR or AR comprises different combinations of the twenty-six ICs, and each second tier RTC comprises different ORs and ARs. There can only exist a finite set of deflations at each hierarchy, but the set expands at each higher tier. The number of higher-order RTCs was not measured in this study, as the system sizes became unwieldy beyond 284,000 polyhedra. Additionally, there exists an inner unchanging structure for each (incomplete) OR and AR, but this has been discussed in previous work (Eric A. Lord et al., 2006). In the context of the layering picture discussed in this thesis, the structure of the AKN also becomes relatively simple—it contains only the rotationally symmetric twin "blue" (in analogy with the blue pentagonal motifs from *Chapter Two*) ICs at each vertex. But their distribution into the different twenty-six layers becomes quite complicated. A simplification for this description was found, but inspiration may be had from the dodecagonal ship tiling, which is similar to the extent that the second-order triangles and second-order squares have different motif definitions beyond the basic chiral twins. In the dodecagonal tiling, I chose to take entire dodecagonal motifs that are constructed from two of the characteristic polygon covering motifs

to create a single, unchanging patch. All second-order triangles and second-order squares were appropriately generated during the layering of this single $n^{th}$-ring dodecagonal motif. If such a motif exists in the AKN, it might similarly remove the necessity of describing the many incarnations of the AR and OR motif deflations. Despite these complications, the layering of the AKN tiling begins very much like the tilings in the preceding chapters.

## Rhombic Triacontahedra in the Ammann-Kramer-Neri Tiling

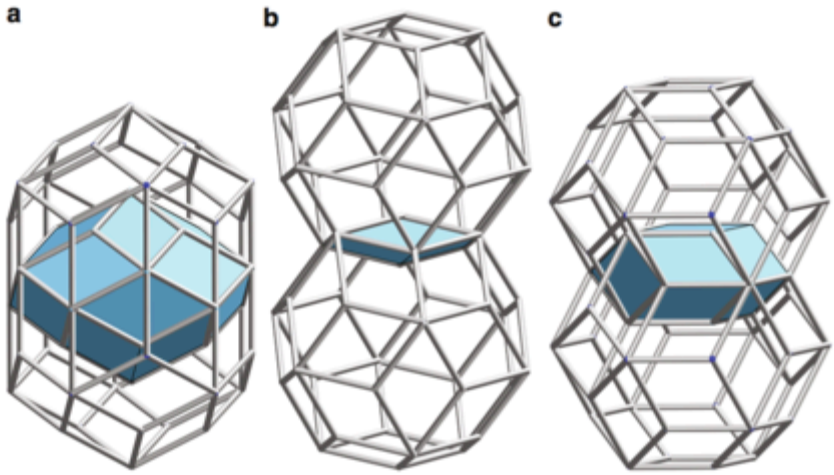


**Fig. 2.5.** Triacontahedra overlapping along the (**a**) 5-, (**b**) 3- and (**c**) 2-fold directions. The shared volumes, a rhombic icosahedron (**a**), an oblate golden rhombohedron and a rhombic dodecahedron (**c**), respectively, are marked

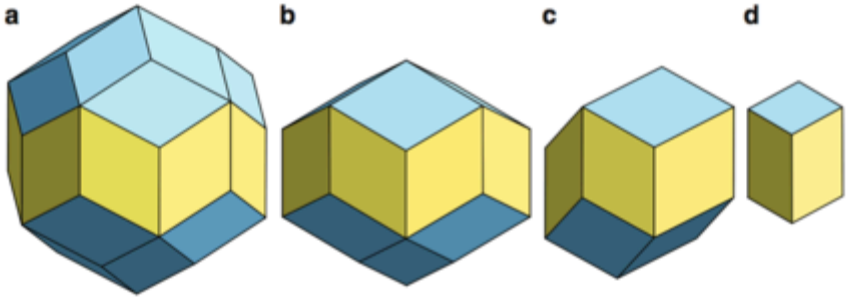


**Fig. 2.6.** The sequence of zonohedra resulting after repeated removal of zones (marked yellow): (**a**) Triacontahedron, (**b**) rhombic icosahedron, (**c**) rhombic dodecahedron, and (**d**) prolate golden rhombohedron

**Figure 6.1:** Images from Steurer, pg. 58 (Steurer & Deloudi, 2009). Triacontahedra can overlap (top) and produce the family of zonohedra (bottom). Not shown, however, is the overlap of triacontahedra comprising their composite rhombohedra, which plays a large role in this chapter's work. Also, while the bottom image shows the zonohedron nature of the triacontahedron, it does not detail the specific assembly of rhombohedra into a triacontahedron. **Only two of the 120 (Katz, 1988) different rhombohedra tilings of the triacontahedra are actually used in the AKN tiling!**

## Matching Rules

These paper models with printed matching rules (Hann et al., 2016) represent one form of the triacontahedron in the Ammann tiling, with the matching rules devised by Ammann. The triacontahedra models without matching rules were constructed by hand from individual rhombohedra. Note that just like previous matching rules, these are **not** sufficient for assembling a quasilattice tiling, but a perfect tiling will lack any matching-rule violations.

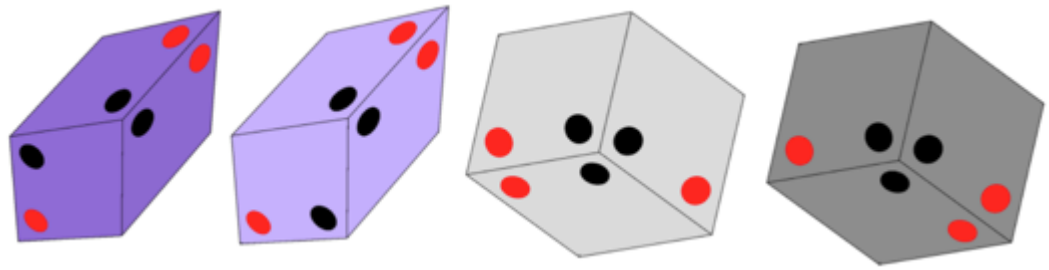

**Figure 6.2:** Image from Hann (Hann et al., 2016) showing the two chiralities of golden acute rhombohedron (left pair) and golden oblate rhombohedron (right pair). The rhombohedra must be assembled such that the black dots match with other black dots, and red dots match with other red dots. These cannot be used to assemble a perfect tiling, but a perfect tiling will not contain matching-rule violations.

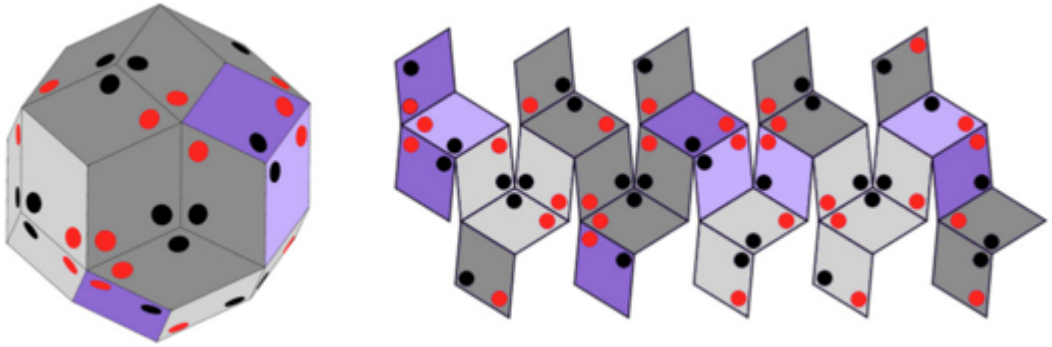

**Figure 6.3:** Image from Hann (Hann et al., 2016) shows the net of a hollow triacontahedron (right) and its image after 3D construction (left).

## Assembly of the Triacontahedron

In the actual quasicrystal tiling, however, this triacontahedron is made from ten acute and ten oblate golden rhombohedra. Because it is a zonohedron, it can be successively reduced into smaller polyhedra by either the removal of the equatorial band (Steurer & Deloudi, 2009), or by

removing rhombohedra from the top or bottom, starting with a five-fold axis, as shown with these paper models,

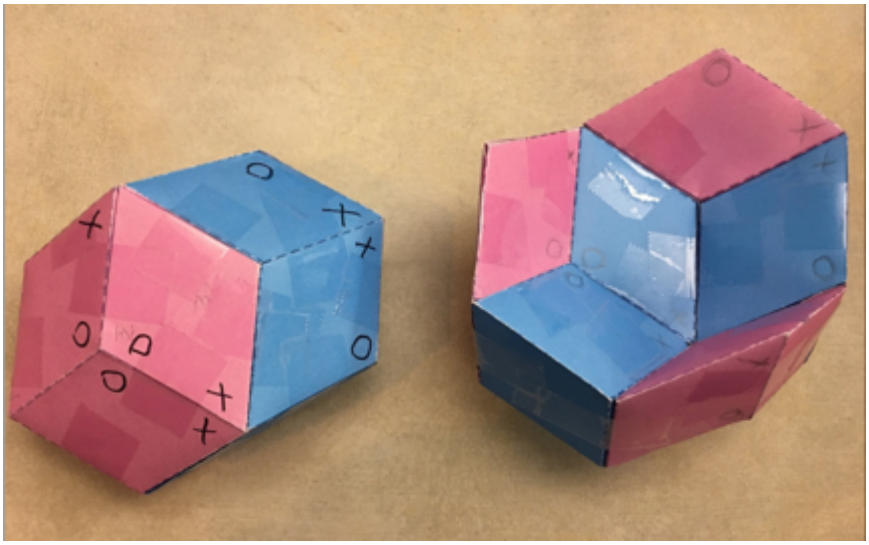

**Figure 6.4:** Acute rhombohedra (blue) combine with oblate rhombohedra (pink) to form a golden rhombic dodecahedron (left). If this shape is then combined with the configuration of additional rhombohedra on the right, a new shape—the golden rhombic icosahedron—is formed.

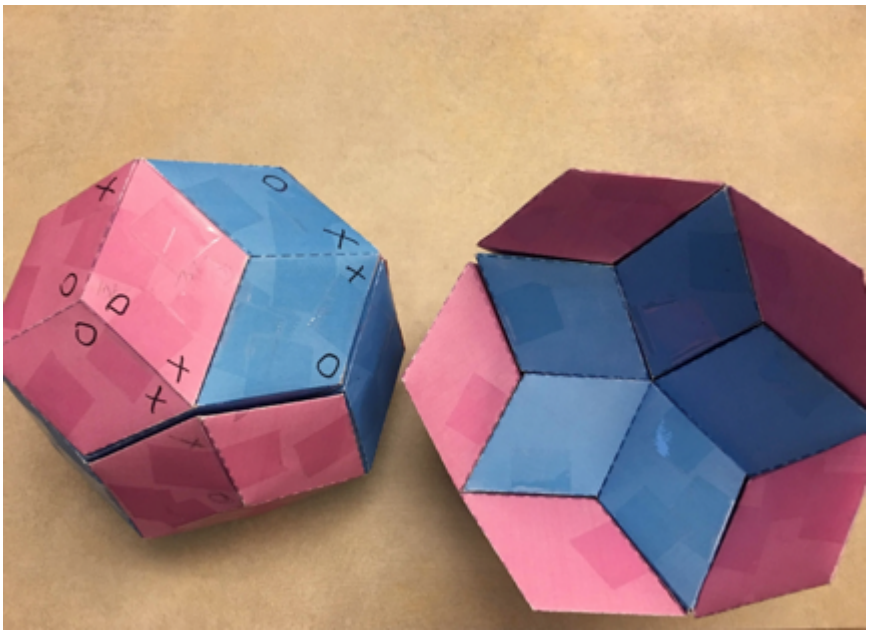

**Figure 6.5:** A golden rhombic triacontahedron can be created by taking a golden rhombic icosahedron (left) and additional rhombohedra (right). Note the rotational symmetry of the added parts on the right. Just like the Penrose tiling, the composite shapes of the fundamental unit—sometimes called a quasi-unit cell—will break rotational symmetry.

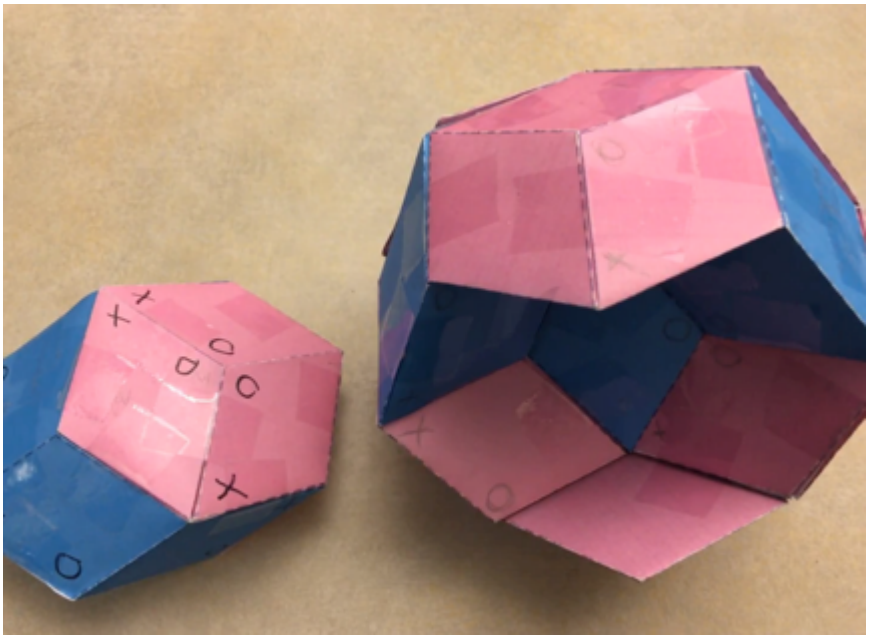

**Figure 6.6:** There are 120 ways of assembling the acute and obtuse rhombohedra into a rhombic triacontahedron, but only two of them occur in the Ammann tiling. The difference between these two configurations is solely in the orientation of the rhombic dodecahedron on the left. A 180° flip will allow the triacontahedron to take on the other chiral form, ignoring for the moment the matching-rule decorations.

## Assembly of the Hexecontahedron

This rhombic triacontahedron is equivalent in function to the decagon at the core of the Gummelt motif in the Penrose tiling. Twelve of these rhombic triacontahedra sit around a core comprising twenty acute rhombohedra. These acute rhombohedra together form a shape called a golden rhombic hexecontahedron. The hexecontahedron is a shape familiar to many, as it is similar to some versions of the Mathematica logo[38].

It is known from the literature that the hexecontahedron forms the core of an icosahedral quasicrystal (Audier & Guyot, 1986). However, the details of exactly how the Ammann tiling can be constructed using this geometry as a type of quasi-unit cell have not been explored.

It is relatively straightforward to pack twelve rhombic triacontahedra around a core rhombic hexecontahedron. But we must remember that each face is actually covered by some

[38] In 2002, a quasicrystal researcher named Sandor Kabai worked heavily with Mathematica to develop computer models for quasicrystalline shapes, and this research then piqued the interest of Mathematica developers for the creation of their logo (Wolfram, 2019). Mathematica has a surprisingly deep history with quasicrystal research!

incarnation of the matching rules. These matching rules will govern not only which faces of the triacontahedra are allowed to sit in the cusps of the hexecontahedron, but also the rotational orientation of each triacontahedron with respect to both the hexecontahedron and the neighboring triacontahedra. The resulting puzzle is dauntingly complex. 2D photos do not do it justice, but I will provide them nonetheless with the understanding that it is much easier to explain with 3D models! To reiterate, none of this has been explored before in the literature.

**Figure 6.7:** This figure shows a disassembled hexecontahedron cusp. Each hexecontahedron has twelve pentagonal cusp faces. They are created by merging five golden acute rhombohedra. Here, the light and dark purple rhombohedra represent different chiral directions of the matching rules—the black dot and cross, respectively—that decorate each face of the rhombohedra. The dark and light purple rhombohedra thus have mirror-image matching rule decorations.

The Ammann tiling is constructed entirely from acute and oblate rhombohedra. The hexecontahedron core, however, contains only the acute rhombohedra. Each rhombohedron is decorated in the manner shown in ***Figure 6.2***. These matching rules must be satisfied for every face. In ***Figure 6.7***, an assembly of five acute rhombohedra creates the pentagonal cusp that creates one of the twelve faces of the hexecontahedron. Note that all of the matching rules between the faces must match—black dots must align with black dots, and likewise for the black crosses. No black dot or black cross can meet a face without a corresponding black dot or cross, respectively. To better understand this, the pentagonal cusp in ***Figure 6.7*** has been left partially

assembled so that the matching rules are (at least partially) seen. Note also that if this shape is folded into its final form, there are no matching-rule markings at the center of the five-fold cusp. This will help us understand the triacontahedron matching rules later on.

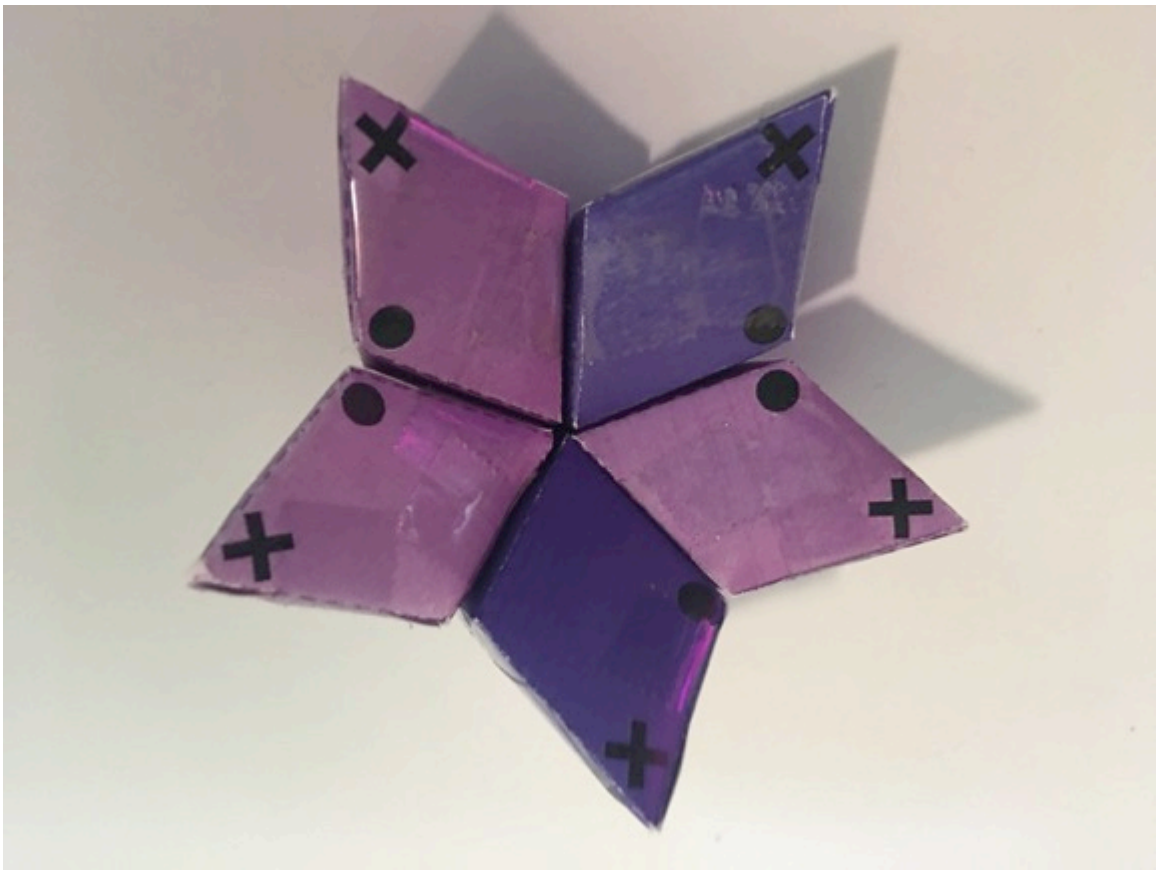

**Figure 6.8:** Hexecontahedron cusp: Note the lack of matching-rule markings near the central vertex.

Hexecontahedron cusps, like the acute rhombohedra that form them, also come in two chiralities. Likewise, each of these pentagonal cusps also comes in many forms.

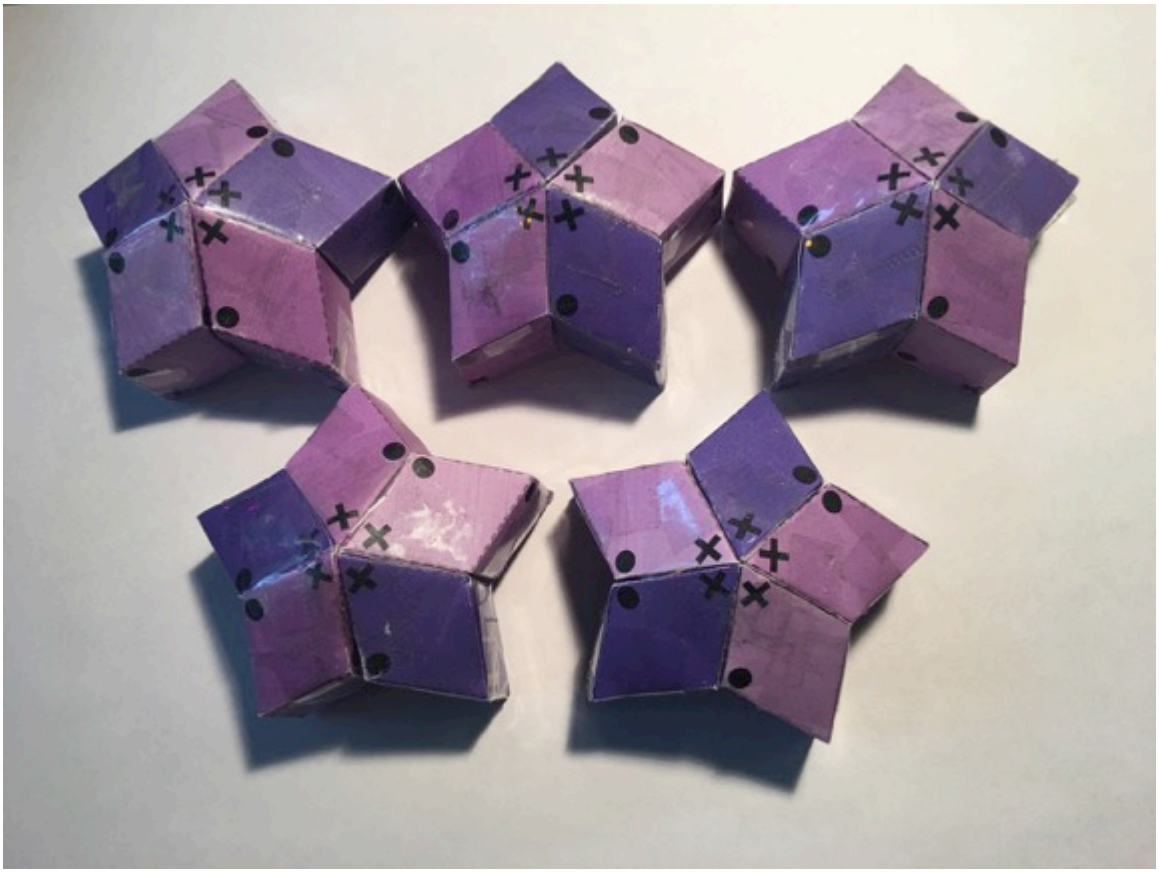

**Figure 6.9:** Five of the cycling permutations of one chirality of the hexecontahedron. In the other chiral form, light purple is swapped for dark purple, and vice versa. Note that I call this a cyclic permutation because although the chirality (light/dark purple) is cycling, the matching rules on the top and bottom (not shown) are **not.**

**Figure 6.10:** This figure shows five of the hexecontahedron cusps. These are the faces that can match with rhombic triacontahedra. Note the absence of matching-rule dots or crosses in the central five-fold vertices. For a cusp of the same chirality, the matching-rule decoration will be of one chirality and never the other. Note the cycling chirality, as in ***Figure 6.9***.

The hexecontahedron cusps also come in two chiral varieties. One form has three of the light purple acute rhombohedra and two of the dark purple acute rhombohedra. The other form, not shown, exchanges each light purple for a dark purple rhombohedron. The top and bottom matching rules remain the same during the cyclic transformation of one cusp into another. Of particular interest is that the central five-fold vertices of the cusps do not have matching-rule dots or crosses. This means that only certain faces of the rhombic triacontahedron are allowed to fit into the cusps. This is in remarkable analogy to the characteristic decagon rotations of *Chapter Two* (***Figure 2.4***, ***Figure 2.10***).

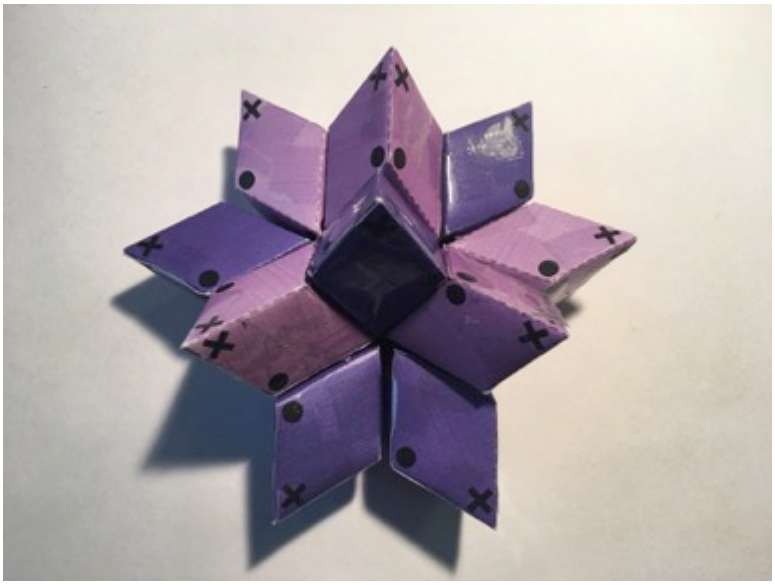

**Figure 6.11:** Partial hexecontahedron—light and dark purple represent different chiralities in the decoration of matching rules (black dots and crosses), which are mirror symmetric for the two different colors. The complete hexecontahedron would contain twenty acute golden rhombohedra.

These cusps then overlap, as coverings, with one another to form the final hexecontahedron. ***Figure 6.11*** shows the partial assembly of a hexecontahedron. Each cusp may be one of the options shown in ***Figure 6.10***, or their chiral twins, and must also obey all internal matching rules with other cusps and overlying rhombic triacontahedra that fit into the cusps.

## Assembling Triacontahedra and Hexecontahedra into Icosahedral Clusters

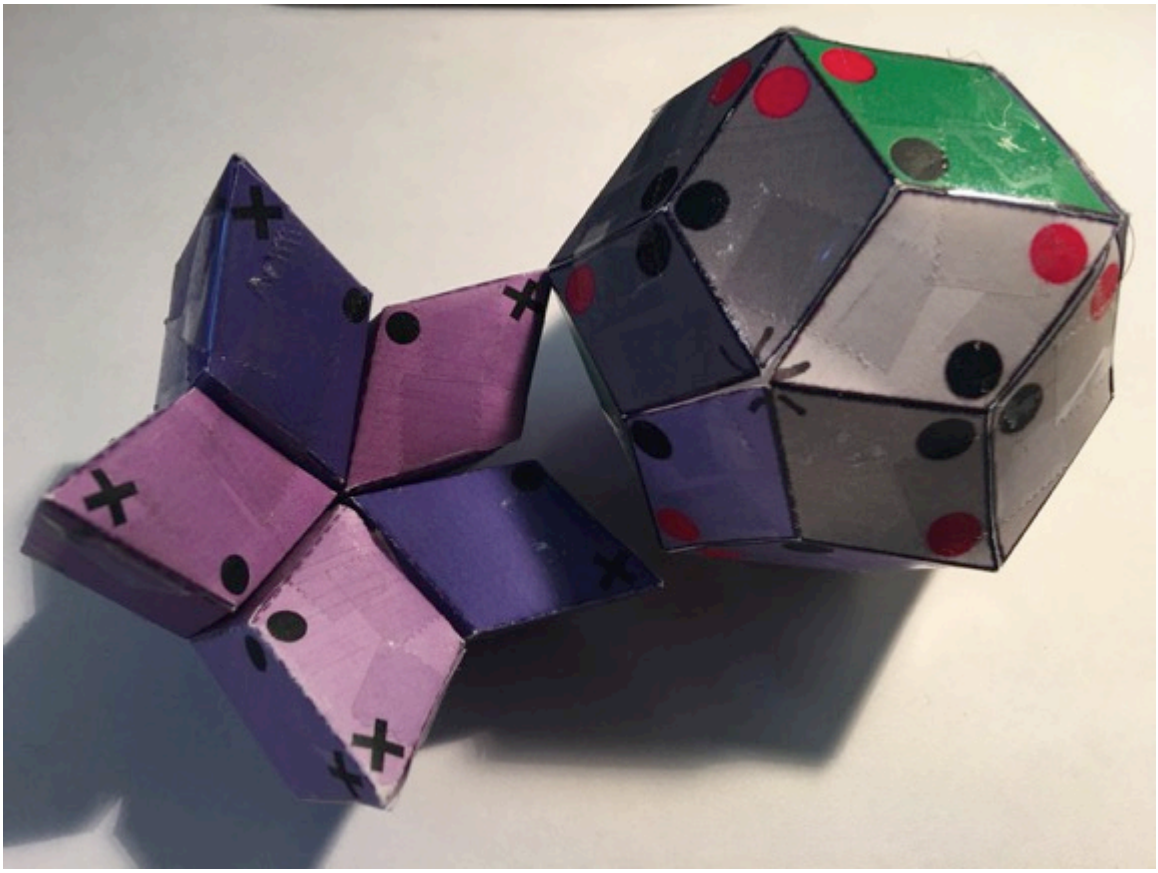

**Figure 6.12:** The face of the hexecontahedron cusp on the left will mate with the matching rules of the rhombic triacontahedron on the right, provided that crosses match with red dots and black dots match with other black dots. Note the absence of matching rules on the five-fold vertex of the rhombic triacontahedron.

The rhombic triacontahedra fit into the hexecontahedron cusps. They must match the rotational orientation of the cusp, as well as the chirality. Like the hexecontahedra, the rhombic triacontahedra come in two chirality types. The chirality type of the triacontahedron, from a construction point of view, is quite straightforward. Each triacontahedron can be deconstructed into composite rhombohedra in 120 ways—but a simple one is demonstrated in ***Figure 6.6***. There, one can see a rhombic dodecahedron that nests inside the rhombohedra that make up the rest of the triacontahedron. Geometrically, the only necessary change for this triacontahedron to swap chiral types is a 180° flip of the rhombic dodecahedron around its short axis. This is the **only** part of the rhombohedral assembly of the triacontahedron that breaks bilateral symmetry. However, this chirality flip also changes all of the matching rules on the triacontahedron (all

purple and grey rhombohedra need to switch to their chiral partners) so that they are a mirror reflection of the other. Just like the Tübingen tiling, this chiral reflection of a polyhedron may not change its polyhedral type or orientation, but it will change how the shape is deflated[39] when the decoration is represented in the next level of hierarchy. This last point **will** result in a geometric change, since the rhombic dodecahedron of the triacontahedron will flip 180º.

Because the triacontahedron has icosahedral symmetry, it has twelve 5-fold axes[40]. However, only three of these vertices are missing the matching rules from their central vertex—a necessary condition for fitting into the hexecontahedron cusps! This means that there are only **three** faces of the triacontahedron that can match with a hexecontahedron cusp.

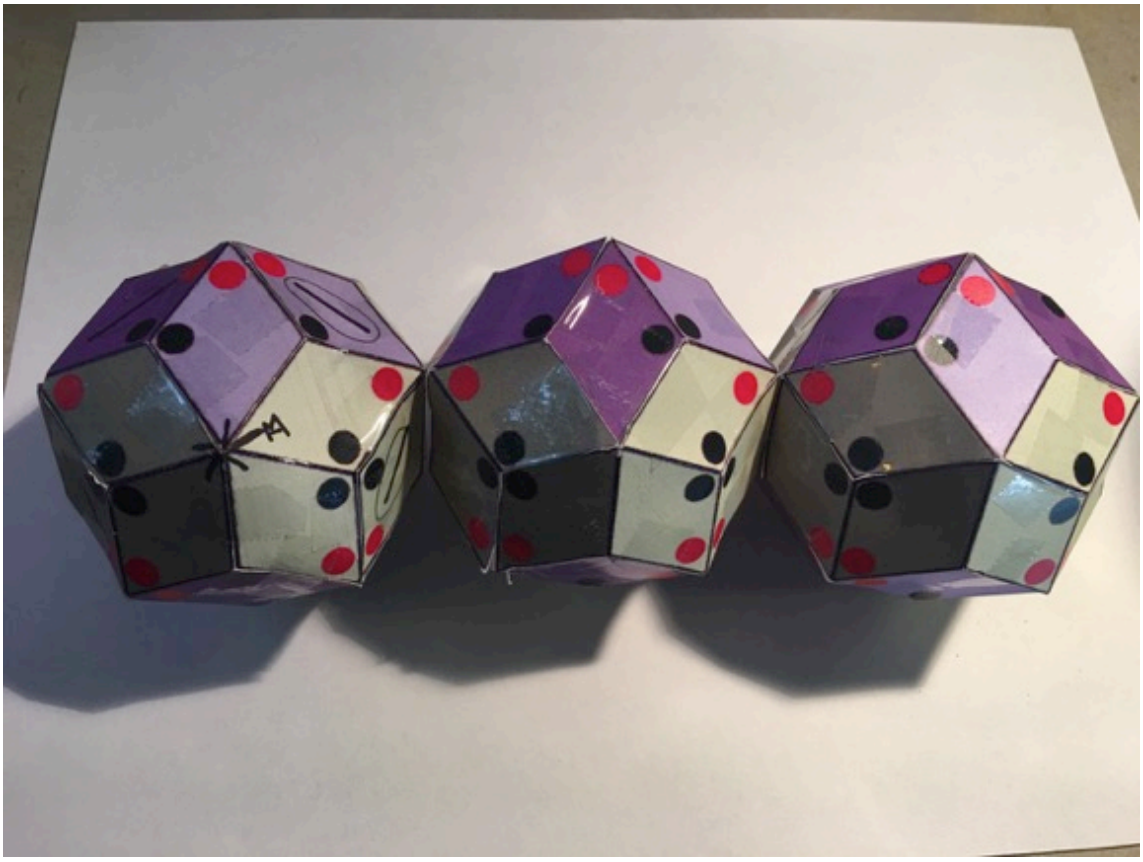

**Figure 6.13:** This is one chirality of rhombic triacontahedron. Note the lack of red or black dots on the central five-fold vertex. This is a quick way of determining whether a triacontahedron five-fold vertex can fit into one of the hexecontahedron cusps. The rotation needs to be found afterwards. Note: ignore the Sharpee markings!

[39] This is assuming each rhombohedron had a unique deflation, which it does not.

[40] A rhombic triacontahedron can be transformed into an icosahedron if we draw lines along the long diagonals of each golden rhombus face. Then we see that the 5-fold vertices of the triacontahedron map exactly to the vertices of an icosahedron, which are all 5-fold.

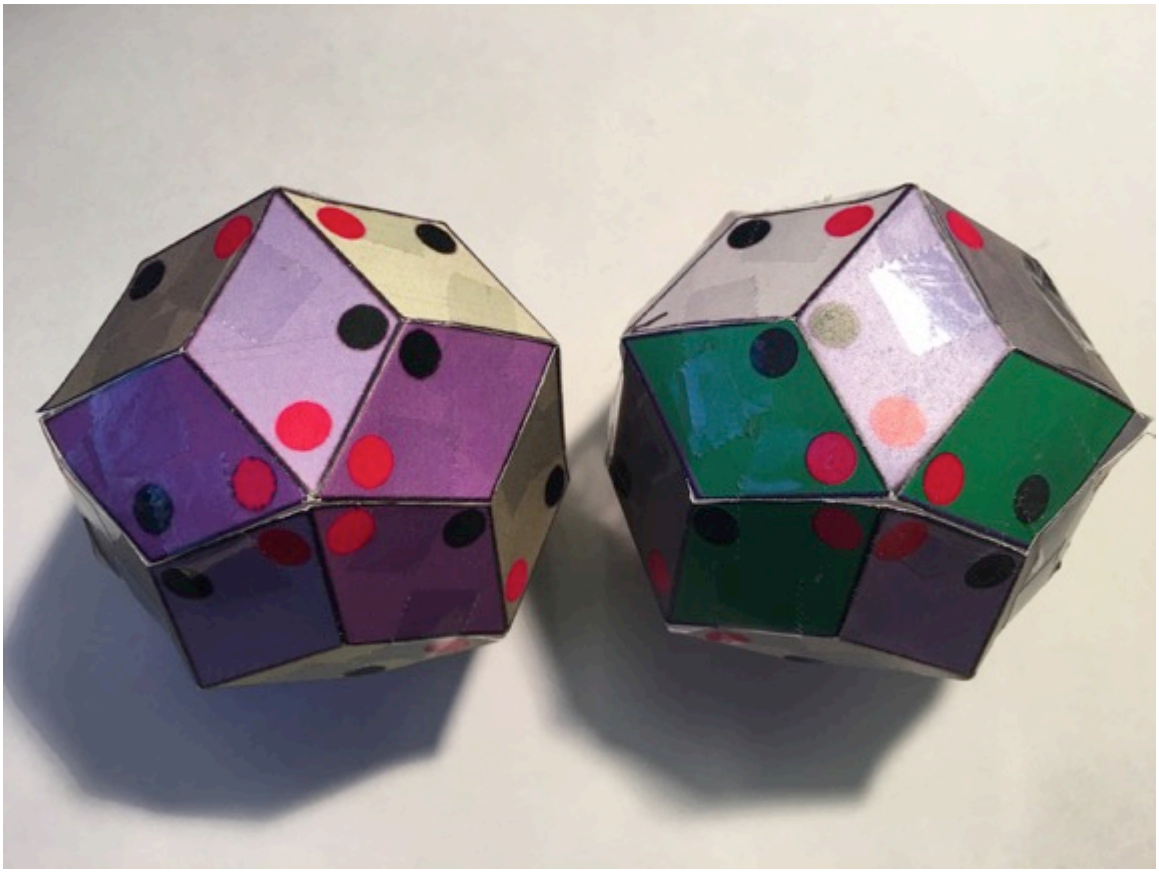

**Figure 6.14:** Purple (left) and green (right) chiral forms of triacontahedra. Note the mirror symmetry of the matching rules. They both comprise the same four types of rhombohedra, but the green triacontahedron has just been colored differently to make the distinction of its chiral type more apparent. Green rhombohedra on the right will have the same chiral decoration as the pink (or light purple) rhombohedra on the left. The purpose of these paper models is to provide an accurately mirrored set of triacontahedra, and a way to easily distinguish between them.

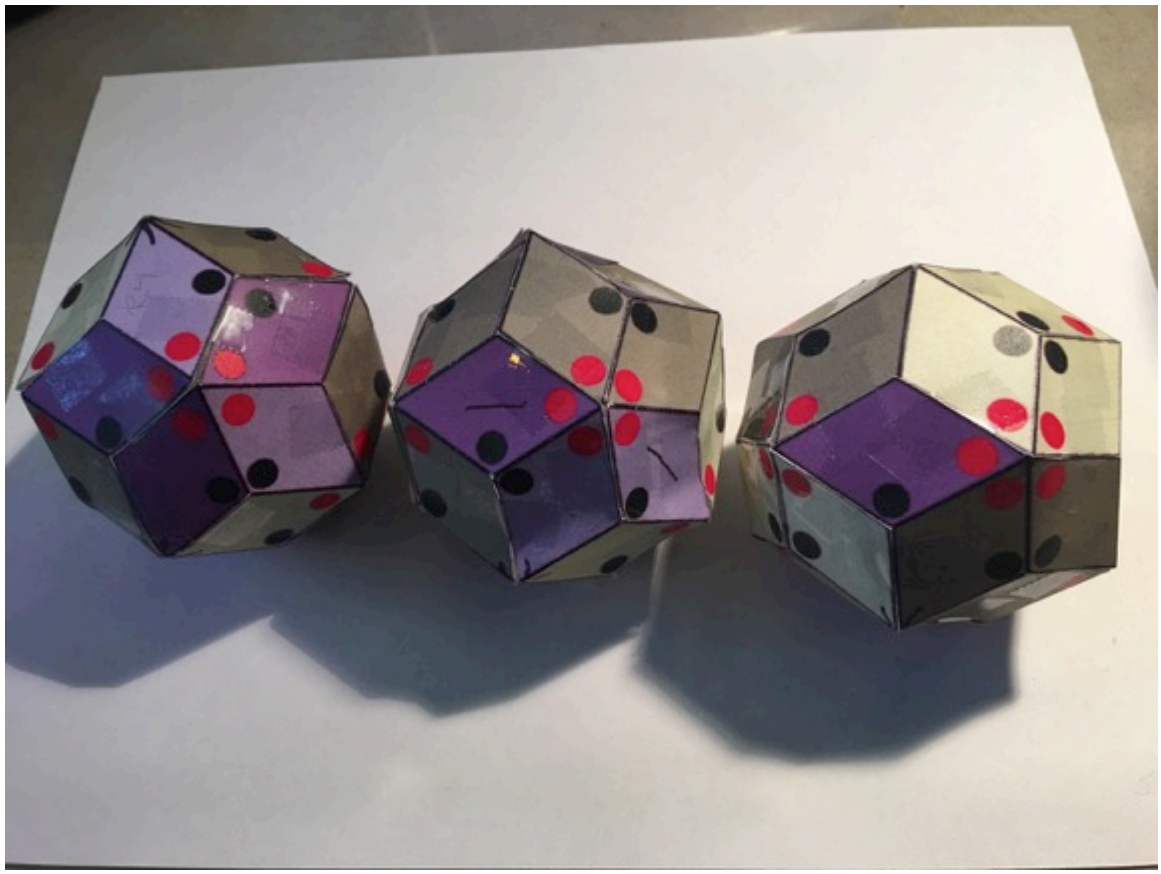

**Figure 6.15:** These are the opposite sides of the triacontahedra shown in ***Figure 6.13***. The two shades of purple correspond to acute rhombohedra, and the shades of grey correspond to oblate rhombohedra. The left face corresponds to the other side of the five-fold acute rhombohedron, or what I am calling the default face, in ***Figure 6.5***.

The five-fold vertex facing us on the leftmost triacontahedron in ***Figure 6.15*** is the face that points outward in the default "blue" cluster that is our starting point for constructing the AKN tiling. Note that it has a different matching-rule decoration than the triacontahedron in the center and the triacontahedron on the right. We can just refer to this as the default face, or "D". In the middle triacontahedron, there are three acute rhombohedra that comprise the face, which I will refer to as the "B" face. The rightmost triacontahedron has only a single acute rhombohedron and will be referred to as the "R" face. Now, looking at ***Figure 6.13***, it can be seen that the opposite side of the default face—the side that must fit into one of the hexecontahedron cusps—has a different chiral pattern than the other two. That means that it cannot fit into one of the five cusps listed in ***Figure 6.10***. Instead, it requires a cusp of opposite chirality, like that shown in ***Figure 6.16***. If we know how the triacontahedra decorate the

hexecontahedron, then we can deduce the location and chirality of the underlying hexecontahedron cusps. Moreover, we can then understand that if a triacontahedron rotates to have its D, B, or R face pointing outward, its opposite side may change the chirality requirements of the underlying hexecontahedron face. E.g., if we go between B and R, then no change is necessary. But any change going from D to B, D to R, or vice versa, will necessitate a chirality change in the underlying hexecontahedron cusp. The hexecontahedron puzzle is not entirely solved by this, however, as there are at least five different subtypes for each of the two chiral types of hexecontahedron cusp. Knowing the location and chiral type for each of the hexecontahedron cusps is, however, a significantly reduced parameter space than what I started with!

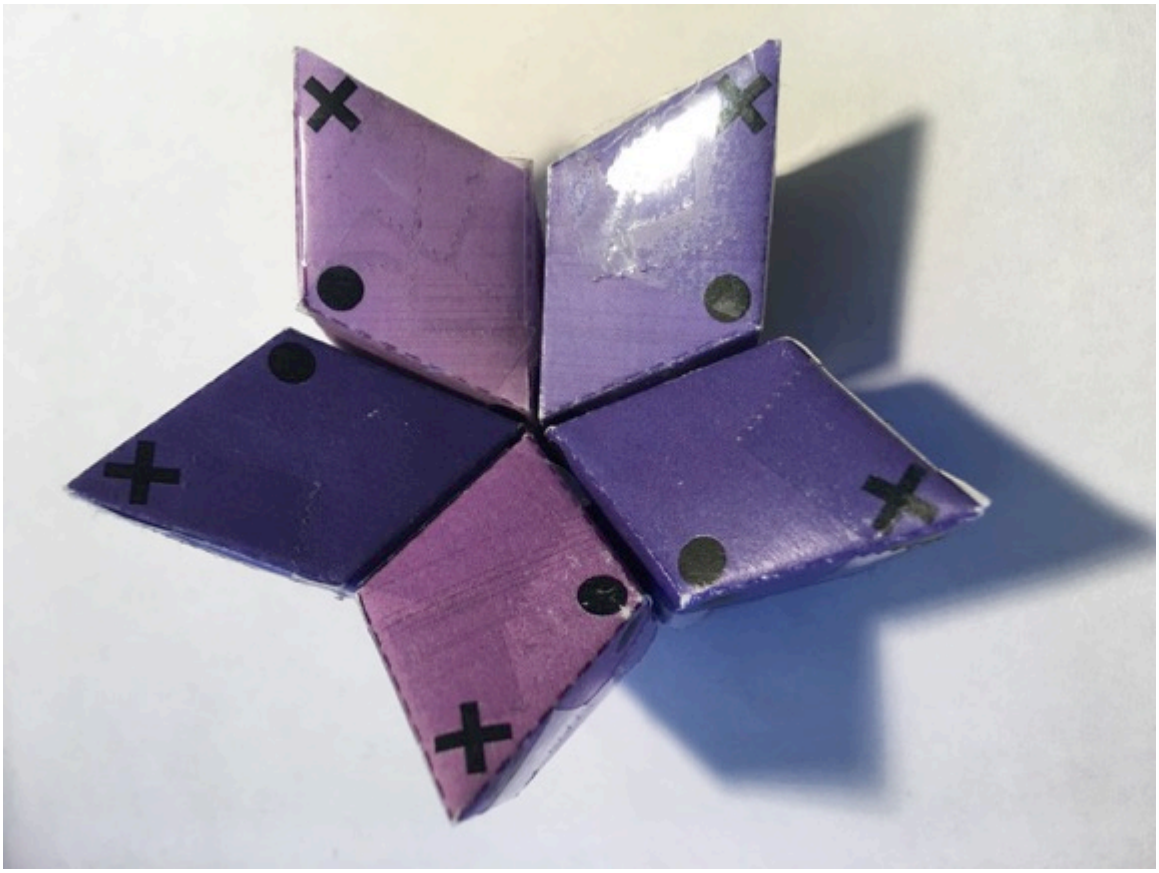

**Figure 6.16:** This cusp has opposite chirality from those in ***Figure 6.10***. Let's call this a "three-purple" hexecontahedron cusp, since it has three acute rhombohedra with the dark purple chirality, and only two of the pink (light purple) chirality.

Now that we have some terminology worked out, a quick examination of the matching rules on the triacontahedra and hexecontahedron cusps reveals the following set of rules. The

purple-type (***Figure 6.14***) triacontahedron on the D face must mate with a three-purple hexecontahedron cusp (***Figure 6.16***). The purple-type triacontahedra on the B face must mate with a two-purple type hexecontahedron cusp (***Figure 6.10***). The purple-type triacontahedron R face must mate with a three-purple hexecontahedron cusp. For a green-type triacontahedron, the requirements are just chirally reversed. Green-type D must mate with a two-purple cusp, Green-type B with a three-purple cusp, and Green-type R with a two-purple cusp.

To summarize, there are two chiralities of triacontahedron, and two chiralities of hexecontahedron cusp. Each triacontahedron has three faces that will mate with a cusp, and each triacontahedron has two of one chirality and one of the other. The chirality of the triacontahedron cusp must match the chirality of the hexecontahedron cusp.

## Ideal Quasicrystal Modeling

Like the decagonal motifs from the Penrose tiling, there exists a default orientation for the twelve rhombic triacontahedra when they sit in the hexecontahedron cusps. Fortunately, this orientation was determined by a perfect icosahedral quasicrystal created by Michael Engel from the projection of a simple cubic 6D hypercubic lattice (Engel et al., 2015). The simple cubic hyperlattice leads to the Ammann-Kramer-Neri tiling[41].

[41] In contrast, the face-centered cubic projection leads to the Socolar-Steinhardt tiling (Socolar & Steinhardt, 1986) and the body-centered cubic is the same single-component icosahedral quasicrystal seen in self-assembly simulations (Engel et al., 2015).

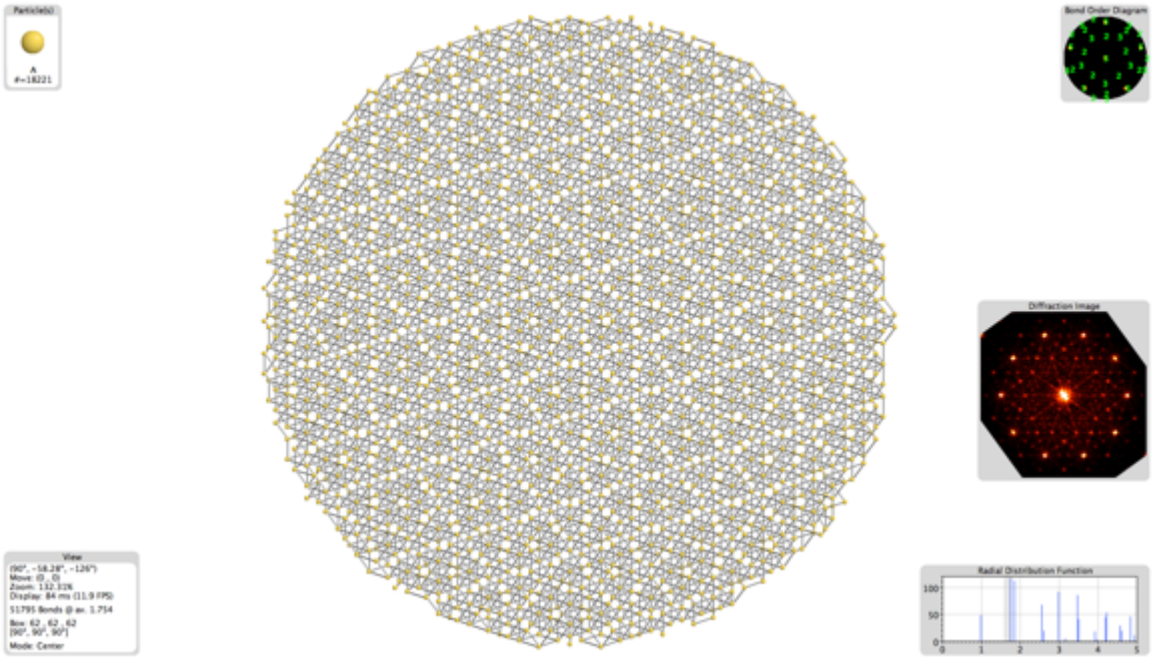

**Figure 6.17:** This is an image of 18,221 particles arranged into an Ammann-Kramer-Neri icosahedral quasicrystal. This view is along one of the five-fold axes. Note the selection of the second and third radial distribution peaks—it is necessary to view only bonds at these two length scales in order to view the composite acute and oblate rhombohedra that make up the quasilattice.

Custom code was used to convert this set of particle positions into acute and oblate rhombohedra.

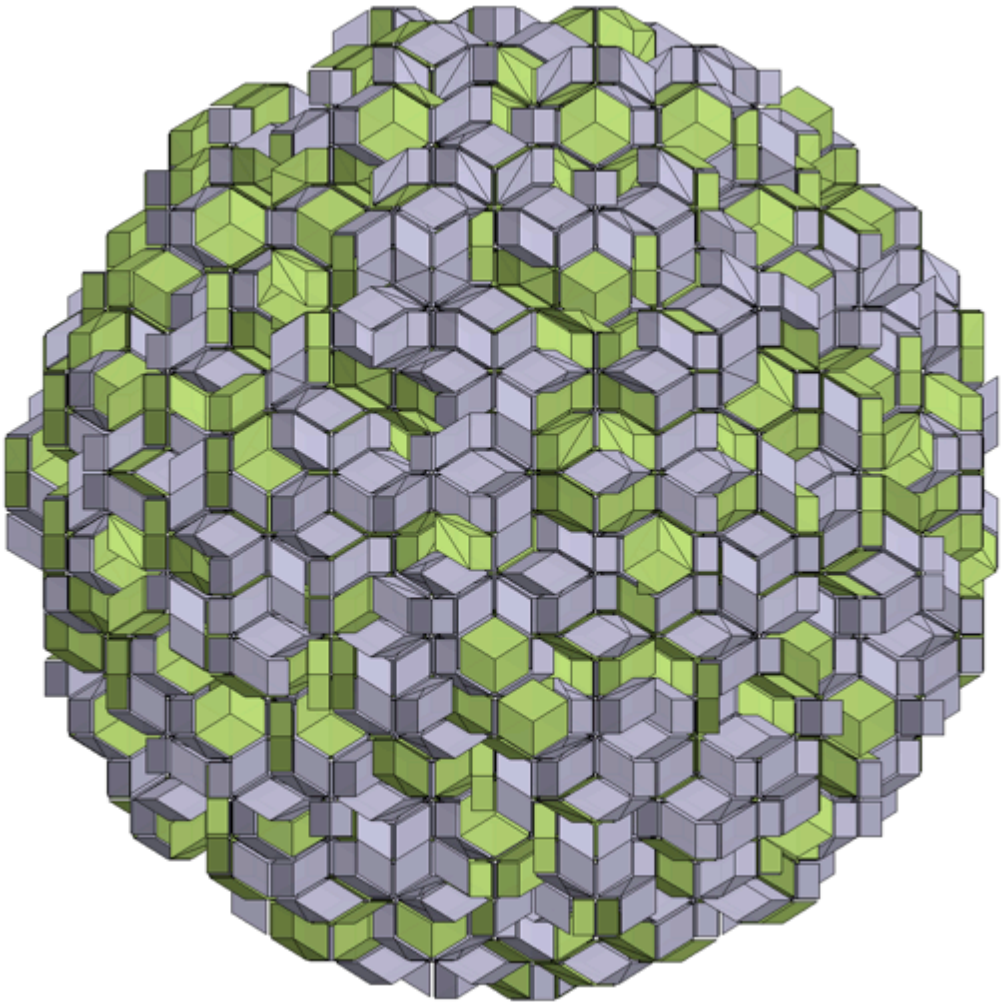

**Figure 6.18:** The Ammann-Kramer-Neri tiling comprising acute rhombohedra (grey) and oblate rhombohedra (green).

Once I had the rhombohedral form, I could begin carving out the shapes that I expected to be there. These included an entire rhombic triacontahedron, a rhombic hexecontahedron, and the full "icosahedron" created from twelve of the triacontahedra around a hexecontahedron core—the icosahedral motif or IC. The spacing between the rhombohedra is for visualization purposes—the real structure is of course space-filling.

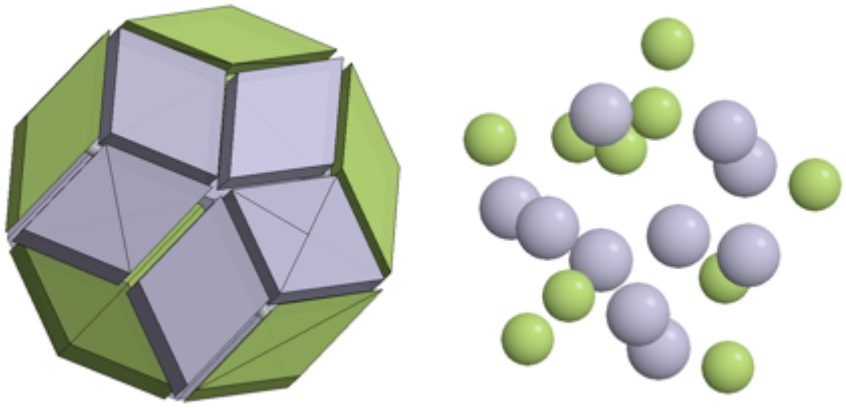

**Figure 6.19:** Rhombic triacontahedron and particle centers. The image on the left shows the five-fold vertex that faces outward from the rhombic hexecontahedron. The right image shows the particle centers—there are ten acute and ten oblate rhombohedra for every rhombic triacontahedron. The rhombic dodecahedron that determines the chirality sits on the five-fold vertex that is opposite to this one. Note: the lines across the polyhedral faces do not represent anything in the model—they are decimal artifacts from the vertex-crawler code that converted the mathematical projection into polyhedra.

**Figure 6.20:** The rhombic dodecahedron will fit to form a rhombic triacontahedron in two ways. One (middle) creates the image from ***Figure 6.15 (middle)*** with the three acute rhombohedra on the left. The other (right) places the three acute rhombohedra on the right.

In ***Figure 6.20***, we see the two chiralities of the rhombic triacontahedron that were mentioned earlier. In the context of ***Figure 6.15***, we see that the flip of the rhombic dodecahedron changes the position of the five-fold vertex that has three exposed acute rhombohedra (B) with the one that has one exposed acute rhombohedron (R). This will provide context for the later section where we look at hexecontahedra with different decorations of triacontahedron chirality and orientation.

**Figure 6.21:** The hexecontahedron comprises twenty acute rhombohedra. Connecting the five-fold vertices will also create an internal icosahedron.

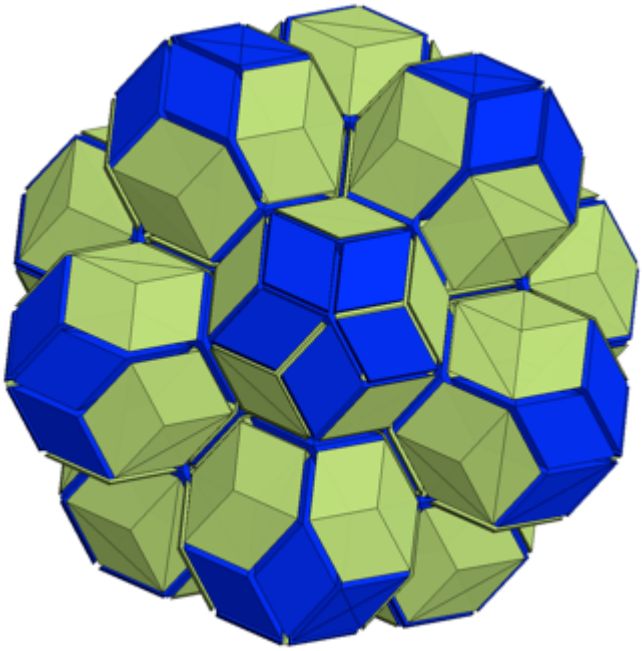

**Figure 6.22:** "Icosahedron" made from twelve rhombic triacontahedra around a rhombic hexecontahedron core—the icosahedral motif or IC. Acute rhombohedra have been colored blue, to emphasize that the five-fold vertex comprises five acute rhombohedra—the D face. As before, the oblate (flat) rhombohedra are shaded with light green.

## Making Sense of Complex Three-Dimensional Models

The shape in ***Figure 6.22*** has a total of 170 acute rhombohedra, and 145 oblate rhombohedra, which is not yet close in approximation to the Golden ratio (~1.172 vs. 1.618). It has some of the same symmetry elements as an icosahedron, so I refer to it as an icosahedral motif/icosahedral cluster. This specific motif, with all of the five-fold acute rhombohedra (D) vertices pointing outward, is the fundamental icosahedral motif—which is the first time this detailed motif has been identified in print, so far as I know. In analogy with the work done in *Chapter Two* on the Penrose tiling, I call this a "blue" icosahedral motif for simplicity. This blue motif will then layer over itself, thereby changing the orientation and chirality of each of the triacontahedra that fully overlap.

To make visualizing this structure easier, the five-fold ring of acute rhombohedra can be instead replaced with a point at its center of mass. When combined with the center-of-mass of the entire triacontahedron, this can be used to create a vector indicating the orientation of the triacontahedron—this accomplishes the same thing as drawing an arrow on the line of mirror symmetry of the characteristic decagons from *Chapter Two*. The arrow is drawn so that it points outwards for the pentagonal or icosahedral motif.

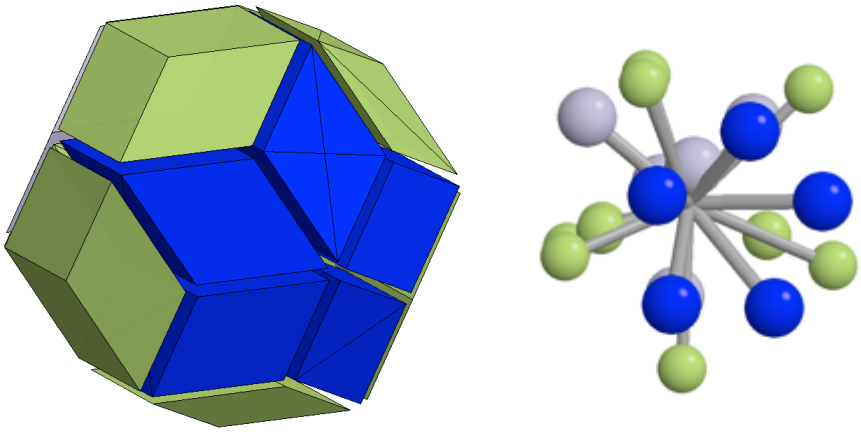

**Figure 6.23:** On the left, a triacontahedron is shown with the five-fold ring of acute rhombohedra colored in blue. The right image shows a particle-center view with this five-fold ring of acute rhombohedra. Grey lines indicate bonds with an imaginary particle at the triacontahedron's center of mass.

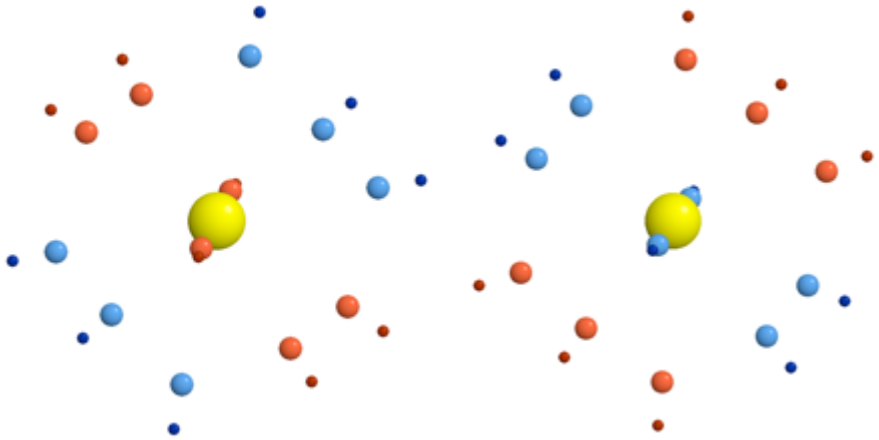

**Figure 6.24:** Left and right show two chiralities of the blue icosahedral motif with the highest degree of rotational symmetry—**all of the triacontahedra sit in their D faces on the hexecontahedron cusps**. The large yellow sphere represents the center of the hexecontahedron. The medium blue and orange spheres represent the center of mass of the triacontahedra. Small blue and orange spheres show the location of the five-fold ring of acute rhombohedra. We can see with a brief glance that this is the rotationally-symmetric icosahedral motif because all of the smallest spheres are pointing outwards from the yellow sphere—this means that each triacontahedron is sitting with its five-fold ring of acute rhombohedra pointing outward. Together, this characterization of the triacontahedra allows for easy visualization of each type of icosahedral motif.

Now that we've characterized the triacontahedra with a yellow sphere at the center of the hexecontahedron, and a sphere at the center of the five-fold ring of rhombohedra, it becomes easier to visualize the construction of the "blue" icosahedral motif—the icosahedral motif with the highest degree of rotational symmetry. **It turns out to be the case that this cluster has a pole of three triacontahedra of one type of chirality at each side, and a band of six of the other triacontahedra going around it. Flipping the chiralities of each triacontahedron produces the chiral decoration of the other blue cluster.** This is interesting detail not found in any other literature.

These blue ICs then layer over each other—two triacontahedra at a time. Given the unique properties of zonohedra—whereby they are made from composite polyhedra—they are allowed to partially overlap and obey the rules of a covering. **This property is essential for a quasicrystal, as these partial overlaps will not require a redefinition of either the chirality or orientation of the overlapping triacontahedra.** Alternately, a full overlap will necessitate the change of both chirality and orientation—just like the Tübingen pentagons in *Chapter Four*. Additionally, up to two overlaps are allowed—so the chirality and orientation can flip **twice**.

This means that **three** complete overlaps of the triacontahedra are allowed. **This number of overlaps is not seen in any of the two-dimensional quasicrystal tilings.**

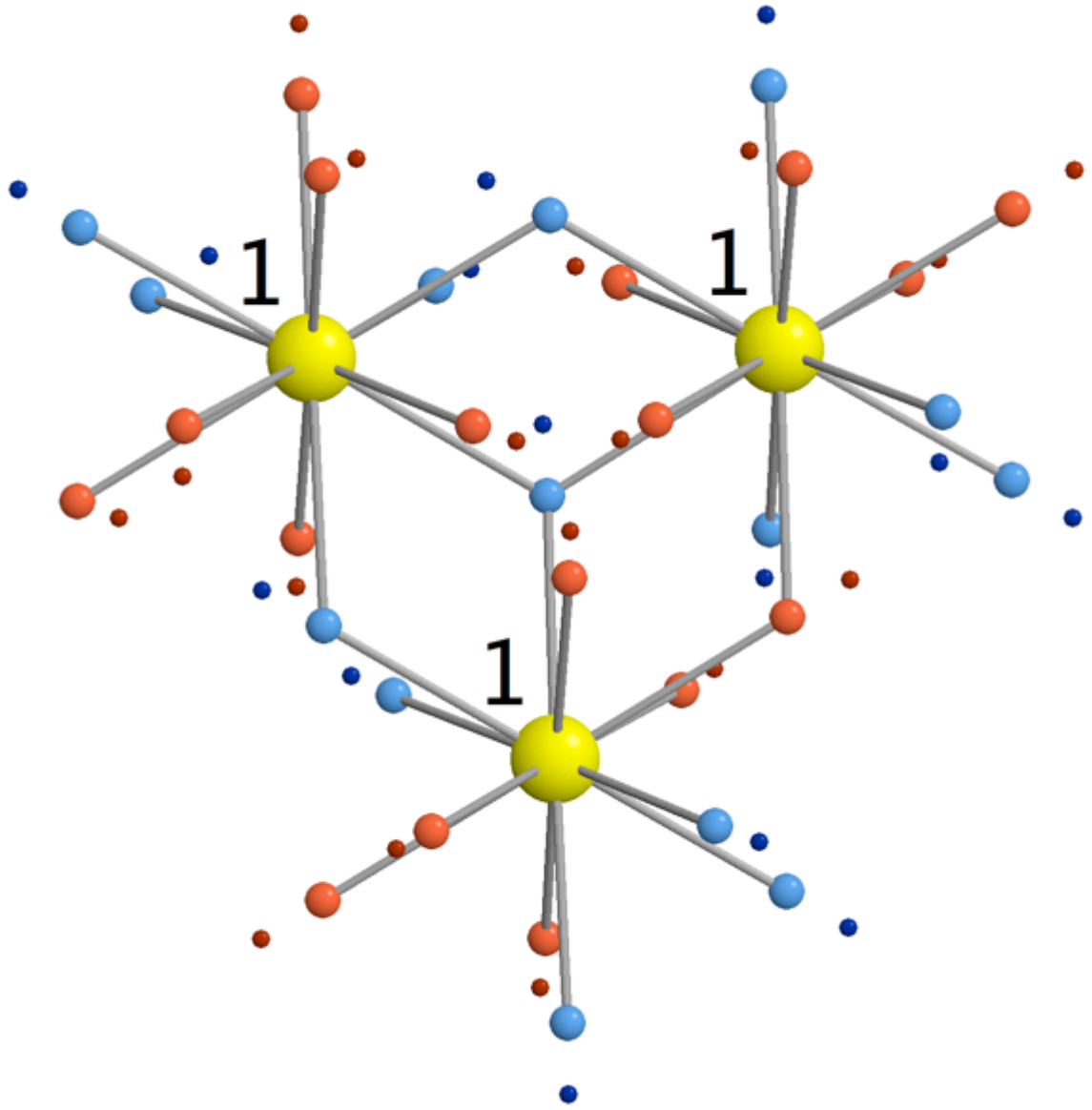


**Figure 6.25:** Three ICs with centers marked by large yellow spheres (and the number 1) overlap with triacontahedra of different chiralities marked by medium-sized blue and orange spheres. Small spheres represent the five-fold ring of acute rhombohedra present on one side of each triacontahedron. The central medium blue sphere has three grey bonds extending from it—this is the triacontahedron that is shared by all three ICs.

In ***Figure 6.25***, three ICs are spaced at the distance necessary for complete triacontahedral overlaps. Each IC overlaps two complete triacontahedra with each of these

neighbors, indicated by the medium blue and orange spheres that are connected with the grey bonds. Depending on the layering hierarchy of each of the given ICs, its triacontahedra will have the five-fold acute rhombohedral ring facing outwards with respect to that yellow sphere. This can be observed in the bottommost IC, which is "blue" because all of its triacontahedra have five-fold rings that point outwards. This type of blue IC has a pole of three triacontahedra with blue chirality, and an equatorial band of triacontahedra with orange chirality. Also of note is the central (center of the hexagon made from bonds) triacontahedron—this has a chirality and orientation consistent with three overlaps. Because the chirality flips twice and it is currently blue, we know that whichever triacontahedron is on the bottom must also be blue.

These ICs sit on the vertices of a new network of rhombohedra, which themselves make up new networks of ICs.

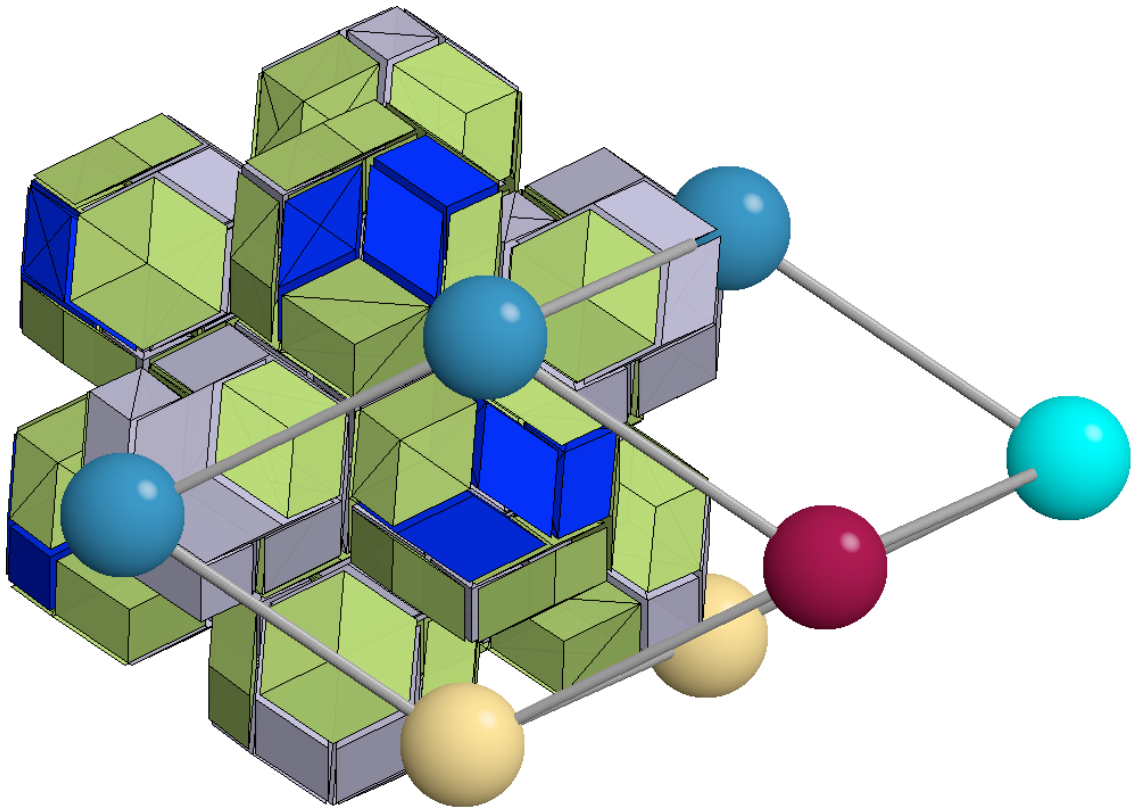

**Figure 6.26:** A single IC placed onto the underlying rhombohedron network. The bonded particles show an acute rhombohedron with spheres marking the location of each of the ICs on the eight vertices. Seven are visible, and the last one is hidden in the center of the single IC that is shown in full.

Interestingly, and in some contrast to existing literature (Audier & Guyot, 1986), the five-fold ring of acute rhombohedra is actually a very special component of the rhombic triacontahedron. This ring, in combination with other partially overlapping triacontahedra, actually creates the hexecontahedron of the neighboring IC. In that respect, the tiling is not made of separate triacontahedra and hexecontahedra, but rather **the hexecontahedra are created entirely by these triacontahedra**. **This is why some of the triacontahedra sit in their D, B, or R faces—the pentagon of acute rhombohedra will create part of the hexecontahedron of neighboring ICs.** Each yet-larger rhombohedron must have hexecontahedra on each vertex, and so different ICs are required to decorate those vertices so as to reproduce the hexecontahedra. These different DBR faces will create parts of hexecontahedra at different distances from the core hexecontahedron. The only caveat is that these triacontahedra do not have to be complete. They may have spaces in the shape of an oblate rhombohedron, for instance, that are actually filled in by various sides of a rhombic dodecahedron. This can be seen in the triacontahedron that makes up the leftmost vertex (teal sphere) of the acute rhombohedron bond network shown in ***Figure 6.26***, where five of the oblate (flat and green) rhombohedra are missing.

The vertices of the second-order rhombohedra will bring the ICs together at different distances. There are three relevant distances for the Ammann-Kramer-Neri tiling discovered and explored in this chapter, shown in ***Figure 6.27***, ***Figure 6.29***, and ***Figure 6.33***.

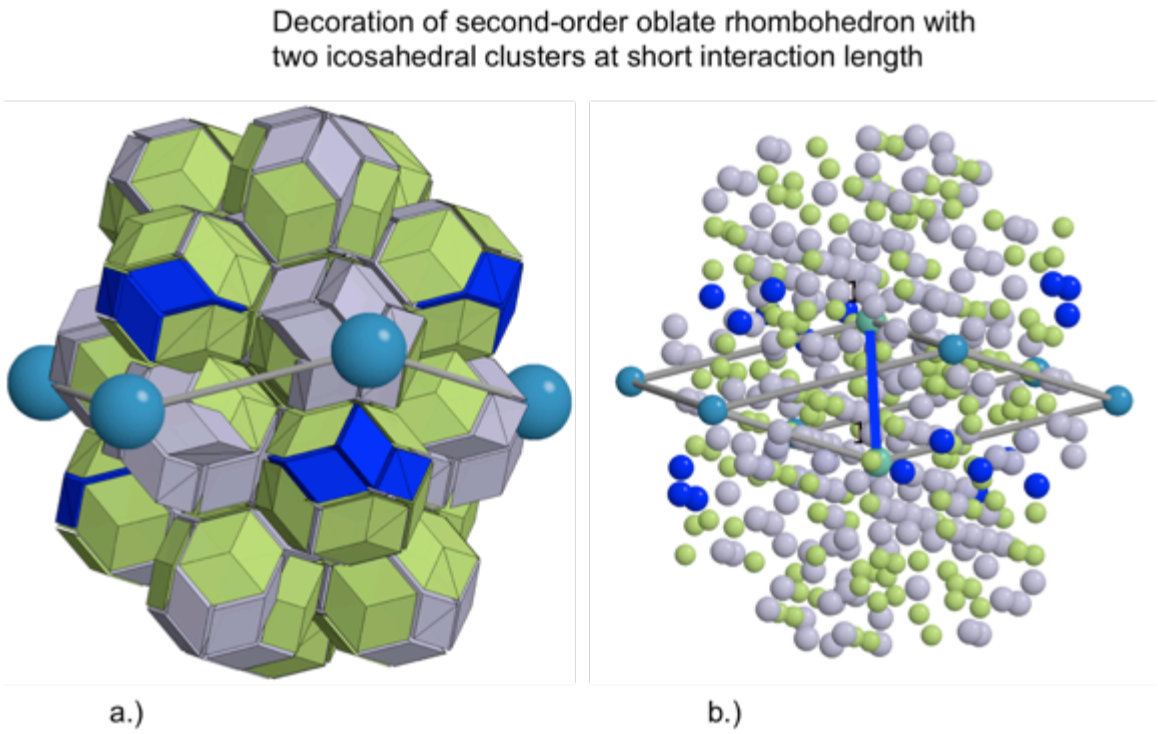


**Figure 6.27:** Here is a second-order oblate rhombohedron decorated with just two of its respective ICs. The other IC locations are centered on the large teal spheres. In (b), the short interaction scale is indicated by the bright blue line.

At the short interaction length, there are no triacontahedra overlaps. But because the triacontahedra are zonohedra, they are allowed to partially overlap without changing their chirality or orientation. This property makes it possible for the two IC to puzzle together in a seemingly miraculous way. Each IC exists independently as a perfect set of twelve triacontahedra around a single hexecontahedron, which is mirrored exactly in the opposite IC with no conflict.

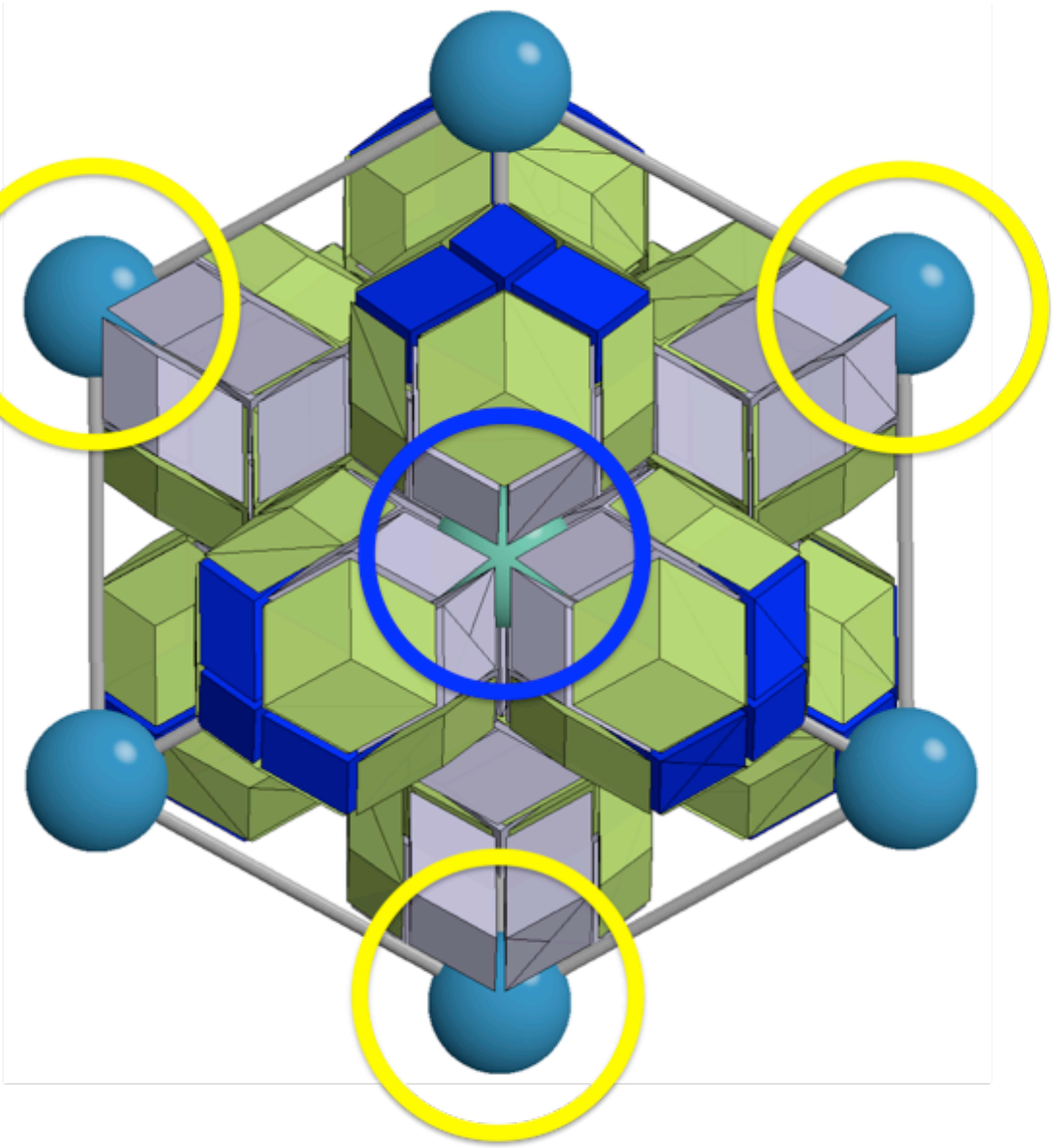

**Figure 6.28:** This figure shows a second-order oblate rhombohedron with only a single IC made visible.

***Figure 6.28*** shows how a single IC plays a role in the creation of neighboring ICs. Recall that if a triacontahedron has three acute rhombohedra marked with blue, then the triacontahedron sits on a "B" face. Here, we see explicitly some of the functionality behind the B face in the dark blue circle. A teal hexecontahedron center is partially created by these D faces with the blue acute rhombohedra all facing away. Likewise, there are D faces in all of the yellow circles that serve the same role. Also of interest are the missing parts of the triacontahedra in the yellow circles. These missing pieces are in the same shape of an oblate rhombohedron, as was

also observed in ***Figure 6.26***, and are likewise filled in by acute and oblate rhombohedra in the form of rhombic dodecahedra from the triacontahedra belonging to neighboring ICs.

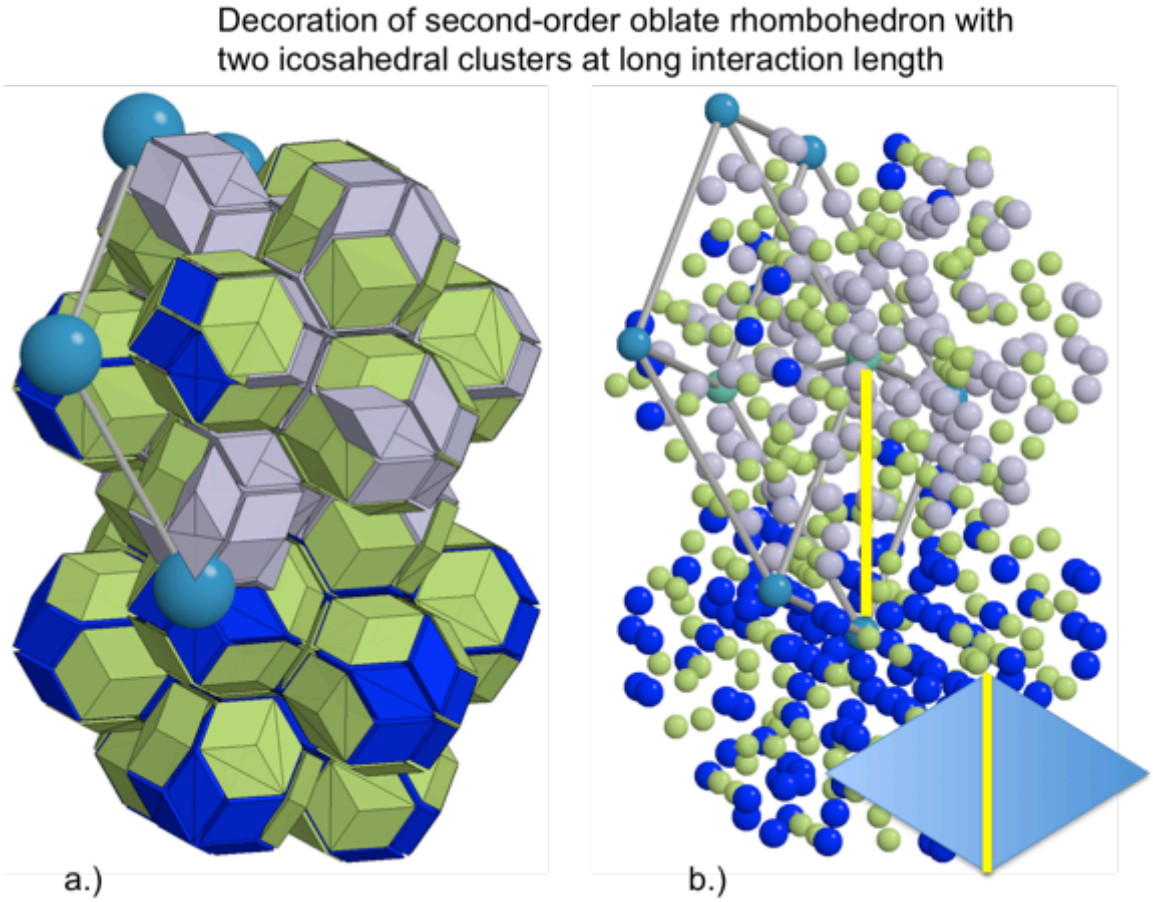


**Figure 6.29:** This is the same second-order oblate rhombohedron, but with different ICs shown. These ICs are at the long interaction length that takes place in the AKN. As in the inset of (b) shows, this is the short diagonal of the golden rhombus face.

The longest length scale that ICs overlap at is actually the short diagonal across the golden rhombus face (a different rhombus than the Penrose rhombuses) of the oblate rhombohedron, which is shown with the yellow line of ***Figure 6.29 (b)***, and again with the yellow line on the blue rhombus. This distance is slightly longer than the edge length of the rhombohedral network—approximately 1.049 if the network edge length is 1. At this distance, the ICs overlap with two complete triacontahedra overlaps. As such, there are two forced triacontahedra chirality flips and re-orientations, depending on the layer hierarchy.

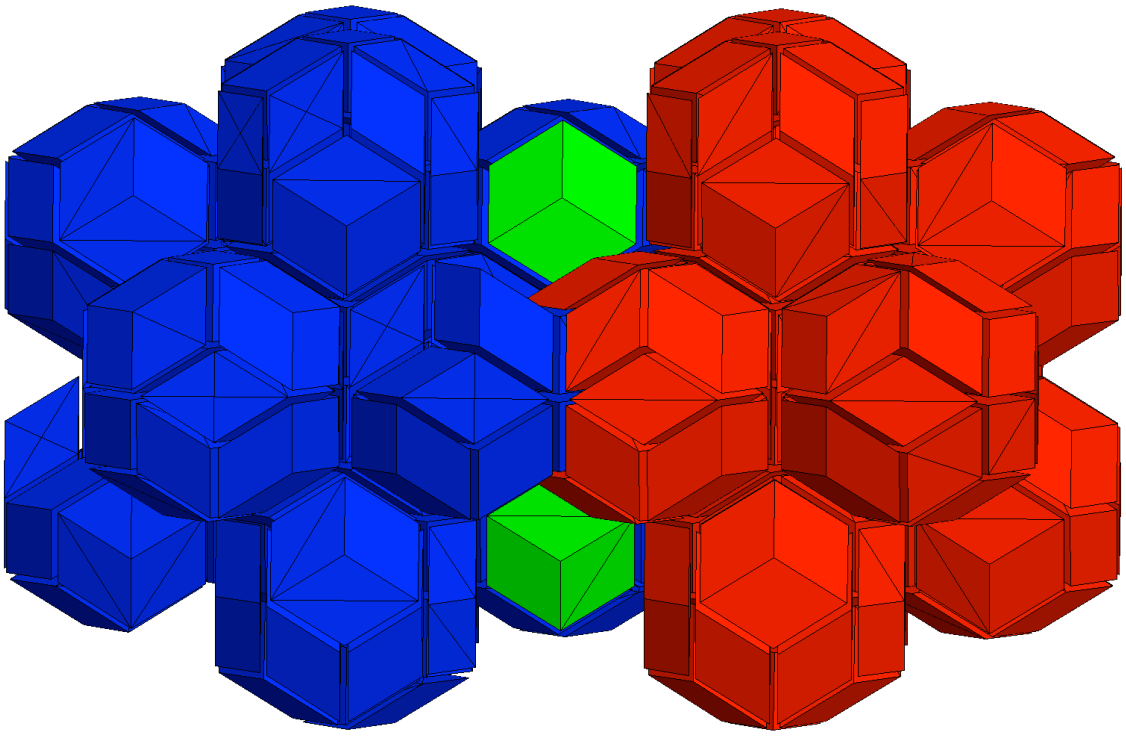

**Figure 6.30:** At the longest length scale, two ICs have been colored entirely blue and red, respectively. The two triacontahedra that undergo complete overlaps have each had a single oblate rhombohedron colored green for clarity.

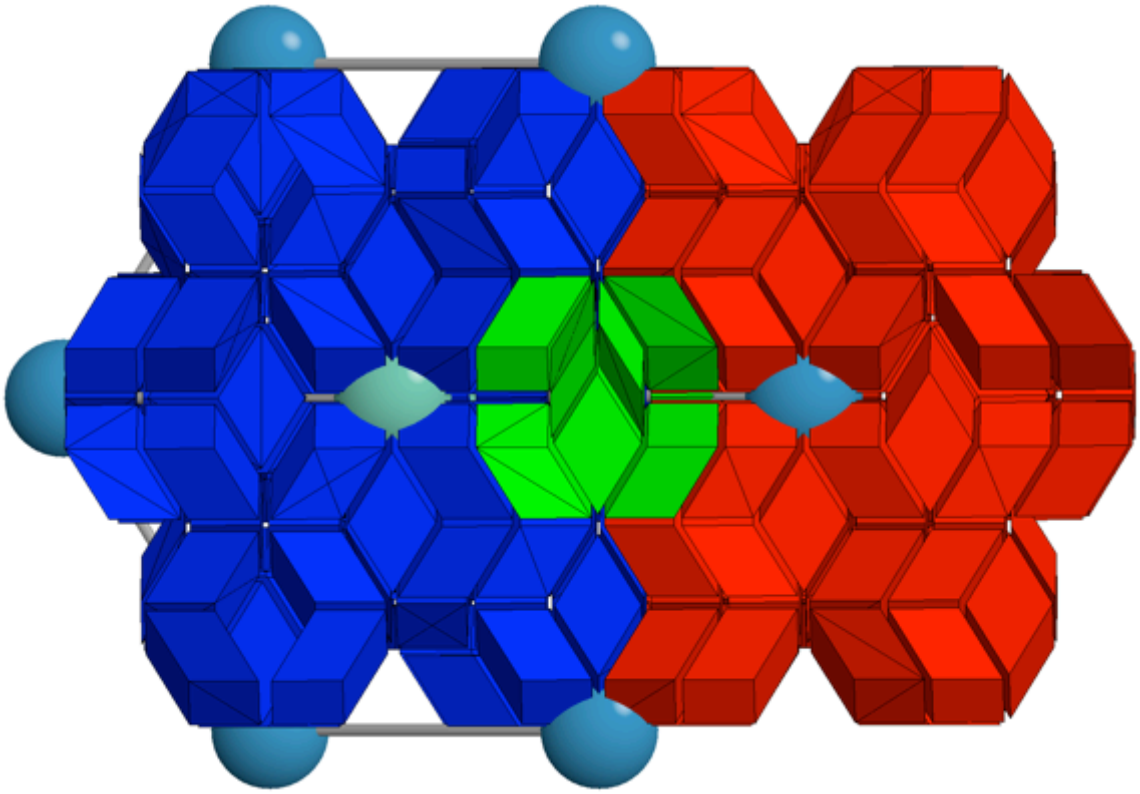

**Figure 6.31:** At the longest interaction length, the two ICs overlap two entire triacontahedra. A cross-section of just one of these is shown in green. It can be seen that this triacontahedron plays no role in the construction of the other hexecontahedron cluster, but rather fits neatly into each hexecontahedron cusp. Consequently, this triacontahedron must decide whether it will orient as D in one, and B or R in the other, or vice versa. This is ultimately what determines the IC covering or layering type.

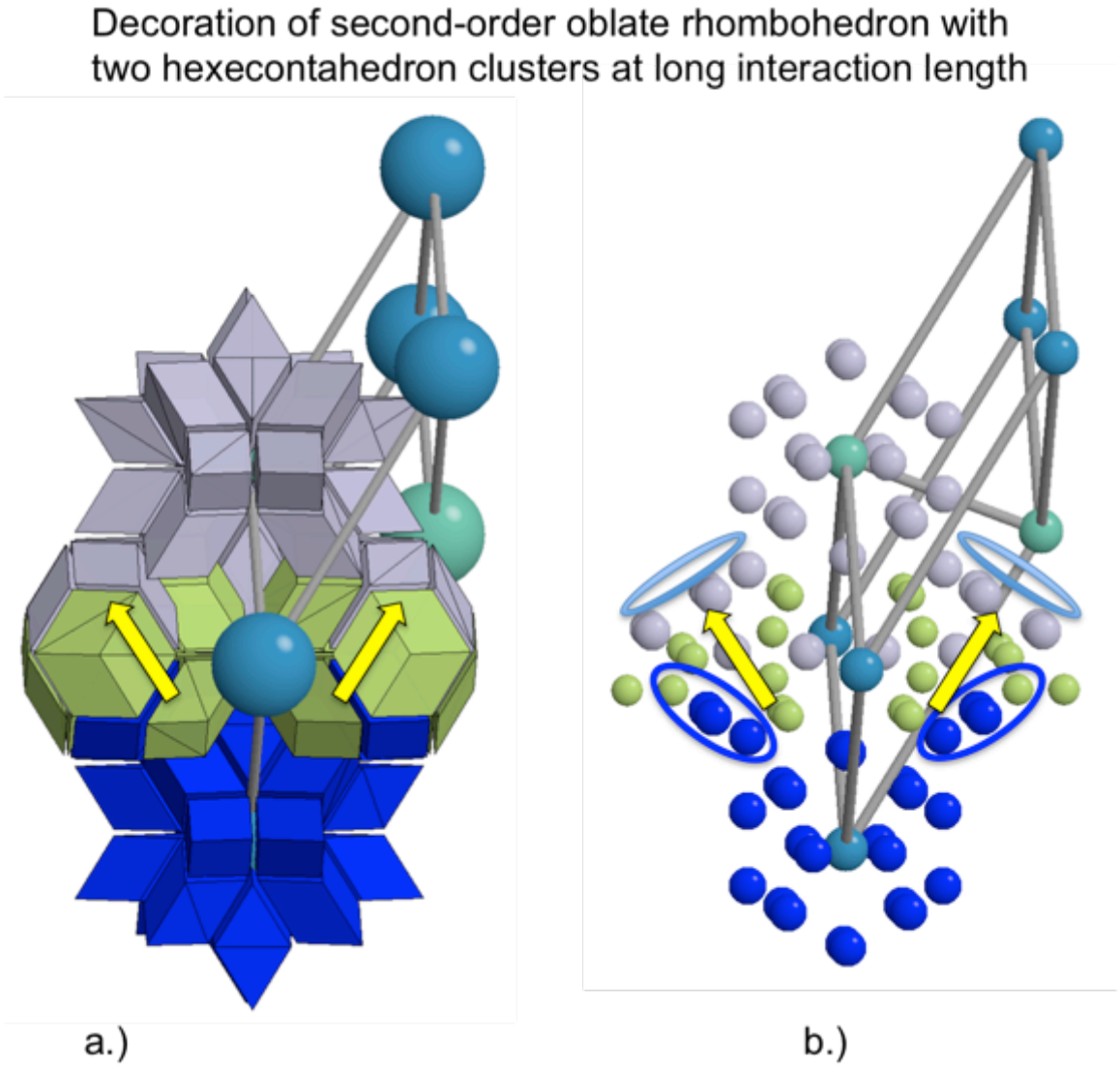


**Figure 6.32:** This cutaway shows two hexecontahedra and two triacontahedra. In (a), yellow arrows point in the direction of each triacontahedron's five-fold ring. This means that the blue hexecontahedron in (a) bottom belongs to an IC that is in a higher layer than the IC with the grey hexecontahedron in (a) top. In (b), there are three acute rhombohedra opposite the grey hexecontahedron (blue circles). This means that both triacontahedra are in position B with respect to the grey hexecontahedron. In (b), light blue rings have also been added just above the five-fold ring of acute rhombohedra. The position of these, of course, indicates that the triacontahedra pair sit in their D faces with respect to the blue hexecontahedron.

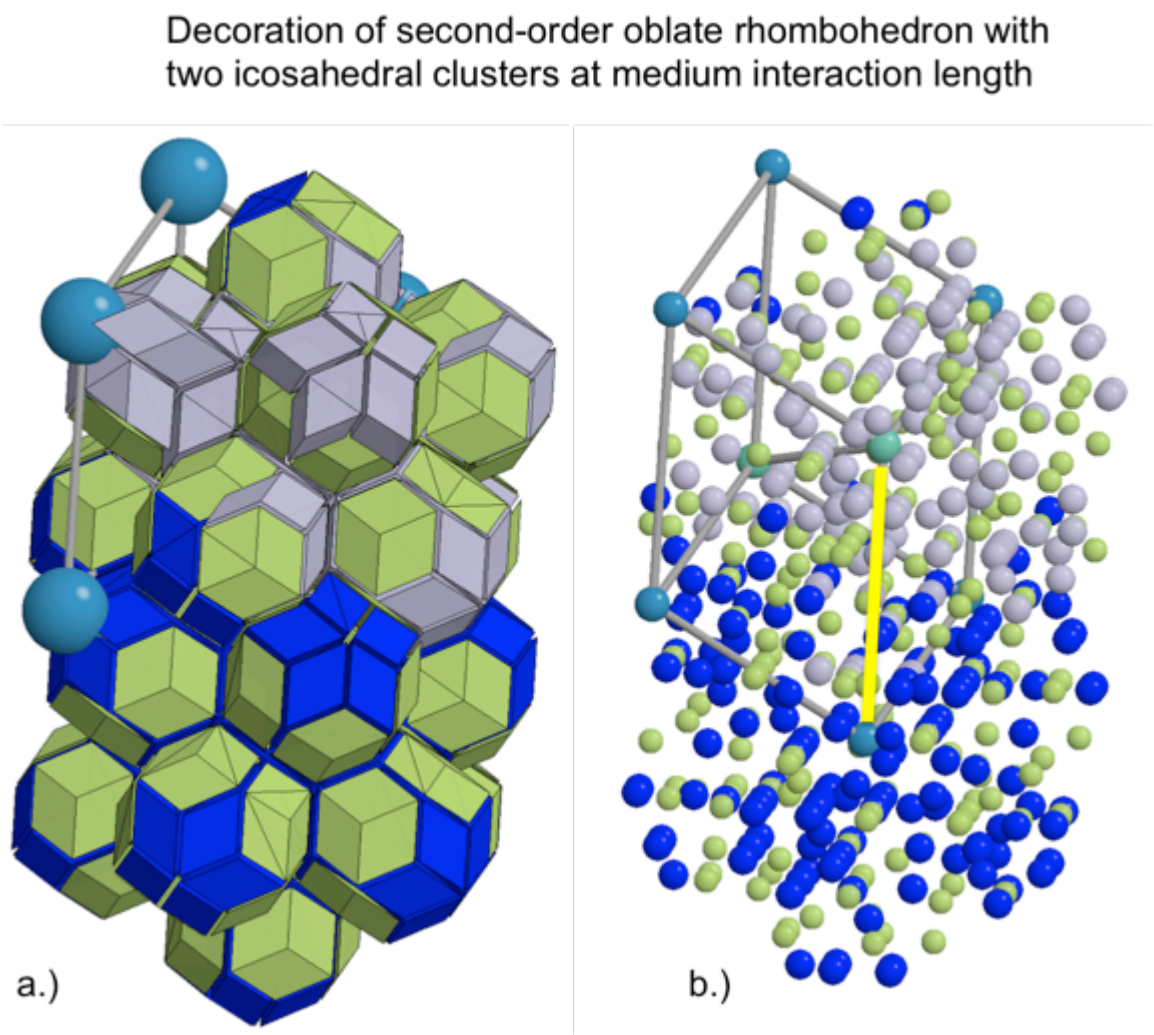


**Figure 6.33:** Here is the second-order oblate rhombohedron with ICs at the medium interaction distance. This distance corresponds to the edge length of the second-order rhombohedral network.

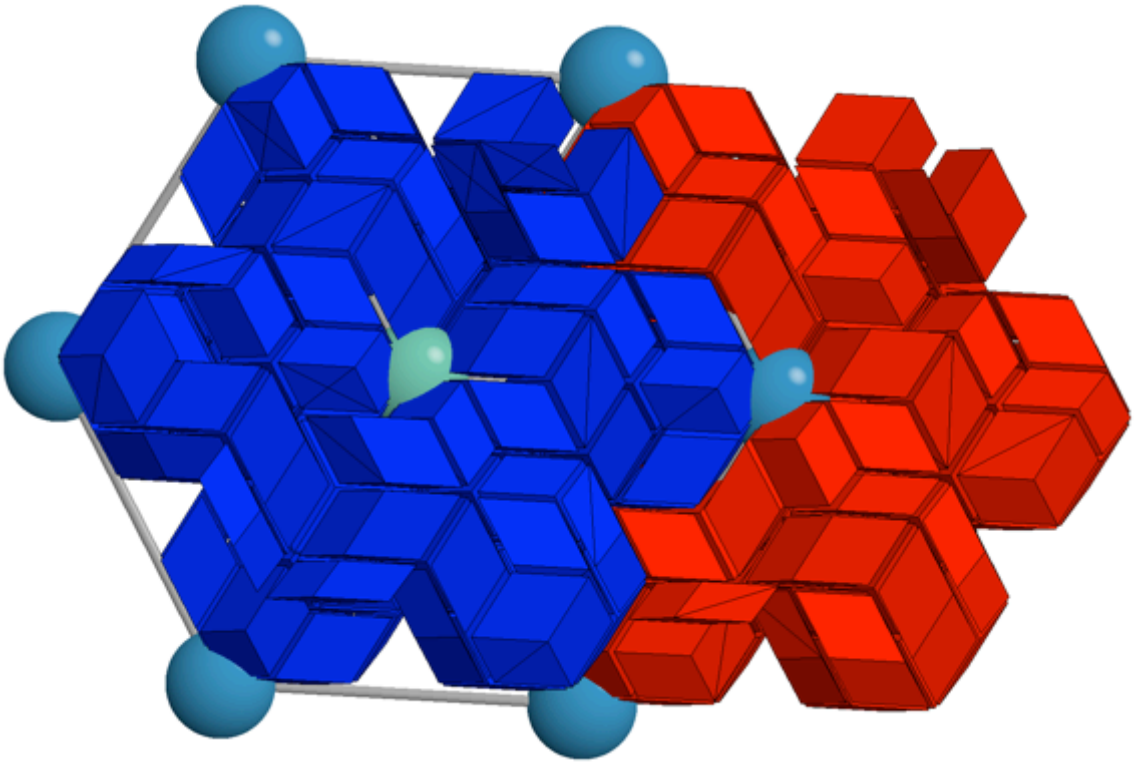

**Figure 6.34:** This figure shows two ICs at the medium interaction distance. One IC has been entirely colored in blue, and the other in red, to make discerning between them easier. The overlapping ICs have been cut roughly in half, making it clear that the five-fold vertex of a ring of acute rhombohedra reaches the center of the red IC, and consequently is part of what defines the red hexecontahedron.

In the short distance interaction between two ICs, three triacontahedra played a role in creating the hexecontahedron center of the other IC. In the medium distance interaction, however, only a single triacontahedron plays a role. Because of this, that triacontahedron is restricted to a D face for the IC that is on top of the other in the layer hierarchy.

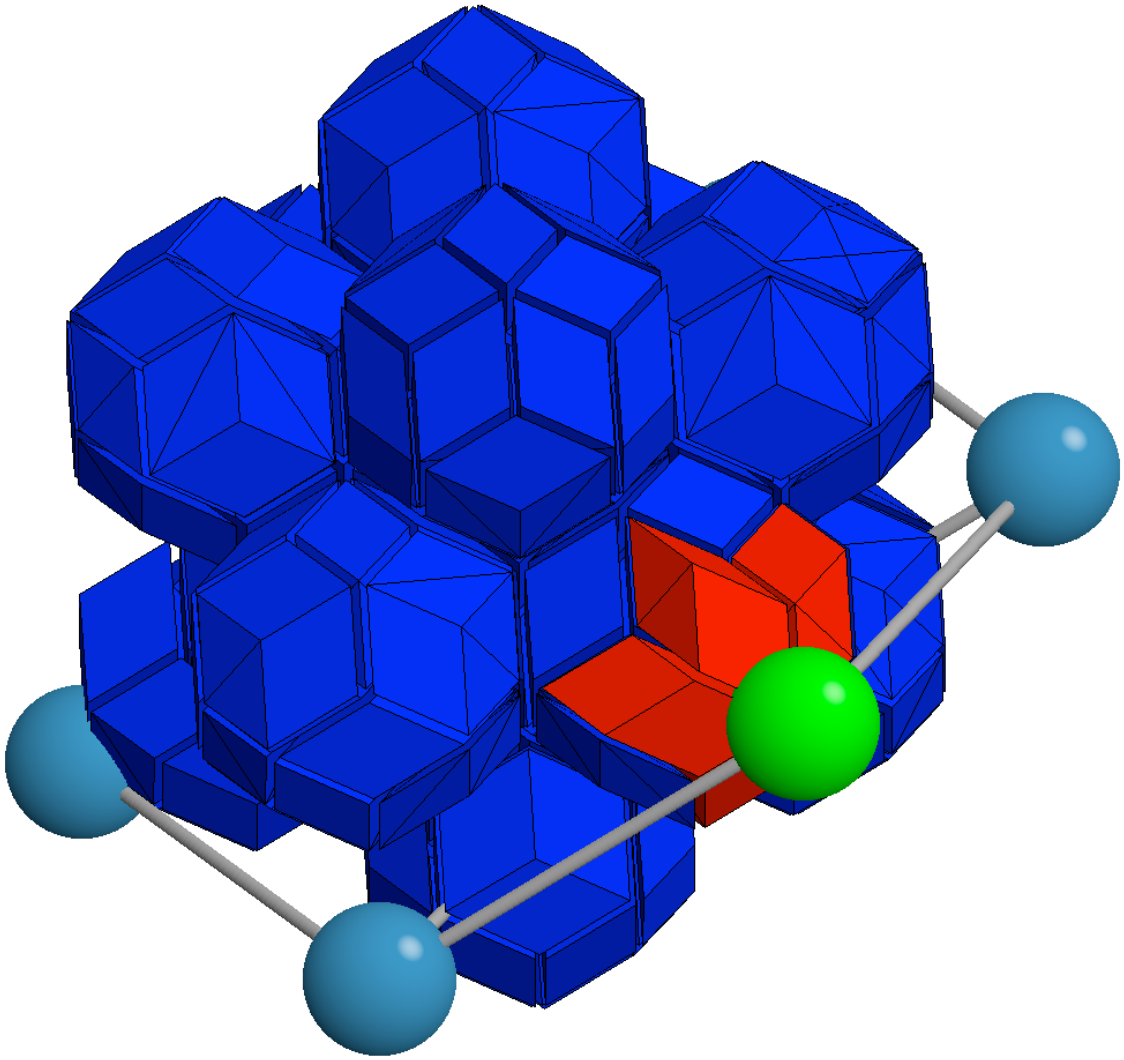

**Figure 6.35:** Here is the same second-order oblate rhombohedron, but now decorated with only a single IC. The IC that is at a medium length scale is gone, but its hexecontahedron center is now colored green. The five-ring acute rhombohedra are now colored red. This shows more explicitly that the triacontahedron that sits in a D face partially composes the red hexecontahedron.

At the medium length scale, the IC has an orientation such that a single triacontahedron plays a partial role in the creation of the hexecontahedron at the center of the IC at the medium distance, as can be seen in ***Figure 6.35***. At this distance, there are no complete triacontahedron overlaps.

Now that we know that each triacontahedron can rotate to sit in one of three possible locations in a given IC, it serves to wonder how many covering ICs are there? Using our cluster search algorithms and successively larger mathematical projections, we found that there are

twenty-six. This software works by first identifying the five-fold ring of acute rhombohedra that exists inside of each rhombic triacontahedron. This allowed us to assign a vector to each rhombic triacontahedron, so that we would know where it was pointing with respect to a given rhombic hexecontahedron. With the center of the hexecontahedron and the shell of twelve rhombic triacontahedra vectors, we were able to create specific environment matching definitions for each kind of IC. These were added to the analysis until all particles were accounted for in successively larger projections. We increased the size of these projections to many hundreds of thousands of particles until we saw no new covering ICs, and then pushed the size of the projections to millions of lattice points (and a quarter million rhombohedra)—until we could no longer adequately run it on our hardware—and saw no new un-assigned particles. This gave us confidence that we had identified all of the covering ICs. The notation used to describe each IC is reflective of how many of each kind of triacontahedra there are, insofar as one may be sitting so that there are five acute rhombohedra facing radially outward—the default face, or there can be three acute rhombohedra facing radially outward, called "B," or there is only one acute rhombohedron facing radially outward, called "R." For example, if there are six triacontahedra with only three acute rhombohedra showing, and two with only two acute rhombohedra showing, then this covering IC is called 6B2R.

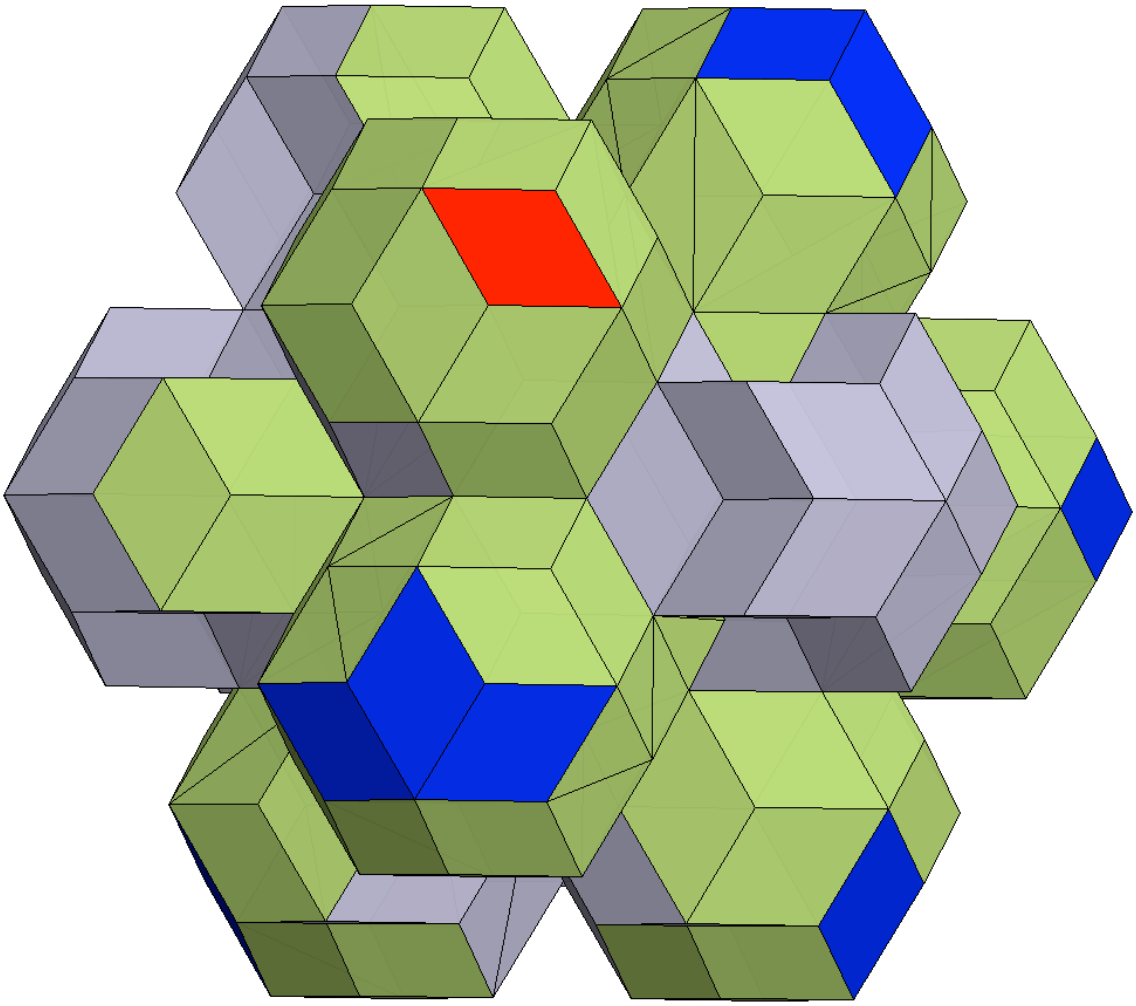

**Figure 6.36:** A 6B2R IC. The acute rhombohedra in the triacontahedra with three radially outward facing acute rhombohedra have been colored blue (B type). The acute rhombohedra in the triacontahedra with only a single acute rhombohedron facing radially outward has been colored red (R type). Here, we can see four of the "B" type with three acute rhombohedra, and one of the "R" type with one rhombohedron. Since this is a 6B2R IC, there are two B types and one R type that cannot be seen on this side.

| | |
|---|---|
| blue (T7) | blue-pole |
| blue (T3) | orange-pole |
| 2B (T0) | blue-pole |
| 2B (T19) | orange-pole |
| 4B (T20) | blue-pole |
| 4B (T23) | orange-pole |

| | |
|---|---|
| 4B1R (T21) | blue-pole |
| 4B1R (T10) | orange-pole |
| 2B3R (T24) | blue-pole |
| 2B3R (T25) | orange-pole |
| 5R (T1) | blue-pole |
| 5R (T12) | orange-pole |
| 6B (T17) | blue-pole |
| 6B (T4) | orange-pole |
| 6B1R (T9) | blue-pole |
| 6B1R (T14) | orange-pole |
| 4B3R (T13) | blue-pole |
| 4B3R (T2) | orange-pole |
| 2B5R (T22) | blue-pole |
| 2B5R (T16) | orange-pole |
| 6B2R (T8) | blue-pole |
| 6B2R (T5) | orange-pole |
| 4B4R (T18) | blue-pole |
| 4B4R (T11) | orange-pole |
| 2B6R (T6) | blue-pole |
| 2B6R (T15) | orange-pole |

**Table 1:** This chart shows all of the different types of IC that are possible in the AKN tiling. They are ordered from top to bottom in decreasing layer hierarchy.

In the new layering picture of quasicrystal tilings, every IC starts out as a rotationally symmetry icosahedral motif. ***Table 1*** was created using the cluster analysis software described in the last paragraph. There are two types of this kind of cluster in the AKN—referred to in ***Table 1*** as T7 and T3. One of these ICs has three of one chiral type of triacontahedra on the poles, and an equatorial band of the other chirality. The other is simply flipped. Each of the twenty-six covering ICs belongs to one of these two original chiral icosahedral motifs—see ***Figure 6.24***. When an IC that is higher up in the hierarchy is layered over an IC that is lower in the hierarchy, they are made compatible by a phason flip. This phason flip in the AKN consists

of a chirality flip, and then a rotation of the triacontahedron to one of its other two allowed faces—see ***Figure 6.15***. When an IC has been layered properly, it will exist as one of the twenty-six possible ICs catalogued in ***Table 1***. If we connect all of the centers of the triacontahedra, we can see exactly how the IC layer over each other.

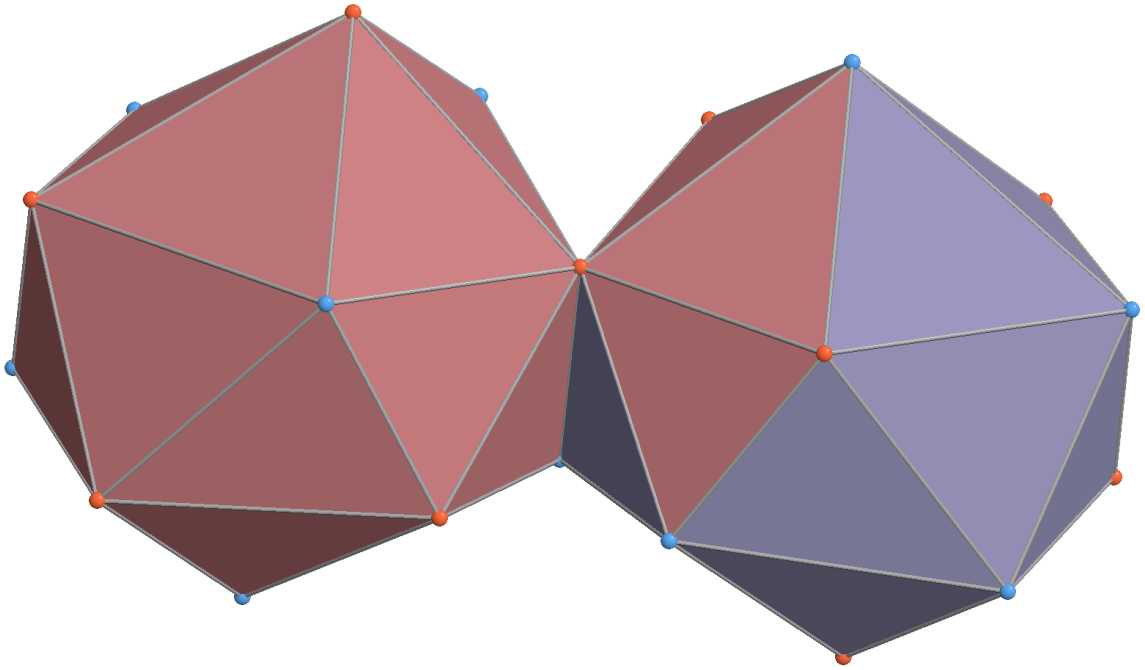

**Figure 6.37:** Two ICs that share a pair of triacontahedra. Note: the blue and orange spheres are at the center of mass of the five-fold ring of acute rhombohedra that exist inside of each triacontahedron, so they can rotate into one of three positions and connecting their centers is not guaranteed to form a perfect icosahedron (which happens only for the rotationally-symmetric blue ICs)—but it is useful for visualization purposes here.

## Layers

When two ICs are at the long overlap distance, they share two complete triacontahedra. This forces a choice—the triacontahedron has three faces it can sit in, and it has the option of sitting in the rotationally-symmetric position—the default face D—in one, and either the B or R position in the other. If two ICs, M and N, share two triacontahedra, and those two triacontahedra sit in D in M, and sit in B or R for N, then M is necessarily in a layer **above** N.

## Sublayers

Likewise, if two ICs, P and Q, share two triacontahedra, and those two triacontahedra sit in B or R for P, and also sit in B or R for Q, then those two ICs sit in the same sublayer. An

example of a sublayer is the group of ICs labeled 6B1R, 4B3R, and 2B5R. These all have a total of seven rotated triacontahedra, which group them all into this same sublayer. Interestingly, triacontahedra chirality numbers are conserved no matter which IC I look at.

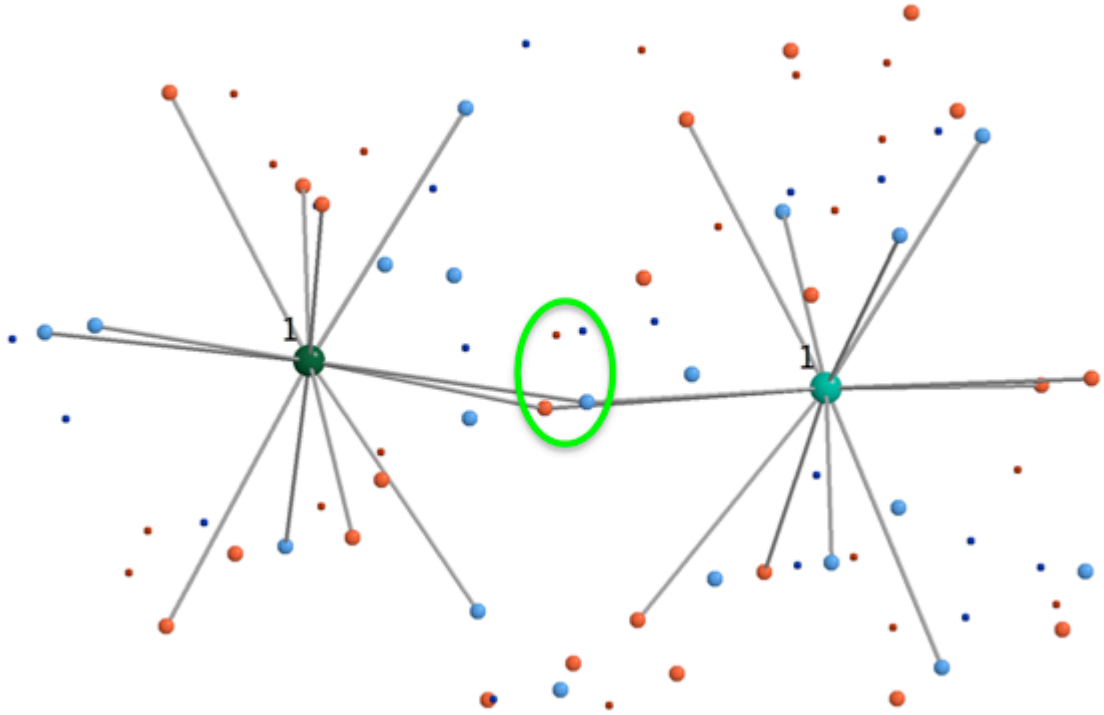


**Figure 6.38:** Two ICs on the same sublayer, in this case T13 (4B3R with an orange pole) and T14 (6B1R with an orange pole) share two triacontahedra. **The fact that there are more than two possible cusps for the triacontahedra to sit in make it possible for this sublayer interaction to exist—neither sits on top of the other, but both can instead share triacontahedra that point away from their mutual cores** (the large spheres in the middle labeled with "1").

The fact that there are more than two possible five-fold vertices on each triacontahedron that can sit in the five-fold cusps of the hexecontahedra makes it possible for this sublayer interaction to occur. Neither IC sits "on top" of the other, but both can instead share triacontahedra that point at an oblique angle relative to each IC center. This is shown in the green circle of ***Figure 6.38***. Geometrically, there is not an immediately obvious reason for this to happen, but the matching rules necessitate and make clear that these are the only ways that two ICS can share a complete triacontahedron. Moreover, it is now clear that if any structure in the AKN were to be outside of one of the twenty-six allowed ICs, that alone would represent some kind of defect.

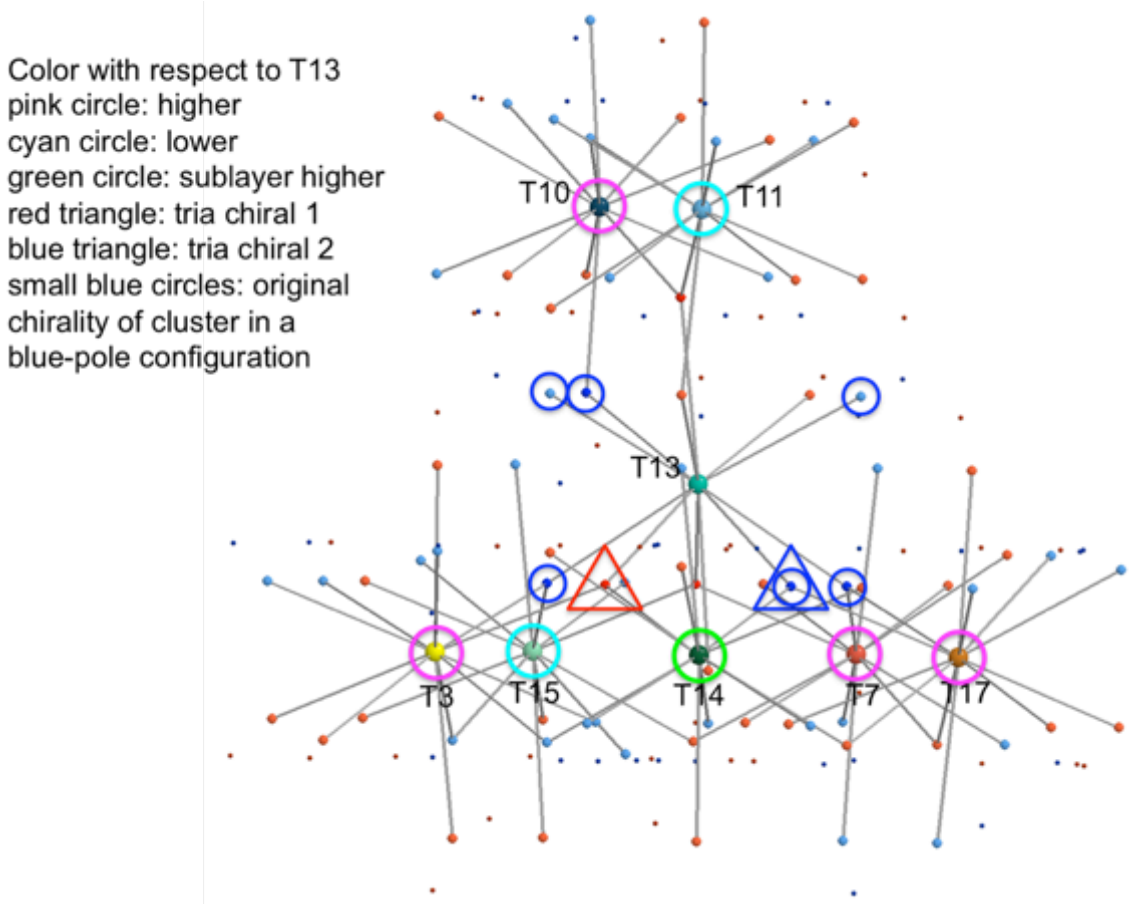


**Figure 6.39:** This image shows the layer hierarchy for a T13 cluster with its seven triacontahedron-overlapping clusters. It has other closer IC, but the triacontahedra only partially overlap and so there is no forced motif redefinition. A pink circle means the neighboring IC is in a higher layer, and cyan means it is in a lower layer—both with respect to the T13 cluster at the center. The green circle indicates that T14 (6B1R) is in the same layer, but that T14 is higher in the sublayer.

***Figure 6.39*** shows a T13 cluster, which is a 4B3R blue-pole IC. It has seven neighbors that are at the appropriate distance for a complete triacontahedron overlap, thereby forcing redefinitions of the IC. When the T13 cluster is surrounded by these neighbors, its triacontahedra chiralities are redefined depending on the layer hierarchy. **We can recover the original chiral decoration by flipping the colors back for each cluster that sits on a higher layer in the hierarchy.** The layer hierarchy for this group of ICs is T3, T7, T10, T17, T14, T13, T11, and T15. We can look at the two triacontahedra shared by the T13 and T3 cluster, and flip their colors to the opposite chirality, here represented as red for a new orange chirality, and dark blue for a new light blue chirality, for clarity's sake. Then we look at the two triacontahedra shared by T7, and flip those two chirality colors, and so on. Since T3 and T7 are the same

except for a chirality difference, they will never share triacontahedra, so it will not matter which one we flip first. Going down the line, we finally get to T13 and T14. Here, they sit on the same sublayer. The hierarchy in the sublayer, for reasons I do not know, follows the priority of whichever cluster has more B than R clusters—perhaps because B has more rotational symmetry than R. If we look closely at a triacontahedron, we can see that B and R are equidistant from D (***Figure 6.40***). It might relate to the fact that D has five acute rhombohedra, B has three, and R has only one. Perhaps there is something in the system that recognizes B as having more similarity to the original high degree of rotational symmetry originally afforded by D—this seems like a reasonable postulate.

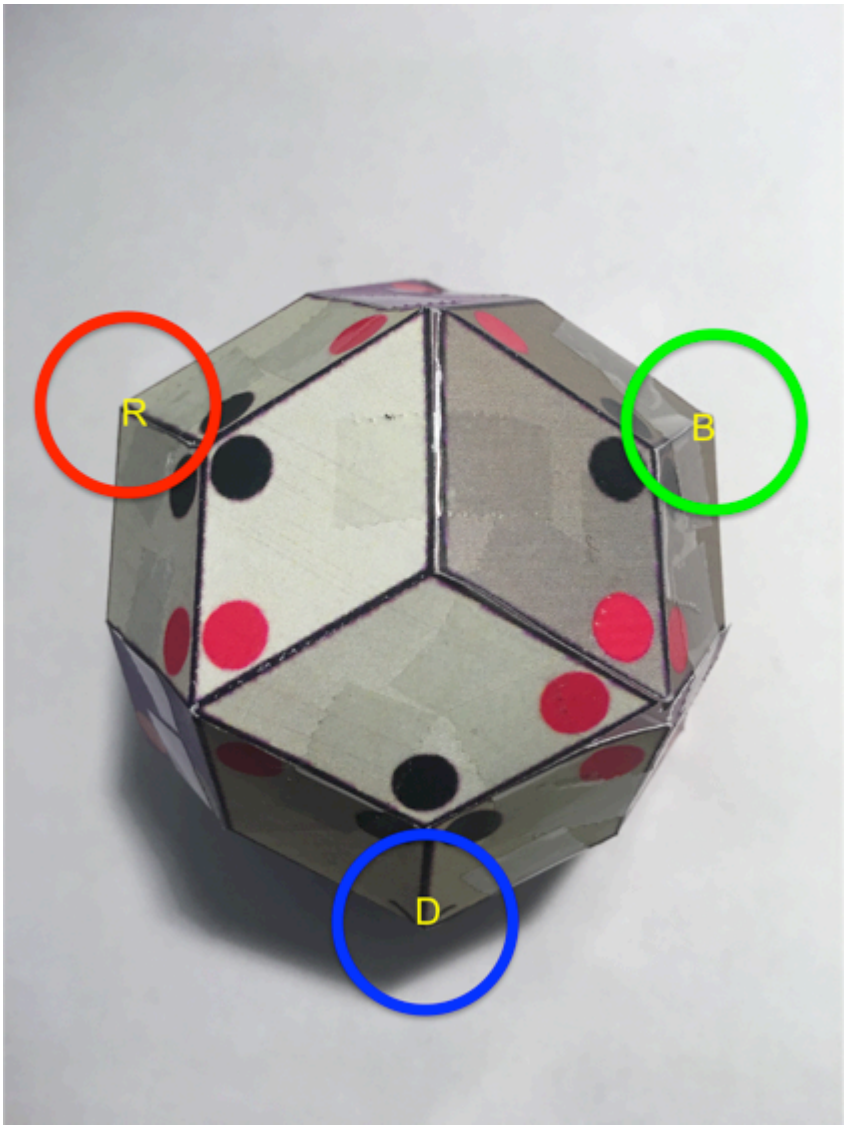


**Figure 6.40:** Purple-chiral type triacontahedron with D, B, R vertices labeled in blue, green, and red, respectively. The B and R vertices are equidistant from D.

So T14 6B1R sits above T13 4B3R. Sitting on the same sublayer means neither of the shared triacontahedra will sit in a D position, but instead have either an R or a B. The chirality still flips, however, and T14 is higher than T13. Flipping that final pair of shared triacontahedra will restore the original blue-pole chiral decoration of the T13 cluster. Since T11 and T15 sit lower in the hierarchy than T13, we do not flip those triacontahedra—instead, T11 and T15 have their chiralities and orientations in part determined by T13. This procedure can be repeated for any of the clusters in ***Table 1*** to restore the blue-pole or orange-pole chiral decoration given in ***Table 1 Column 2***. Note that some triacontahedra can be shared by either one or two ICs. This means that the chirality will flip once for a single higher-lying cluster, or twice for two higher-lying clusters.

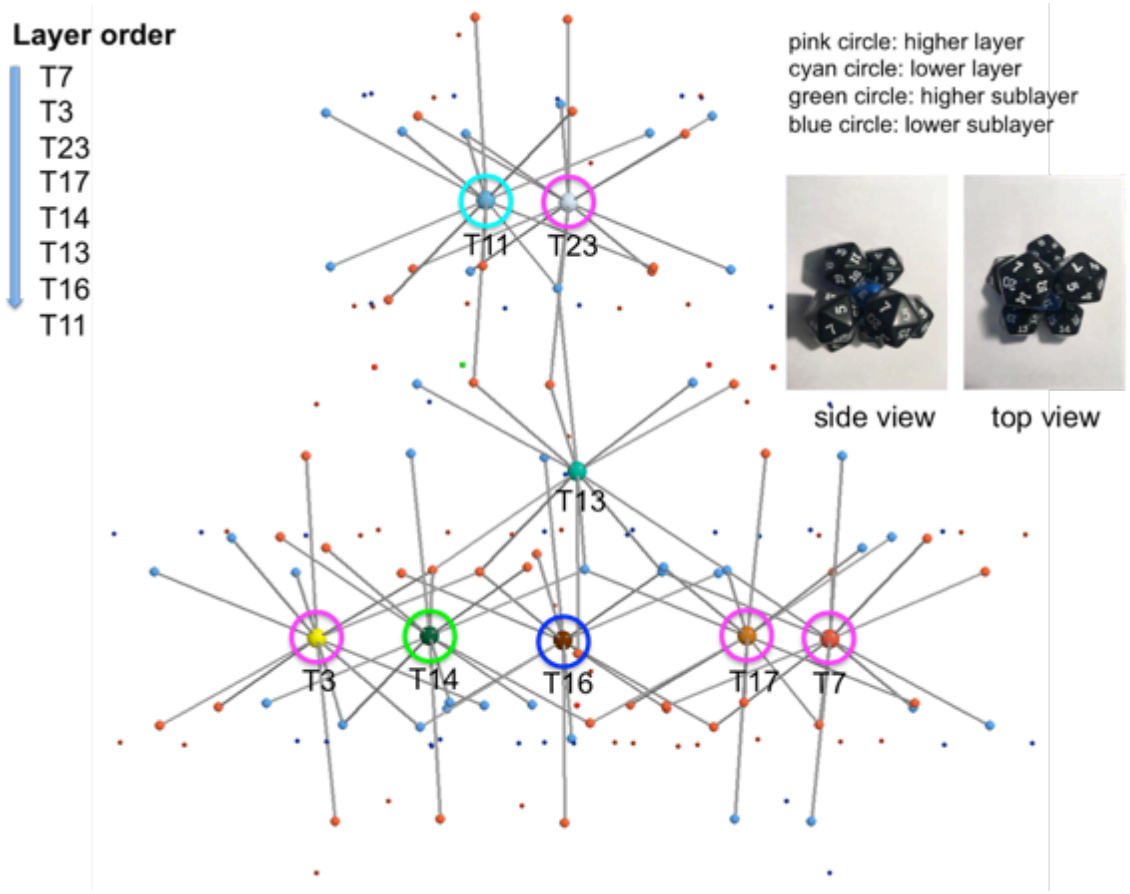


**Figure 6.41:** This is one example of how to construct a T13 IC. This configuration has seven neighboring ICs, which are close enough for a complete triacontahedron overlap. However, only five of these sit in a higher layer and so contribute to the triacontahedra re-orientations and chirality flips that create the T13 IC.

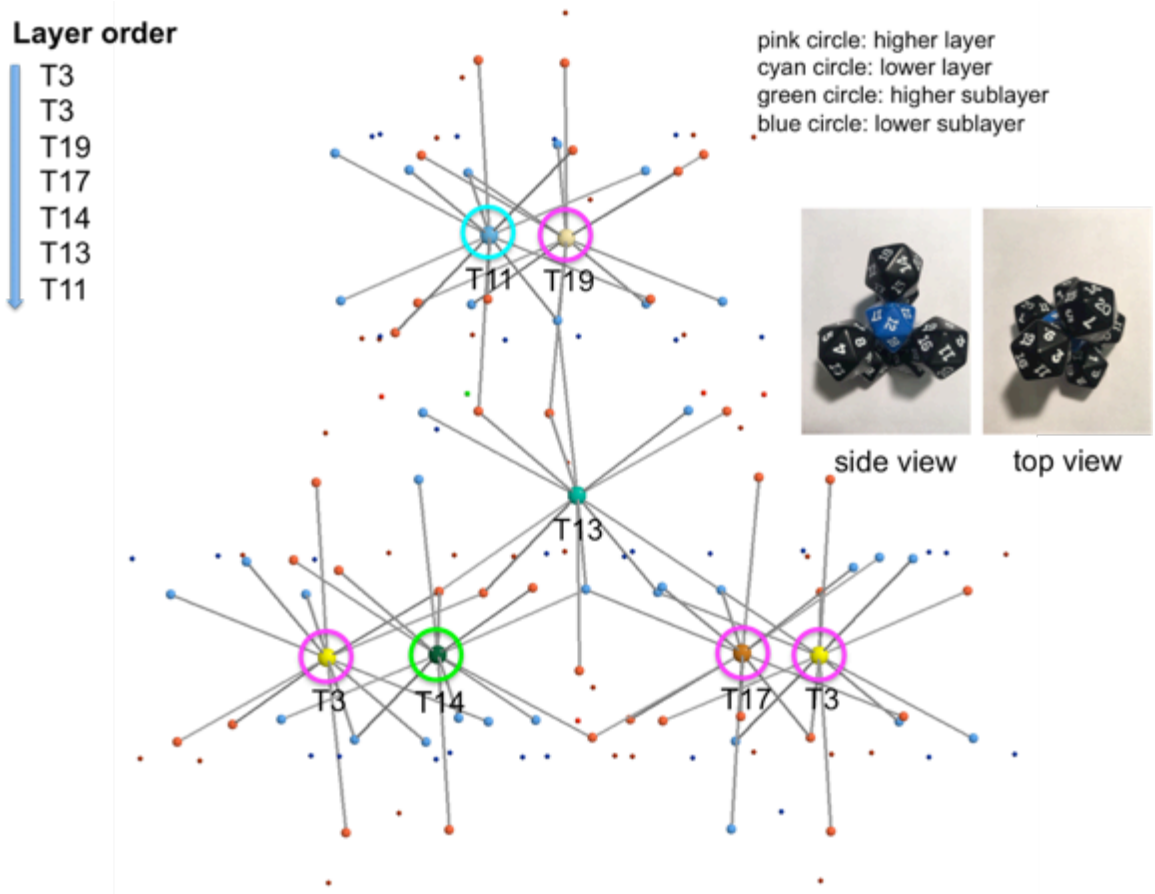


**Figure 6.42:** This shows another way of creating a T13 IC. Unlike ***Figure 6.41***, this T13 cluster has only six ICs that are close enough to completely overlap triacontahedra. Like ***Figure 6.41***, there are still five ICs that contribute triacontahedra re-orientations and chirality flips to create T13. T13 is a 4B3R cluster, which means it needs five higher-layered ICs in order to have the correct number of flips.

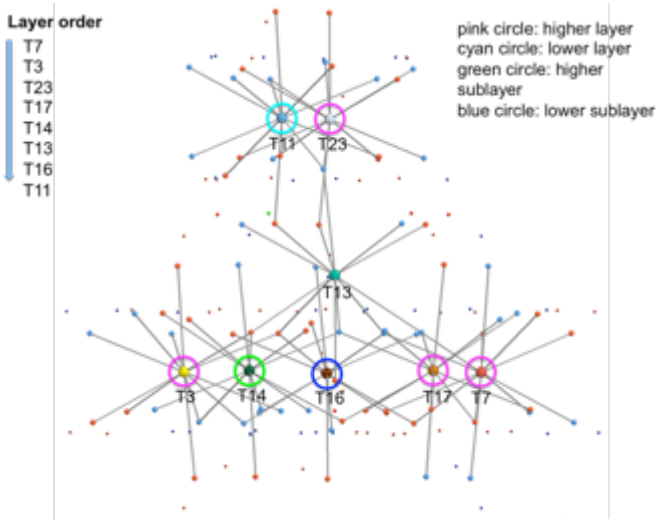
Layer order
T7
T3
T23
T17
T14
T13
T16
T11
pink circle: higher layer
cyan circle: lower layer
green circle: higher sublayer
blue circle: lower sublayer
T11
T23
T13
T3
T14
T16
T17
T7

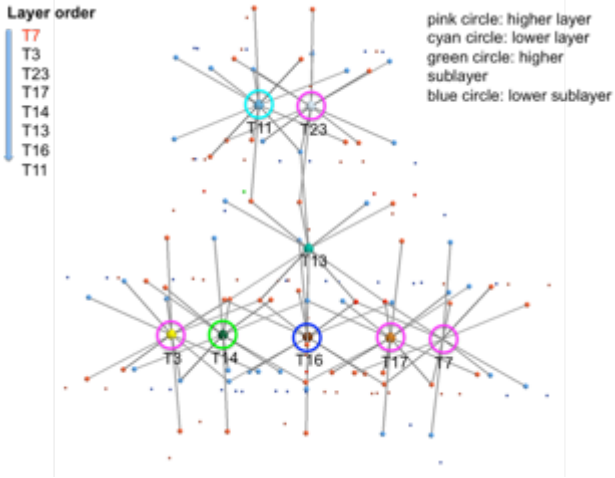
Layer order
T7
T3
T23
T17
T14
T13
T16
T11
pink circle: higher layer
cyan circle: lower layer
green circle: higher sublayer
blue circle: lower sublayer
T11
T23
T13
T3
T14
T16
T17
T7

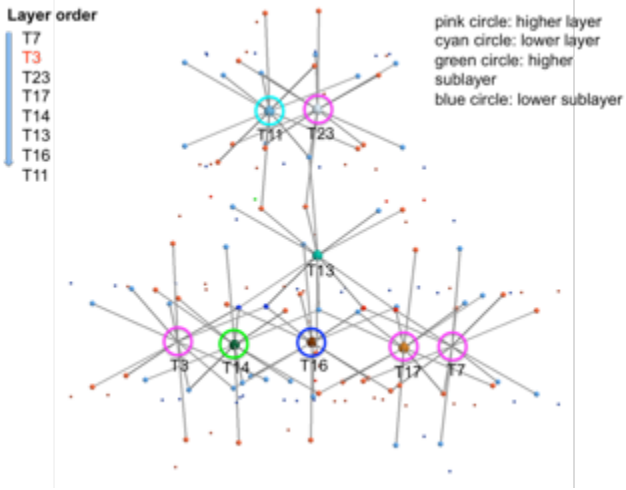
Layer order
T7
T3
T23
T17
T14
T13
T16
T11
pink circle: higher layer
cyan circle: lower layer
green circle: higher sublayer
blue circle: lower sublayer
T11
T23
T13
T3
T14
T16
T17
T7

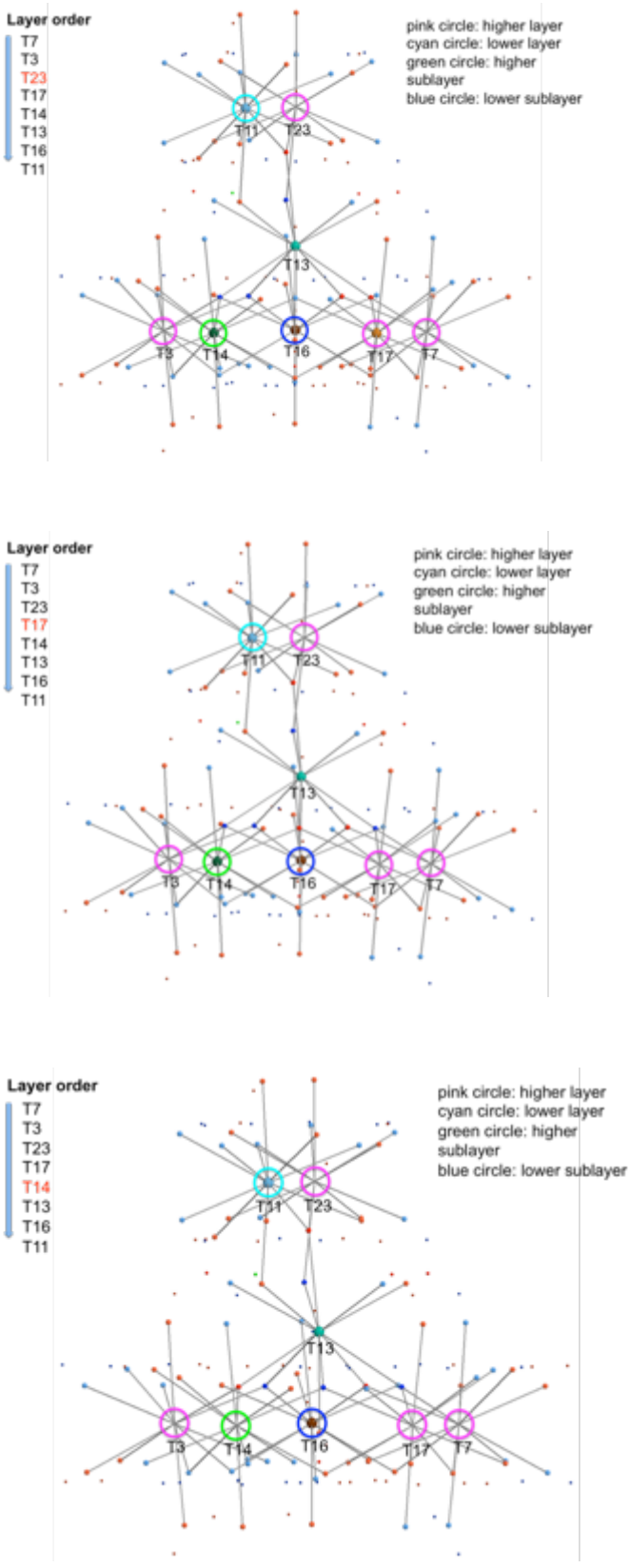


**Figure 6.43:** This series of images shows the removal of neighboring ICs. If an IC has been removed, its type is highlighted in red under "Layer order." As each IC is removed, the triacontahedra they share with T13 have their chiralities flipped in color,

from blue to red or vice versa. This undoes the effect of the layering and allows the recovery of the original default "blue" IC, of either blue-pole or orange-pole chirality. In the case of T13, it is a blue-pole, which can be seen below in ***Figure 6.44.***

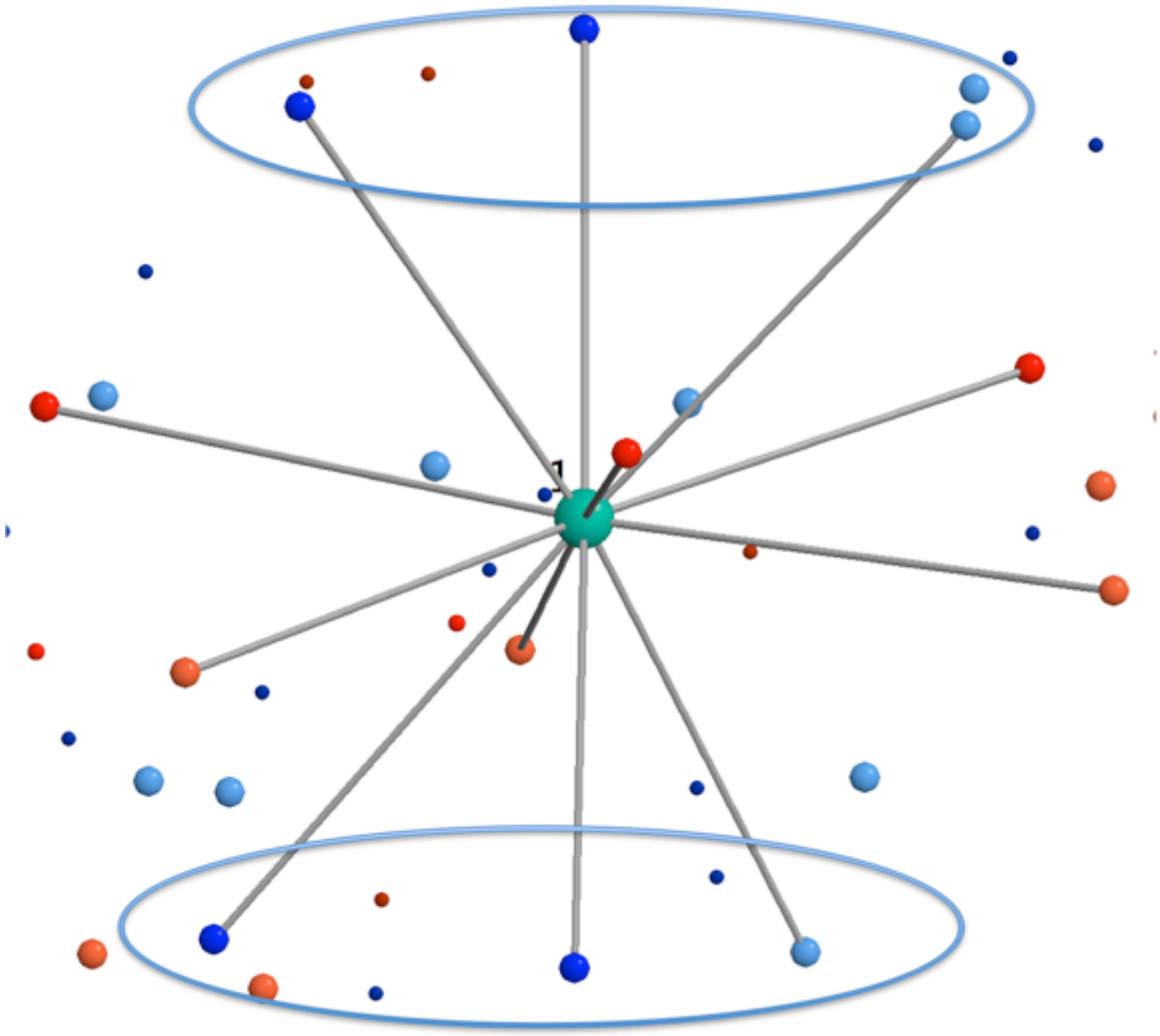

**Figure 6.44:** This is the final form of T13 after all of the higher-layer ICs have been removed. It is a blue-pole, as listed in ***Table 1***. During the removal of the ICs, some triacontahedra have been flipped once and others have been flipped twice. Note that colored spheres not attached with a line are not part of the IC. Note also that dark blue and red (instead of orange) represent shared triacontahedra that have had their chiralities reversed in the manner described in ***Figure 6.43***.

In essence, this means that all of the ICs are in some sense just one of the two original chiral-twin blue ICs. There are twenty-six in total. Two are the original blue ICs, and there are twelve versions of each chirality that are made through a series of rotations and chirality flips of

the composite triacontahedra. These all sit on the vertices of a yet-larger acute or oblate rhombohedron. For all ICs that sit on the longest (diagonal of the golden rhombus face) distance of this new rhombohedra system, they will experience chiral flips and orientations governed by this layer hierarchy.

## Second-Order Rhombohedra

Now that we have all twenty-six ICs, we can begin assembling them into larger rhombohedra. This is accomplished by taking one of the appropriate twenty-six ICs and placing it at each vertex of either a new second-order oblate rhombohedron, or new second-order acute rhombohedron. These can then be formed into another yet-larger series of triacontahedra, which can be formed into yet-larger ICs, and so forth. Note that because of the many types of IC, we yield a great many more types of rhombohedra, and consequently an even larger number of triacontahedra. It is unclear to me at what point this multiplication stops, and in essence I believe it is similar in scope to the same problem addressed by other researchers that the AKN tiling does not have a known deflation protocol . This effectively means that the AKN rhombohedra can be decorated in many different ways. The observation of this chapter is thus consistent with this apparent fact about the AKN lattice, but also provides a convenient way to visualize it.

## Conclusion

In conclusion, this chapter has shown that even a quasilattice tiling as complex as the AKN can be reduced in the same manner as explored in the other chapters of this thesis. Although there does not appear to be a closed deflation protocol (it appears to expand indefinitely in variety at each additional hierarchy level), it is still possible to take any of these variations and break it back down into one of the icosahedral motifs, and ultimately understand that it is derived from the original blue icosahedral motif that represents the fundamental form, along with its chiral twin—unique among the tilings covered in this thesis. The interplay of chirality throughout this chapter has many analogs in the previous chapters, but also uses a new process, whereby three triacontahedra (characteristic polyhedral) can sit on top of each other, which is also not at all present in the previous chapters, which have so far been limited to two!

Perhaps higher-dimensional quasicrystals allow an *n-dimensional* number of complete characteristic n-gon overlaps? Maybe a ten-dimensional quasicrystal can allow ten n-gons to all share a single "decagon" equivalent, in the case of the Penrose tiling, or its equivalent, the rhombic triacontahedron, in the AKN tiling. We saw in *Chapter Four* that although there is a chiral twin for the characteristic decagon, that it is not used in the tiling—although I know of no reason why a mirrored tiling could not be created. This chapter also made heavy use of analysis software to break down the complexity of the AKN in a way that is simple enough to visualize. This kind of analysis is not needed for the 2D quasilattice examples.

## Chapter Seven

# Self-Assembly of a Space-Tessellating Structure in the Binary System of Hard Tetrahedra and Octahedra

Authors: Andrew T. Cadotte, Julia Dshemuchadse, Pablo F. Damasceno, Richmond S. Newman, Sharon C. Glotzer

This chapter is reproduced from Cadotte, A. T.; Dshemuchadse, J.; Damasceno, P. F.; Newman, R. S.; Glotzer, S. C. Self-Assembly of a Space-Tessellating Structure in the Binary System of Hard Tetrahedra and Octahedra Soft Matter 2016, DOI: 10.1039/C6SM01180B

## Abstract

This chapter reports the formation of a binary crystal of hard polyhedra due solely to entropic forces. Although the alternating arrangement of octahedra and tetrahedra is a known space-tessellation from Maurolyctus in 1529 (Lagarias, 2015), it had not previously been observed in self-assembly simulations. Both known one-component phases—the dodecagonal quasicrystal of tetrahedra and the densest-packing of octahedra in the Minkowski lattice—are found to coexist with the binary phase. Apart from an alternative, monoclinic packing of octahedra, no additional crystalline phases were observed.

## Introduction

Hard polyhedra crystallize through entropic interactions (Frenkel, 1999; Van Anders, Ahmed, et al., 2014; Van Anders, Klotsa, et al., 2014) and their rich self-assembly behavior has been studied in increasing detail in recent years (Agarwal & Escobedo, 2011; Damasceno et al., 2012a, 2012b; Haji-Akbari et al., 2009; Henzie et al., 2012; Tasios et al., 2014). Most of these studies were performed on one-component systems and studying the self-assembly of mixtures of polyhedra represents a natural extension of this work. Structures of binary mixtures have many applications, e.g., the suitability of binary colloidal crystals for photonic applications

(Hynninen et al., 2007; Wan et al., 2009), and are subject to the growing interest of the community.

Regular octahedra and tetrahedra with identical edge lengths tile space at a composition of 1 : 2, respectively. Because both shapes have very few facets, they represent one of the simplest space-tessellating binary mixtures. Previous studies of this system did not observe the self-assembly of the space-filling structure unless attractive interactions were added (Khadilkar & Escobedo, 2012). Other studies on binary mixtures of different shapes produced disordered mixed lattices, but not the formation of ordered structures (Khadilkar et al., 2013; Khadilkar & Escobedo, 2014).

Experimentally, both shapes have been studied in recent years. Octahedra were found to form a variety of structures, among them a low-density body-centered cubic (bcc) structure with vertex-sharing octahedra (J. Zhang et al., 2011), vertex- and edge-sharing packings derived from the binary structure (W. Lu et al., 2008), a high-pressure lithium phase (cI16-Li (Hanfland et al., 2000)), induced by a depletion effect (Henzie et al., 2011), lower-symmetry structures with stacking variants (Chang et al., 2008; Xie et al., 2009; L. Zhang et al., 2009), and distorted bcc arrangements that likely correspond to the densest-packing structure (Henzie et al., 2011; Jing et al., 2008; Song et al., 2006). Most recently, a new monoclinic assembly of octahedra was observed (Gong et al., 2017). Tetrahedral nanoparticles have been more difficult to synthesize and experiments have not yet reproduced the predicted quasicrystal, but rather a superlattice structure (Boles & Talapin, 2014). Millimeter-sized frictional tetrahedra and macroscopic tetrahedral dice were found to produce only jammed (Neudecker et al., 2013) and random packings (Jaoshvili et al., 2010).

To my knowledge, mixtures of octahedra and tetrahedra have not been investigated experimentally. Superlattices of other combinations of two shapes have been studied recently, e.g., spheres and octahedra, as well as spheres and cubes (F. Lu et al., 2015). The coexistence of multiple solid phases, on the other hand, had previously been discovered in systems of spheres with two different radii (Filion et al., 2011), but has not directly been observed in a number of studies on binary systems with polyhedral (Khadilkar et al., 2013; Khadilkar & Escobedo, 2012, 2014).

Here we use Monte Carlo simulations to investigate the self-assembly of mixed octahedra and tetrahedra. Other phases known to self-assemble in the one-component systems are a dodecagonal quasicrystal formed by tetrahedra (Haji-Akbari et al., 2009), as well as a distorted bcc structure of octahedra (Damasceno et al., 2012a), both of which may compete with a co-assembled binary phase. We investigate the phase behavior of different stoichiometries of hard tetrahedra and hard octahedra. We found that both pure phases that have been reported in one-component systems coexisting with the binary crystal that is reported in self-assembly simulations here for the first time.

## Methods

We performed hard-particle Monte Carlo (MC) simulations with HPMC (Anderson et al., 2013, 2016), a plugin to the HOOMD-blue software (Anderson et al., 2008, 2020), in the NVT thermodynamic ensemble to study the behavior of mixtures of hard tetrahedra and octahedra. The polyhedra are modeled as perfectly faceted shapes of unit length, with sharp vertices and edges. Simulations were carried out in cubic boxes with periodic boundary conditions, containing 10 648 particles for each state point in the phase diagram.

The phase diagram was sampled at packing fractions f = 0.50 0.65 (Df = 0.01) for octahedra–tetrahedra compositions (O:T) = 0:10, 1:9, 2:8, 3:7, 4:6, 5:5, 6:4, 7:3, 8:2, 9:1, 10:0, as well as O:T = 1:999, 5:995, 1:99, 2:98, 5:95, and the special stoichiometry 1:2. A Steinhardt order parameter was used to categorize particles as either liquid or solid, based on their local environment (Keys et al., 2011; Steinhardt et al., 1983). This allowed for subsequent crystal structure identification and mapping of the phase diagram.

## Results and Discussion

### Phase Diagram

Three crystal structures were observed for the stoichiometries and packing fractions studied, with two solid–solid coexistence regions between them. A schematic phase diagram is given in ***Figure 7.1***. The quasicrystal 12-QC is shown in red, the pure binary crystal phase $OT_2$ is shown in green, the pure crystals of octahedra are shown in blue, and the coexistence of binary

and pure octahedral crystals is shown in brown. Snapshots of all crystal structures are depicted as well.

At low numbers of octahedra and around 50% packing fraction (f = 0.50), the tetrahedra self-assemble into the dodecagonal quasicrystal (12-QC) that had been reported for systems composed solely of tetrahedra (Haji-Akbari et al., 2009). As the octahedra content increases, the quasicrystal phase quickly disappears: it is observed up to stoichiometries O : T = 0.01 : 0.99, but not in simulations with O : T = 0.1 : 0.9. The packing fractions at which the dodecagonal quasicrystal forms are at the low end of the investigated phase diagram, at 50–53%.

In the low O : T regions of the phase diagram, the tetrahedra begin forming the 12-QC within about 8 million MC sweeps. Together with the octahedra, they are expected to form a more stable phase, the space-filling $OT_2$ structures, but the octahedra diffuse relatively slowly through the dense quasicrystal. For O:T = 0.02:0.98 at f = 52%, for example, there are no hints of order in the arrangement of octahedra until after nearly 160 million MC sweeps. Thus, a rough sweep of the phase diagram does not detect a coexistence region between the 12-QC and $OT_2$ phases, however, extensive runs in the intermediate compositional region suggest that the binary crystal will form whenever any number of octahedra is present in addition to the quasicrystal-forming tetrahedra. Additional simulations at f = 52% revealed local motifs of the binary structure at O : T = 0.02 : 0.98 and 0.03 : 0.97 after 140 million MC sweeps, whereas the addition of octahedra to a system consisting mostly of tetrahedra further suppresses the growth of the 12-QC at O:T = 0.04:0.96 and no 12-QC phase was observed at 140 million MC sweeps.

When octahedra are present next to the quasicrystal, they begin to aggregate in binary face-to-face alignments with tetrahedra after approximately 40 million MC sweeps. As the mixture begins to form the binary crystal, octahedra take the place of a dimer of two tetrahedra along one of the columns of the quasicrystal. Correspondingly, the angle at which the binary crystal forms is offset from the main axis of the quasicrystal, as shown in ***Figure 7.2***. Any octahedra introduced into the quasicrystal eventually form the c-$OT_2$ structure with the corresponding amount of tetrahedra.

At intermediate compositions of octahedra and tetrahedra, the binary $OT_2$ structure forms, with a small amount of stacking faults. The binary crystal forms with ease at packing fractions 54–61% and O:T = 3:7–6:4 around the stoichiometry of the ideal structure, O:T = 1:2. The high flexibility of the packing with respect to the amount of tetrahedra that are available in the polyhedral mixture likely stems from the ability of the structure to accommodate a number of tetrahedral voids.

At high O:T ratios, the system forms pure packings of octahedra. They can mostly be observed for O:T = 7:3–9:1 and at packing fractions of 56–60%. A large coexistence region is located between the stability regions of the binary crystal and the crystal of octahedra, where both ordered phases were detected.

## Structures and Motifs

The most important motifs that occur in the crystal structures found in this system are depicted in ***Figure 7.1*** and ***Figure 7.3***.

Tetrahedra alone form the same arrangements that were previously observed in the dodecagonal quasicrystal (Haji-Akbari et al., 2009)(12-QC): columns of pentagonal bipyramids alternating with rings of six dimers that are arranged in a dodecagonal square-triangle tiling. This local arrangement of 22 tetrahedra has also been found to occur in spherical confinement (Teich et al., 2016).

In the binary mixture, octahedra and tetrahedra are arranged alternatingly and face-to-face in a dense layer. Within the layer, each triangular face is shared between an octahedron and a tetrahedron. These binary octahedra–tetrahedra (O : T = 1 : 2) layers can be stacked in two different ways, while having polyhedra between layers align face-to-face: alternatingly—with only O–T contacts between layers—or vice versa, with only O–O and T–T contacts. Employing only one kind of stacking results in two regular honeycombs, i.e., space-filling tessellations: the alternated cubic honeycomb and the gyrated honeycomb, respectively. (A more expansive description of these structures is given in the Supplementary Information section that follows). Both structures have the same composition as each individual layer (O : T = 1 : 2; $OT_2$) and can

be combined in infinitely many different stacking variants. I label the basic cubic and hexagonal structures by their symmetries: c-$OT_2$ and h-$OT_2$.

The c-$OT_2$ structure corresponds to the arrangement of octahedral and tetrahedral interstices in a cubic close packed structure (ccp), where each octahedron shares all of its 8 faces with a tetrahedron and each tetrahedron shares all 4 faces with neighboring octahedra. Equivalently, the h-$OT_2$ structure represents the arrangement of the same interstices in a hexagonal close packed structure (hcp), each octahedron sharing 6 faces with tetrahedra and 2 with fellow octahedra, while each tetrahedron shares 3 of its faces with octahedra and the remaining 1 with another tetrahedron.

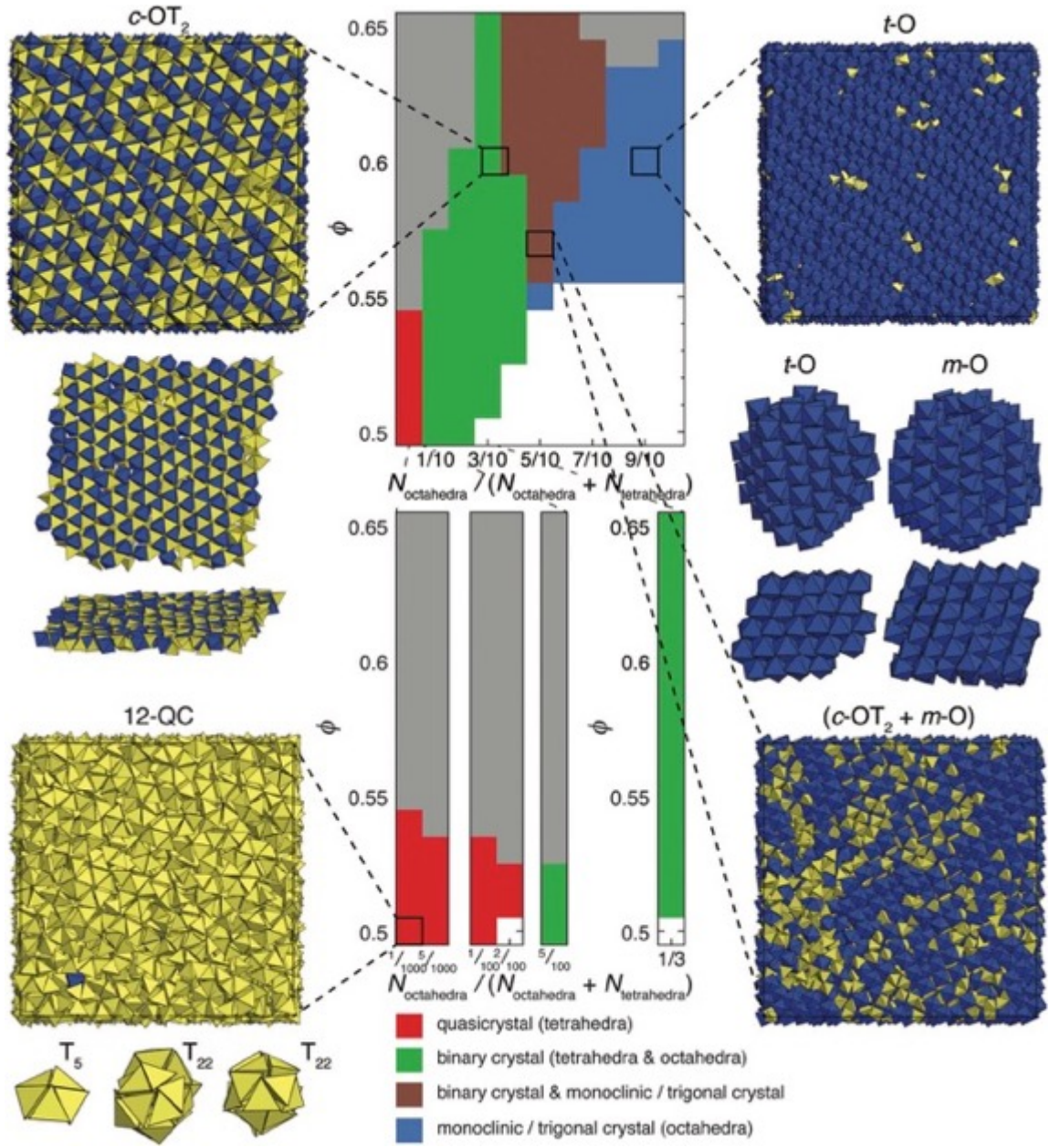


**Figure 7.1:** Phase diagram of the binary system octahedra:tetrahedra displaying several crystalline phases. The entire compositional region is shown in the upper middle. Two highlighted regions are shown below—the tetrahedra-rich regime and the ideal composition of the space tessellation of octahedra and tetrahedra with O:T = 1:2. Compositions are given in terms of the number of octahedra $N_{octahedra}$ divided by the total number of particles $N_{octahedra} + N_{tetrahedra}$. Samples from self-assembly simulations are shown for all relevant phase-diagram regions (tetrahedra – yellow; octahedra – blue): the dodecagonal quasicrystal (12-QC) comprising tetrahedra (lower left), the binary cubic phase (c-OT2) (upper left), the trigonal phase comprised of octahedra (t-O) (upper right), and a sample containing coexisting c-OT2 and m-O regions (lower right). Structural motifs of the 12-QC are shown (left to right: pentagonal bipyramid $T_5$; topview, and sideview of the $T_{22}$ building block), on the middle left, a representative layer that builds the c-OT2 structure, and on the middle right a topview and sideview of the layers of octahedra in the t-O and m-O structures. Gray regions in the phase diagram signify simulations that did not fully crystallize within the performed number of MC sweeps. White regions did not exhibit any ordered phases and can be regarded as fluid.

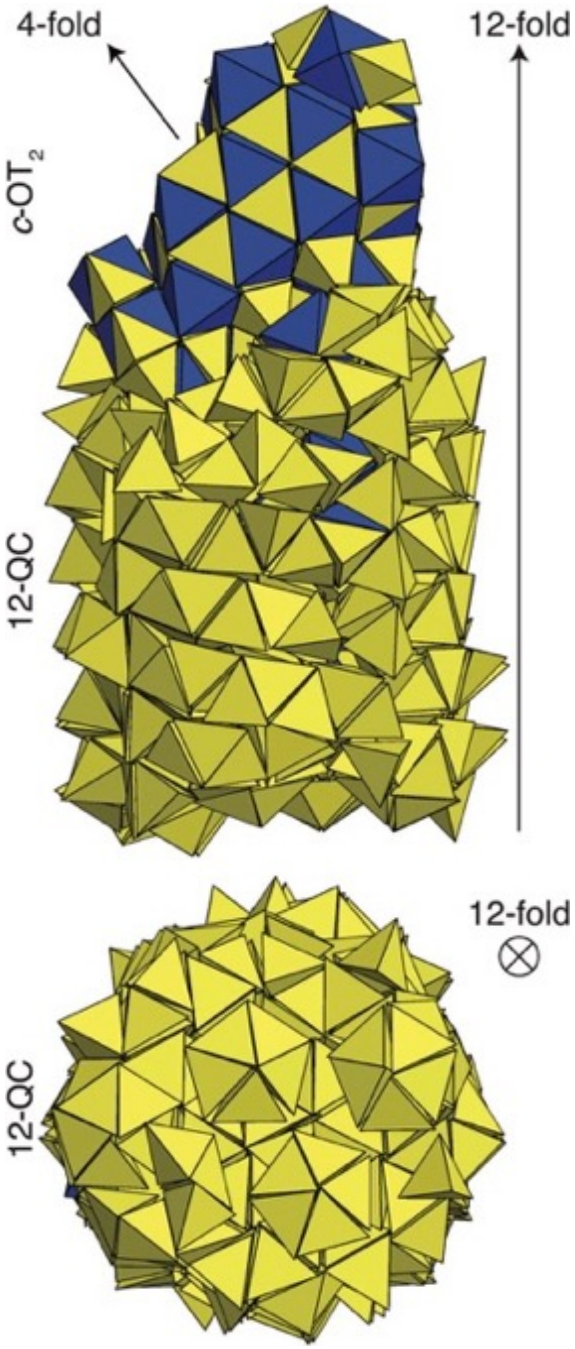


**Figure 7.2:** Oriented intergrowth of the 12-QC structure and the binary phase. The 12-fold symmetry axis of the quasicrystal is oriented in the vertical direction and the intergrowth angle becomes visible in the orientation of the cubic binary phase.

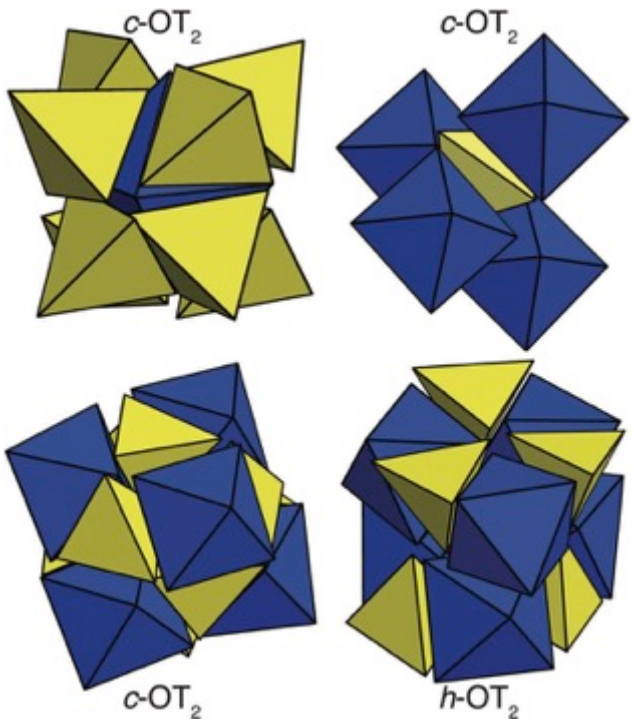


**Figure 7.3:** Structural motifs observed in binary assemblies of octahedra and tetrahedra. Tetrahedra are depicted in yellow, octahedra in blue color. Shown are: one octahedron surrounded by 8 tetrahedra as found in c-OT2 (upper left), one tetrahedron surrounded by four octahedra as found in c-OT2 (upper right), c-OT2-type stacking with alternating octahedra and tetrahedra in the stacking direction (lower left), and h-OT2-type stacking with octahedra stacked on top of octahedra and tetrahedra on tetrahedra (lower right).

Octahedra alone have been found to pack in two different phases, a monoclinic (Gong et al., 2017) and a trigonal one, m-O and t-O, the latter being the conjectured densest packing also known as the Minkowski phase (Betke & Henk, 2000; Minkowski, 1904), which has previously been confirmed by packing simulations (Torquato & Jiao, 2009). There are no shear planes in the t-O phase, which entropically favors the m-O structure, except at the highest packing fractions. In most mixed systems of octahedra and tetrahedra, both phases occur; an increased content of tetrahedra seems to facilitate the formation of the m-O structure, while the pure system of octahedra exhibits mainly t-O.

Octahedra self-assemble at larger packing fractions than tetrahedra and also have a higher maximum packing fraction corresponding to the respective densest packings. The densest known packing of tetrahedra—a 4-particle unit cell composed of dimer (Chen et al., 2010)—has

a packing fraction of 85.6%, whereas the densest packing of octahedra—the Minkowski structure, here termed the t-O phase—has a packing fraction of 94.7%. In addition, the self-assembled 12-QC structure has an even lower maximum packing fraction (Haji-Akbari et al., 2009), whereas the denser dimer-packing is not formed via self-assembly at these moderate packing fractions (Haji-Akbari et al., 2011).

There are additional (unpublished) results from this research that address the other two systems attempted by Khadilkar et al. (Khadilkar et al. 2021). These are the octahedra + cuboctahedra system, and octahedra + truncated cube systems. It was found that the octahedra + cuboctahedra system self-assembles at the 1:1 oct:cuboct ratio, but the octahedra + truncated cube system will phase separate at the 1:1 oct:truncated cube ratio.

## Summary & Conclusions

We have shown for the first time that binary crystal structures self-assemble from mixtures of hard, non-interacting polyhedra. We observed that the here-discussed binary phase coexists with both neighboring phases in self-assembly simulations: one comprising only tetrahedra and the other only octahedra.

In the binary phase diagram of mixtures of tetrahedra and octahedra, we report crystal structures self-assembling in three regions: the known dodecagonal quasicrystal formed by tetrahedra, assemblies of octahedra only, and the binary $OT_2$ phase.

The phase diagram contains only a very narrow coexistence region between the 12-QC and c-$OT_2$ phases. Generally, the quasicrystal forms at much lower packing fractions than the binary crystal. However, even at low packing fractions, this small number of octahedra rearrange in $OT_2$-like building units and incorporate the respective amount of tetrahedra to form the binary crystal.

There is a distinct range of stoichiometries that allows for coexistence of the $OT_2$ structure and a pure octahedral crystal. Both occur at similar packing fractions for stoichiometries around O : T = 6 : 4–7 : 3. Thus in the respective simulation runs, both crystalline phases were detected.

All in all, the phase diagram of mixtures of octahedra and tetrahedra exhibits typical features, such as pure and mixed phases, coexistence regions, etc. The phase behavior of this entropically stabilized system thus does not fundamentally differ from that observed in systems with enthalpic interactions.

## Supplementary Information: Self-assembly of a Space-Tessellating Structure in the Binary System of Hard Tetrahedra and Octahedra

### Structure Analysis with Bond Order Diagrams

The crystal structures observed in this study were analyzed primarily by visual inspection. However, bond-orientational order diagrams (BODs) (Roth & Denton, 2000) were also found to be instructive, especially when investigating structural subtleties. In the binary structure, the BODs were also generated both for the mixture of polyhedra and for tetrahedra and octahedra separately. In the binary crystal, the centers of the tetrahedra form a simple cubic lattice, and the octahedra form a face-centered cubic lattice. The BODs of the binary structure and the octahedra packings are shown in ***Figure 7.4***, the ones of the dodecagonal quasicrystal in ***Figure 7.5***. The quasicrystal of tetrahedra has a particular signature in the BOD, resembling a cylinder and resulting in dark spots aligned with the 12-fold axis of the dodecagonal structure.

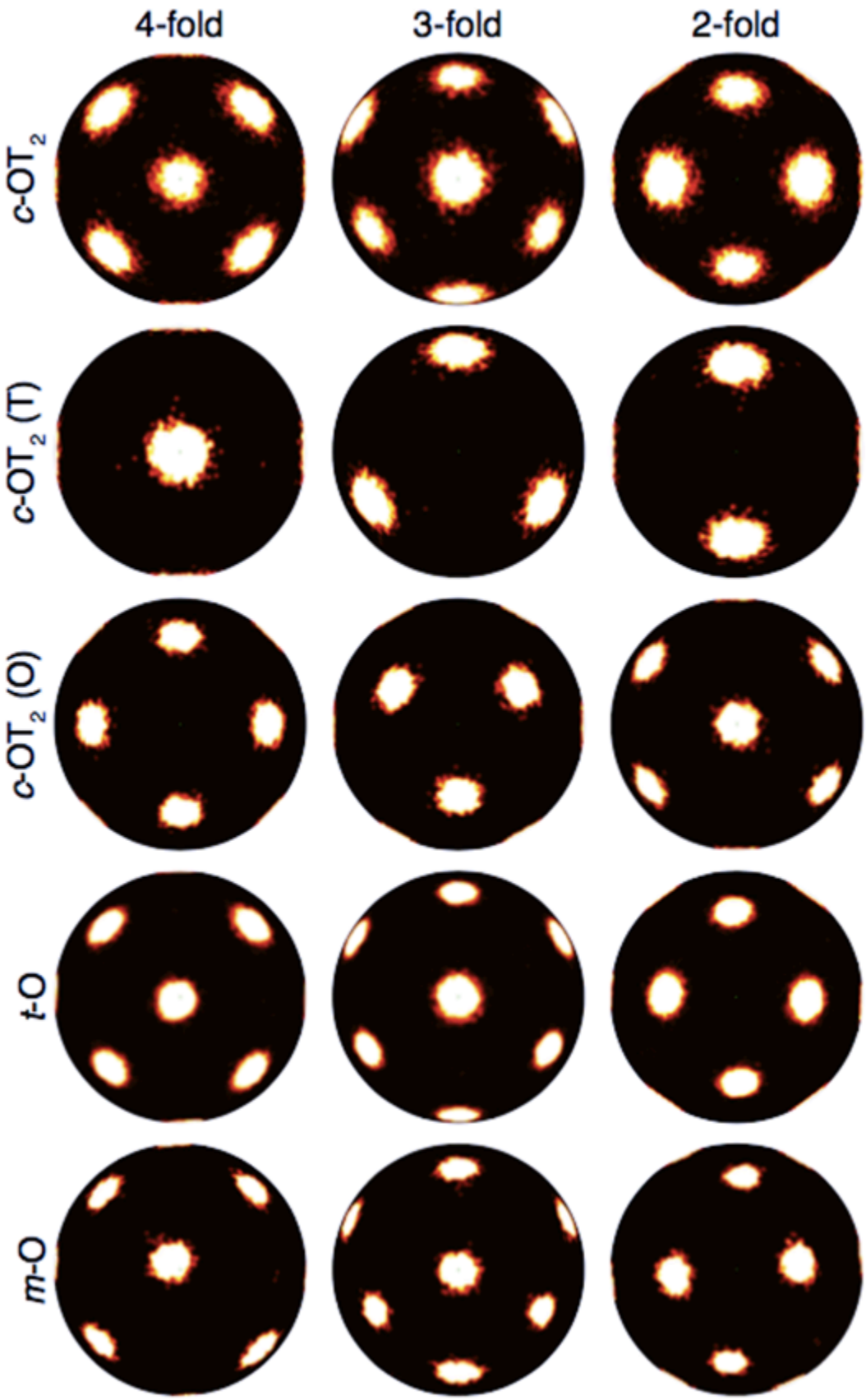
4-fold
3-fold
2-fold
c-OT2
c-OT2 (T)
c-OT2 (O)
t-O
m-O

**Figure 7.4:** Bond-orientational order diagrams (BODs), from top to bottom, of the full binary structure *c*-$OT_2$, as well as of only the tetrahedra (T), only the octahedra (O), and of the trigonal and monoclinic octahedra packings, *t*-O and *m*-O, respectively. Shown are the 4-fold / pseudo-4-fold, 3-fold / pseudo-3-fold, and 2-fold crystallographic directions.

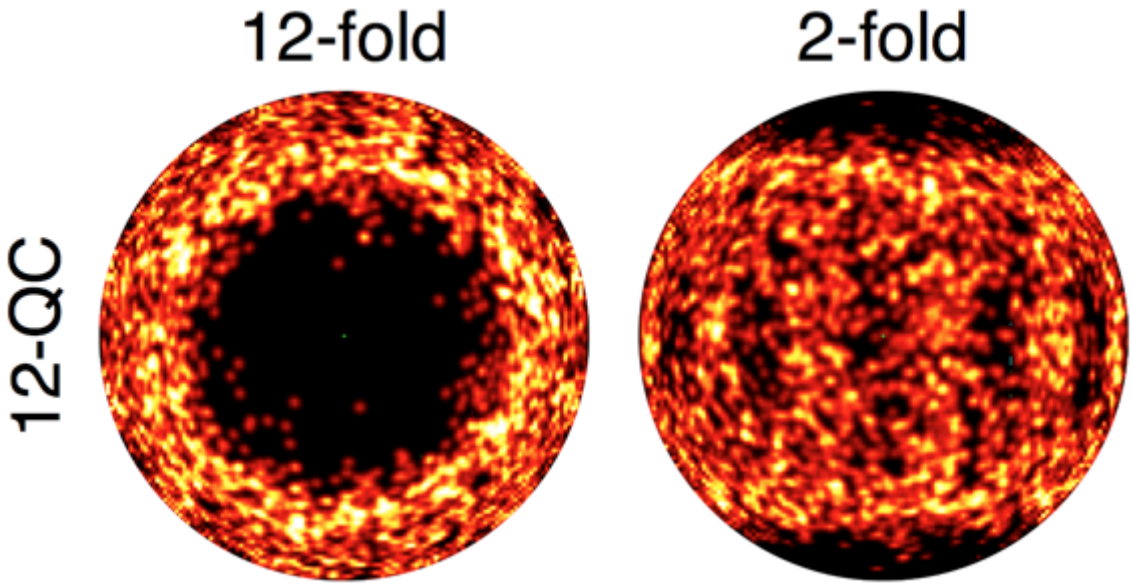


**Figure 7.5:** Bond-orientational order diagrams (BODs) of the dodecagonal structure 12-QC made up of tetrahedra. Shown are the 12-fold and 2-fold crystallographic directions.

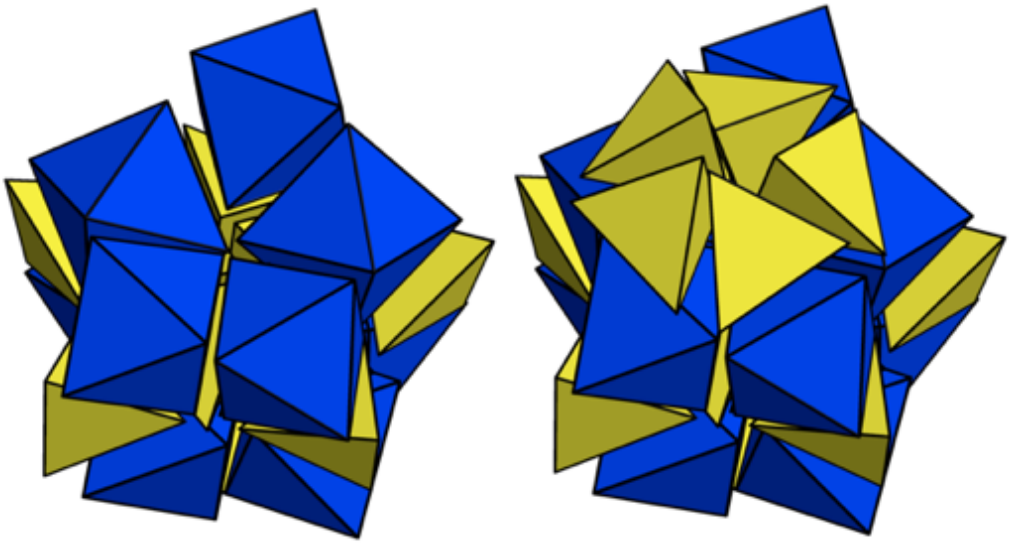

**Figure 7.6:** An intergrowth motif of octahedra with the 12-QC structure, consisting of a ring of five octahedra that can be stacked with pentagonal bipyramids of tetrahedra.

**Quasicrystal Binary-Crystal Coexistence**

Small numbers of octahedra that are present in a simulation of mainly tetrahedra have a preferred alignment within the quasicrystal. In some cases, they form five- rings, alternating with pentagonal bipyramids of tetrahedra, similar to a model of dodecagonal Al–Mn (X. Z. Li, 1995; X. Z. Li & Frey, 1995; Eric A. Lord et al., 2006), as shown in ***Figure 7.6***.

**Binary Crystal Structure**

The binary crystal consists of layers of alternating tetrahedra and octahedra that share faces with each other, *i.e.*, with only O–T nearest neighbor contacts. This leads to each octahedron having six neighbors within the layer (all tetrahedra) and each tetrahedron having three neighbors within the layer (all octahedra). The remaining faces—two per octahedron and one per tetrahedron—form a triangular lattice on the outside of the layer and are again arranged alternatingly. The ratio of octahedral to tetrahedral faces in this tiling is O:T = 1:1; each octahedron contributes two triangles and each tetrahedron contributes one, but their 1:2 composition overall and in the layer results in equal numbers on the outside of the layer (see ***Figure 7.1*** in the main text).

The resulting triangular lattices can be aligned alternatingly, joining octahedral faces with tetrahedral ones and vice versa, creating the same contacts that already occur within the layer. Alternatively, they can be rotated by 60° around any vertex so that each octahedral face joins another octahedral face and tetrahedral faces from different layers join one another, forming a mirror plane between layers. As is the case with different stacking variants in sphere-packings, both arrangements can be combined in an infinite number of ways.

If only the first kind of stacking—resulting in alternating polyhedral arrangements between layers—is employed, the alternated cubic honeycomb emerges. A honeycomb is a space-filling tessellation. Both of the honeycombs discussed in this manuscript are also uniform or vertex-transitive, *i.e.*, all vertices are equivalent, as well as convex, as they are built from convex polyhedra. The alternated cubic honeycomb structure is also edge-transitive, while the gyrated, hexagonal structure has two kinds of edges. A structure composed solely of the second kind of stacking results in the gyrated honeycomb. Edges in the alternated cubic honeycomb are

shared by a tetrahedron, an octahedron, another tetrahedron, and another octahedron, respectively. The gyrated, hexagonal honeycomb also exhibits this configuration, however, there is also a second kind of edge located between neighboring layers, shared by, in the following order, a tetrahedron, another tetrahedron, an octahedron, and a second octahedron.

The crystallographic structure type corresponding to the alternated cubic honeycomb is fluorite $CaF_2$: the space group is $Fm\bar{3}m$ (no. 225), octahedra occupy the Ca-Wyckoff position 4*a* 0, 0, 0 and tetrahedra the F-position 8*c* 1/4, 1/4, 1/4. The gyrated honeycomb structure has no atomic equivalent; its crystallographic description can be derived from the cubic structure equivalent to the analogy between cubic-close and hexagonal-close packings *ccp* and *hcp*. The space group is $P6_3/mmc$ (no. 194) with octahedra occupying Wyckoff position 2*a* 0, 0, 0 and tetrahedra 4 *f* 1/3, 2/3, 5/8.

Within the stability range of the binary $OT_2$ phase, the cubic *c*-$OT_2$ structure is dominant, but is interspersed with a few stacking faults, which come in the form of the hexagonal *h*-$OT_2$ structure. The short bond length between face- sharing tetrahedra that are located between layers can be used to easily map these stacking faults within the *c*-$OT_2$ structure.

As expected, the binary crystal seems to form best at the ideal stoichiometry of O:T = 1:2 and at a packing fraction of 60%. This was determined by the clarity of the BOD, as well as the highest number of particles that were identified as having a crystalline environment with the employed Steinhardt order parameter.

**Octahedra Crystal Structure(s)**

The two octahedra structures are shown in ***Figure 7.7***. The *m*-O structure can be understood as a packing of octahedra with tetrahedral voids [T] in a stoichiometry O:[T] = 1:4, where the edge length of the tetrahedral voids is 1/2 the edge length of the octahedra. The octahedra are arranged in stacked trigonal layers that allow for a parallel shear plane (the layers can be sheared with respect to one another) and another perpendicular shear plane that can move along one direction. The *t*-O structure, also termed the Minkowski phase, can be thought of as a

packing of octahedra with O:[T] = 1:6, where the edge length of the tetrahedral voids [T] is 1/3 the edge length of the octahedra. The re-tessellations of tilings of octahedra and tetrahedra with different edge lengths—here introduced as packings of octahedra with tetrahedral voids—have been described in detail (Gabbrielli et al., 2012).

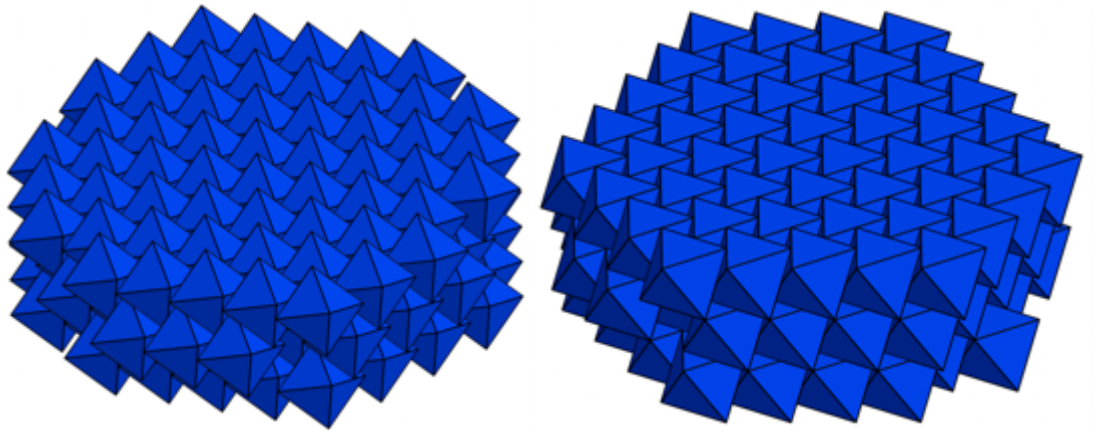

**Figure 7.7:** Two packings of octahedra: the trigonal closest packing of octahedra, t-O structure (left) and the monoclinic layered structure m-O (right).

## Conclusion and Outlook

We are still learning a lot about quasicrystals and it is my hope that the analysis presented in this thesis is useful to other researchers who, like me, just wanted to know what a quasicrystal *is*. There are many beautiful ways of generating and analyzing a quasicrystal, and I hope that the perspective offered in this thesis offers a unique look at these fascinating ways of creating patterns in matter. We can use deflation, multi-grid, higher-dimensional projections, or any of the other methods presented in the literature, and still come away with little idea of what a quasicrystal looks like, beyond a jumble of subtly changing patterns. This thesis offers something unique—a distinct mental picture of what it means for a pattern to be quasicrystalline.

Some of the tilings analyzed in this thesis are quite complex, and some are quite simple. But it is interesting to note how surprisingly simple some of them are. The Penrose tilings, for instance, are all simple enough that it is practical to memorize their construction. This can enable all manner of artists and workers to build Penrose tilings with an approach that involves little in the way of mathematics, or even without pencil and paper. Do you want to tile your bathroom with defect-free Penrose tilings? Now anyone can do it. This is not something that has been done before, as all other methods of assembly involve grids, computer models, or at least some very careful drawing as in the case for deflation. The laying method just requires the fundamental polygon/polyhedron, and an idea for how to construct them into a second-order polygon/polyhedron. The situation is different for the icosahedral quasicrystal, of course—memorizing its hierarchical polyhedral assembly would be formidable. But there is no picture of the AKN in the existing literature that provides any kind of picture at all, let alone a complex one. In that respect, this work represents an important contribution to the body of quasicrystal literature.

Any quasicrystal could, in principle, be analyzed using this kind of order parameter. Note that while I intended this specifically as an order parameter for computational applications, applying it to experimental data is certainly possible if accurate data can be collected for particle positions. The same tilings hierarchies analyzed here are present in any quasicrystal that is sufficiently far-removed from a random tiling. Unlike many other order parameters, such as

Steinhardt or machine learning protocols, this type of order parameter is tied in a fundamental way to understanding the hierarchy of the quasilattice, and for that reason I find it particularly fulfilling. A real-space understanding of quasilattices may open new doors for self-assembly since it can show a researcher exactly what needs to change in a structure in order to make it more quasicrystalline. Perhaps a minor change needs to be made in a potential, or a phason flip is stuck in a kinetic trap. It is my hope that this may provide a perspective that is otherwise lacking in quasicrystal research, and that it will allow researchers to grasp the scaling of the structure in a way that supersedes simple matching rules and particle ratios and use this knowledge to build matching rules that bias structures toward the hierarchy necessary for more ideal quasicrystals. Whatever the case may be, it should all be easier if we have a real-space model in our mind as the goal.

# APPENDEX

# Appendix A

## Application of Layering and Patchy Potentials to Simulation of Hard Penrose Rhombuses

The purpose of this cluster analysis is to provide a definitive reference point in answering the question of whether a given local motif is correct, and to continue answering that question for every size of motif out to, in principle, the infinite tiling. In practical use for simulation, we need only extend it out to the edges of the simulation box. Even recent papers on covering clusters focus heavily on local descriptors and not overall hierarchical patterns (Li et al., 2017).

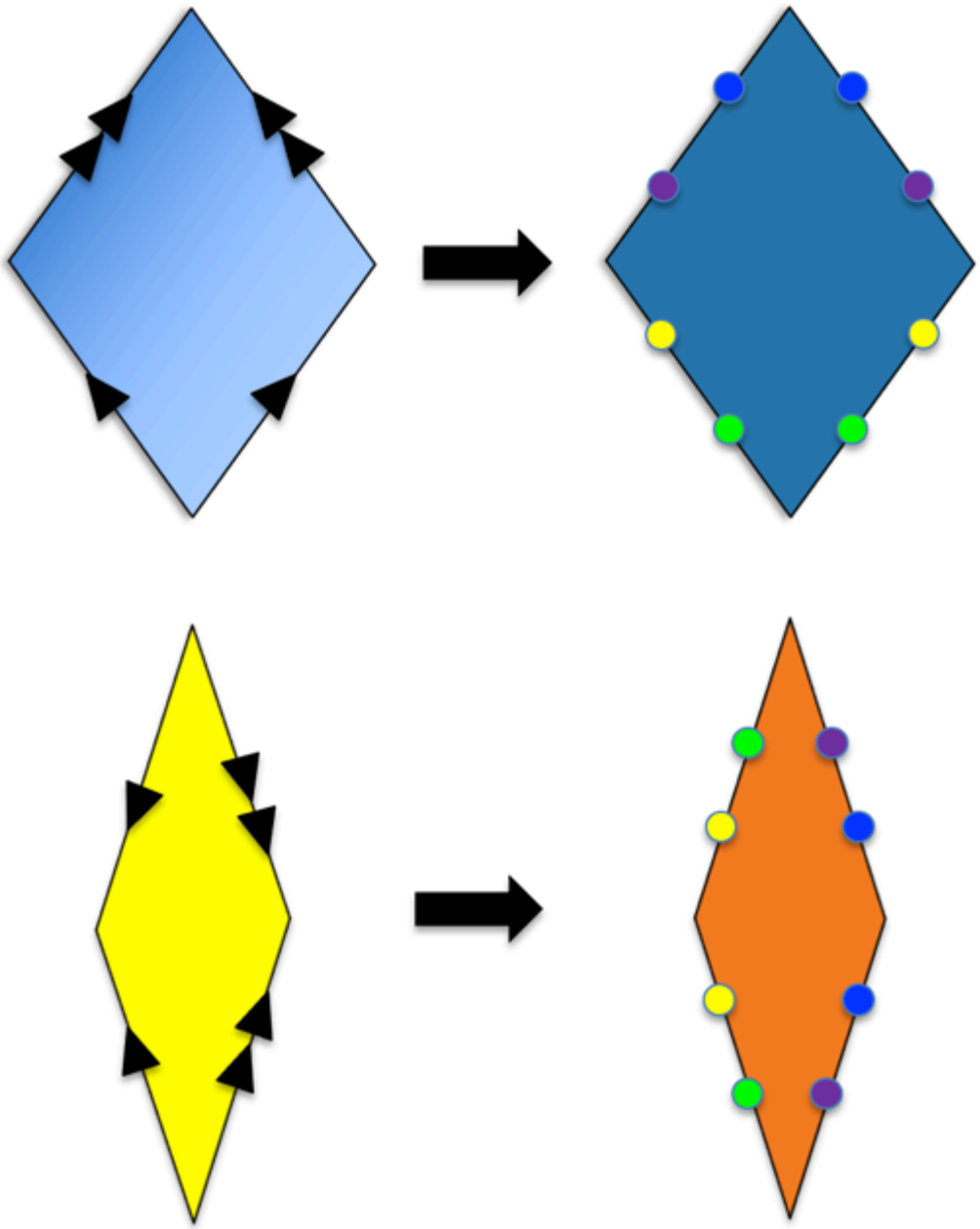

**Appendix Figure A.1** Penrose rhombuses have been decorated with eight patchy potential wells to implement the matching rules as explicitly energetic. Matching rules cannot be entropic with hard symmetric shapes, since the matching rule has to bias one symmetric orientation over another. This would not be the case if I had instead implemented something like Penrose chickens (Penrose, 1979), which have asymmetric puzzle-like pieces instead (Harper et al., 2015). Like-colors attract, and unlike colors repel. This reproduces both the type of arrow (single or double arrow) and its directionality. An ideal Penrose tiling, if the simulation were to reach it in equilibrium, will therefore necessarily be the lowest energy configuration.

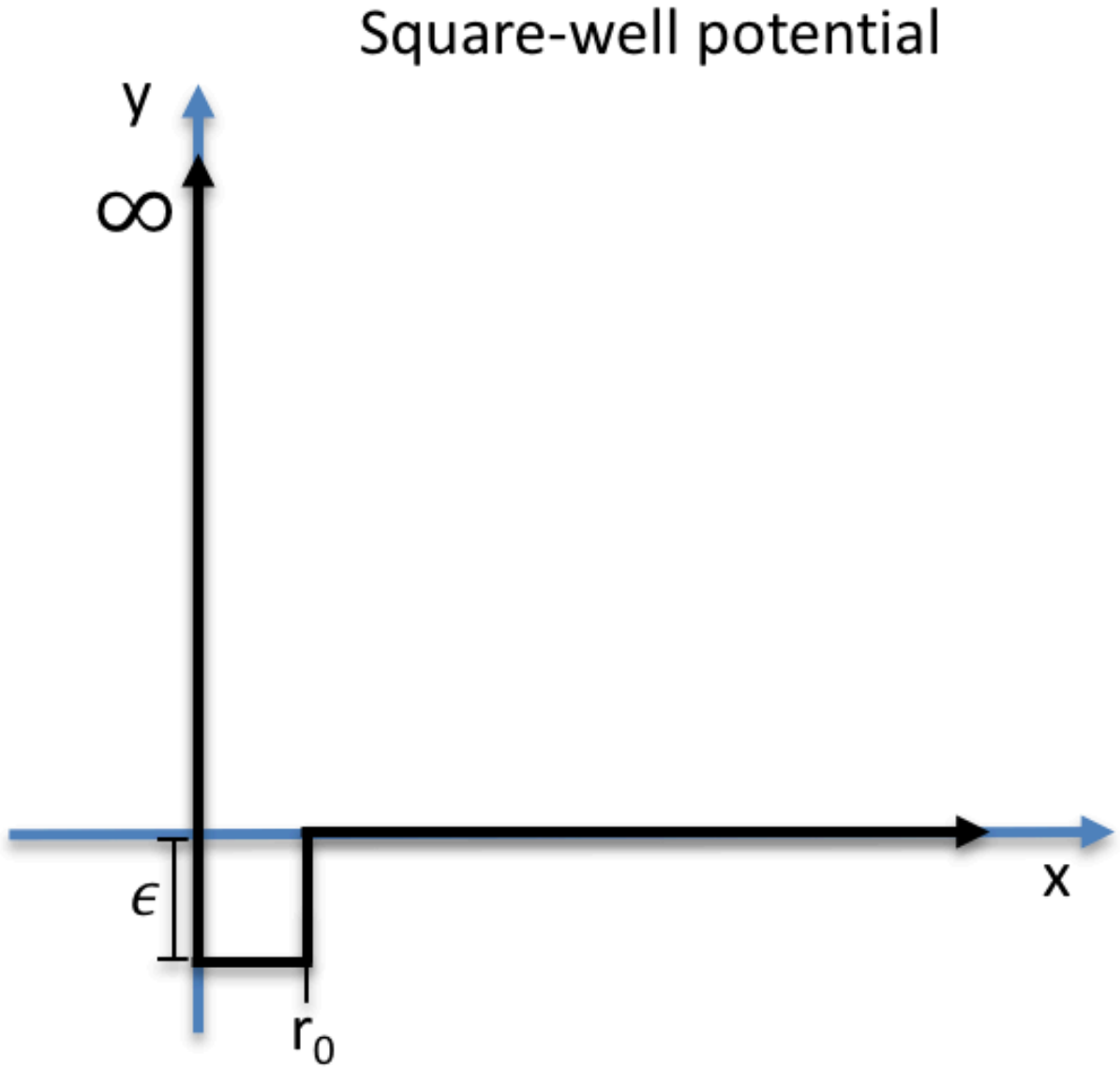


**Appendix Figure A.2** A simple square-well potential is used for each patch. The well-depth epsilon was taken as a tunable simulation parameter. The patch position can also be changed, but was not taken as a tunable parameter.

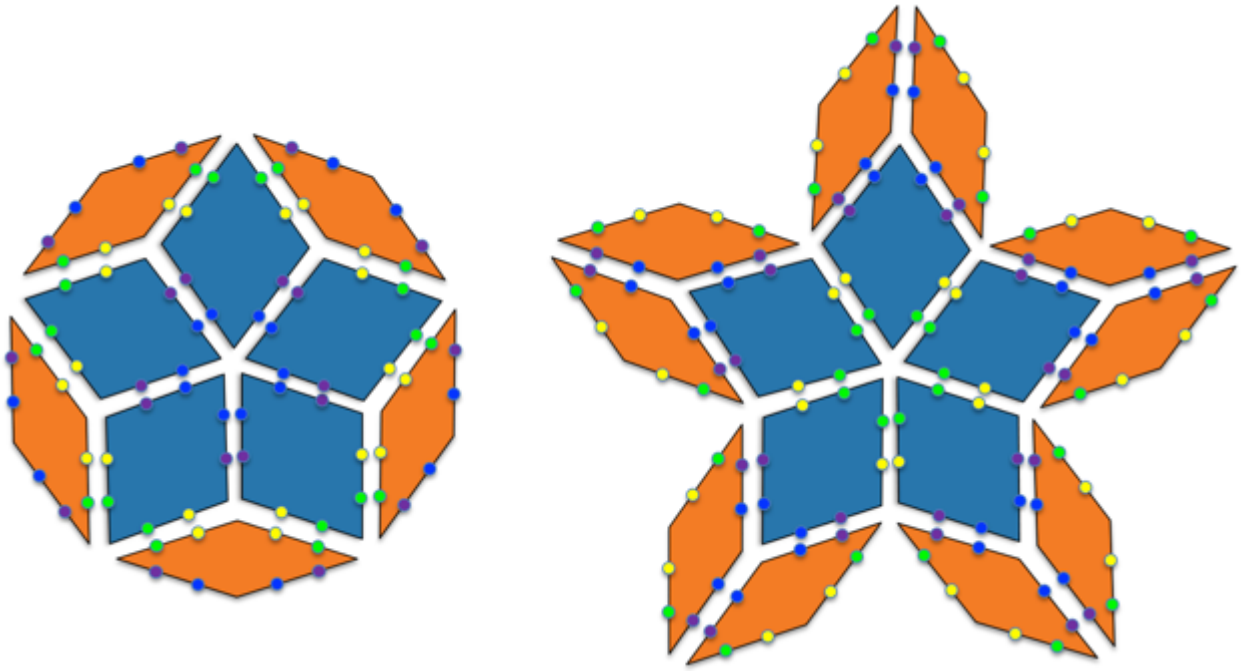

**Appendix Figure A.3** The Penrose matching rules contain a natural asymmetry, and the different five-fold oblate rhombus stars displayed above highlight one of the different pathways that can be chosen during assembly. Each star simply has oblate rhombuses rotated by 180°. These motifs can be seen in the simulation snapshot of **Appendix Figure A.4**. The left image forms the core of the hierarchical protocol discussed in this chapter, whereas the right image is an incidental, or secondary, motif created by the overlaps. **As mentioned earlier, both motifs are used as vertices of the second-order ideal Penrose lattice.**

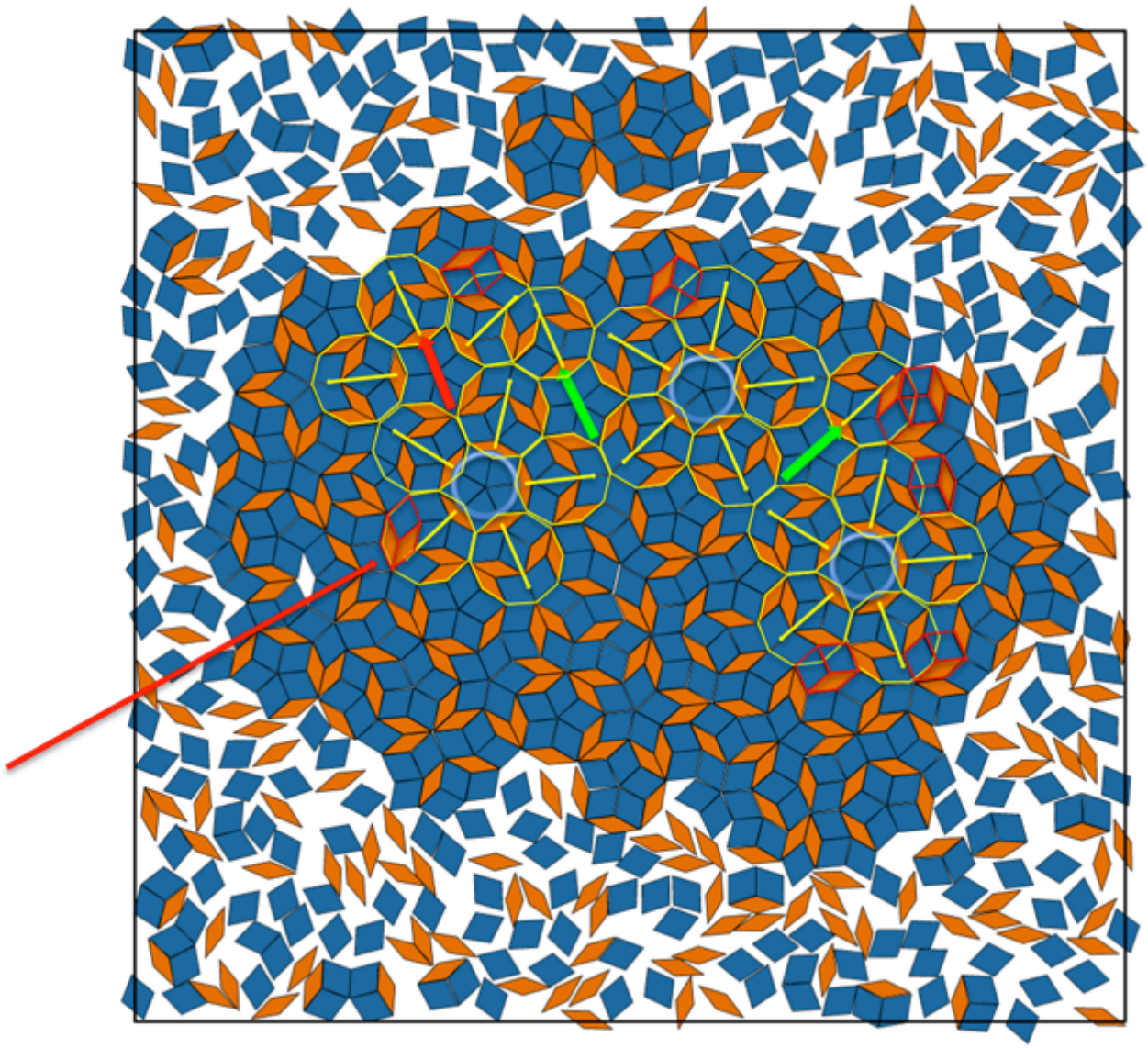

**Appendix Figure A.4** 1251 patchy obtuse and 774 acute rhombuses are simulated in Monte Carlo for 2e6 timesteps and epsilon well-depth of 2.4. The same motifs from ***Figure 2.4(d)*** can be seen, highlighted with blue circles, and red and green arrows. Phason errors, which manifest as hexagons with the wrong 180° orientation, are highlighted with small red hexagons. One example of a phason error is pointed out with a long red arrow on the left of the image. Although this represents a more ideal quasicrystal than seen in the majority of self-assembly experiments, its defects are readily apparent with the cycling polygonal covering/layering procedure detailed in this chapter for the Penrose tiling. **Visualizing these kinds of phason defects is not otherwise possible with the phason-strain measurements that currently exist in the literature**.

Self-assembly[42] simulations were carried out by Will Zygmunt using HOOMD-blue, with the patches sometimes forming precursor structures in the melt. A phase co-existence between liquid and solid Penrose tiling was attained.

A common obstacle in the growth of any quasicrystal, whether in simulation or experiment, is the lack of perfect matching rules, and/or the lack of phason re-arrangement, **but never have both perfect matching rules and the allowance of phason re-arrangement been maintained in the same simulation.** Ideally, the system would be able to flip entire hexagons. This would allow the correction of phason errors like those outlined in red in ***Appendix Figure A.5.*** Despite implementing Monte Carlo rotation moves, which choose clusters at random, the system was unable to properly rotate the hexagons to fix these errors. **I believe a working implementation of these pi/180° Monte Carlo flips would be a fascinating future project.** In an atomic system, these phason flips would represent the movement of a single atom, and so in principle are more easily achieved with that kind of simulation (Boissieu, 2007). The advantage of a patchy hard-particle system is that perfect matching rules can be implemented explicitly. I think with proper cluster identification, the 180º flip could be made to work in this system. If this were successful, then we would have a simulation that not only executed proper phason flips, but also did so with perfect matching rules. **It would be possible to test the hypothesis of whether these two features will lead to an ideal quasicrystal in equilibrium conditions—something never before achieved in simulation or experiment.**

[42] 1251 patchy obtuse and 774 acute rhombuses (corresponding to the approximate stoichiometry of the golden ratio 1251:774 ≈ $\phi$, the golden ratio) were run using the HOOMD-blue Monte Carlo plugin for 2e6 timesteps with an epsilon well-depth of 2.4.

## Appendix B

### Traditional Deflation of Tübingen Triangle Tiling

The deflation protocol for the Tübingen triangle tiling starts first with the golden triangle and golden gnomen. This geometric deflation protocol, like the Penrose tiling, uses triangles that are scaled down by a factor of the golden ratio to subdivide the original triangles. This can proceed indefinitely until one arrives at a Tübingen tiling of whatever desired size. Unlike the ”imperfect” or pseudo-deflation of the Penrose tiling (Frank, 2008), the deflation of the Tübingen tiling is restricted to the boundaries of the original proto-tile.

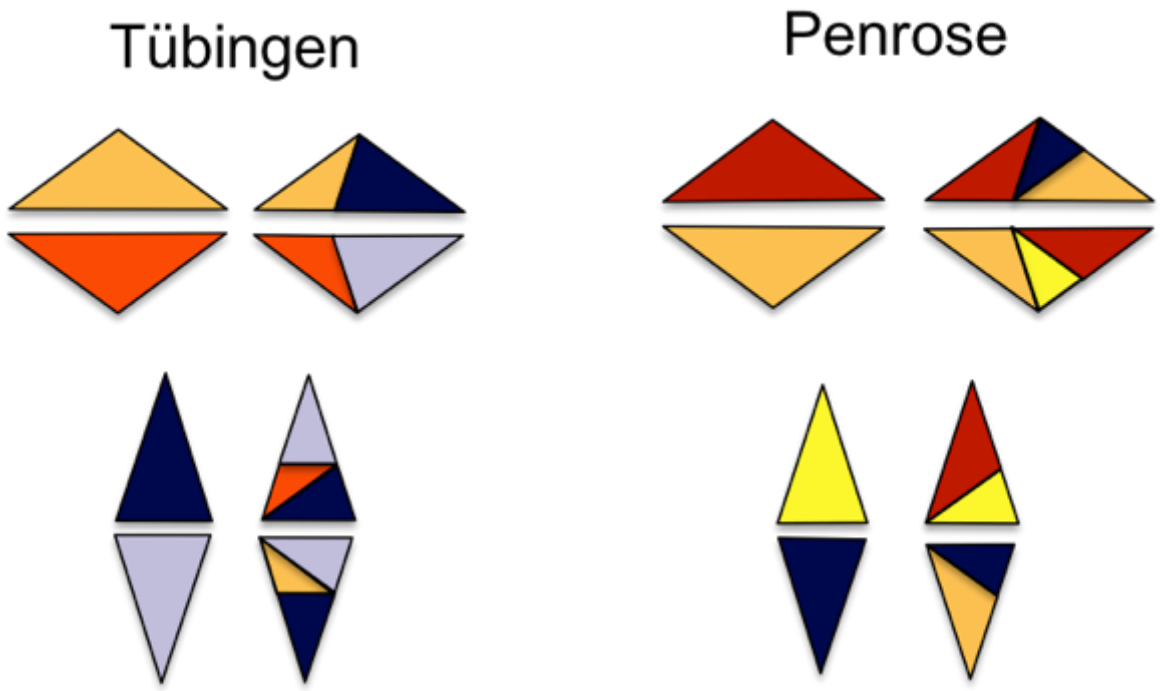


**Appendix Figure B.1** Tübingen tiling deflation (left), Penrose deflation (right). The Tübingen and Penrose tiling can both be described using the Robinson triangles, and both have their own respective deflation protocols, whereby each golden gnomen (top) or golden triangle (bottom) is re-tiled with copies of each triangle, which have been scaled down by the golden ratio.

It is possible to create both the Tübingen tiling and the Penrose tiling from the same golden triangle and golden gnomen. In this version of the deflation protocol, we see that the

Tübingen gnomen (left) is scaled down so that its duplicated (the isosceles triangle has two of these) edge is equal to the distinct edge (the isosceles triangle only has one of these) of the golden triangle. In contrast, the Penrose decomposition (right) scales the duplicated edge of the golden gnomen to also match the duplicated edge of the golden triangle. There are also other deflations that function differently (Baake, 1999).

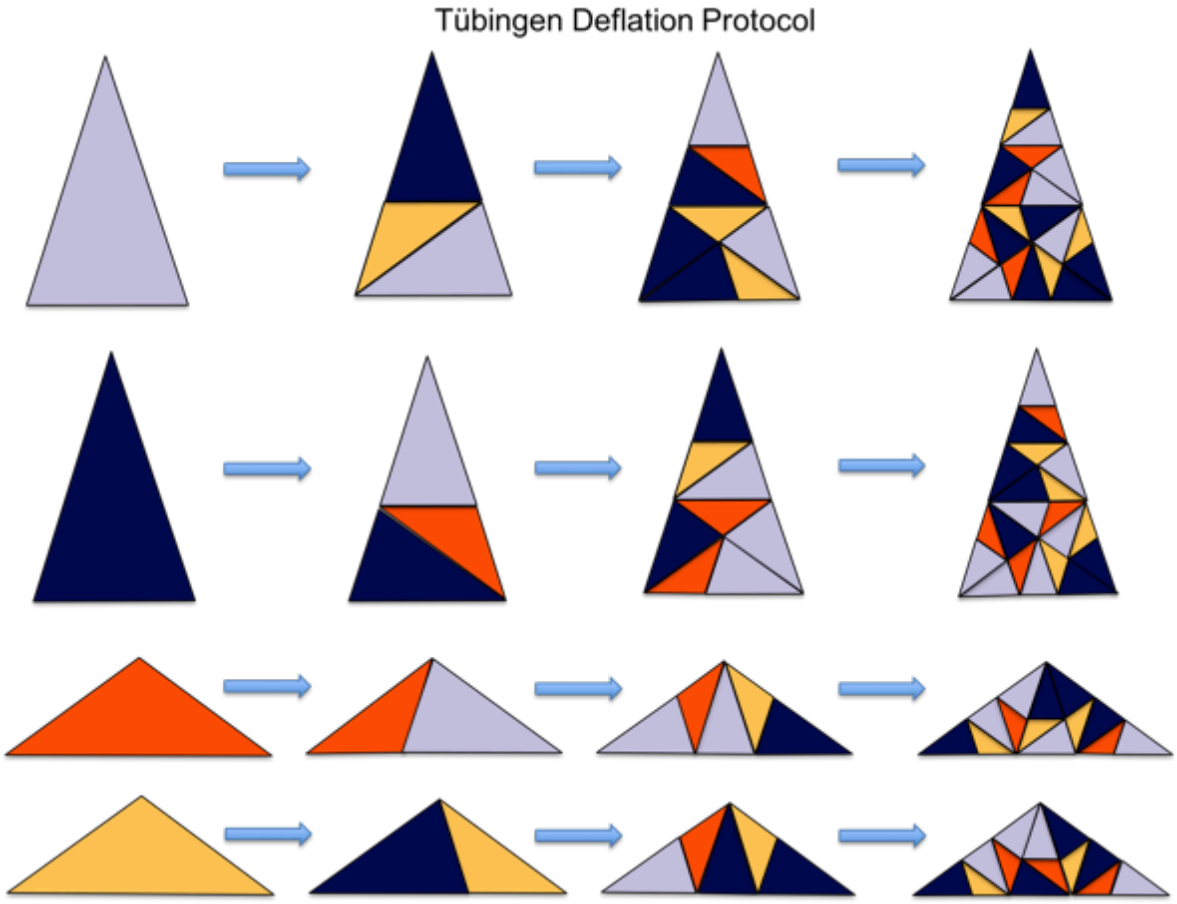


**Appendix Figure B.2** Three iterations of the Tübingen tiling deflation/substitution protocol for each of the two types of prototile (grey triangle, left; orange gnomen, left) and their chiral twins (dark blue triangle, left; yellow gnomen, left), respectively. The deflation protocol allows for the creation of an infinite plane of Tübingen tiling.

### Robinson Triangle Deflation of the Tübingen Tiling

The Robinson triangle decomposition is a deflation method to generate the Tübingen triangle tiling. As has been shown with many other tilings, the deflation rules also allow the creation of natural matching rules (A. E. Madison, 2015). The Tübingen triangle tiling (TTT) is made from two types of triangle—a golden triangle, and a golden gnomen, with matching short and long edge lengths, respectively. It is named for the mathematics group in Tübingen, Germany, (sister

city to Ann Arbor, MI!) that first studied them. The golden triangle is an acute isosceles triangle that has the duplicated side equal in length to the golden ratio times the length of the distinct side. The vertex angle is equal to 36° and the two base angles are equal to 72°. The golden gnomen is named for the fact that it "gnoms on" to other shapes to make the same shape. In contrast to the triangle, the golden gnomen has a distinct side that is equal to the golden ratio times the duplicated side. Golden triangles and gnomens are inherently associated with pentagonal symmetry, as can be seen by a simple cut of a pentagon into a golden triangle and two golden gnomens. Ultimately, this "gnom on" ability is closely related to the self-similarity hierarchy in the TTT (Baake, 1999). Within the TTT, there are also chiral twins for each of the golden triangles and golden gnomens, respectively. This chirality comes into play during phason flips, and when a shape is deflated—the different chiralities, or handedness, will deflate in different ways. Deflation, or substitution, is a process that will be discussed in many parts of this thesis.

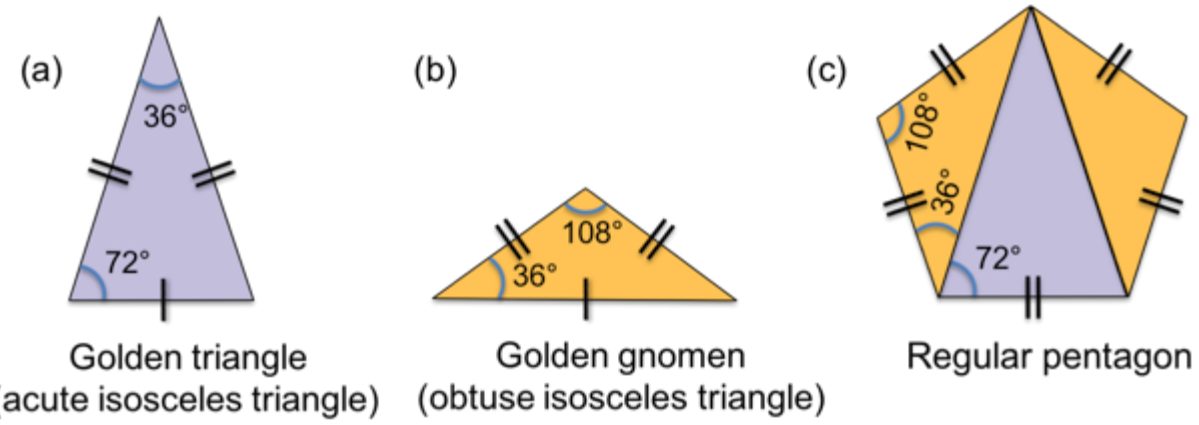


**Appendix Figure B.3** A golden triangle (a), golden gnomen (b), and composite pentagon made from both (c).

Interestingly, these are the same triangles used in the Robinson decomposition of the Penrose tilings, but they are assembled in a way that is instead dual to the Penrose tiling (Frettlöh, 2008). The concept of duality can be understood by comparing a cube and an octahedron. The vertices of the octahedron meet the faces of the cube, so we say that the cube and octahedron are dual to each other. Likewise, a square, when rotated by 90°, will fit inside

itself with the inside vertices touching the outside edges, so we say the square is dual to itself. All regular polygons are, in fact, self-dual.

**Appendix Figure B.4** In this figure, from left to right, we see a triangle, square, pentagon, and octagon, with scaled down copies placed inside. Each vertex meets an edge, so each of these regular polygons are self-dual.

## Robinson Deflation and Penrose Layering

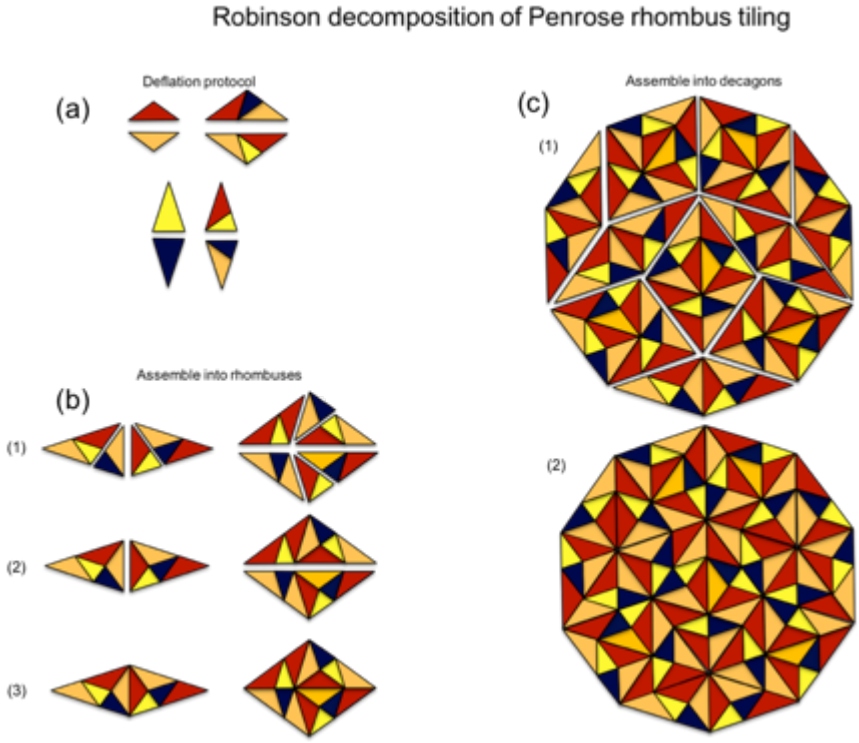


**Appendix Figure B.5** Robinson decomposition of Penrose tiling into golden triangles and gnomens: the known deflation protocol is used in (a) to generate deflated copies of each golden triangle and gnomen. We could keep deflating the tiles to make more tiling, but instead we use them to assemble new Penrose rhombuses in (b). Step (1) shows the triangles we start with from (a). Step (2) shows the merging of these triangles into larger triangles. Step (3) shows the merging of these larger triangles into rhombuses. In (c)(1), we assemble the rhombuses into the decagon motif that plays a central role in understanding the construction of the Penrose rhombus tiling. (c)(2) shows the merging of these rhombuses into the decagon.

The Robinson decomposition starts with the golden triangle and golden gnomen, colored to indicate opposite deflation chiralities—each handedness is subdivided in a different, but

mirror-symmetric, way. After each successive subdivision, each of the two triangles of the same type remains a mirror image of the other. These triangles can then either continue to be deflated to produce a plane of Robinson triangles in the Penrose configuration, or they can be assembled into the acute and oblate rhombuses of the Penrose tiling. These can then be assembled into a decagonal motif, which can then be assembled into a pentagonal motif, and so on, in the same manner that is outlined in *Chapter Two* for the Penrose tiling. The deflation protocol and re-assembly into rhombuses is known (Baake, 1999), and the purpose of this section is to show that it is consistent with the layering method that I have proposed for the Penrose tiling.

**Natural Matching Rules Derived by Robinson Deflation**

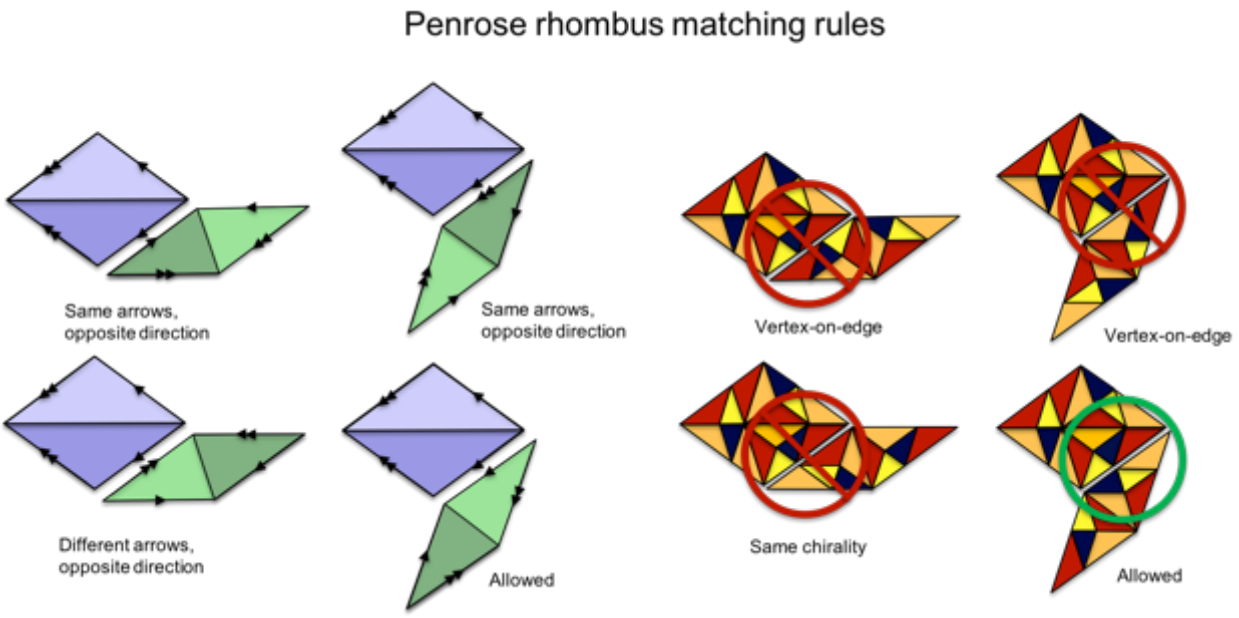


**Appendix Figure B.6** The Penrose rhombuses (left) have matching rules in the form of single and double arrows. Both the number of arrows and their directions must match in the perfect Penrose tiling. Natural matching rules can be derived for both from the deflation/substitution process. The Robinson decomposition (right) produces rhombuses that must avoid vertex-on-edge meetings, and also same-chirality meetings between the golden triangle and golden gnomen prototiles. This presentation of matching rules for the Robinson decomposition of the Penrose rhombuses has, to my knowledge, not yet been presented in the literature—but the analogue for it has been explored for the Penrose system (Penrose, 1979).

**Consistency of Penrose Robinson Deflation with Layering**

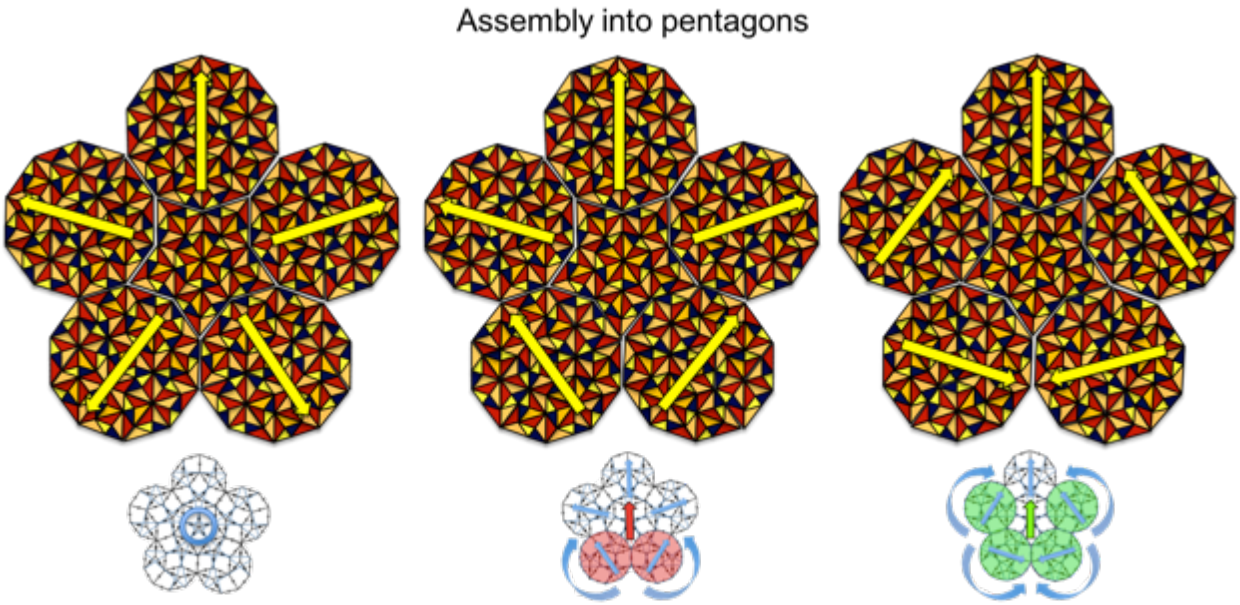


**Appendix Figure B.7** The same assembly process, detailed in *Chapter Two*, can be performed with the Robinson decomposition (top row) as in the Penrose tilings (bottom row). Note that each edge along the border of a decagonal motif must agree with the matching rules as defined in ***Figure 1.10***. Each orange gnomen must match with a red gnomen, and each black golden triangle must match with a yellow golden triangle, with no edge-to-vertex meetings in the boundary between decagons.

At this stage, there are two rules for assembling the Penrose tiling in the Robinson decomposition. The first is that the vertex of one triangle cannot lay on the edge of another triangle. The second is that if two triangles are edge-to-edge, they must be of opposite chirality. As in the Tübingen tiling, this chirality is not reflected in the set of vertices, but rather in the higher-order deflation that would follow. On the left of ***Appendix Figure B.7*** is a "blue" pentagonal motif, which is rotationally symmetric. The middle pentagonal motif is "red," and has two pentagonal motifs on the bottom which are rotated CCW 108° for the bottom right, and CW 108° for the bottom left. The rightmost pentagonal motif is "green," and has four rotated characteristic (ignoring order) decagons. The middle left and middle right are CW 108° and CCW 108°, respectively. The bottom left and right are rotated CCW 108° and CW 108°, respectively.

Note that if we only perform a 36° or 72° rotation, we create either vertices that land on edges, or chiral types that meet another of the same type along an edge. Since both of these rotations are forbidden, we can see how the Robinson decomposition creates a set of natural matching rules for this decagon level of assembly. The same procedure can be performed with the Penrose rhombus deflation protocol. It is also worth noting that if we consider an atomic

decoration involving only vertices, it is possible to see how an atom would satisfy more interaction lengths by not laying on the edge of another shape. This can help us understand how matching rules might arise naturally from atomic decorations that produce asymmetries in the prototiles (Mihalkovič et al., 2002).

## Appendix C

## Onoda Forced-Vertex Method

Nothing in this thesis relies on understanding the Onoda method, but it is interesting to contrast it with other construction methods. **It is special because it is as close as we can currently get toward *constructing* a Penrose tiling with matching rules and no reconfiguration.** In that spirit, I am providing this review of the method. The Onoda method relies on matching rules, but with a non-local condition. Since matching rules inevitably lead to errors during construction, if they cannot rearrange (or even, perhaps, if they can rearrange!), early researchers sought to find other solutions. One of these attempts is the protocol devised by Onoda (Onoda et al., 1988). A Fibonacci Sequence has forced and unforced moves because of its deflation rules. In the Fibonacci Sequence, LL is allowed, but not LLL. Likewise, S is allowed, but not SS. If we start with a sequence that reads LSL, then an L can follow, or an S. But if we have a sequence that reads LSLL, then we know the next letter must be S, or we will be in violation of the deflation protocol. To understand this fully, it is best to sit down with paper and work out the Fibonacci deflation by hand! Two-dimensional tiles also have a set of vertex rules: some vertex arrangements are allowed and some are not. There are, for example, eight allowed vertices in the Penrose rhombus tiling. If we grow a Penrose tiling by adding rhombuses, then some placements allow either a fat or skinny rhombus, and some other placements will require one or the other. The latter is a *forced move* and the former an *unforced move*. Onoda showed that if we first restrict our tile placements to forced moves, then we can propagate a nearly defect-free tiling by later filling in the unforced moves—which are then turned into forced moves when all of the locally existing forced locations are filled. Hann and Socolar (Hann et al., 2016) extend this protocol to three-dimensional icosahedral quasicrystals, specifically the Ammann-Kramer-Neri tiling where there are 39 allowed vertices, and they observed a linear increase in defects in similarity with Onoda's work. This linear increase means that as the quasicrystal gets exponentially larger, the number of defects diminishes on a per-particle basis—hence our fascination with it as a possible growth mechanism. **As noted,**

**however, this requires non-local information. A tile cannot know from local conditions whether its placement is forced or unforced, and so there is no local way to add tiles via Onoda's method. This would appear to exclude it from explaining experimental growth.**

## BIBLIOGRAPHY


Abe, E., Pennycook, S. J., & Tsai, A. P. (2003). Direct observation of a local thermal vibration anomaly in a quasicrystal. *Nature*, *421*(6921), 347–350. https://doi.org/10.1038/nature01337

Abe, E., Yan, Y., & Pennycook, S. J. (2004). Quasicrystals as cluster aggregates. In *Nature Materials* (Vol. 3, Issue 11, pp. 759–767). Nature Publishing Group. https://doi.org/10.1038/nmat1244

Aboufadil, Y., Thalal, A., & Raghni, M. A. E. I. (2014). Moroccan ornamental quasiperiodic patterns constructed by the multigrid method. *Journal of Applied Crystallography*, *47*(2), 630–641. https://doi.org/10.1107/S1600576714001691

Agarwal, U., & Escobedo, F. A. (2011). Mesophase behaviour of polyhedral particles. *Nature Materials*, *10*(3), 230–235. https://doi.org/10.1038/nmat2959

Al Ajlouni, R. A. (2011). A long-range hierarchical clustering model for constructing perfect quasicrystalline formations. *Philosophical Magazine*, *91*(19–21), 2728–2738. https://doi.org/10.1080/14786435.2010.532515

Allouche, J.-P., & Shallit, J. (1999). The Ubiquitous Prouhet-Thue-Morse Sequence. In *Sequences and their Applications* (pp. 1–16). Springer London. https://doi.org/10.1007/978-1-4471-0551-0_1

Anderson, J. A., Eric Irrgang, M., & Glotzer, S. C. (2016). Scalable Metropolis Monte Carlo for simulation of hard shapes. *Computer Physics Communications*, *204*, 21–30. https://doi.org/10.1016/j.cpc.2016.02.024

Anderson, J. A., Glaser, J., & Glotzer, S. C. (2020). HOOMD-blue: A Python package for high-performance molecular dynamics and hard particle Monte Carlo simulations. *Computational Materials Science*, *173*, 109363. https://doi.org/10.1016/j.commatsci.2019.109363

Anderson, J. A., Jankowski, E., Grubb, T. L., Engel, M., & Glotzer, S. C. (2013). Massively parallel monte carlo for many-particle simulations on GPUs. *Journal of Computational Physics*, *254*, 27–38. https://doi.org/10.1016/j.jcp.2013.07.023

Anderson, J. A., Lorenz, C. D., & Travesset, A. (2008). General purpose molecular dynamics simulations fully implemented on graphics processing units. *Journal of Computational Physics*, *227*(10), 5342–5359. https://doi.org/10.1016/j.jcp.2008.01.047

Audier, M., & Guyot, P. (1986). QUASICRYSTALLINE AND CRYSTALLINE ATOMIC STRUCTURES OF Al4Mn. *Journal de Physique Colloques*, *47*(C3). https://doi.org/10.1051/jphyscol:1986341ï

Baake, M, Schlottmann, M., Kramer, P. H., & Zeidler, D. (1990). *Planar patterns with five-fold symmetry as sections of periodic structures in 4-space*.

Baake, Michael. (1999). *A guide to mathematical quasicrystals*.

Bak, P. (1985). Phenomenological Theory of Icosahedral Incommensurate ("Quasiperiodic") Order in Mn-Al Alloys. *Physical Review Letters*, *54*(14), 1517–1519. https://doi.org/10.1103/PhysRevLett.54.1517

Betke, U., & Henk, M. (2000). Densest lattice packings of 3-polytopes. *Computational Geometry*, *16*(3), 157–186. https://doi.org/10.1016/S0925-7721(00)00007-9

Bindi, L., Yao, N., Lin, C., Hollister, L. S., Andronicos, C. L., Distler, V. V., Eddy, M. P., Kostin, A., Kryachko, V., MacPherson, G. J., Steinhardt, W. M., Yudovskaya, M., & Steinhardt, P. J. (2015). Natural quasicrystal with decagonal symmetry. *Scientific Reports*, *5*(1), 1–5. https://doi.org/10.1038/srep09111

Boles, M. A., & Talapin, D. V. (2014). Self-assembly of tetrahedral cdse nanocrystals: Effective "patchiness" via anisotropic steric interaction. *Journal of the American Chemical Society*, *136*(16), 5868–5871. https://doi.org/10.1021/ja501596z

Boström, M., & Hovm̈ller, S. (2001). A pentagonal cluster in certain approximants to decagonal quasicrystals. *Acta Crystallographica Section B: Structural Science*, *57*(5), 646–651. https://doi.org/10.1107/S0108768101010539

Buganski, I., Wolny, J., & Takakura, H. (2020). The atomic structure of the Bergman-type icosahedral quasicrystal based on the Ammann-Kramer-Neri tiling. *Acta Crystallographica Section A: Foundations and Advances*, *76*, 180–196. https://doi.org/10.1107/S2053273319017339

Burkov, S. E. (1991). Structure model of the Al-Cu-Co decagonal quasicrystal. *Physical Review Letters*, *67*(5), 614–617. https://doi.org/10.1103/PhysRevLett.67.614

Chang, C. C., Wu, H. L., Kuo, C. H., & Huang, M. H. (2008). Hydrothermal synthesis of monodispersed octahedral gold nanocrystals with five different size ranges and their self-assembled structures. *Chemistry of Materials*, *20*(24), 7570–7574. https://doi.org/10.1021/cm8021984

Chen, E. R., Engel, M., & Glotzer, S. C. (2010). Dense crystalline dimer packings of regular tetrahedra. *Discrete and Computational Geometry*, *44*(2), 253–280. https://doi.org/10.1007/s00454-010-9273-0

Damasceno, P. F., Engel, M., & Glotzer, S. C. (2012a). Crystalline assemblies and densest packings of a family of truncated tetrahedra and the role of directional entropic forces. *ACS Nano*, *6*(1), 609–614. https://doi.org/10.1021/nn204012y

Damasceno, P. F., Engel, M., & Glotzer, S. C. (2012b). Predictive self-assembly of polyhedra into complex structures. *Science*, *337*(6093), 453–457. https://doi.org/10.1126/science.1220869

Damasceno, P. F., Glotzer, S. C., & Engel, M. (2017). Non-close-packed three-dimensional quasicrystals. *Journal of Physics Condensed Matter*, *29*(23). https://doi.org/10.1088/1361-648X/aa6cc1

de Bruijn, N. G. (1981). Algebraic theory of Penrose's non-periodic tilings of the plane. I. *Indagationes Mathematicae (Proceedings)*, *84*(1), 39–52. https://doi.org/10.1016/1385-7258(81)90016-0

DiVincenzo, D. P., & Steinhardt, P. J. (1999). *Quasicrystals* (Vol. 16). WORLD SCIENTIFIC. https://doi.org/10.1142/4293

Dixon, R. A. (1991). *Mathographics—Robert A. Dixon*. Dover Publications.

Dotera, T., Bekku, S., & Ziherl, P. (2017). Bronze-mean hexagonal quasicrystal. *Nature Materials*, *16*(10), 987–992. https://doi.org/10.1038/nmat4963

Duneau, M., & Gratias, D. (2007). Covering Clusters in Icosahedral Quasicrystals. In *Coverings of Discrete Quasiperiodic Sets* (pp. 23–62). Springer Berlin Heidelberg. https://doi.org/10.1007/3-540-45805-0_2

Durer, A. (1525). *Die Unterweysung der Messung, mit dem Zirckel unn Richtscheyt in Linien ebnen ganken corporen. &c. By DURER, Albrecht.: (1525) Signed by Author(s) | Sims Reed Ltd ABA ILAB*.

Dworkin, S., & Shieh, J. I. (1995). Deceptions in quasicrystal growth. *Communications in Mathematical Physics*, *168*(2), 337–352. https://doi.org/10.1007/BF02101553

Engel, M., & Trebin, H. R. (2008). Stability of the decagonal quasicrystal in the Lennard-Jones-Gauss system. *Philosophical Magazine*, *88*(13–15), 1959–1965. https://doi.org/10.1080/14786430802132548

Engel, Michael, Damasceno, P. F., Phillips, C. L., & Glotzer, S. C. (2015). Computational self-assembly of a one-component icosahedral quasicrystal. *Nature Materials*, *14*(1), 109–116. https://doi.org/10.1038/nmat4152

Filion, L., Hermes, M., Ni, R., Vermolen, E. C. M., Kuijk, A., Christova, C. G., Stiefelhagen, J. C. P., Vissers, T., Van Blaaderen, A., & Dijkstra, M. (2011). Self-assembly of a colloidal interstitial solid with tunable sublattice doping. *Physical Review Letters*, *107*(16), 168302. https://doi.org/10.1103/PhysRevLett.107.168302

Frank, N. P. (2008). A primer of substitution tilings of the Euclidean plane. *Expositiones Mathematicae*, *26*(4), 295–326. https://doi.org/10.1016/j.exmath.2008.02.001

Frenkel, D. (1999). Entropy-driven phase transitions. *Physica A: Statistical Mechanics and Its Applications*, *263*(1–4), 26–38. https://doi.org/10.1016/S0378-4371(98)00501-9

Frettlöh, D. (2008). Self-dual tilings with respect to star-duality. *Theoretical Computer Science*, *391*(1–2), 39–50. https://doi.org/10.1016/j.tcs.2007.10.028

Gabbrielli, R., Jiao, Y., & Torquato, S. (2012). Families of tessellations of space by elementary polyhedra via retessellations of face-centered-cubic and related tilings. *PHYSICAL REVIEW E*, *86*, 41141. https://doi.org/10.1103/PhysRevE.86.041141

Gähler, F. (1993). Matching rules for quasicrystals: The composition-decomposition method. In *Journal of Non-Crystalline Solids* (Vol. 153, Issue 154).

Gähler, F., M. Baake and M. Schlottmann. (1994). Binary tiling quasicrystals and matching rules. *Phys. Rev. B50* 12458–67.

Gähler, F. (2000). *CLUSTER COVERINGS: A POWERFUL ORDERING PRINCIPLE FOR QUASICRYSTALS*. 118–127. https://doi.org/10.1142/9789812793201_0004

Gardner, M. (1997). *Penrose Tiles to Trapdoor Ciphers: And the Return of Dr Matrix*. Cambridge University Press.

Gong, J., Newman, R. S., Engel, M., Zhao, M., Bian, F., Glotzer, S. C., & Tang, Z. (2017). Shape-dependent ordering of gold nanocrystals into large-scale superlattices. *Nature Communications*, *8*(1), 1–9. https://doi.org/10.1038/ncomms14038

Grimm, U., & Joseph, D. (1999). *ArXiv:cond-mat/9903074v1 [cond-mat.dis-nn] 4 Mar 1999*.

Grünbaum, B., & Shepherd, G. C. (1986). *Tilings and Patterns: Second Edition*. Dover Publications.

Gummelt, P. (1996). Penrose tilings as coverings of congruent decagons. *Geometriae Dedicata*, *62*(1), 1–17. https://doi.org/10.1007/BF00239998

Haji-Akbari, A., Engel, M., & Glotzer, S. C. (2011). Phase diagram of hard tetrahedra. *Journal of Chemical Physics*, *135*(19), 194101. https://doi.org/10.1063/1.3651370

Haji-Akbari, A., Engel, M., Keys, A. S., Zheng, X., Petschek, R. G., Palffy-Muhoray, P., & Glotzer, S. C. (2009). Disordered, quasicrystalline and crystalline phases of densely packed tetrahedra. *Nature*, *462*(7274), 773–777. https://doi.org/10.1038/nature08641

Han, I., Wang, K.L., Cadotte, A.T. *et al.* Formation of a single quasicrystal upon collision of multiple grains. *Nat Commun* **12,** 5790 (2021). https://doi.org/10.1038/s41467-021-26070-9

Hanfland, M., Syassen, K., Christensen, N. E., & Novikov, D. L. (2000). New high-pressure phases of lithium. *Nature*, *408*(6809), 174–178. https://doi.org/10.1038/35041515

Hann, C., Socolar, J. E. S., & Steinhardt, P. J. (2016). *Local growth of icosahedral quasicrystalline tilings*.

Harper, E. S., Marson, R. L., Anderson, J. A., Van Anders, G., & Glotzer, S. C. (2015). Shape allophiles improve entropic assembly. *Soft Matter*, *11*(37), 7250–7256. https://doi.org/10.1039/c5sm01351h

Henle, F. (2012). *Space-Filling Curves on Non-Periodic Tilings*.

Henley, C. L. (1988). Random tilings with quasicrystal order: Transfer-matrix approach. *Journal of Physics A: Mathematical and General*, *21*(7), 1649–1677. https://doi.org/10.1088/0305-4470/21/7/028

Henley, Christopher L. (1989). *Progress on the Atomic Structure of Quasicrystals*.

Henzie, J., Grünwald, M., Widmer-Cooper, A., Geissler, P. L., & Yang, P. (2011). Self-assembly of uniform polyhedral silver nanocrystals into densest packings and exotic superlattices. *Nature Materials*, *11*(2), 131–137. https://doi.org/10.1038/nmat3178

Henzie, J., Grünwald, M., Widmer-Cooper, A., Geissler, P. L., & Yang, P. (2012). Self-assembly of uniform polyhedral silver nanocrystals into densest packings and exotic superlattices. *Nature Materials*, *11*(2), 131–137. https://doi.org/10.1038/nmat3178

Hong, F., Long-Guang, L., & Xiu-Jun, F. (2009). Covering Rules and Nearest Neighbour Configurations of the Dodecagonal Quasiperiodic Structure. *Chinese Physics Letters*, *26*(5), 056103. https://doi.org/10.1088/0256-307x/26/5/056103

Hynninen, A.-P., Thijssen, J. H. J., Vermolen, E. C. M., Dijkstra, M., & van Blaaderen, A. (2007). Self-assembly route for photonic crystals with a bandgap in the visible region. *Nat. Mater.*, *6*(3), 202–205. https://doi.org/10.1038/nmat1841

Indelicato, G., Keef, T., Cermelli, P., Salthouse, D. G., Twarock, R., & Zanzotto, G. (2012). Structural transformations in quasicrystals induced by higher dimensional lattice transitions. *Proceedings of the Royal Society A: Mathematical, Physical and Engineering Sciences*, *468*(2141), 1452–1471. https://doi.org/10.1098/rspa.2011.0680

IUCr. (1992). Report of the Executive Committee for 1991. *Acta Crystallographica Section A Foundations of Crystallography*, *48*(6), 922–946. https://doi.org/10.1107/s0108767392008328

Janot, C. (1997). Atomic clusters, local isomorphism, and recurrently localized states in quasicrystals. *Journal of Physics Condensed Matter*, *9*(7), 1493–1508. https://doi.org/10.1088/0953-8984/9/7/013

Janot, C., & De Boissieu, M. (1994). Quasicrystals as a hierarchy of clusters. *Physical Review Letters*, *72*(11), 1674–1677. https://doi.org/10.1103/PhysRevLett.72.1674

Jaoshvili, A., Esakia, A., Porrati, M., & Chaikin, P. M. (2010). Experiments on the Random Packing of Tetrahedral Dice. *Physical Review Letters*, *104*(18), 185501. https://doi.org/10.1103/PhysRevLett.104.185501

Jarić, M. V. (1988). *Introduction to Quasicrystals—1st Edition*. Academic Press.

Jazbec, S. (2009). *The Properties and Applications of Quasicrystals Seminar II*.

Jeong, H. C., & Steinhardt, P. J. (1994). Cluster approach for quasicrystals. *Physical Review Letters*, *73*(14), 1943–1946. https://doi.org/10.1103/PhysRevLett.73.1943

Jing, S., Xing, S., Wang, Y., Hu, H., Zhao, B., & Zhao, C. (2008). Synthesis of 3D well-packed octahedral PbS nanocrystal arrays. *Materials Letters*, *62*(6–7), 977–979. https://doi.org/10.1016/j.matlet.2007.07.024

Katz, A. (1988). Theory of Matching Rules for the 3-Dimensional Penrose Tilings. *Communications in Mathematical Physics*. *118*, 263–288.

Keys, A. S., Iacovella, C. R., & Glotzer, S. C. (2011). Characterizing complex particle morphologies through shape matching: Descriptors, applications, and algorithms. *Journal of Computational Physics*, *230*, 6438–6463. https://doi.org/10.1016/j.jcp.2011.04.017

Khadilkar, M. R., Agarwal, U., & Escobedo, F. A. (2013). Phase behavior of binary mixtures of hard convex polyhedra. *Soft Matter*, *9*(48), 11557–11567. https://doi.org/10.1039/c3sm51822a

Khadilkar, M. R., & Escobedo, F. A. (2012). Self-assembly of binary space-tessellating compounds. *The Journal of Chemical Physics*, *137*(19), 194907. https://doi.org/10.1063/1.4765699

Khadilkar, M. R., & Escobedo, F. A. (2014). Heuristic rule for binary superlattice coassembly: Mixed plastic mesophases of hard polyhedral nanoparticles. *Physical Review Letters*, *113*(16). https://doi.org/10.1103/PhysRevLett.113.165504

Kramer, P. (1999). Quasicrystals: Atomic coverings and windows are dual projects. *Journal of Physics A: Mathematical and General*, *32*(31), 5781–5793. https://doi.org/10.1088/0305-4470/32/31/304

Lagarias, J. (2015). *Packing Space with Regular Tetrahedra*.

Levine, D., & Steinhardt, P. J. (1984). Quasicrystals: A New Class of Ordered Structures. *Physical Review Letters*, *53*, 2477. https://doiorg/10.1103/PhysRevLett.53.2477

Levine, D., & Steinhardt, P. J. (1986a). Quasicrystals. I. Definition and structure. *Physical Review B*, *34*(2), 596–616. https://doi.org/10.1103/PhysRevB.34.596

Levine, D., & Steinhardt, P. J. (1986b). Quasicrystals. I. Definition and structure. *Physical Review B*, *34*(2), 596–616. https://doi.org/10.1103/PhysRevB.34.596

Li, H., Ma, H., Hou, L., Guo, M., & He, Z. (2017). Shield-like tile and its application to the decagonal quasicrystal-related structures in Al-Cr-Fe-Si alloys. *Journal of Alloys and Compounds*, *701*, 494–498. https://doi.org/10.1016/j.jallcom.2017.01.105

Li, X. Z. (1995). Structure of Al–Mn decagonal quasicrystal. I. A unit-cell approach. *Acta Crystallographica Section B*, *51*(3), 265–270. https://doi.org/10.1107/S0108768194012954

Li, X. Z., & Frey, F. (1995). Structure of Al–Mn decagonal quasicrystal. II. A high-dimensional description. *Acta Crystallographica Section B*, *51*(3), 271–275. https://doi.org/10.1107/S0108768194013078

Liao, L., Fu, X., & Hou, Z. (2010). Quasi-unit cell description of two-dimensional octagonal quasilattice. *Physica B: Condensed Matter*, *405*(3), 875–879. https://doi.org/10.1016/j.physb.2009.10.006

Liao, L. G., Zhang, W. Bin, Yu, T. X., & Cao, Z. X. (2013). A single cluster covering for dodecagonal quasiperiodic ship tiling. *Chinese Physics Letters*, *30*(2), 026102. https://doi.org/10.1088/0256-307X/30/2/026102

Liao, L., Zhang, W., Yu, T., & Cao, Z. (2013). A self-similar transformation for a dodecagonal quasiperiodic covering with T-clusters. *Journal of Physics A: Mathematical and Theoretical*, *46*(24), 245205. https://doi.org/10.1088/1751-8113/46/24/245205

Lifshitz, R. (2000). *The definition of quasicrystals*.

Lin, C., Steinhardt, P. J., & Torquato, S. (2017). Hyperuniformity variation with quasicrystal local isomorphism class. *Journal of Physics Condensed Matter*, *29*(20). https://doi.org/10.1088/1361-648X/aa6944

Livio, M. (2003). *The Golden Ratio: The Story of PHI, the World's Most Astonishing Number*. Broadway Books.

Lord, E. A., & Ranganathan, S. (2001). The Gummelt decagon as a "quasi unit cell." *Acta Crystallographica Section A: Foundations of Crystallography*, *57*(5), 531–539. https://doi.org/10.1107/S0108767301007504

Lord, Eric A., Mackay, A. L., & Ranganathan, S. (2006). *New geometries for new materials | Request PDF*.

Lu, F., Yager, K. G., Zhang, Y., Xin, H., & Gang, O. (2015). Superlattices assembled through shape-induced directional binding. *Nature Communications*, *6*(1), 1–10. https://doi.org/10.1038/ncomms7912

Lu, W., Liu, Q., Sun, Z., He, J., Ezeolu, C., & Fang, J. (2008). Super crystal structures of octahedral c-In2O3 nanocrystals. *Journal of the American Chemical Society*, *130*(22), 6983–6991. https://doi.org/10.1021/ja078303h

Lück, R. (1990). Matching rules for the icosahedral penrose tiling derived by inflation-deflation procedures. *Journal of Non-Crystalline Solids*, *117–118*(PART 2), 820–823. https://doi.org/10.1016/0022-3093(90)90654-5

Madison, A. E. (2014). Self-similarity and self-inversion of quasicrystals. *Physics of the Solid State*, *56*(8), 1706–1716. https://doi.org/10.1134/S1063783414080162

Madison, A. E., & Madison, P. A. (2019). Looking for alternatives to the superspace description of icosahedral quasicrystals. *Proceedings of the Royal Society A: Mathematical, Physical and Engineering Sciences*, *475*(2221). https://doi.org/10.1098/rspa.2018.0667

Madison, Alexey E. (2015). Substitution rules for icosahedral quasicrystals. *RSC Advances*, *5*(8), 5745–5753. https://doi.org/10.1039/c4ra09524c

Mihalkovič, M., Mihalkovič, M., Al-Lehyani, I., Cockayne, E., Henley, C. L., Moghadam, N., Moriarty, J. A., Wang, Y., & Widom, M. (2002). Total-energy-based prediction of a quasicrystal structure. *Physical Review B - Condensed Matter and Materials Physics*, *65*(10), 1042051–1042056. https://doi.org/10.1103/PhysRevB.65.104205

Minkowski, H. (1904). Dichteste gitterförmige Lagerung kongruenter Körper. *Nachrichten von Der Gesellschaft Der Wissenschaften Zu Göttingen, Mathematisch-Physikalische Klasse*, *1904*, 311–355.

Mukhopadhyay, N. K., Chattopadhyay, K., & Ranganathan, S. (1996). Ordering transformation in icosahedral quasicrystals and related crystalline phases. *Bulletin of Materials Science*, *19*(5), 717–723. https://doi.org/10.1007/BF02745191

Nagao, K., Inuzuka, T., Nishimoto, K., & Edagawa, K. (2015). Experimental Observation of Quasicrystal Growth. *Physical Review Letters*, *115*(7), 075501. https://doi.org/10.1103/PhysRevLett.115.075501

Neudecker, M., Ulrich, S., Herminghaus, S., & Schröter, M. (2013). Jammed frictional tetrahedra are hyperstatic. *Physical Review Letters*, *111*(2), 028001. https://doi.org/10.1103/PhysRevLett.111.028001

Onoda, G. Y., Steinhardt, P. J., Divincenzo, D. P., & Socolar, J. E. S. (1988). Growing perfect quasicrystals. *Physical Review Letters*, *60*(25), 2653–2656. https://doi.org/10.1103/PhysRevLett.60.2653

Oxborrow, M., & Henley, C. L. (1993). Random square-triangle tilings: A model for twelvefold-symmetric quasicrystals. *Physical Review B*, *48*(10), 6966–6998. https://doi.org/10.1103/PhysRevB.48.6966

Penrose, R. (1974). The role of aesthetics in pure and applied mathematical research. *Bull.Inst.Math.Appl.*, *10*, 266–271.

Penrose, R. (1979). *Pentaplexity1.gif (666×919)*.

Penrose, R. (1989). *Tilings and Quasi-Crystals; a Non-Local Growth Problem?* (Vol. 2, pp. 53–79). Elsevier. https://doi.org/10.1016/b978-0-12-040602-9.50007-5

Polyakov, A. A. (2008). Presentation of Penrose tiling as set of overlapping pentagonal stars. *Journal of Physics: Conference Series*, *98*(1). https://doi.org/10.1088/1742-6596/98/1/012025

Pope, A. L., & Tritt, T. M. (2006). Thermal Conductivity of Quasicrystalline Materials. In *Thermal Conductivity* (pp. 255–259). Springer US. https://doi.org/10.1007/0-387-26017-x_11

Posamentier, A. S. (2007). *The Fabulous Fibonacci Numbers—Harvard Book Store*. Prometheus Books.

Robinson, R. M. (1971). Undecidability and Nonperiodicity for Tilings of the Plane. In *Lnventiones math* (Vol. 12). Springer-Verlag.

Rokhsar, D. S., Mermin, N. D., & Wright, D. C. (1987). Rudimentary quasicrystallography: The icosahedral and decagonal reciprocal lattices. *Physical Review B*, *35*(11), 5487–5495. https://doi.org/10.1103/PhysRevB.35.5487

Roth, J., & Denton, A. R. (2000). Solid-phase structures of the Dzugutov pair potential. *Physical Review E - Statistical Physics, Plasmas, Fluids, and Related Interdisciplinary Topics*, *61*(6 B), 6845–6857. https://doi.org/10.1103/PhysRevE.61.6845

Ryltsev, R., Klumov, B., & Chtchelkatchev, N. (2015). Self-assembly of the decagonal quasicrystalline order in simple three-dimensional systems. *Soft Matter*, *11*(35), 6991–6998. https://doi.org/10.1039/c5sm01397f

Schenk, S., Zollner, E. M., Krahn, O., Schreck, B., Hammer, R., Förster, S., & Widdra, W. (2019). Full real-space analysis of a dodecagonal quasicrystal. *Acta Crystallographica Section A: Foundations and Advances*, *75*, 307–313. https://doi.org/10.1107/S2053273319000056

Senechal, M. (2008). Mapping the aperiodic landscape. *Philosophical Magazine*, *88*, 13–15. https://doi.org/10.1080/14786430802077917

Senechal, Marjorie. (2007). Thoughts on “crystal.” *Zeitschrift Für Kristallographie*, *222*(6), 311–311. https://doi.org/10.1524/zkri.2007.222.6.311_2

Shechtman, D., Blech, I., Gratias, D., & Cahn, J. W. (1984). Metallic phase with long-range orientational order and no translational symmetry. In *Physical Review Letters* (Vol. 53, Issue 20). https://doi.org/10.1103/PhysRevLett.53.1951

Singh, P. (1985). The so-called fibonacci numbers in ancient and medieval India. *Historia Mathematica*, *12*(3), 229–244. https://doi.org/10.1016/0315-0860(85)90021-7

Socolar, J. E. S., & Steinhardt, P. J. (1986). Quasicrystals. II. Unit-cell configurations. *Physical Review B*, *34*(2), 617–647. https://doi.org/10.1103/PhysRevB.34.617

Song, Q., Ding, Y., Wang, Z. L., & Zhang, Z. J. (2006). Formation of orientation-ordered superlattices of magnetite magnetic nanocrystals from shape-segregated self-assemblies. *Journal of Physical Chemistry B*, *110*(50), 25547–25550. https://doi.org/10.1021/jp0652695

Steinhardt, P. J., & Jeong, H. C. (1996). A simpler approach to Penrose tiling with implications for quasicrystal formation. *Nature*, *382*(6590), 431–433. https://doi.org/10.1038/382431a0

Steinhardt, P J, & Ostlund, S. (1987). The Physics of Quasicrystals. In *The Physics of Quasicrystals*. WORLD SCIENTIFIC. https://doi.org/10.1142/0391

Steinhardt, Paul J., Nelson, D. R., & Ronchetti, M. (1983). Bond-orientational order in liquids and glasses. *Physical Review B*, *28*(2), 784–805. https://doi.org/10.1103/PhysRevB.28.784

Steurer, W. (2018). Quasicrystals: What do we know? What do we want to know? What can we know? In *Acta Crystallographica Section A: Foundations and Advances* (Vol. 74, Issue 1, pp. 1–11). International Union of Crystallography. https://doi.org/10.1107/S2053273317016540

Steurer, W., & Deloudi, S. (2009). *Crystallography of Quasicrystals* (Vol. 126). Springer Berlin Heidelberg. https://doi.org/10.1007/978-3-642-01899-2

Strandburg, K. J. (1991). Entropy of a three-dimensional random-tiling quasicrystal. *Physical Review B*, *44*(9), 4644–4646. https://doi.org/10.1103/PhysRevB.44.4644

Strandburg, K. J., & Dressel, P. R. (1990). Thermodynamic behavior of a Penrose-tiling quasicrystal. *Physical Review B*, *41*(4), 2469–2478. https://doi.org/10.1103/PhysRevB.41.2469

Suck, J. B. (2002). *Quasicrystals: An Introduction to Structure, Physical Properties and Applications*.

Takakura, H., Gómez, C. P., Yamamoto, A., De Boissieu, M., & Tsai, A. P. (2007). Atomic structure of the binary icosahedral Yb-Cd quasicrystal. *Nature Materials*, *6*(1), 58–63. https://doi.org/10.1038/nmat1799

Tasios, N., Gantapara, A. P., & Dijkstra, M. (2014). Glassy dynamics of convex polyhedra. *The Journal of Chemical Physics*, *141*(22), 224502. https://doi.org/10.1063/1.4902992

Teich, E. G., Van Anders, G., Klotsa, D., Dshemuchadse, J., & Glotzer, S. C. (2016). Clusters of polyhedra in spherical confinement. *Proceedings of the National Academy of Sciences of the United States of America*, *113*(6), E669–E678. https://doi.org/10.1073/pnas.1524875113

Torquato, S., & Jiao, Y. (2009). Dense packings of the Platonic and Archimedean solids. *Nature*, *460*(7257), 876–879. https://doi.org/10.1038/nature08239

Van Anders, G., Ahmed, N. K., Smith, R., Engel, M., & Glotzer, S. C. (2014). Entropically patchy particles: Engineering valence through shape entropy. *ACS Nano*, *8*(1), 931–940. https://doi.org/10.1021/nn4057353

Van Anders, G., Klotsa, D., Ahmed, N. K., Engel, M., & Glotzer, S. C. (2014). Understanding shape entropy through local dense packing. *Proceedings of the National Academy of Sciences of the United States of America*, *111*(45), E4812–E4821. https://doi.org/10.1073/pnas.1418159111

Wan, Y., Cai, Z., Xia, L., Wang, L., Li, Y., Li, Q., & Zhao, X. S. (2009). Simulation and fabrication of binary colloidal photonic crystals and their inverse structures. *Materials Letters*, *63*(24–25), 2078–2081. https://doi.org/10.1016/j.matlet.2009.06.034

Wang, H. (1961). Proving Theorems by Pattern Recognition—II. *Bell System Technical Journal*, *40*(1), 1–41. https://doi.org/10.1002/j.1538-7305.1961.tb03975.x

Wolfram, S. "The Story of Thorn." 2019, https://sudonull.com/post/1486-The-Story-of-Thorn

Wolny, J., Bugański, I., & Strzałka, R. (2018). Model refinement of quasicrystals. In *Crystallography Reviews* (Vol. 24, Issue 1, pp. 22–64). Taylor and Francis Ltd. https://doi.org/10.1080/0889311X.2017.1340276

Xie, S., Zhou, X., Han, X., Kuang, Q., Jin, M., Jiang, Y., Xie, Z., & Zheng, L. (2009). Supercrystals from Crystallization of Octahedral MnO Nanocrystals. *The Journal of Physical Chemistry C*, *113*(44), 19107–19111. https://doi.org/10.1021/jp907651d

Yamamoto, A., Takakura, H., & Tsai, A. P. (2003). Six-dimensional model of icosahedral Al-Pd-Mn quasicrystals. *Physical Review B - Condensed Matter and Materials Physics*, *68*(9), 094201. https://doi.org/10.1103/PhysRevB.68.094201

Zhanbing, H., Maurice, J, Ma, H., Wang, Y., Zhang, T., Ma, X., Steurer, W., (2021). Carousel-like phason flips in $Al_{60}Cr_{20}Fe_{10}Si_{10}$. *Acta Crystallographica,* A77. https://doi.org/10.1107/S2053273321007518

Zhang, J., Luo, Z., Quan, Z., Wang, Y., Kumbhar, A., Smilgies, D. M., & Fang, J. (2011). Low packing density self-assembled superstructure of octahedral Pt 3Ni nanocrystals. *Nano Letters*, *11*(7), 2912–2918. https://doi.org/10.1021/nl201386e

Zhang, L., Wu, J., Liao, H., Hou, Y., & Gao, S. (2009). Octahedral Fe3O4 nanoparticles and their assembled structures. *Chemical Communications*, *29*, 4378. https://doi.org/10.1039/b906636e